Studies in Framework Science

Metal-organic Framework Composites
BET Theory and Adsorption
Reticular Chemistry and DNA Frameworks

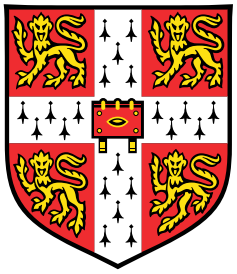

Johannes W. M. Osterrieth

Department of Chemical Engineering & Biotechnology
University of Cambridge

This dissertation is submitted for the degree of
Doctor of Philosophy

St. Edmunds College September 2021

'*It is better to be lucky. But I would rather be exact. Then when luck comes you are ready*' -
Ernest Hemingway, The Old Man and the Sea

To my family to whom I owe so much

Declaration

I hereby declare that except where specific reference is made to the work of others, the contents of this dissertation are original and have not been submitted in whole or in part for consideration for any other degree or qualification in this, or any other university. This dissertation is my own work and contains nothing which is the outcome of work done in collaboration with others, except as specified in the text and Acknowledgements. This dissertation contains fewer than 65,000 words including appendices, bibliography, footnotes, tables and equations and has fewer than 150 figures.

Johannes W. M. Osterrieth
September 2021

Acknowledgements

It would be impossible to thank everyone who has contributed to this dissertation. My particular thanks go to my supervisor Dr David Fairen-Jimenez for his constant mentorship and guidance. I have learnt so much from his patient and thorough approach to research, and it will always have been a great pleasure to have had the chance to study and work in his research group.

Likewise, I would like to thank senior postdoc and my particular friend Dr David Madden for his inspiration and his believing in me. I wish him and his new family all the best for the future years.

Thank you to the NanoDTC and its leadership during my years, Dr Karishma Jain and Prof Jeremy Baumberg. The Engineering and Physical Sciences Research Council (EPSRC) has kindly funded my project.

I would also particularly like to thank Prof Omar Farha for letting me join his lab in the beginning of my PhD – I can safely say that none of this work would have happened without him and his kind invitation to come to the US at the beginning of my PhD.

During my PhD, I have had the great privilege to travel to many places, including Paklenica, Croatia (2016); Eindhoven, the Netherlands (2017); Berkeley, California (2017); Evanston and Chicago, Illinois (2017-2018); Praia de Porto Novo, Portugal (2018); Auckland, New Zealand (2018); Stockholm, Sweden (2019); Tokyo, Japan (2019); Paris, France (2019). I would like to thank all funding bodies that have made this possible: the Winton Programme, the EPSRC, and St Edmunds College, Cambridge.

Demelza Wright, Luka Skoric, Bill Stockham, and the whole NanoDTC have been fantastic friends and collaborators. I would also like to thank the following collaborators: Dr Hyunho Noh, Prof Chung-wei Kung, Dr Louis Redfern, Sylvia Hanna, and the rest of the Northwestern MOF team. They have been great friends and co-workers and have made me feel very welcome during my stay in Illinois. Dr Ermanno Miele and Dr Ioanna Mela have been a huge help conducting experiments in optics and and other imaging techniques. I am

especially grateful to James Rampersad who patiently translated my first version of BETSI from MATLAB into python. Without his incredible work, the little pet project I started on a rainy afternoon would never have ended up being so significant to this dissertation. Thanks to Nakul Rampal who has taken this project over and is designing a shiny website to host BETSI.

Finally, I would like to thank all those people closest to me: My incredible friends and housemates in Cambridge, my wonderful partner Rachael, and my family, which, to my great delight, has grown during my years in Cambridge.

Abstract

Surfaces and self-assembly, two quintessential parts of modern nanotechnology, meet in the porous framework, a material formed by self-assembly and consisting only of surfaces, no bulk. This dissertation outlines the triangular relationship between frameworks, surfaces, and self-assembly. As such, it is organised in three distinct projects each corresponding to one of the three poles of this triangle.

Frameworks | In this project, the chemistry of metal-organic framework (MOF) composites is explored. MOFs are porous coordination crystals made from the assembly of metal nodes and organic linkers. The Zr-MOF NU-901, which is known for its high thermal and chemical stability, is grown around plasmonic gold nanorods (AuNRs) in a core-shell bottle-around-ship encapsulation, and the synthesis is optimised to various morphology parameters. The resulting AuNR@NU-901 composites have multiple plasmonic applications. First, their use as drug delivery vehicles is explored: in this project, the photothermal energy conversion of AuNRs is used to trigger drug release from a MOF's porosity under near-infrared light activation. In the second application, the composites were used as size-selective Raman sensors. Here, the MOFs porosity was used as a size-exclusion filter to gate the access of molecules to the plasmonic core where their characteristic Raman signal was amplified. In this proof-of-principle study, size-selective sensing from a mixed analyte solution was demonstrated, making AuNR@NU-901 a viable candidate for potential pollutant or pesticide sensing.

Surfaces | The Brunauer-Emmett-Teller (BET) theory is one of the most widely used equations in physical chemistry. Developed in the 1930s, to this day it remains the most important figure of merit in porosimetry with far-reaching industrial and academic influences. Despite its widespread use, there remain significant issues with the manual calculation of BET surface areas. To probe this, 115 international collaborators with a strong track record in the study of nanoporous materials were brought together in a round-robin experiment: they were sent 18 anonymised isotherms and were asked to calculate their BET areas in the way they most saw fit. The results from this study show that reproducibility of BET area determination from identical isotherms is a largely ignored issue, raising critical concerns

over the reliability of reported BET areas in the literature. To solve this major issue, a new algorithmic approach was developed to accurately and systematically determine the BET area of nanoporous materials.

Self-assembly | Metal-organic frameworks and periodic DNA nanostructures are both assembled from constituent nodes and linkers. The similarities between these assemblies are herein described, and a common language for MOF chemistry and DNA crystals is developed: *reticular colouring design* (RCD). RCD not only represents a novel lens through which existing DNA crystals can be viewed, it can also lead to new and innovative designs by exploiting graph theoretical concepts of network topology that were developed for MOFs and related frameworks. As such, this project connects the dots and introduces two fields to one another that have traditionally little association.

The triangular relationship *frameworks – surfaces – self-assembly* has appeared throughout this dissertation and my academic career at Cambridge. It has blessed me with an unconventionally multipolar PhD with interdisciplinary research and outside-the-box inspirations at the forefront. I hope that the dissertation standing at the end of this incredible journey will be of interest to the reader and contribute to some small extent to academic research and society.

Publications pertaining to this thesis:

1. Johannes W. M. Osterrieth; Demelza Wright; Hyunho Noh, Chung-Wei Kung; Diana Vulpe; Aurelia Li; Ji Eun Park; Richard P. Van Duyne; Peyman Z. Moghadam; Jeremy J. Baumberg; Omar K. Farha; David Fairen-Jimenez; **Core - Shell Gold Nanorod@Zirconium-Based Metal - Organic Framework Composites as in Situ Size-Selective Raman Probes**; J. Am. Chem. Soc. **2019**, 141, 3893–3900.

2. Johannes W. M. Osterrieth; David Fairen-Jimenez; **Metal–Organic Framework Composites for Theragnostics and Drug Delivery Applications**; Biotechnol. J. **2021**, 16, 2000005.

3. Johannes W. M. Osterrieth, James Rampersad, David Madden, Nakul Rampal, Luka Skoric, Bethany Connolly; Mark Allendorf, Vitalie Stavila, Jonathan Snider; Rob Ameloot, João Marreiros; Conchi Ania; Diana Azevedo, Enrique Vilarrasa-Garcia, Bianca Santos; Xian-He Bu, Xe Zang; Hana Bunzen; Neil Champness; Banglin Chen, Rui-Biao Lin; Benoit Coasne; Seth Cohen, Jessica C Moreton; Yamil Colon; Andrew Cooper, Linjiang Chen; FX Coudert; Yong Cui, Bang Hou; Deanna D'Alessandro, Patrick Doheny; Mircea Dincă, Chenyue Sun; Christian Doonan, Michael Thomas Huxley; Jack D. Evans; Paolo Falcaro, Raffaele Ricco; Omar Farha, Karam Idrees; Pingyun Feng, Huajun Yang; Ross Forgan, Dominic Bara; Shuhei Furukawa, Eli Sanchez; Jorge Gascon, Selvedin Telalovic; Sujit K. Ghosh, Soumya Mukherjee; Patricia Horcajada, Pabledo Salcedo; Katsumi Kaneko, Radovan Kukobat; Jeff Kenvin; Seda Keskin; Susumu Kitagawa, Kenichi Otake; Ryan Lively, Stephen Dewitt; Phillip Llewellyn; Bettina Lotsch, Sebastian T. Emmerling, Alexander M. Pütz; Carlos Martí-Gastaldo, Natalia Padial; Javier García-Martínez, Noemi Linares; Daniel Maspoch, Jose Antonio Suarez; Peyman Moghadam, Rama Oktavian; Russel Morris, Paul Wheatley; Jorge Navarro; Camille Petit, David Danaci; Matthew Rosseinsky, Alexandros Katsoulidis; Martin Schröder, Xue Han, Sihai Yang; Christian Serre, Georges Mouchaham; David S. Sholl, Raghuram Thyagarajan; Daniel Siderius; Randall Q. Snurr, Rebecca Goncalves; Valeska Ting, Jemma Rowlandson; Takashi Uemura, Tomoya Iiyuka; Monique van der Veen, Davide Rega; Veronique Van Speybroeck, Sven M. J. Rogge, Aran Lamaire; Krista Walton; Stefan Wuttke, Jacopo Andreo; Omar Yaghi, Bing Zhang; Cafer T. Yavuz, Thien S. Nguyen; Felix Zamora, Carmen Montoro; Hongcai Zhou, Angelo Kirchon; David Fairen-Jimenez; **How reproducible are surface areas calculated from the BET equation?**; Under review; preprint DOI 10.26434/chemrxiv.14291644

4. Johannes W. M. Osterrieth; David Fairen-Jimenez; **Reticular Design in DNA Nanotechnology**; **(in preparation)**

Table of contents

List of figures

List of tables

Nomenclature

Acronyms / Abbreviations

AFM Atomic force microscopy

AuNP Gold nanoparticle

AuNR Gold nanorod

BDC Benzene dicarboxylic acid

BET Brunauer-Emmett-Teller

BETSI BET Surface Identification

CARS Coherent anti-stokes resonance spectroscopy

CCD Charge-coupled device

CCSD Cambridge Crystallography Structural Database

cit citrate

CTAB Cetrimonnium bromide

CVD Chemical vapour deposition

DCM Dichloromethane

DLVO Derjaguin-Landau-Verwey-Overbeek

DMF Dimethyl formamide

DX Double crossover

EDTA Ethylenediaminetetraacetic acid

HKUST-1 Hong Kong University of Science and Technology - 1

HRTEM High-resolution transmission electron microscopy

IDT Integrated DNA Technologies

IRMOF Isoreticular MOF

LED Light-emitting diode

LMCT Ligand-to-metal charge transfer

LSPR localised surface plasmon resonance

MIL Materials Institute Lavoisier

MOF Metal-organic framework

MUA Mercaptoundecanoic acid

nIR near-infrared

nMOF nano-MOF

NP Nanoparticle

PAGE Polyacrylamide gel electrophoresis

PBS Phosphate-buffered saline

PCP Porous-coordination polymer

PCR Polymerase chain reaction

PDT Photodynamic therapy

PEG Poly(ethylene)glycol

PPTT Plasmonic photothermal therapy

PVP Polyvinylpyrrolidone

PXRD Powder X-ray diffraction

QCM Quartz crystal microbalance

QD Quantum Dot

RCD Reticular colouring design

RCSR Reticular Chemistry Structural Database

RT Room temperature

SBU Secondary vuilding unit

SDS Sodium dodecylsulfate

SEM Scanning electron microscopy

SERS Surface-enhanced Raman spectroscopy

SURMOF Surface MOF

TEM Transmission electron microscopy

Tris Tris(hydroxymethyl)aminomethane

UV/vis Ultra-violet/visible

UV Ultra-violet

ZIF-8 Zeolite imidazolate framework - 8

Chapter 1

Introduction

Surfaces and self-assembly, two integral parts of modern nanotechnology, meet in the porous framework, a material formed by self-assembly consisting only of surfaces, no bulk. In this introduction to the thesis, the reader is familiarised with the three distinct projects that make up the thesis and their connection to the triangular relationship of *frameworks–surfaces–self-assembly* that is this dissertation's golden thread. Relevant principles and themes that appear throughout the thesis are introduced as well as the most prevalent characterisation techniques.

1.1 Surfaces, Self-assembly, and the porous Framework

Nanotechnology is a cause célèbre these days. Capturing the imagination of Hollywood screenwriters and science fiction authors alike, it is perceived to be futuristic, dystopean, dark, powerful, and near magical in its ability to transform the material world. We are promised nanobots that rejuvenate us like a molecular Fountain of Youth, molecular 'assemblers' that create objects literally from constituent atoms, and of course the disastrous consequence of our phaetonic ambitions: a world covered in self-replicating nanomachines, also known as *grey goo*.

In the academic world, things are (somewhat) more humble. Here, 'nanotechnology' (from Ancient Greek *'nanos'* for *dwarf*) refers to the manipulation of matter on the nanoscale, that is between 1-100 nm. Unfortunately, this means everything and nothing, for under this broad definition, nanotechnology covers probably 50% of chemistry, pretty much all of molecular biology, and more and more of solid-state physics. As a consequence, the term has, regrettably, become inflationary – after all, what do enzymes and computer chips really have in common?

In this author's personal opinion, nanotechnology means two things: first of all, *interfaces*, or *surfaces*. Far from the notion of the impenetrable, liminal barrier that we associate surfaces with in our everyday experience, they are instead the stages for rich chemistry, physics, and biology. They appear almost metaphorically at precisely those interdisciplinary realms where the lines between traditional disciplines of science blur – just think of cell membranes, with their biophysical ion-pumps, or the ozone-layer, in which a triatomic oxygen molecule shields us from solar UV-radiation. In any case, enrichment of matter near an interface, or *adsorption*, is required for interfaces to fulfil their role as chemical stages. Naturally, therefore, adsorption plays a crucial role in this thesis. In nanotechnology, surfaces are ubiquitous: the small surface area/volume ratios that nanoparticles exhibit is arguably the only overarching property that all species in the nano-domain have in common, making surfaces an integral part of this field of science.

The second notion that the author considers vital to nanotechnology is that of *self-assembly*. At this point a personal disclaimer must be made: as a trained chemist, the author is forevermore partial towards this *bottom-up* nanoconstruction than to its cousin, *top-down* fabrication, with its technical micromanipulation of matter. In a universe that is constantly trying to achieve the greatest state of disorder and randomness, it is hard to imagine anything more beautiful than the self-organisation of matter from its constituent building blocks. Self-assembly can take place from direct molecular recognition, in which complementary information of two or more building blocks drives the association; this is famously true for DNA strand hybridisation. Alternatively, self-assembly can emerge from less-specific but

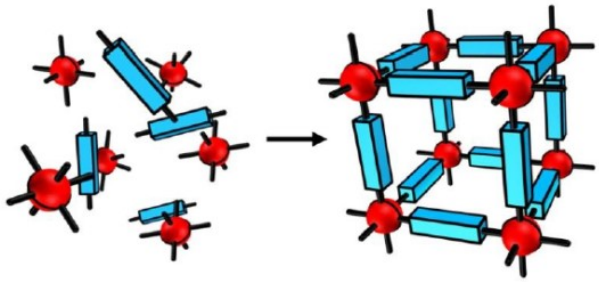

Fig. 1.1 Formation of a Framework | Surfaces and self-assembly meet in the porous framework, a material formed by self-assembly consisting only of surfaces and no bulk. Image credit Chris Wilmer.

nonetheless local interactions between constituent building blocks, the total sum of which exerts a global, self-organising influence. In this case, the assembly becomes more than the sum of its parts, *e.g.* self-assembled monolayers or colloidal super-crystallisation.

These quintessences of nanotechnology, surfaces, and self-assembly meet at the porous *framework*, a material formed by the self-assembly of molecules and consisting virtually only of surfaces, no bulk. It is the colossal porosity of a framework that gives it its enormous surface area: practically every atom in a framework lies at an interface, be it on the exterior or in the internal porosity. Frameworks form when rigid, molecular building blocks with highly directional bonding self-assemble. In those where the chemical bonds between the building blocks are dative/coordinate, the resulting structure is called a *porous-coordination polymer*. The most prominent of this class are *metal-organic frameworks* (MOFs), consisting of metal atom clusters that are connected by organic linkers. MOFs are, for the large part, the basis of this thesis and due to their pivotal role they are later introduced in this chapter.

This dissertation moves along the triangular relationship of surfaces, self-assembly, and frameworks, that sits at the very centre of nanotechnology. In its wide scope, the reader is introduced to interdisciplinary science spanning multiple theories, characterisation techniques, and synthetic methods.

1.2 Themes & Organisation

The dissertation is organised in three distinct projects that fall within the triangular relationship between frameworks, surfaces, and self-assembly (Figure 1.2).

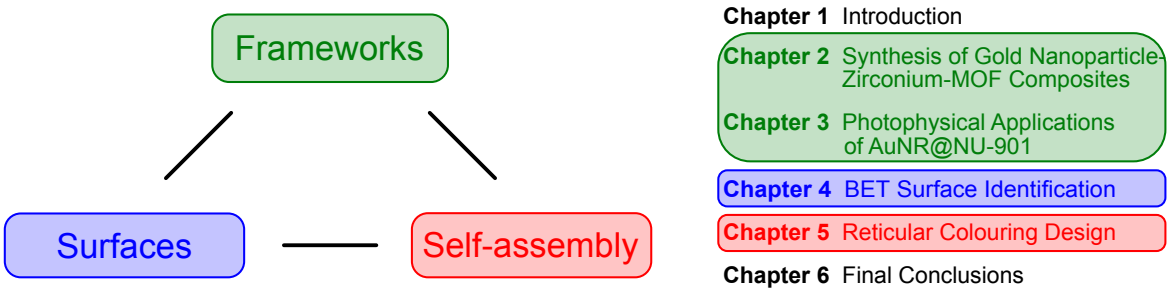

Fig. 1.2 Organisation of Dissertation | The triangular relationship between frameworks, surfaces and self-assembly, and where the dissertation's projects lie in it.

The first project, laid out in Chapters 2 & 3 starts at the top of this triangle, with an example of the chemistry and applications of metal-organic frameworks in nanotechnology. In this work, a highly porous and chemically stable Zr-MOF is grown around gold nanoparticles, encapsulating them in a bottle-around-ship fashion. This advanced synthesis is characterised extensively and optimised to yield a core-shell composite. It serves as a telling example of how self-assembly can be used to create multifunctional porous materials, whose photophysical applications are further explored in Chapter 3. The composite was initially made for therapeutic applications, whereby the unusual optical properties of the gold nanoparticles would trigger drug release under near-infrared irradiation. Unencouraging preliminary data motivated the author to traverse to other optical applications. This is realised in the second half of Chapter 3, in which the composites are exploited as size-selective optical sensors. The MOFs porosity here acts as a molecular sieve gating the access of only small molecules to the optical antenna (*i.e.* the gold nanoparticle) at the core, where SERS-Raman sensing takes place. This proof-of-principle study makes the synthesised composite a promising candidate for size-selective molecular sensing, such as pesticides in ground water or cancer markers in patient's breaths.

The surface area characterisation of the composites synthesised in Chapter 2 led to the more fundamental study of adsorption and its role in the porosimetry of frameworks in Chapter 4. It was noticed that surface area calculations from gas adsorption isotherms according to the BET method were prone to inconsistencies; not necessarily because of the irreproducibility of the underlying raw data, but rater due to ambiguous data fitting protocols used by scientists to calculate the surface areas. Pursuing this suspicion, an unprecedented round-robin evaluation was conducted involving over 60 international laboratories and 115

collaborators, in which the inter-rater reliability of surface calculations by experts in the field was assessed. In response to the critical reproducibility issues raised by the results, an algorithmic approach called *BET Surface Identification* (BETSI) was developed that mitigates these concerns and makes, for the first time, an unambiguous BET surface area assignment possible.

Finally, in Chapter 5 the triangle is closed by looking at the role that self-assembly can play in the formation of frameworks. This more theoretical work was inspired by observations of some polymorphic phases in the composites of Chapter 2, which correspond to different underlying crystal topologies. This chapter explores the many parallels between the fields of MOF chemistry and structural DNA nanotechnology, which lie right at the heart of network topology and self-assembly. Drawing on these parallels, the graph-theoretical principle that guides MOF design – *reticular chemistry* – is here extended upon to design a novel class of porous DNA crystals called *DNA frameworks*. From this, the author hopes to demonstrate that the notion of a framework-assembly can extend to much more flexible building blocks than those of MOFs and other rigid frameworks, and to bring two areas of science together that have been previously unconnected.

The multipolar nature of this thesis requires that each chapter has its own introduction and literature background associated with it. The aims and objectives for these chapters are clearly specified and contextualised by the preceding literature. In addition, fundamental concepts that appear throughout the thesis are presented in this introduction, as are the most important characterisation techniques. Readers who are familiar with fundamental concepts of MOFs, plasmonics, adsorption, and the characterisation techniques, may choose to skip this section and move straight to Chapter 2.

1.3 Principles

1.3.1 MOFs

There can be no doubt that one of the most profound academic achievements in materials science of the 21st century so far was the discovery of porous coordination polymers (PCPs) [1], most importantly metal-organic frameworks (MOFs) [2–4]. These crystalline, highly porous materials with previously unachievable surface areas have revolutionised the world of inorganic chemistry and are projected to have far reaching influences in the future of the industrial chemistry and modern society. The following gives a brief account of the chemistry and main applications of MOFs.

1.3.1.1 Chemistry of MOFs

MOFs are hybrid materials composed of metal atom clusters that are interconnected with organic linkers. The chemical coordination between highly directional atom clusters and rigid organic 'struts' repeats throughout the material, giving crystalline order to both the material and the void space within it. This porosity yields unparalleled surface areas that can reach levels of up to 10,000 $m^2\ g^{-1}$ [5].

MOFs are remarkably varied synthetic platforms. Metal clusters and organic linkers can be exchanged relatively freely to create new structures with new physico-chemical properties. The identification of several common chemical building blocks and bonding motifs has propelled MOF development in the last 20 years, with now more than 100,000 MOF structures reported in the Cambridge Crystallography Structural Database (CCSD) [11]. Such inorganic building blocks can be a single atom, such as Zn in the case of (zeolite imidazolate framework) ZIF-8 [10], or they can be more complex, such as the Zn_4O-cluster found in the (isoreticular MOF) IRMOF series [7], the Cu-Cu paddlewheel in (Hong Kong University of Science and Technology) HKUST-1 [9], or the variable metal clusters of the (Materials Institute Lavoisier) MIL-series [8]. Organic building building blocks are frequently polyvalent organic acids. However, other classes of linkers exist, for instance imidazolate [10], azolate [12], or phosphonate [13] to only name a few. A targeted design strategy for the 'judicious' assembly of MOFs called *reticular chemistry* was developed by Yaghi and O'Keeffe in the early 21st century [2]. It will be more thoroughly revisited in Section 1.3.1.2 and it will be the topic of Chapter 5.

Most commonly, MOFs are synthesised solvothermally from metal salts and organic linkers, however, other methods such as electrochemical synthesis, sonochemistry, mechanochemical syntheses, and chemical vapour deposition (CVD) have also been reported [14, 15].

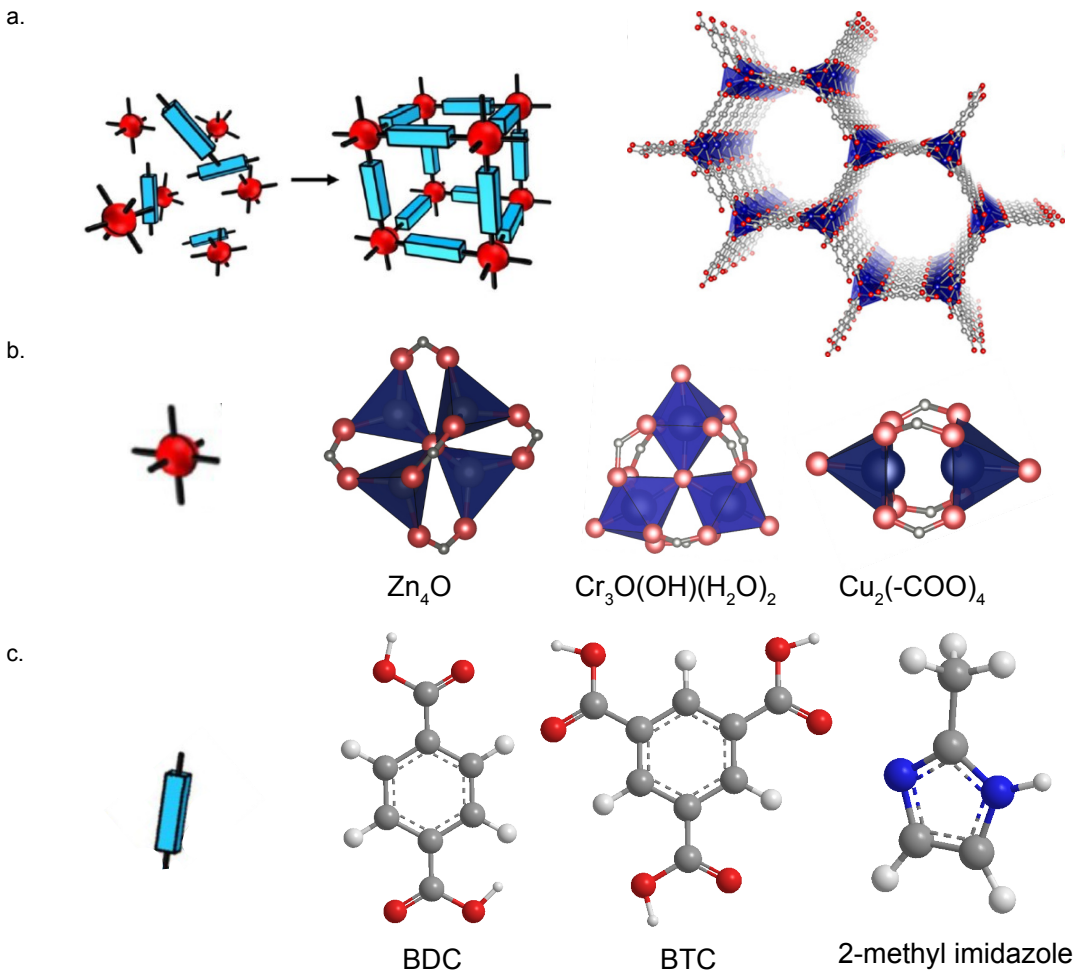

Fig. 1.3 Metal-organic Frameworks | a. Formation of a MOF from inorganic or organic building blocks. Reproduced with permission from Chris Wilmer and Vervoorts *et al.* [6] b. Inorganic clusters, found in typical MOFs. Zn_4O of the IRMOF-series [7], $Cr_3O(OH)(H_2O)_2$ of the MIL-series [8], and Cu-Cu paddlewheel of HKUST-1 [9]. b. Organic strut connecting the inorganic linkers. Benzenedicarboxylic acid (BDC) of IRMOF-1 [7], benzenetricarboxylic acid (BTC) of MIL-100 [8], and 2-methyl imidazole of ZIF-8 [10].

In a typical solvothermal synthesis route, the precursors are heated in a sealed vessel for some time allowing the crystallisation of the powderous material, and the precipitate is extracted and washed. Notionally, MOF crystallisation can thus be separated into two steps: (i) formation of the rigid inorganic cluster and (ii) coordination by organic linkers connecting the nodes. It is critical here that the connection between clusters occurs under reversible conditions to favour thermodynamically stable, ordered structures [16]. The labile coordination bonds encountered in MOFs lend themselves particularly well to this chemistry.

1.3.1.2 Reticular Chemistry – The Basics

The recent success in MOF syntheses can be attributed to the reticular design strategy developed Yaghi and O'Keeffe in the early 2000's [2]. In essence, a reticular synthesis is a retrosynthetic strategy to assemble frameworks from chemically discreet, often isolable chemical units. These units can be abstracted into idealised geometric shapes, which represent the maximum of points of extension and connection of the chemical unit. For instance, the Cu-Cu paddlewheel of Figure 1.3 c, $Cu_2(-COO)_4$, is abstracted as a square because the points of connection to the organic moiety (the terminal C-C bonds of the carboxylic acid, represented as white spheres inbetween the larger, red oxygen atoms) are in a square planar arrangement. Likewise, the organic moieties can be abstracted. For instance, trivalent benzenetricarboxylic acid (BTC) becomes a triangle, and the simpler divalent benzenedicarboxylic acid (BDC) becomes a one-dimensional strut. These shapes are dubbed secondary building units (SBUs), and they form the basis of the abstraction of the framework – the underlying topology or net. Note here that a particular SBU depends on the abstraction of the corresponding chemical subunit, and, consequently, a framework can be identified as having different underlying topologies, depending on which SBUs were defined. A catalogue of crystal topologies and their embeddings, called the *Reticular Chemistry Structural Database* (RCSR) has been developed by O'Keefe, and the notation suggested in it is used throughout this dissertation [17].

The advantage of the reticulation approach is to work backwards from this abstraction: A MOF can be judiciously designed, by choosing a target topology and finding the corresponding SBUs and chemical species. As such, the species can be exchanged with one another relatively freely so long as they are represented by the same SBU. Two MOFs made from different chemical subunits but based on the same SBUs and having the same underlying topology are called *isoreticular*. A prominent example of such an isoreticular series is the IRMOF-series published by Yaghi and co-workers, featuring consecutive extensions of the organic moiety [18].

A more thorough account of reticular chemistry is given in the Chapter 5, where it is argued that its design principles can be extended to DNA nanotechnology.

1.3.1.3 Applications of MOFs

Due to their immense surface area and chemical versatility, MOFs have been proposed for a sheer endless range of applications. A full review of these would fall outside the scope of this thesis, but the interested reader is directed to some reviews listed below in a brief overview.

Arguably, the greatest potential for MOFs lies in the energy and sustainability sector. Anthropogenic CO_2 emissions have been a global cause for concern, given that CO_2 is the greatest contributor to climate change [19]. Here, carbon capture by MOFs using selective adsorption of CO_2 in industrial waste streams could help mitigate such problems [20]. In another example, the storage of energy-rich gases such as H_2 [21] and hydrocarbons [22–24] is significantly less energy-intensive if it takes place on a strong adsorbent such as a MOF. Selective adsorption can also take place in the liquid phase and help to remove environmental pollutants in water [25, 26].

The well-defined and regular porosity of MOFs plays an important role in catalytic applications [27]. In one of those iterations, MOFs in themselves are catalytically active, for instance using Lewis-acidic open-metal sites [28]. Organic reactions and polymerisations have been studied in MOFs, as well as more recently, enantioseletive processes and C-H activations [29]. They can also provide a support for other catalytically active species such as nanoparticles or enzymes and protect them from degradation (Section 1.3.4).

The rich chemistry of MOFs also translates to tunable host-guest chemistry, which is particularly useful when trying to sense the presence of guest analytes [30]. For instance, solvatochromic or vapochromic MOFs change colour upon interaction with a guest. An emerging application in this field is biological sensing of molecular disease markers by MOFs [31].

In addition to sensing, MOFs have been proposed as drug carriers [32]. Their large pore spaces allow for high loading capacities [33, 34] and slow release profiles preventing a therapeutically inactive *burst-release* [35–37]. The drug delivery applications of MOFs are important in Chapter 3 of this thesis and will be further discussed therein.

Yet more novel and emergent applications of MOFs include supports for crystallisation platforms and microelectronics [38]. The creativity and speed with which researchers suggest MOFs for novel applications is breathtaking, leaving many scientists in the field with optimistic anticipation.

1.3.2 Nanoparticles

Nanoparticles (NPs) have been present in nature and generated by mankind for millennia in the form of soot, but as a source of academic interest, they are a relatively new contribution [39]. Whilst there is no strict definition for a nanoparticle, the term usually applies to particles between 1-100 nm in size. This brief review covers the chemistry and stability of NPs in solution, which is of particular importance to their synthesis in Chapter 2.

NPs that are dispersed in a liquid (sol) are fundamentally unstable. Their high surface-area/volume ratios cause high interfacial energies which can lead to aggregation of NPs or

reactions at their surface. The interactions between nanoparticles in a solution is mathematically described by the Derjaguin, Landau, Verwey, Overbeek (DLVO) theory which balances the attractive dispersion (van-der-Waals) forces with the repulsive double-layer forces and steric repulsion [40].

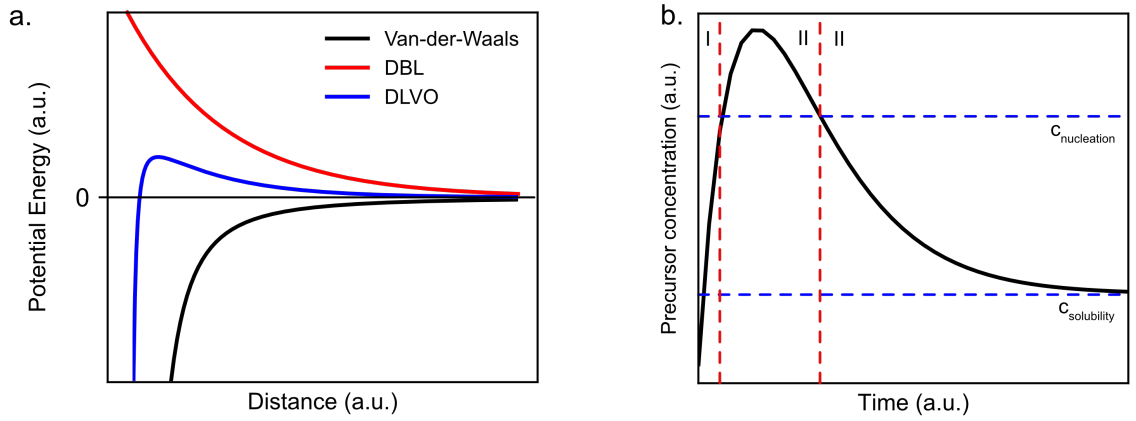

Fig. 1.4 Nanoparticles in Solution | a. DLVO theory accounts for the repulsive and attractive forces between nanoparticles. b. LaMer growth mechanism. Blue lines mark the solubility limit and the critical nucleation concentration. Red lines separate the mechanism into three steps; I addition of precursor, II nucleation, and III the growth phase.

Van-der-Waals forces are temporary induced dipole interactions arising from the non-uniform distribution of electrons in atoms and molecules. They act over a broad range of distances and are strong, causing the aggregation of NPs when they are in close contact. The repulsive forces between NPs can be steric, such as those exerted from surface ligands or polymers. In addition, charged NPs are surrounded by an electric double-layer, an excess of counterions held close to the surface by the electric field gradient. As two electric double-layer start to overlap the local increase in the ion concentration creates an osmotic pressure pushing the NPs apart from each other. The origin of the electric double-layer repulsion is therefore, somewhat counter-intuitively, not electrostatic but entropic in nature.

The addition of salts to the sol screens all ion charges and can therefore deplete the strength of the double-layer repulsion. This can result in the balance of forces tipping towards the attractive potential, resulting in salt-induced aggregation. In addition, both steric and double-layer forces can be overcome with sufficient thermal energy, meaning that NPs are less colloidally stable at higher temperatures. Salt-induced and thermal aggregation of NPs again play an important role in Chapter 2.

The formation of NPs in solution is explained relatively straightforwardly by the LaMer mechanism [41]. Commonly, NPs are made from the reduction of a precursor salt, such as

$HAuCl_4$. The addition of a precursor to a growth solution, however, does not immediately cause nucleation above the solubility threshold. Instead, the high interfacial energies of atom clusters can prevent nucleation, resulting in a kinetically stable solution. If the precursor concentration increases further, it reaches the critical nucleation concentration. Following the complete addition of the precursor, the precursor concentration drops, eventually plateauing back to the solubility limit. The mechanism can therefore be separated into three steps: (i) precursor addition; (ii) nucleation, occurring whenever the precursor concentration is above the critical nucleation concentration; and (iii) the growth phase, including steps such as Ostwald-ripening at the later stage. In order to produce monodisperse samples, it is imperative to keep the nucleation phase as short as possible, ensuring that all crystallites grow for roughly the same amount of time. A LaMer-type growth mechanism is invoked in Chapter 2 to account for core-shell MOF encapsulation developed there.

1.3.3 Plasmonics

The optical properties of noble metal NPs, such as gold nanoparticles (AuNPs) have been the source of great curiosity, indeed for many decades [42]. The often cited Lycurgus cup (Roman, 4th century CE, British Museum) contains gold and silver nanoparticles in the glass, causing it to appear in different colours when illuminated from the outside or from the inside [43]. It is probably the oldest known example of nanotechnology crafted by mankind – albeit, it can be safely assumed, unknowingly.

Noble metal NPs derive their optical properties from their electronic structure. The interaction between small metal NPs and light is described by Mie theory, a complete solution of the Maxwell equations for spheres of arbitrary sizes [44]. A full mathematical derivation would lie outside the scope of this thesis but a qualitative interpretation suffices at this stage. The interested reader in search for more mathematical detail is directed to reviews on plasmonics [45–47].

Mie theory only requires the size of the nanoparticle and the dielectric constant of the metal and its surroundings, which can be modelled by the 'free-electron gas' Drude theory. An incoming electromagnetic field interacts with the electrons on the surface of noble metal NPs, inducing a dipole. A restoring force arises in consequence and the balance of forces sustains dipole oscillations. These dipole oscillations are called *localised surface plasmon resonances* (LSPR) and they play an important role in plasmonics. From Mie theory, the total extinction coefficient can be calculated as well as the individual scattering and absorption components. Both will be important in the following chapters in this thesis; in Sections 2.1.2 and 3.1 the absorptive properties are discussed for UV/vis characterisation and photothermal

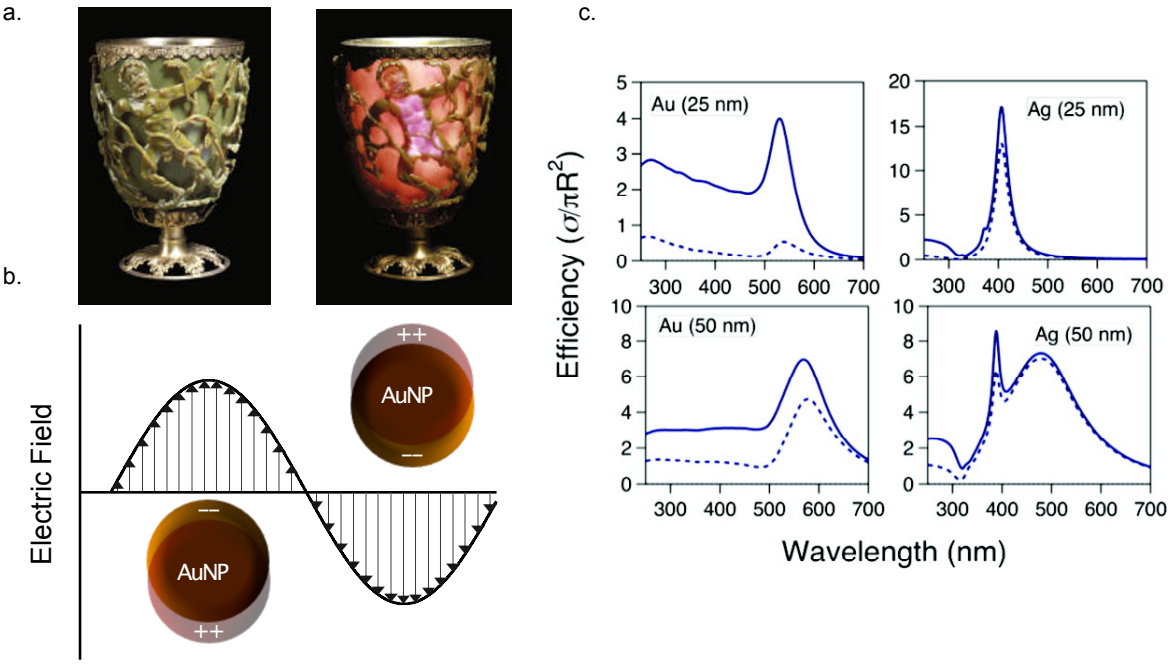

Fig. 1.5 Plasmonics | a. The Lycurgus cup (Roman, 4th century CE, British Museum) appearing green in reflection and red in transmission [48]. b. Illustration of LSPR on an AuNP. c. Calculated extinction spectra (solid) and scattering contributions (dashed) for differently sized Au and Ag NPs. Reprinted with permission [49]

energy conversion respectively, and in Section 3.2 the strong scattering off AuNRs is used as a nanoantenna for Raman spectroscopy.

1.3.4 NP@MOF Composites

MOF composites are hybrid materials, in which a MOF is either guest or host to another supramolecular or nanosized material [50]. Under this broad definition, a vast class of materials is represented. The interested reader is directed to Table 1.1 for the corresponding reviews. Due to the focus of this thesis, the review will be biased towards nanoparticle-MOF composites (NP@MOF).

NP@MOF composites see the MOFs as the host to nanoparticles [51]. Depending on the synthesis method, different morphologies of particles can form: (i) impregnation composites feature small NPs inside the pores of a MOF. They are generally made by infiltrating the porosity of a MOF with a nanoparticle precursor and forming the NPs inside the porosity [59]. This can be done *via* chemical vapour infiltration [60], solution impregnation [61], or incipient wetness techniques [62], and the NP growth is triggered by reduction [63], or else. (ii) Encapsulation composites are formed by consecutive growth of MOF layers around NPs

MOF composite	References
NP@MOF	[51, 52]
Polymer/MOF	[53]
QD@MOF	[54]
SURMOFs	[55]
Glass/MOF	[56]
Enzyme/MOF	[57]
Silica/MOF	[58]

Table 1.1 MOF Composites

[64]. In this arrangement, the NPs do not occupy the porosity itself, but are nonetheless immobilised in the crystallite. Spatial control over the NPs inside the MOFs is difficult but can be achieved by timed addition of the NPs to the growth solution [64]. Finally, (iii) core-shell composites are formed when a MOF nucleates around an NP. This is different to the encapsulation composites mentioned above, as these autonucleate in free solution rather than on the surface of a NP.

The high surface area/volume ratio of metal NPs makes them superior heterogeneous catalysts compared to their bulk counterparts. However, NPs suffer from thermal and chemical stability impairing their catalytic properties. Immobilisation in a MOF [65] can serve to protect NPs, pre-concentrate substrates, and preclude undesired substrates from accessing the catalyst. Consequently, NP@MOF composites have been used for various catalytic applications, such as hydrogen splitting from ammonia borane [62, 66] or olefin hydrogenation [67].

Another common application of NP@MOF composites is hydrogen storage [68]. In search for green fuels, hydrogen is an obvious candidate but there are severe safety concerns over the storage of H_2 at high pressures. H_2 is only a weakly adsorbing species, but upon adsorption on Pd or Pt surfaces, the molecule can split and the remaining H atoms are chemically bound to the surface. Additionally, these nanoparticles can be immobilised in a MOF matrix, and the chemisorbed H atoms can migrate to the MOF structure [69, 70]. Whilst such a 'spillover' effect is still being debated, it demonstrates the synergistic capabilities of NP@MOF composites that cannot be found in any of the individual components alone.

Two other principal applications of NP@MOF composites, sensing and drug delivery, are discussed in more detail in Sections 3.1.1 and 3.2.1, respectively.

1.3.5 Adsorption In Porosimetry

Adsorption is the process of molecular enrichment near or at a surface or interface [71–73]. An *adsorptive* is a free molecule that upon adsorption onto an *adsorbent* surface is bound and becomes an *adsorbate*. Depending on the strength and the nature of the adsorbate/adsorbent interactions, adsorption can be classified as *chemisorption* or *physisorption*. In *chemisorption*, strong forces such as covalent bonds are formed, generally leading to irreversible adherence to the adsorbent. On the other hand, physisorption accounts for looser forces such as dispersion forces and dipole-dipole interactions. Physisorption can be reversible, and the reversed process is referred to as *desorption*. The principles outlined above apply to both gases and liquids, but for the purpose of this thesis, only gas physisorption will be considered.

Physisorption of gases is a pressure- and temperature-dependent phenomenon, but it is generally studied under constant-temperature conditions at the saturation vapour pressure of the adsorptive, P_0: an adsorbent is evacuated and degassed to maximise the number of adsorption sites on its surface. It is then subjected to the adsorptive at different pressures P and the amount adsorbed N is recorded. The details of the experimental procedures can be found in Section 1.8. The relationship between the *relative pressure* P/P_0 and N is called the *adsorption isotherm* and it is highly telling of the adsorbate-adsorbent interactions, and thus also the structure of the adsorbent. The International Union of Pure and Applied Chemistry (IUPAC) classifies gas adsorption isotherms according to their shapes into Types I-VI [74].

1. Type I isotherms feature a sharp increase at low pressures and plateau at higher pressure. The former feature is indicative of strong adsorptive/adsorbent interactions, whilst the latter points to saturation of the surface and no further loading at higher pressures. Type I isotherms can be expected for microporous materials with small pores, which limit the uptake. I(a) isotherms describe (ultra)microporous materials (pore size < 0.7 nm), whilst I(b) isotherms point towards lower adsorptive energies, generally expected for materials with larger micropores (pore size < 2 nm).

2. Type II isotherms have a sharp increase at low relative pressure followed by an inflexion towards higher pressures. This behaviour is more indicative of more open materials, such as non-porous or macroporous adsorbents, where substantive multilayer formation is possible. They tend toward infinity at higher relative pressures due to gas condensation on the bare surface. Point B marks the isotherm-knee, where the curvature of the isotherms starts to change. It is generally accepted that this point marks the difference between monolayer and multilayer formation.

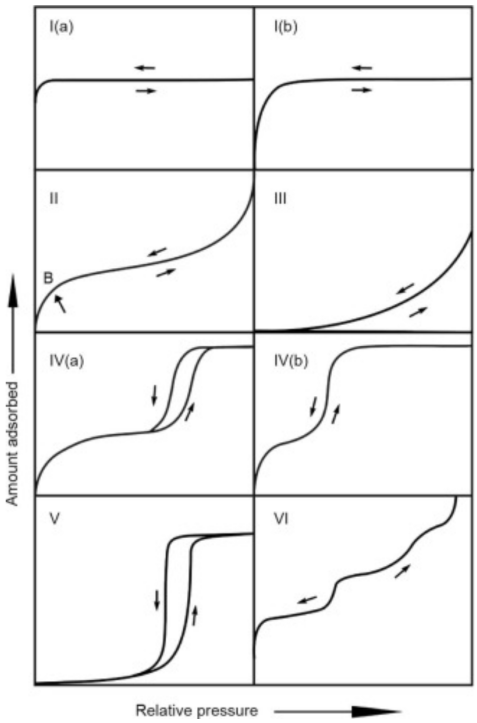

Fig. 1.6 IUPAC Isotherm Classification | Isotherms are classified according to their shapes, which are telling of adsorbate/adsorbent interactions. Figure reprinted with permission [71]

3. Type III isotherms do not form distinct monolayers due to very weak adsorptive interactions. Instead, favourable adsorbate-adsorptive energetics drive multilayer formation with a quadratic dependency on pressure.

4. Type IV isotherms are similar to Type II in that they comprise both monolayer and multilayer formation. Unlike Type II isotherms, however, they do not tend toward infinity at high pressures, indicating the presence of a porosity wide enough to allow multilayer growth, yet limiting it at higher pressures. Such isotherms are observed for mesoporous materials (pore size 2-50 nm). Hysteresis loops in the desorption branch, such as those in Type IV(a) isotherms are encountered when capillary forces of condensed gases in the mesopores hinder evaporation.

5. Type V isotherms again indicate weak adsorbate/adsorbent interactions, with limited uptake at low relative pressures. This is followed by rapid pore-filling due to condensation in pores at higher pressures. Expect Type V isotherms for adsorption phenomena such as water vapour condensation on a hydrophobic surface.

6. Type VI isotherms finally features steps indicative of layer-by-layer adsorptions on non-uniform, non-porous surfaces.

Adsorption and its role in porosimetry feature prominently in Chapter 4 of this thesis, in which the BET method for surface-area measurements is contextualised in a modern way.

1.4 Characterisation Techniques

1.4.1 Transmission Electron Microscopy

Transmission electron microscopy (TEM) is a characterisation technique in which the wave-like character of electrons is used to image a thin sample. If accelerated through high enough voltages, the momentum of electrons corresponds to very short wavelengths – for instance an electron accelerated through a 200 kV field will have a wavelength of 2.51 pm. This overcomes one of the major physical limitations to optical microscopy, namely the Abbe diffraction limit [75], which limits the resolution of light microscopes to roughly half the wavelength of light used.

In contrast to scanning electron microscopy (SEM), where the surface of a sample is probed, in TEM the electrons pass directly through a sample. The setup of a TEM is shown in Figure 1.7. The entire assembly takes place in a radiation-shielded column under a high vacuum. The source of electrons is usually either a thermionic emitter such a hot tungsten wire or LaB_6 or the higher quality field emission gun in the shape of a very fine tungsten tip. Additional monochromators may be used to reduce the effects of chromatic abberation later down the line. The electrons are then accelerated through electric fields and focused using electron lenses – sets of coils that surround the column. In the conventional bright-field imaging mode, the condenser lenses and condenser aperture form an illumination spot on the sample. Having passed through the sample, the electrons travel through the objective or image forming lens, before being projected on a screen using projector lenses. An additional objective aperture may be used in bright-field mode to enhance contrast. In diffraction mode, a selected area aperture images a direct view of the back focal plane on the projector (diffraction pattern).

The contrast mechanism is principally two-fold: (i) Rutherford scattering of the electrons off the atomic nuclei in the sample accounts yields the so-called scattering contrast, meaning that denser samples and those containing heavier elements will scatter the electrons more strongly and appear darker on the screen (mass-thickness contrast). Diffraction contrast can additionally occur for crystalline samples when the Bragg condition is satisfied. (ii) Out of focus, the phases of even lightly-scattered beams change. These delayed phases give so-called phase contrast for light and thin samples.

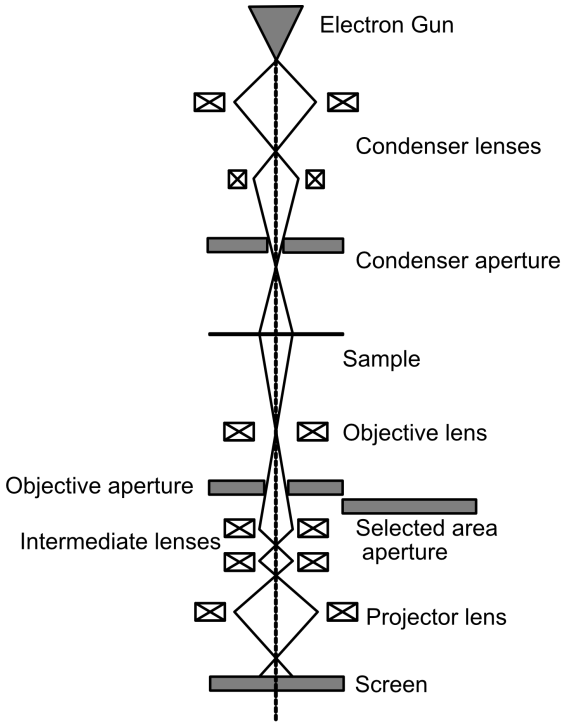

Fig. 1.7 Transmission Electron Microscopy | Basic Setup of a TEM. Electrons are emitted from a field emission gun and spiral down a high vacuum column. Condenser lenses and apertures form a spot on the sample, which is imaged using the objective lens and projected onto a screen or camera.

1.4.2 Gas Adsorption Rigs

Gas adsorption isotherms such as those introduced in Section 1.3.5 are measured in specialised adsorption rigs. These measure the amount adsorbed N of a calibrated dose amount of an inert probe gas such as Ar or N_2 onto a sample which was previously evacuated and weighed. In general, two methods are used to quantify the amount adsorbed N: (i) in volumetric equipment, the resultant pressure drop ensuing the adsorptive process is used to calculate N, whereas (ii) in a gravimetric measurement, the mass of the sample is tracked using a highly sensitive quartz-crystal microbalance (QCM), and the increase in mass corresponds to N.

The experiments in this thesis were carried out using volumetric equipment (Figure 1.8). The sample is degassed *in vacuo* under heating to remove all previously adsorbed gases and moisture from its porosity. It is then held in a sample cell, which is placed in a temperature-controlled environment. Since the probe gas for this experiment is N_2, it is placed in a liquid N_2 bath; alternatively, if Ar is used as a probe gas, in a liquid Ar bath. The cell is connected through a manifold to a high-vacuum pump, a pressure transducer, and a gas

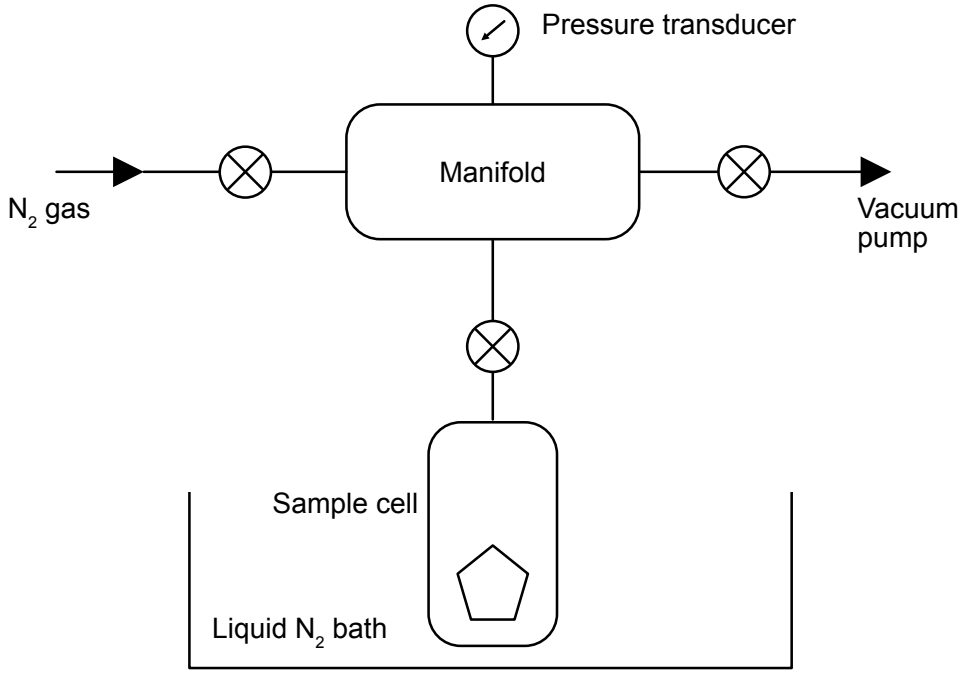

Fig. 1.8 Gas Adsorption Rig | An analyte gas (commonly N_2) is passed through a manifold to the sample cell which is immersed in a cryogenic bath at the boiling of the analyte gas. A pressure transducer connected to the manifold records the pressure following adsorption. The pressure in the sample cell is gradually increased or decreased using valves to the probe gas and high vacuum pumps for the adsorption or desorption branch respectively.

source. Following another full evacuation of the sample, the manifold subjects the sample to a dose amount of N_2 and the pressure transducer records the pressure *after equilibration*. This process is repeated incrementally over an operator-controlled range and step-size until the entire isotherm is recorded.

1.4.3 Powder X-ray Diffraction

Powder X-ray diffraction (PXRD) is a crystallography technique used to analyse the crystal structure of a material. The principles of this technique were discovered by Bragg and are illustrated in Figure 1.9.

If an incident beam of X-rays is directed at a sample, the X-rays are elastically scattered. When the sample has periodic atomic planes spaced at a distance d from one another, Bragg's law predicts that constructive interference from scattered beams occurs when

$$2d\sin\theta = m\lambda \tag{1.1}$$

where θ denotes the incident and scattered angle, λ is wavelength of the X-rays and m is the order of diffraction. The constructive interference pattern is known as the diffraction pattern and gives direct information about the lattice spacing in the sample.

In a typical experiment, X-rays are generated when electrons from a filament are bombarded into a target. This causes inner shell electrons in the target to be ejected and the subsequent relaxation from a higher shell electrons releases a photon with a characteristic X-ray wavelength. For instance, a Cu target may release Cu Kα radiation with a wavelength of 1.5418 Å. The X-ray beam is then directed at the sample, which is mounted on a rotating stage. An X-ray detector such as a charge-coupled device (CCD) is arranged at the same angle opposite the source, giving a total angle between the detector and the source of 2θ. The entire assembly of radiation source, rotating stage and detector is known as a goniometer. Note that for the Bragg condition to be satisfied, the crystalline grain of the sample also has to be in the correct orientation with respect to the detector and the radiation source. In PXRD, this is generally not a problem since the sample is ground into a fine powder to ensure that there are always some crystals in the correct orientation to diffract. Single crystal X-ray diffraction on the other hand uses – as the name suggests – single crystals for diffraction, with multiple goniometers.

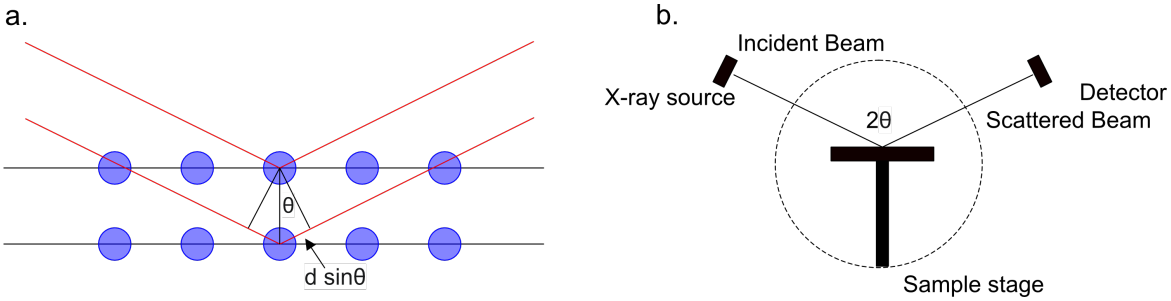

Fig. 1.9 PXRD Schematic | a. If an incident beam of X-rays scatters of a crystalline sample, constructive interference occurs when the atomic planes, d, the incident and scattered angle θ, and the wavelength λ are related by Equation 1.1, b. Basic setup of a vertical diffractometer.

Applying Equation 1.1 may then be used to calculate the d-spacing in the crystalline material from the 2θ values producing the greatest number of counts on the detector.

More specialised information can be obtained from X-ray diffraction patterns as well. For instance, the peak-broadening of the reflections can be related to nanoparticle size *via* the Scherrer equation.

A general 'problem' with PXRD is that crystalline reflections are much more powerful and produce sharp peaks, whilst amorphous phases leave broad and shallow bands in the diffraction pattern. This can sometimes lead to over-estimations of the crystalline quality of the material.

1.4.4 Raman Spectroscopy

Raman Spectroscopy is a characterisation technique relying on inelastic scattering to probe vibrational states in molecules. In a typical Raman spectroscopy measurement, a monochromatic laser is focused on a sample and the scattered light is collected through a series of lenses and gratings. The light-sample interaction for Raman spectroscopy is summarised in Figure 1.10 in a simplified Jablonski Diagram. Unlike absorption or fluorescence, scattering involves electron movement between virtual states of a molecule. It can be thought of as a two-photon process, where an electron is excited and instantaneously relaxed to and from a virtual state of the molecule. In most cases, the two photons have the same energy, resulting in the elastic Rayleigh scatter. The Raman effect describes the much rarer inelastic scatter (about one in a million scattering incidents): the light-sample interaction either transfers energy to the sample (Stokes scatter) or removes it from it (Anti-stokes).

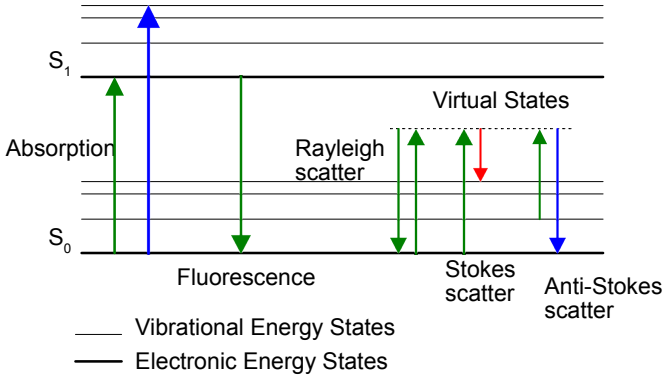

Fig. 1.10 Raman Spectroscopy | Jablonski diagram for the Raman effect, here labelled as the Stokes and Anti-Stokes scatter. Unlike absorption or fluorescence, scattering can be thought of a as a two-photon process involving virtual states.

Due to the two-photon nature of the Raman scatter, the selection rules for absorption spectroscopy do not apply here. Rather, the Raman effect is only observable, when the transition between the states is associated with a change in the polarisability during the mode. Such modes are highly characteristic of a particular molecule, earning Raman spectroscopy the reputation of yielding a molecular 'fingerprint'.

The rarity of Raman scattering means that whilst this technique is highly characteristic of a molecule, it has also an inherently weak signal. Experimental techniques such as coherent anti-Stokes resonance scattering (CARS) and surface-enhanced Raman spectroscopy (SERS) can amplify the Raman effect. SERS will feature prominently in the Chapter 3 of this thesis, in which core-shell NP@MOF composites are used as size-selective Raman sensors.

Chapter 2

Synthesis of Gold Nanoparticle/Zirconium-MOF Composites

"*God created the bulk, but he left surfaces to the Devil*" - Wolfgang Pauli

This chapter discusses the development of gold nanoparticle/Zr-MOF composites. Both spherical and rod-shaped gold nanoparticles were synthesised using existing methods and were subsequently encapsulated by the Zr-MOFs NU-901, NU-1000, and UiO-66 in a room temperature assembly. A gold nanorod/NU-901 core-shell composite was successfully prepared and the synthesis was optimised to varying parameters. Further promising results were obtained towards the room temperature synthesis of NU-1000, and gold nanorod/NU-1000 and UiO-66 composites. Sections 2.1.1 and 2.1.2 will introduce the reader to the chemistry of Zr-MOFs and the synthesis of gold nanoparticles respectively. Section 2.3 describes the methods for synthesis and characterisation of the composites. The following discussion of the results in Section 2.4 spans the synthesis of AuNRs, surface ligand exchange, and MOF encapsulation.

2.1 Background

2.1.1 Zirconium MOFs

The development of UiO-66 by Cavka *et al.* in 2006 introduced the world to the first Zr-MOF [76]. UiO-66 emerged from the search for highly robust inorganic building units, leading the authors to contemplate strong Zr−O bonds and Zr-clusters. Nowadays, Zr-MOFs are among the worlds' most studied MOFs, standing out for their outstanding chemical stability, high porosity, and textural properties, such as mechanical robustness [77].

By and large, Zr-MOFs are comprised of $Zr_6O_4(OH)_4$-clusters, which are connected by polytopic carboxylic acids. In the Zr-oxocluster the Zr(IV) ions are octahedrally arranged and $(\mu_3\text{-O})_4$ and $(\mu_3\text{-OH})_4$-connected over the faces of the octahedron. The carboxylic acids link over the edges of the octahedra; the highest connectivity that Zr-MOFs can therefore obtain is twelve. Uncoordinated sites are often loosely stabilised by labile water molecules and have catalytic potential due to their Lewis-acidity [77].

Like most other MOFs, Zr-MOFs are most commonly prepared solvothermally by combining Zr-salts with carboxylic acids. An extensive review of the chemistry and applications of Zr-MOFs would be outside scope of this thesis, hence the reader is only introduced to the Zr-MOFs used in this study.

2.1.1.1 UiO-66

The pivotal UiO-66 (UiO: Universitetet i Oslo) is a terephtalic acid (1,4-benzenedicarboxylic acid, BDC) 12-connected MOF, with **fcu** topology (Figure 2.1). The terephtalate moieties connect the inorganic building blocks *via* η^2-bonding over all twelve edges of the $Zr_6O_4(OH)_4$-clusters. UiO-66 is known for its high chemical stability due to the strong Zr−O bonds and a permanent porosity (S_{BET} = 1,200 $m^2\ g^{-1}$, pore size 8.5 Å) [76].

Its ease of synthesis and functionalisation make UiO-66 one of the most widely featured MOFs in the literature with applications spanning gas adsorption [78], catalysis [79], sensing [80], water purification [81], and drug delivery [36, 35, 82].

UiO-66 is typically synthesised in DMF by heating a Zr(IV) salt such as $ZrCl_4$, $ZrOCl_2$ or $Zr(nOPr)_4$ with BDC [83, 84]. Early UiO-66 syntheses were marked by poor crystallinity and a lack of size control over the crystallites. Later, the advent of *modulated* syntheses improved the crystallinity of Zr-MOFs vastly [85]. A so-called modulator is typically a monovalent carboxylic acid such as acetic or benzoic acid, which competes with the MOF linker for coordination to the Zr(IV) sites. While the exact mechanism of modulation is still unclear, it is generally accepted that a modulator slows down the rate of nucleation,

which in turn allows fewer nuclei to grow into larger particles. Other studies suggest that the role of the modulator in UiO-66 syntheses goes much further than nucleation control, with involvement in the colloidal stability of the MOFs during growth [86], defect density [87], and topology [88].

Recent advances in synthesis have produced a solution-based synthetic route carried out at room temperature [89]. While a mechanochemical room temperature protocol was already known [90], solution-based methods are more versatile as they allow for easier functionalisation and better size control.

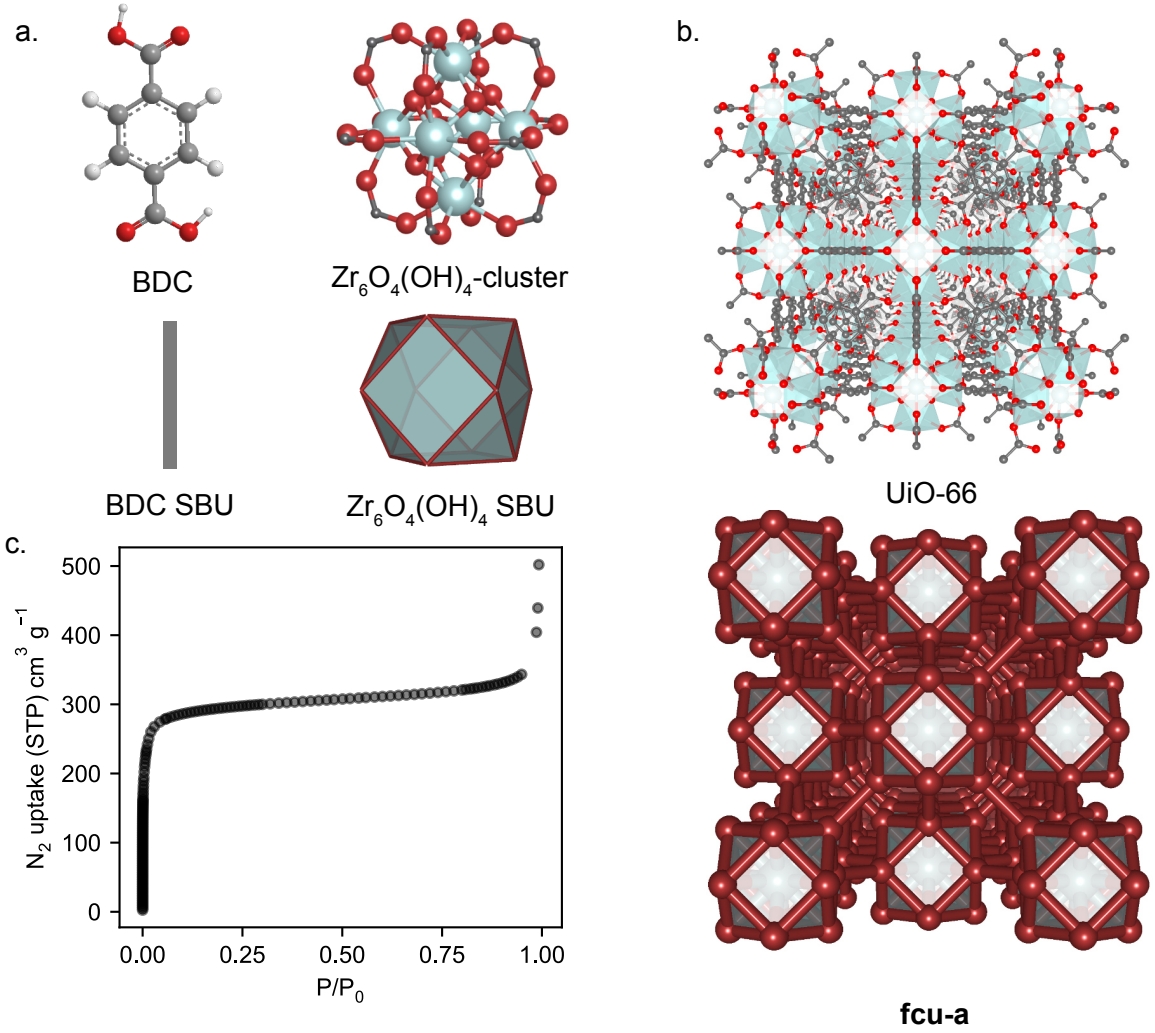

Fig. 2.1 UiO-66 | a. the organic moiety, the ditopic BDC linker; the inorganic moiety, the $Zr_6O_4(OH)_4$ cluster. b. Crystal structure of UiO-66 and the underlying **fcu** topology (augmented topology shown), Dr. Frank Hoffman is kindly acknowledged for this contribution. c. N_2 adsorption isotherm at 77K for UiO-66.

2.1.1.2 NU-1000 & NU-901

Another class of Zr-MOFs of particular interest to this study are the much more open NU-1000 [91] and NU-901 [92]. In contrast to UiO-66, they are 8-connected by tetratopic 1,2,6,8-tetrakis(p-benzoic acid) pyrene (H_4TBAPy) linkers spanning the axial edges of the $Zr_6O_4(OH)_4$-clusters and leaving the equatorial edges coordinatively unsaturated. The global structure of NU-1000 can be described as having **csq** topology and featuring two channels: a smaller triangular channel with pore-diameter of 12 Å and a larger hexagonal pore with a diameter of 33 Å, the latter placing NU-1000 in the category of mesoporous MOFs. With a reported BET area of 2,320 m^2 g^{-1} and a pore volume of 1.4 cm^3 g^{-1}, NU-1000 is a highly porous structure.

Its wide pores and uncoordinated metal sites place NU-1000 at a perfect position for catalysis. It has shown remarkable versatility, *e.g.* in facilitating the hydrolysis of nerve agents [93] and the encapsulation and protection of enzymes [94, 95]. The ability of NU-1000 to protect biological molecules was further employed by Teplensky *et al.*, who loaded siRNA into NU-1000 for gene therapy treatments [96].

The sister structure, NU-901, is isomeric but its underlying crystal topology is **scu**. NU-901 has only one kind of diamond-like channel, with a pore diameter of 16 Å, and is therefore microporous [92]. With a pore volume of 1.29 cm^3 g^{-1} its adsorptive capacity is slightly lower than that of NU-1000, whilst having a comparable BET area of 2,500 m^2 g^{-1} when synthesised at high-temperature.

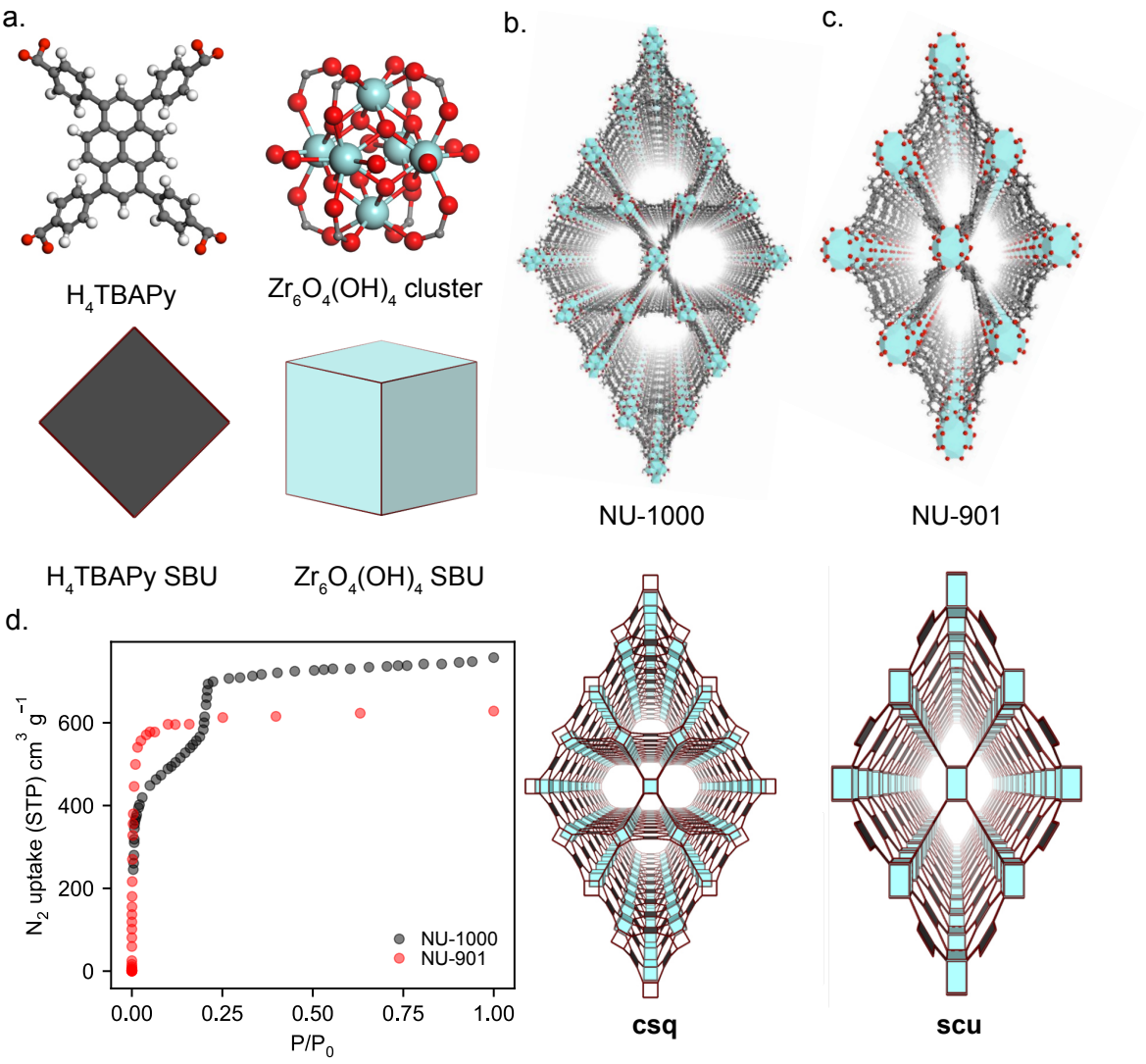

Fig. 2.2 H_4TBAPy Zr-MOFs | a. The organic moiety, the tetratopic H_4TBAPy linker, and the inorganic moiety, the $Zr_6O_4(OH)_4$-cluster. b. Crystal structure of NU-1000 and underlying **csq** topology. c. Crystal structure of NU-901 and underlying **scu** topology. d. N_2 adsorption isotherm at 77 K for both NU-1000 and NU-901.

Both NU-1000 and NU-901 are synthesised solvothermally, however, achieving a phase-pure sample can be challenging as phase impurities are common [97–99]. A closer look at the crystal structure shows that the different topologies result from different conformations of the H_4TBAPy linker [98]; indeed, Islamoglu *et al.* showed that NU-1000 nano-MOF (nMOF) crystallites nucleates as NU-901 before a conformational change in the linker causes the topology to change to **csq**. It is also known that the identity and concentration of modulators in these syntheses can influence the topologies of the structures [99, 100]. Whilst it is possible

to synthesise NU-901 at room temperature, a comparable procedure for NU-1000 has yet to be achieved [101].

2.1.2 Gold Nanoparticles

2.1.2.1 Spherical Gold Nanoparticles

The recent high demand for gold nanoparticles (AuNPs) in plasmonics (Section 1.3.3), catalysis and biomedical research has driven a large volume of research in AuNP syntheses [102–107]. Whilst various optimising protocols exist, arguably, the most prominent and straightforward method was developed by Turkevich in 1951 [108]: a sodium citrate (cit) solution is rapidly added to aqueous $HAuCl_4$. The citrate here acts as both a reducing agent, reducing the Au(III) oxidation state to the desired Au(0), and as a capping ligand, lending colloidal stability to the newly formed particles.

The AuNP growth mechanism was extensively studied by Polte *et al.*, who separate it into four steps [109]: (i) nucleation; (ii) growth by aggregation, either of gold ions or atomic clusters; (iii) a slower growth period in which $HAuCl_4$ is consumed; followed by (iv) a rapid depletion of Au(III). This broadly follows the steps of the LaMer-mechanism introduced in Section 1.3.2. It should be noted here that AuNP syntheses must be carried out under meticulously controlled reaction conditions. Chemical impurities or scratches on the glassware that can serve as nucleation sites that can severely impact the results [105].

The Turkevich method has been modified over the years, by varying the $HAuCl_4$/cit ratios [105], each of them yielding different particle sizes between 4 nm [110] and 40 nm [111], resulting in different absorption spectra (Figure 2.3 b.). The interested reader is directed to the many excellent reviews cited in this section.

2.1.2.2 Gold Nanorods

Anisotropic growth of NPs in solution can be more challenging and requires shape-directing co-factors. For gold nanorods (AuNRs), this is cetrimonnium bromide (CTAB), a common cationic surfactant [112–114]. The exclusion of impurities and contaminants is even more important for AuNRs than it is for AuNPs. Indeed, several research groups have described that switching chemical suppliers, especially for CTAB, can yield different results [115, 116]. Likewise, temperature control during the growth is important, as this can influence the aspect ratio of the resultant particles [117]. Nikoobakht *et al.* developed the now standard method for producing AuNRs in bulk, and, like the AuNP synthesis, it involves reduction of $HAuCl_4$. As before, protocols varying from this method have been reviewed elsewhere [112, 114] and only the main commonalities are discussed here.

In Nikobaakht's two-step, seeded growth method, ultrasmall spherical AuNPs are made first. Single crystal spheres made from $NaBH_4$ yield single-crystal AuNRs, and citrate-capped single crystals grow to form larger, pentatwinned AuNRs [118]. For single crystal AuNRs, the brownish-yellow seeds are aged for up to two hours at room temperature before use to ensure the decomposition of $BH_4{}^-$ anions. Meanwhile, a growth solution with $HAuCl_4$ in CTAB is prepared. Successful complexation of Br^- to the Au(III) species can visually be confirmed by a colour change from yellow to orange as Br^- is a stronger field ligand for Au(III) [112]. Next, ascorbic acid is added reducing Au(III) to Au(I) but crucially not to Au(0). This causes the growth solution to become colourless as Au(I) (d^{10}) inhibits ligand-to-metal charge transfer (LMCT). Reduction of the Au(I) species takes place after addition of the seeds to the growth solution, with CTAB directing the anisotropic growth. The underlying mechanism is still under discussion, but some studies suggest that the presence of the Br^- counter-ion may actually be more important than the surfactant itself [119]. Furthermore, $AgNO_3$ is added, as this is shown to tune the aspect ratio of AuNRs and improve the shape yield, albeit the mechanism for this effect being also unclear [120, 121, 113].

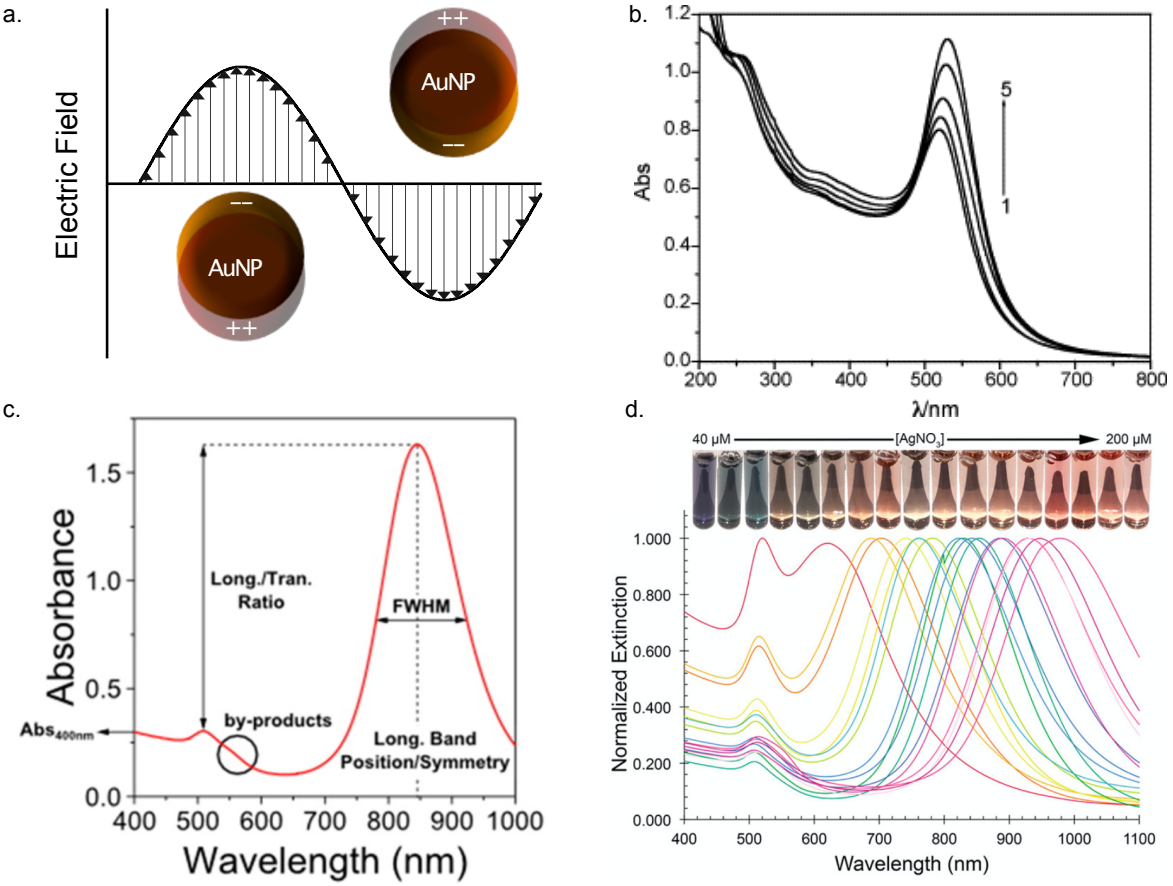

Fig. 2.3 Characterisation of AuNPs and AuNRs from UV/vis Spectra | a. Schematic of surface plasmon resonance in spherical AuNPs b. UV/vis spectra of AuNPs with different sizes: (1) 12 nm; (2) 19 nm; (3) 24 nm; (5) 41 nm. Reprinted with permission [122] c. Absorbance of AuNRs, annotated different spectral contributions from the sample. Reprinted with permission [112] d. Variation of the LSPR mode in AuNRs with increasing $AgNO_3$ concentration. Reprinted with permission [120].

Whilst TEM is a powerful characterisation technique for individual AuNRs, the polydispersity of the sample can only be obtained from statistical analyses. A much faster and informative way to assess the sample quality in bulk is therefore UV/vis spectroscopy [114, 120]. The different spectral contributions from sample features are illustrated in Figure 2.3 c. There are two principal absorption peaks in AuNR spectra, corresponding to the transverse and longitudinal plasmonic modes at short and long wavelength respectively. The position of the longitudinal LSPR peak is dependent on the aspect ratio, which can be tuned with the addition of $AgNO_3$ (Figure 2.3 d.). Heavy-tailed or asymmetric longitudinal modes are observed for polydisperse samples with a large distribution of aspect ratios. Since spherical and cubic AuNPs absorb between 500-550 nm, high absorptions at these wavelengths

indicates their presence. A large ratio between the longitudinal and transverse modes however (>3) suggests a good morphology yield [112].

2.1.3 Encapsulating Nanoparticles into Zr-MOFs

The high temperature typically required in the solvothermal crystallisation of Zr-MOFs can make NP encapsulation challenging, with thermally induced NP aggregation being a common problem (Section 1.3.2). Consequently, only few composites have been reported, which vary considerably in morphology. The most common application here is catalysis [123, 124, 62, 84, 125]. Some composites of particular interest are introduced in the following.

Zhao *et al.* synthesised Fe_3O_4@UiO-66 core-shell composites for theranostic cancer treatment [126] and similar core-shell composites were obtained by Zhou *et al.* [127], who encapsulated AuNPs with polydopamine (PDA) prior to the MOF growth. A thick layer (6 nm) of PDA was grafted on the AuNPs which was clearly visible in TEM micrographs. It is expected that this steric barrier yielded the colloidal stability during the growth. Another very impressive encapsulation was carried out by Runtaweevoranit *et al.*, who grew UiO-66 on notoriously reactive copper NPs for CO_2-to-methanol conversion [128]. In what is arguably the most exotic synthesis, Volosskiy *et al.* grew ultrathin Au wires through the porosity of MOF-545 using glacial acetic as a mild reducing agent [129].

The successful encapsulations cited above were achieved under high-temperature synthesis conditions, but they are typically associated with difficulties and extensive optimisations. In search of a more straightforward protocol, Noh *et al.* developed a room temperature synthesis for platinum NP@NU-901 composites capable of alkene hydrogenation [101]. In this bottle-around-ship encapsulation, the $Zr_6O_4(OH)_4$-cluster is pre-formed at high temperature and the H_4TBAPy linker is later added for the room temperature framework assembly.

2.2 Aims & Objectives

The principal aim of this study was to expand the chemistry of AuNP@Zr-MOF composites. Initially, drug-delivery was considered a viable application and therefore a composite featuring AuNRs and NU-1000/NU-901 was pursued. AuNRs have powerful plasmonic properties which can be harnessed in cancer treatments [130]. The H_4TBAPy-MOFs on the other hand, have shown advantageous properties in biomedical applications, such as sizeable pores that can uptake large drug molecules, good biocompatibility, instability in PBS, *etc.* [37]. The aims and objectives pertaining to the drug-delivery application of the composites are detailed in Section 3.1.1. In addition to an application-driven need for such a composite, it was noted that the studies cited above often do not show optimisation protocols, leaving the interested reader in a state of limbo attempting (and failing) to prepare an NP@MOF composite. This synthesis, if successful, should therefore be characterised as far as possible, with an emphasis on the growth mechanism and nucleation.

The developed NU-901 room temperature synthesis presented an excellent starting point in this study. First, AuNRs would be synthesised and then encapsulated in a bottle-around-ship fashion. Here, detailed protocols reported by Scarabelli *et al.* for the synthesis of single crystal 20 x 40 nm AuNRs were targeted [112]. Methods and experiments are discussed in detail below.

2.3 Materials & Methods

2.3.1 General Methods

All chemicals were purchased from Sigma Aldrich or Alfa Aesar. UV/vis spectra were recorded on a BMG Labtech Spectrostar Nano, a Cary 5000 UV-vis-nIR Agilent spectrophotometer, or a TECAN Spark. TEM analysis was carried out on a FEI Tecnai F20 with an acceleration voltage of 200 kV or a Hitachi HT-7700 TEM with an acceleration voltage of 120 kV. Samples were prepared on 400 Mesh Cu grids and were dropcasted from a methanolic suspension. PXRD diffraction patterns were obtained on a Bruker B1 vertical diffractometer with Cu Kα radiation (1.5406 Å) on zero-reflection Si chips. N_2 adsorption/desorption experiments were carried out at 77 K on a Micromeritics 3Flex system and the BET area was calculated according to the Rouquerol criteria.

2.3.2 Gold Nanorod Synthesis

AuNRs were synthesised according to a literature procedure by Nikoobakht *et al.* described below. [113, 112]

2.3.2.1 Seeds@CTAB

The process takes place in a water bath thermostatted at 30 °C. 25 µL of 50 mM $HAuCl_4$ solution is added to 4.7 mL of 100 mM CTAB and the resulting mixture is stirred until fully dissolved. 300 µL of an ice-cold 10 mM $NaBH_4$ solution is rapidly added under vigorous stirring, changing to colour immediately from yellow to light-brown. The seed solution is aged up to 2 hrs to break down the remaining BH_4^- ions.

2.3.2.2 AuNR@CTAB

The process takes place in a water bath thermostatted at 30 °C. In a typical experiment, 100 µL of 50 mM $HAuCl_4$ solution is added to 10 mL of 100 mM CTAB and the resulting mixture is gently shaken until fully dissolved (orange colour). After adding ascorbic acid (75 µL, 100 mM) the solution turns colourless and subsequently $AgNO_3$ (120 µL, 10 mM) is added. Finally, the seeds solution (120 µL) is added, the mixture is shaken vigorously one last time and left undisturbed in a water bath for 30 minutes. Optionally, 1 M HCl is added to adjust the pH of the solution.

2.3.3 AuNR Ligand Exchange

2.3.3.1 AuNR@PVP

The AuNRs were polyvinylpyrrolidone (PVP)-coated according to a procedure by Li *et al.* [131]. As-synthesised AuNRs (4 mL) were centrifuged and re-dispersed in a methanolic PVP solution (10 mL, 50 mg mL^{-1}, M_w = 40,000 Da). The sample was then sonicated for 2 hrs until homogenous, washed with MeOH to remove excess PVP and stored in DMF.

2.3.3.2 AuNR@(PVP+SDS)

This procedure was adopted from Pekcevik *et al.* [132]. As-synthesised AuNRs (1 mL) were centrifuged and washed three times with a phosphate buffered solution (PBS; 3 mL, pH 8) containing sodium dodecylsulfate (SDS) (30 mg). Meanwhile, an ethanolic PVP solution (10 % w:v, M_w: 30,000 Da) was prepared and added dropwise under vigorous stirring to the NR suspension. The suspension was heated to 40 °C overnight and subsequently washed and stored in DMF.

2.3.3.3 AuNR@MUA

Mercaptoundecanoic acid (MUA) ligand exchange was carried out according to Thierry *et al.* [133]. Following PEGylation of the AuNRs (Section 2.3.3.4), the AuNRs were transferred into water and an MUA solution (250 µL, 10 mM, 50:50 H_2O:EtOH) was added. The suspension was then sonicated for 1 hr, centrifuged and re-dispersed in DMF.

2.3.3.4 AuNR@PEG-SH

Poly(ethylene) glycol (PEG)ylation of the AuNRs was carried out according to Alkilany *et al.* [134]. As-synthesised AuNRs (2 mL) were added on top of a DCM solution containing PEG-SH (2 mL, 0.1 mg mL^{-1} in a 12 mL centrifuge tube. MeOH (3 mL) was added and the tube was vigorously shaken. As the microemulsion separates, the PEGylated AuNRs visibly migrate to the denser DCM phase. The NRs were then centrifuged, washed in DMF and finally dispersed in DMF. Due to poor long-term stability of the NRs in DMF, this procedure has to be repeated every week. A UV/vis spectrum of a 10% solution of the AuNR suspension was recorded and the sol was subsequently labelled as AuNR-Ynm-X, where Y denotes the wavelength of the longitudinal LSPR mode and X denotes the absorption at Y.

2.3.4 Spherical Gold Nanoparticle Synthesis

AuNPs were synthesised according to Seitz' modification of the Turkevich method [111]. $HAuCl_4 \cdot 3H_2O$ (22.73 mg, 0.0577 mmol) was dissolved in in 150 mL of water and the solution was brought to a vigorous boil. A sodium citrate solution (1 mL, 0.52 M) in water was rapidly injected and the sol was left to boil vigorously for 20 minutes, after which it was cooled to room temperature.

2.3.5 Room Temperature MOF Syntheses

2.3.5.1 Room Temperature NU-901 Synthesis

This method was developed by Noh *et al.* [101]: The benzoate capped $Zr_6O_4(OH)_4$-cluster was prepared according to Piszczek *et al.* [135]. A solution of $Zr(OBu)_4$ (15 mL, 80 %, 5 mmol) was added into a solution containing benzoic acid (100 g) and *n*-propanol. The mixture was refluxed overnight and the white solid was washed extensively in anhydrous *n*-propanol and dried under vacuum. Next, 10 mL of a DMF:acetic acid mixture (7:4, v:v) was used to disperse 200 mg of the isolated $Zr_6O_4(OH)_4$-powder and subsequently 10 mL of a H_4TBAPy solution in DMF (10 mg mL^{-1}) was added under mild stirring and at room temperature over the course of 2 hrs using a syringe pump. The precipitated MOF was isolated the following day, washed extensively in DMF and solvent exchanged to acetone.

2.3.5.2 Room Temperature UiO-66 Synthesis

The protocol for this reaction was modified from DeStefano *et al.* [89]. $Zr(OnPr)_4$ (71 µL, 70 % wt in propanol) was added to a 7:4 (v:v) mixture of DMF and AcOH (11 mL) and the solution was heated to 130 °C in a sealed scintillation vial for 2 hrs to pre-form the $Zr_6O_4(OH)_4$-cluster. Following, the solution was cooled to room temperature and stored until further use. In a typical framework assembly, an aliquot of the $Zr_6O_4(OH)_4$-bearing mother solution (2.75 mL) was combined with a highly concentrated suspension of terephtalic acid (BDC; 469 µL, 40 mg mL^{-1}) and the mixture was stirred overnight at room temperature. The resulting precipitate was washed extensively in DMF and solvent exchanged to acetone.

2.3.6 Encapsulations

2.3.6.1 AuNR@NU-901 Synthesis

In a typical experiment, 3.63 mg of $Zr_6O_4(OH)_4$-cluster were dispersed in 386 µL of DMF and 363 µL AcOH in a 1.5 dram vial. 250 µL of an AuNR@PEG-SH solution in DMF (AuNR-

800nm-1.33) was added and the mixture was sonicated to a fine dispersion. Subsequently, the H_4TBAPy solution (1 mL, 2 mg mL^{-1}, DMF) was added using a syringe pump (0.005 mL min^{-1}) under vigorous stirring and the solution was left stirring overnight. The precipitate was washed using DMF and solvent exchanged to acetone.

2.3.6.2 Attempted AuNP@NU-901 Synthesis

In a typical experiment, 3.63 mg of $Zr_6O_4(OH)_4$-cluster were dispersed in DMF in a 1.5 dram vial, along with 363 µL of AcOH and varying concentrations of AuNPs@PEG-SH dispersed in DMF, resulting in a 7:4 mixture (v:v) of DMF:AcOH. Subsequently, varying amounts of a H_4TBAPy solution (2 mg mL^{-1}) were added either using a syringe pump or directly to the sol and the mixture was stirred at room temperature overnight. The precipitate was washed extensively using DMF and solvent exchanged to acetone.

2.3.6.3 Attempted AuNR@UiO-66 Synthesis

This method follows the same protocol as laid out in Section 2.3.5.2, except for the addition of AuNRs to the $Zr_6O_4(OH)_4$-bearing mother solution. In a typical experiment, a 500 µL AuNR@PEG-SH solution in DMF (AuNR-800nm-2.5) was added to the growth solution and AcOH and DMF were added accordingly to retain the modulator concentration of that in the control experiments. The mixtures were stirred overnight and washed extensively in DMF and solvent exchanged to acetone on the next day.

2.4 Results & Discussion

2.4.1 Gold Nanoparticle Synthesis

2.4.1.1 Gold Nanorod Synthesis

AuNRs were synthesised using the conventional seed-mediated growth method, laid out in section 2.1.2.2. A seed solution was prepared from $HAuCl_4$ and $NaBH_4$, aged for two hours, and then added to the growth solution with CTAB, ascorbic acid, and $AgNO_3$. After 30 minutes of growth, the AuNRs were removed from the solution by centrifugation and washed to remove excess CTAB.

Characterisation by UV/vis spectroscopy showed initially disappointing results, with spectra indicating poor shape yields and size distributions. For the expected size of 20 x 40 nm AuNRs, the transverse and longitudinal LSPR mode peak positions should be 517 nm and 800 nm, respectively, with a transverse/longitudinal mode absorption ratio greater than 3 [112]. This synthesis was generally characterised by poor reproducibility (Figure 2.4 a.) and lack of control over the aspect ratio upon addition of increasing volumes of $AgNO_3$ (Figure 2.4 b.). Additional peaks between 500 and 600 nm indicated the presence of spherical and cubic NPs as did the small transverse/longitudinal mode absorption ratio.

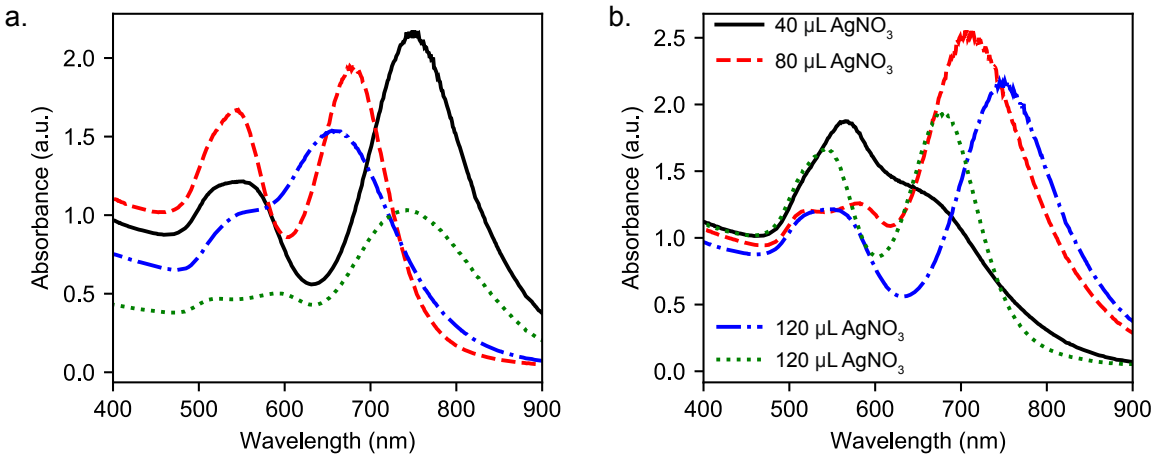

Fig. 2.4 UV/vis Spectra of various Batches of AuNRs synthesised from low-quality CTAB | a. Identical experiments. Note the poor batch-to-batch reproducibility and the poorly defined transverse and longitudinal bands. b. Addition of increasing volumes of $AgNO_3$ to the growth solution. Increasing concentrations of $AgNO_3$ did not yield the expected red-shift of the longitudinal mode [112].

Numerous changes to the protocol were made including varying the concentrations of ascorbic acid, the pH, and the spherical seeds, but no significant improvements were observed.

It was thus hypothesised that the relatively low CTAB purity was responsible for the poor results, and upon switching suppliers from Alfa Aeasar (+98 %) to Sigma Aldrich (+99.9 %) the product quality improved drastically. Using higher purity CTAB, the expected red-shift of the longitudinal band with increasing $AgNO_3$ concentrations could be reproduced as the aspect ratio of the AuNR increased [112, 113].

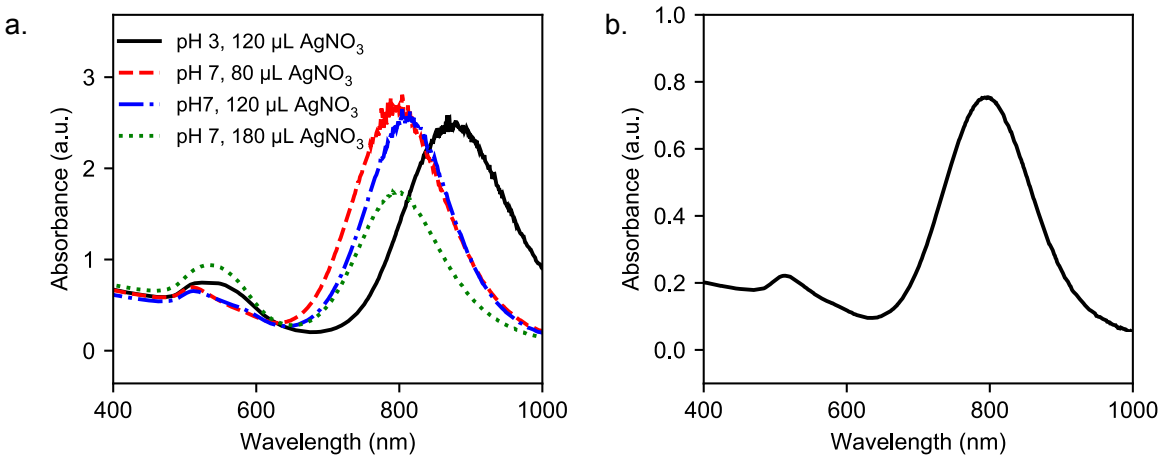

Fig. 2.5 UV/vis Spectra of various Batches of AuNRs synthesised from higher Quality CTAB | a. Varying synthetic conditions produce the desired effect in red-shifting the longitudinal band. b. UV/vis spectrum of large batch of AuNRs synthesised at pH 7 with 80 µL $AgNO_3$ which was used for all further experiments.

2.4.1.2 Spherical Gold Nanoparticle Synthesis

Gold nanoparticles (AuNPs) were synthesised according to the Turkevich method. A solution of H_4AuCl_4 was brought to reflux and a Na_3cit solution was rapidly injected. An immediate colour change was observed from yellow Au(III) to colourless Au(I) and then to dark purple Au(0). After 20 minutes of refluxing, the solution was cooled to room temperature, and centrifuged to remove excess citrate and unreacted Au species. UV/vis spectroscopy confirmed the formation of AuNPs with a characteristic plasmon peak centered at 538 nm. Some additional absorption in the nIR-region suggested that some aggregates had formed.

2.4.2 Gold Nanorod - NU-901 Encapsulation

2.4.2.1 NU-901 Room Temperature Synthesis

The room temperature synthesis of NU-901 was first reported by Noh *et al.* [101]. In this two-step synthesis, the benzoate-capped $Zr_6O_4(OH)_4$-cluster was pre-formed at high temperature

from $Zr(OBu)_4$ and benzoic acid. Isolation of the white precipitate produced the $Zr_6O_4(OH)_4$-cluster in affordable yields. Next, the precipitate was dispersed in a DMF/AcOH mixture and stirred vigorously at room temperature, while the organic H_4TBAPy linker is added dropwise using a syringe pump. Slow addition of the linker here prevented precipitation of the poorly soluble H_4TBAPy. After overnight stirring, the MOF was collected by centrifugation, washed extensively in DMF and solvent exchanged to acetone.

PXRD confirmed the presence of the NU-901 phase (Figure 2.6 a.) and N_2 gas adsorption porosimetry gave an adsorption isotherm (Figure 2.6 b.) from which a respectable BET area of 2,130 m^2 g^{-1} could be calculated. Interestingly, the N_2 isotherm featured a marked increase at a relative pressure of 0.2, indicative of mesoporous pore-filling. With pore-dimensions of 16 Å however, crystalline NU-901 is not a mesoporous MOF, which lead the authors of the study to conclude that defects such as missing linkers and nodes accounted for the mesoporosity of the material [101].

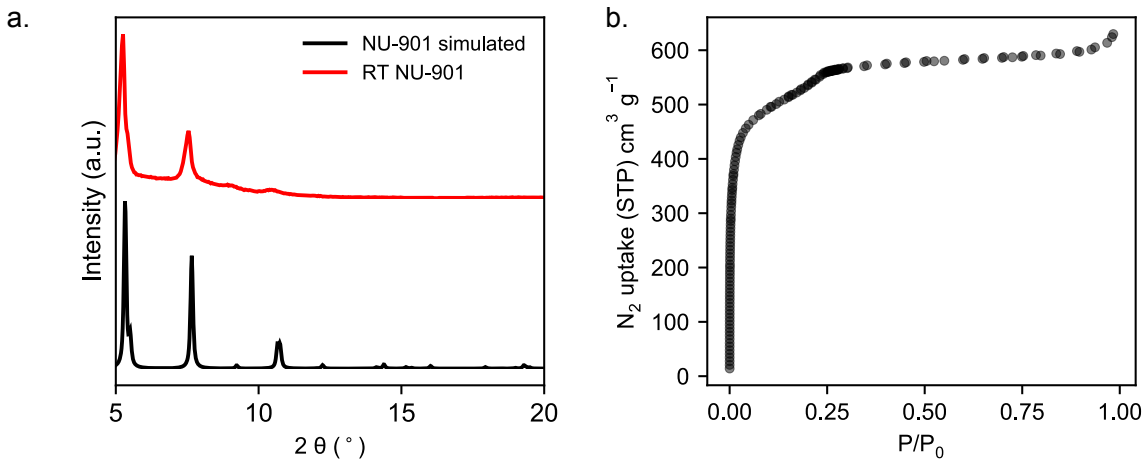

Fig. 2.6 Room Temperature NU-901 Physical Characterisation | a. PXRD of RT NU-901. Reflections coincide with the reflections in the simulated diffraction pattern for NU-901. b. N_2 adsorption isotherm at 77 K of RT NU-901. A step in the relative pressure range from 0.1-0.27 is indicative of mesoporous cavities in the sample, however the crystalline form of NU-901 is entirely microporous.

2.4.2.2 Gold Nanorod Functionalisation and NU-901 Encapsulation

The existing protocol for the room temperature synthesis of NU-901 [101] was modified for AuNR encapsulation. The AuNRs were surface-decorated with a suitable ligand to improve the colloidal stability and to aid encapsulation.

Initial attempts were made with the AuNRs' native CTAB surface ligand. As-synthesised AuNR@CTAB were centrifuged, re-suspended in DMF and added to the $Zr_6(OH)_4O_4$-

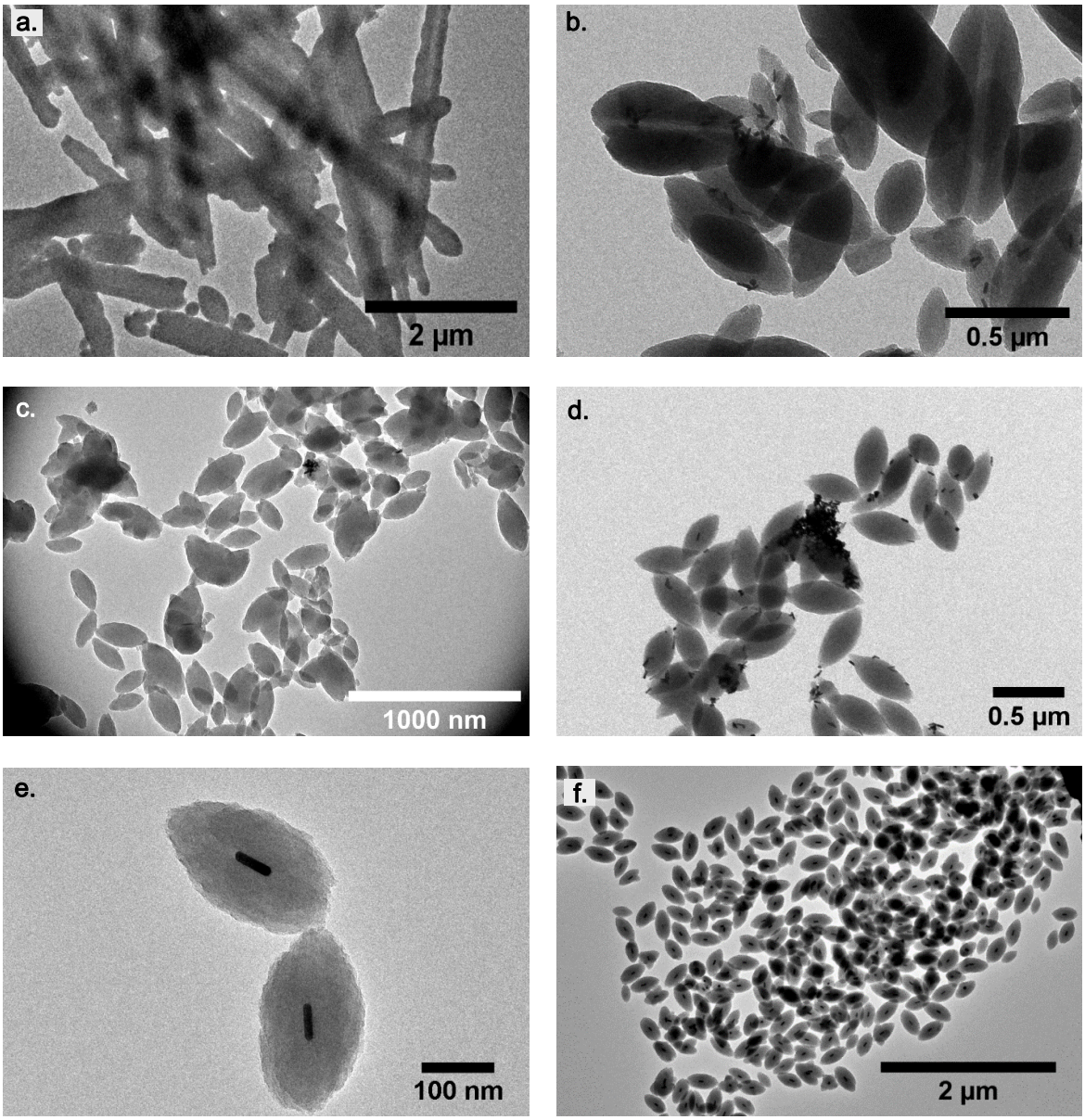

Fig. 2.7 Encapsulation Attempts | TEM micrographs of attempted AuNR/NU-901 encapsulations with a. CTAB b. PVP c. PVP+SDS d. MUA e-f. PEG-SH. In comparison to other AuNR surface ligands, PEG-SH is vastly superior to facilitate encapsulation.

bearing mother solution. Upon addition, a distinct colour change from burgundy red to light blue was immediately noticeable, suggesting NR aggregation. After the MOF formation, TEM analysis (Figure 2.7 a.) was used to characterise the encapsulation. No composites were found here, which was attributed to the likely early aggregation of AuNRs.

The next ligand under investigation was polyvinylpyrrolidone (PVP), which has been exhaustively used for NP encapsulation into MOFs [64]. The CTAB to PVP exchange was

first attempted by adopting a literature procedure from Carbo-Argibay *et al.*, which suggests dropwise addition of an aqueous PVP solution to the AuNRs [121]. This proved to be far more problematic than expected, with visible aggregation of AuNRs occurring in many attempts. Eventually, the problem was rectified by using a procedure reported by Li *et al.*, involving a phase transfer of the AuNRs to MeOH before exchanging the ligand [136]. The subsequent composite growth was promising, with some NR encapsulation observed (Figure 2.7 b.). The vast majority of nMOF particles however did not contain AuNRs and the AuNRs were not evenly distributed throughout the sample despite vigorous stirring.

Based on this initial success, it was hypothesized that a more negatively-charged ligand combination might increase the affinity for the cationic $Zr_6O_4(OH)_4$-species. Pekcevik *et al.* reported a surface functionalisation with PVP and sodium dodecylsulfate (SDS) by ligand exchange from CTAB in phosphate buffered saline (PBS) [132]. This ligand exchange was more efficient, but no significant improvement for AuNR encapsulation by the MOF was observed (Figure 2.7 c.).

Another anionic surfactant, mercaptoundecanoic acid (MUA), was promising due to its terminal carboxylic acid group, which could bond to the $Zr_6O_4(OH)_4$-cluster in a similar way to the H_4TBAPy linker. Direct ligand exchange from CTAB to MUA according to Sugikawa *et al.* was irreproducible in many attempts, with immediate visible aggregation taking place upon MUA addition [137]. Therefore, a two-step method was employed, whereby the AuNRs were first functionalised with thiolated poly(ethylene glycol) (PEG-SH) and then exchanged with MUA [133]. TEM analysis (Figure 2.7 d.) revealed that the AuNRs aggregated in relatively small clusters which either adhered to or protruded from the MOF crystallites.

Observing that all previous encapsulation attempts with ionic surfactants had suffered from salt-induced aggregation, attempts were made with the neutral PEG-SH layer grafted on the AuNRs before MUA exchange. Undoubtedly, this produced the greatest success for encapsulation (Figure 2.7 e. and f.). A detailed discussion of the synthesis and characterisation of AuNR@PEG-SH@NU-901 composites, hereafter simply denoted as AuNR@NU-901, follows.

2.4.2.3 Synthesis and Physical Characterisation of AuNR@NU-901

The AuNRs' native CTAB was replaced by PEG-SH using an elegant phase-transfer method involving water, DCM and MeOH [134]. The PEGylated AuNRs (AuNR@PEG-SH) were then dispersed in a 7:4 (v:v) mixture of DMF and acetic acid containing the $Zr_6O_4(OH)_4$-cluster. The H_4TBAPy-linker was dissolved in DMF and added to the deep-red growth solution under vigorous stirring. The dark red precipitate was removed by centrifugation, washed extensively with DMF and solvent exchanged to acetone.

TEM analysis confirmed the core-shell morphology of single AuNRs encapsulated by prolate NU-901 crystallites, hereafter denoted as AuNR@NU-901. The prolate morphology of the AuNR@NU-901 crystallites is similar to that of pristine NU-901, arising from facet selectivities during the growth [138, 101]. Nearly all AuNRs are at the center of the MOF crystallites and have a parallel orientation with respect to the principal prolate axis. This suggests that AuNR@PEG-SH seed the MOF growth, presumably due to favourable interactions (dispersion forces, dipole-dipole interactions, etc.) between the PEG and the MOF precursors. The growth mechanism is further elucidated in section 2.4.2.4.

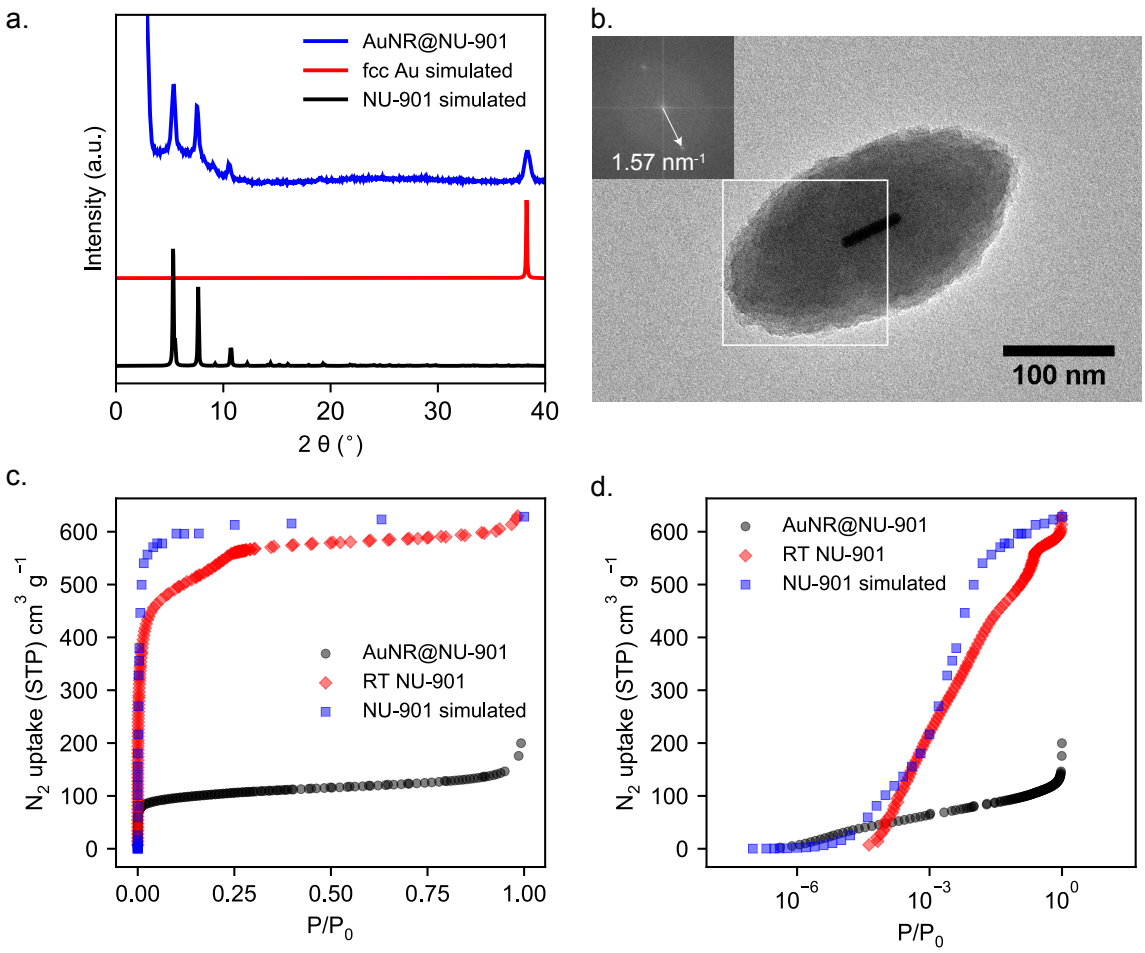

Fig. 2.8 Physical Characterisation of AuNR@NU-901 | a. Reflections of the experimental PXRD of AuNR@NU-901 and the simulated diffraction patterns of its components match well in position, affirming the crystallitiny of the sample. b. TEM micrograph of AuNR@NU-901. Note the central position of the AuNR inside the NU-901 crystallite and its orientation with respect to the principle prolate axis. Inset shows FFT of marked area, with a reflection at reciprocal 1.57 nm, consistent with the d-spacing of NU-901. c. N_2 adsorption isotherm at 77 K of AuNR@NU-901. Note the large reduction in gravimetric porosity with respect to both RT NU-901 and NU-901 simulated. d. N_2 adsorption isotherms from c. in semilog representation.

The PXRD pattern of AuNR@NU-901 features both low-angle reflections from NU-901 ($2\theta = 5.3°$, 7.7°, 10.7°) and the (111)-diffraction from fcc Au ($2\theta = 38.2°$), confirming the crystallinity of the material. N_2 adsorption at 77 K resulted in a Type I isotherm, albeit with a substantial decrease in the gravimetric porosity compared to pristine NU-901. The calculated BET area of AuNR@NU-901 is 350 $m^2\ g^{-1}$, while that of pristine NU-901 is 2,000 $m^2\ g^{-1}$. A calculation of the hypothetical BET area for AuNR@NU-901 by comparing the size of the crystallites, the core, and their relative densities, revealed that for large AuNR@NU-901

particles (ca. 320 nm) the BET area should be roughly 1,800 m^2 g^{-1}. The large reduction in the gravimetric porosity was attributed either to a higher non-porous defect density in the comparatively small AuNR@NU-901 crystallites, or to partial pore-blocking by the PEG surface ligands.

2.4.2.4 Elucidation of the Growth Mechanism

The results observed in the TEM analysis in Section 2.4.2.3 suggest that the AuNRs seed the MOF growth. Herein, the growth mechanism was further elucidated by changing the concentration and the addition speed of the H_4TBAPy linker. Figure 2.9 shows the qualitative mechanism that is proposed. In this LaMer-type growth (Section 1.3.2), the H_4TABPy concentration rises initially from zero as the reagent is added to the $Zr_6(OH)_4O_4$ and AuNR-bearing mother solution. Above the critical nucleation concentration, $[Nuc_{solution}]$, nucleation occurs followed by a simple first-order decay until the precursors are consumed or their concentration saturates to the solubility limit. The model has two additional features in the nucleation and growth phase, respectively: (i) favourable interactions between the PEGylated AuNRs and the MOF precursors lower the nucleation threshold locally on the AuNRs to $[Nuc_{AuNR}]$; and (ii) at a critically low concentration of H_4TBAPy during the growth phase, the topology changes from **scu** to **csq**, resulting in the less dense NU-1000 structure [91]. The concentration difference between $[Nuc_{solution}]$ and $[Nuc_{AuNR}]$ is dubbed the *core-shell window*. Nucleation events within this window will preferentially occur on the AuNRs, resulting in core-shell morphologies. If the H_4TBAPy concentration rises above the core-shell window, nucleation will indiscriminately occur in free solution resulting in non-encapsulated crystallites.

To quantify the success of encapsulation, the *core-shell yield* was defined as the fraction of crystallites with core-shell morphology. In addition, the size distributions of different batches synthesized from varying H_4TABPy concentrations were obtained from statistical analyses of TEM micrographs. Figure 2.9 b. shows the analysis based on more than 150 randomly selected particles. The core-shell yield was lowered as the H_4TBAPy concentration increased under fast addition, suggesting that the peak H_4TBAPy concentration exceeded the core-shell window. In turn, the particle size distribution for encapsulated crystallites became narrower as the precursor concentration increased, possibly due to the elevated number of seeds. Notably, non-encapsulating crystallites were on average consistently larger than their AuNR-encapsulating counterparts. This fits the qualitative growth model, as it suggests that a higher fraction of non-encapsulating crystallites form at an earlier stage of the reaction before the H_4TBAPy concentration depletes to the core-shell window.

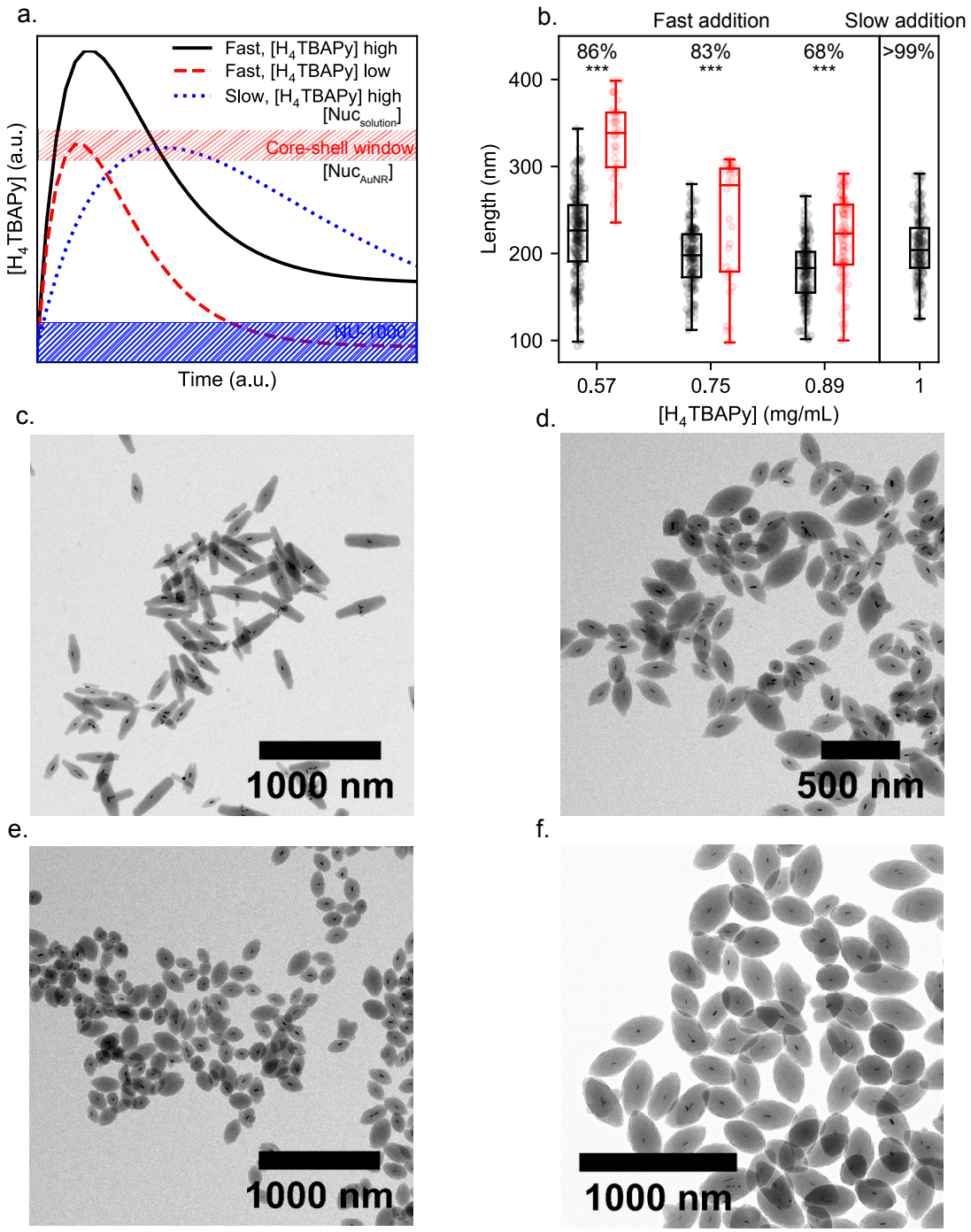

Fig. 2.9 AuNR@NU-901 Growth Mechanism | a. Qualitative growth mechanism. Fast addition: H_4TBAPy solution added using a pipette, slow addition: H_4TBAPy added dropwise using a syringe pump (0.005 mL min^{-1}) b. Statistical analysis of TEM micrographs of AuNR@NU-901 batches synthesised with different amounts of H_4TBAPy added (>150 particles each). Length measured along the principal prolate axis. Top label gives core-shell yield. Black points: core-shell crystallites; red points: non-encapsulated crystallites. Line: median; box: range; whiskers: range. *** indicates ANOVA testing result between unencapsulated and encapsulated populations, populations are significantly different with $p < 0.001$. c-f. TEM micrographs of batches synthesised with different concentrations of H_4TBAPy: c. 0.33 mg mL^{-1} d. 0.57 mg mL^{-1} e. 0.89 mg mL^{-1} f. 1.00 mg mL^{-1}, slow addition (0.005 mL min^{-1})

The marked shift in the morphology of the crystallites at low concentrations of H_4TBAPy (Figure 2.9 c.) suggested a structural change to the isomeric NU-1000 structure with **csq** topology. It has been previously reported that NU-1000 nMOFs are cylindrical as opposed to the prolate NU-901 crystallites [37, 138, 101, 91, 92]. Careful analysis of TEM micrographs showed that AuNR@NU-901 nMOFs synthesized from low H_4TBAPy concentrations of 0.75 mg mL^{-1} frequently had cylindrical rather than prolate tips, and at a concentration of 0.57 mg mL^{-1} the particle morphology is almost entirely cylindrical (Figure 2.9 c.). These cylindrical nMOFs are better described as encapsulation composites rather than true core-shell, as they frequently contain multiple AuNRs aggregated inside the particles. Direct measurement of the crystal lattice using high-resolution TEM (HRTEM) revealed a *d*-spacing of ca. 3 nm that is consistent with the NU-1000 phase (Figure 2.10) [91]. Whilst it has long been known that the linker/modulator ratio can affect the topology of Zr-MOFs, a clear understanding is still lacking. The model here presented suggests that as the linker is consumed during the reaction, the H_4TBAPy/AcOH ratio reaches a critically low value in which the NU-1000 phase is favoured.

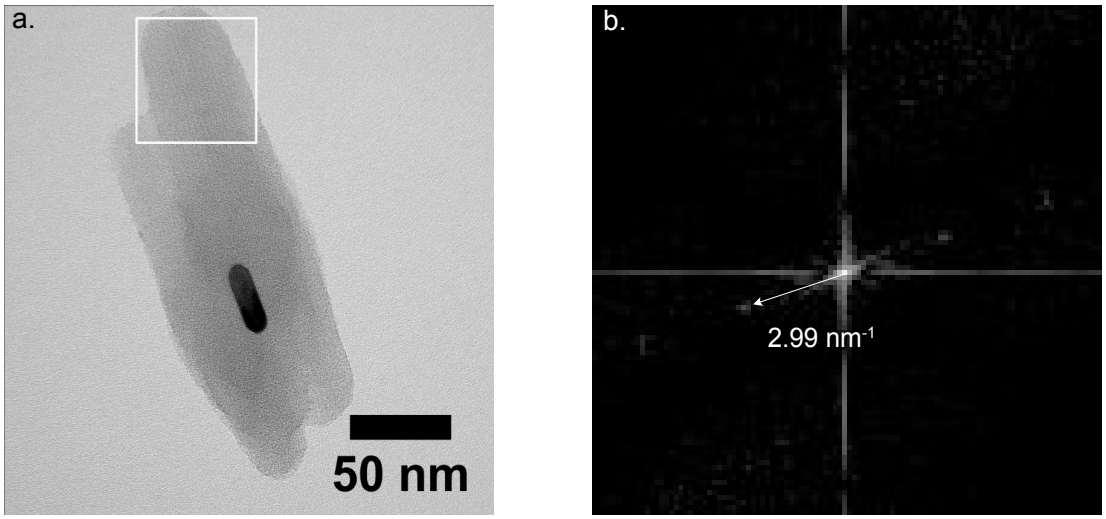

Fig. 2.10 AuNR@NU-1000 HRTEM | a. High-resolution TEM micrograph of AuNR@NU-1000 crystallites b FFT of selected area in a., reflection is at reciprocal 2.99 nm which is in good agreement with the interplanar spacing of the (001)-plane of NU-1000 of 33.13 Å.

Either exceeding the core-shell window or growing a mixed phase could be avoided if the linker addition profile was modulated. Controlled dropwise injection using a syringe pump increased the H_4TBAPy concentration more slowly, ensuring that nucleation only occurred in the desired core-shell window. Simultaneously, the linker concentration decreased more slowly compared to the fast injection method, since the reagent was continuously added,

thereby preventing the NU-1000 growth. Using this slow-injection method, core-shell yields greater than 99 % were achieved as well as exclusively prolate NU-901 crystallites.

Interestingly, fewer morphological changes were observed when smaller amounts of H_4TBAPy were added dropwise (Figure 2.11). This suggests that it is not the absolute of concentration of H_4TBPy that is of critical relevance, but rather the slow addition that controls morphology and topology.

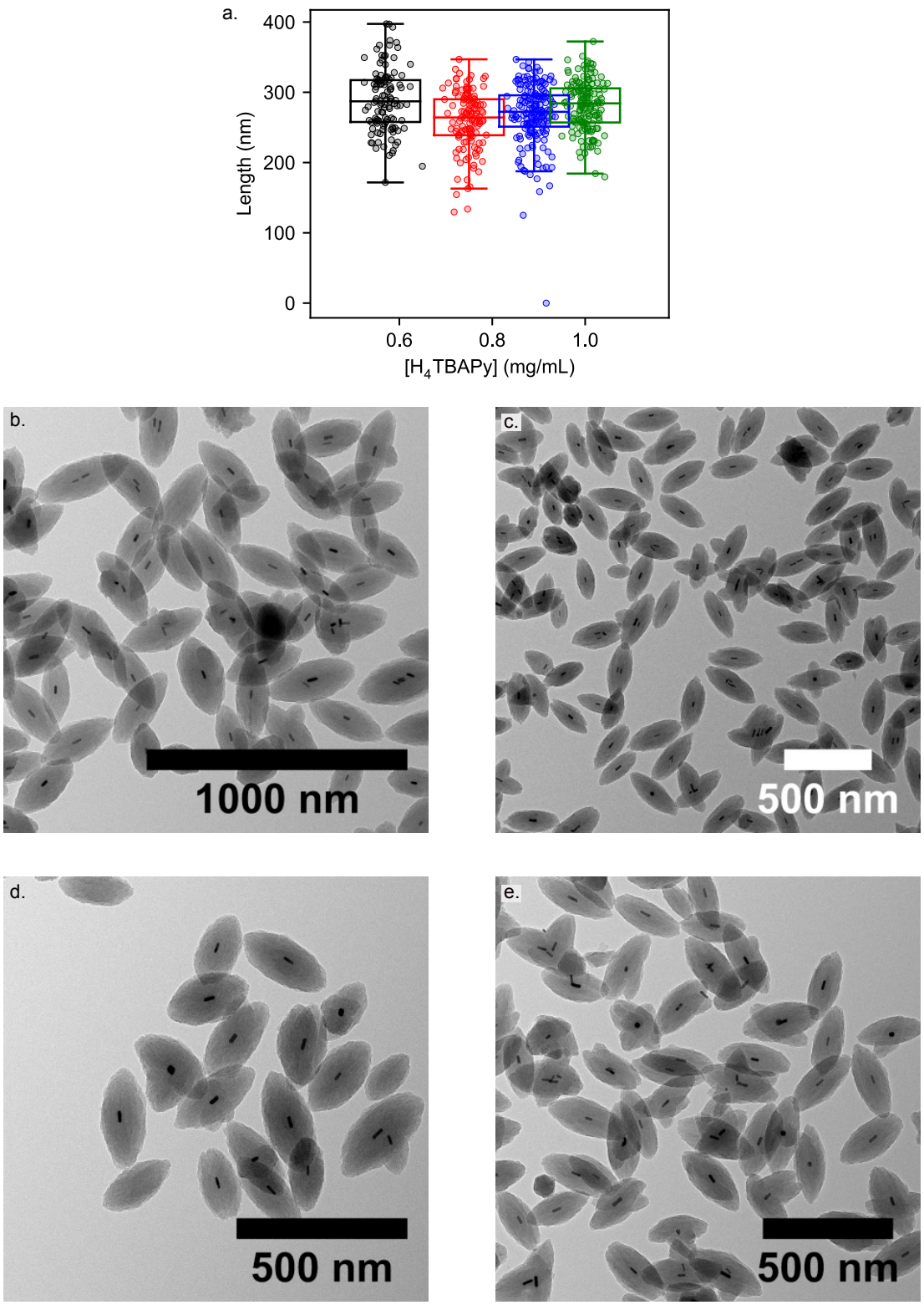

Fig. 2.11 Variation of AuNR@NU-901 Particle Size with H_4TBAPy Concentration under slow-addition Condition I a. Statistical analysis b-f. Representative TEM micrographs of AuNR@NU-901 batches synthesised at H_4TBAPy concentrations of b. 1 mg mL^{-1}; c. 0.89 mg mL^{-1}; d. 0.75 mg mL^{-1}; e. 0.57 mg mL^{-1}

2.4.2.5 Tuning the Particle Size with varying Gold Nanorod Concentrations

The results from section 2.4.2.4 evidence that the AuNRs play a vital role in the seeding process of AuNR@NU-901 nMOFs. To further investigate the seeding behaviour, TEM micrographs of pristine, room temperature synthesised NU-901 and AuNR@NU-901 were compared (Figure 2.12). The statistical analysis of the micrographs, shows not only that AuNR@NU-901 crystallites were on average smaller than their NU-901 counterparts, but they had a significantly narrower size distribution as well, again suggesting a seeded growth.

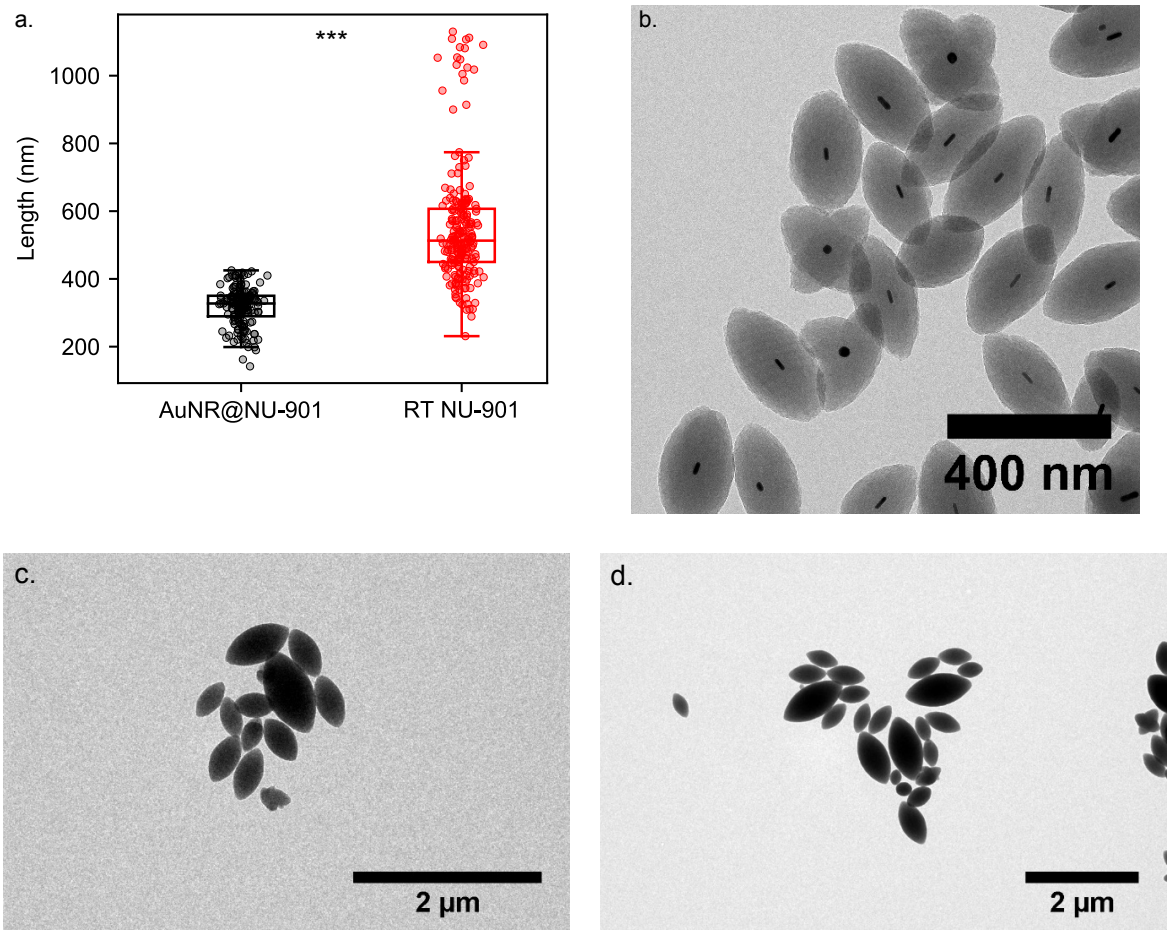

Fig. 2.12 Comparison AuNR@NU-901 and Room Temperature NU-901 | a. Size distribution of AuNR@NU-901 and RT NU-901 crystallites. Length measured along the principal prolate axis. Line: median; box: interquartile range; whiskers: data range. *** indicates ANOVA testing result between unencapsulated and encapsulated populations, populations are significantly different with $p < 0.001$ b-c. Representative TEM micrographs of RT NU-901 crystallites. Note the comparatively large size and wider size distribution compared to AuNR@NU-901.

From this, it was hypothesised that the AuNR@NU-901 size distribution could be tuned by varying the AuNR concentration. Assuming that the growth rate is unaffected by the AuNR concentration, the particle size should decrease if the AuNR concentration increases, as more particles grow into smaller crystallites and *vice versa*. Again, statistical analyses of TEM micrographs were used to evaluate the size of AuNR@NU-901 composites grown in the presence of different AuNR concentrations.

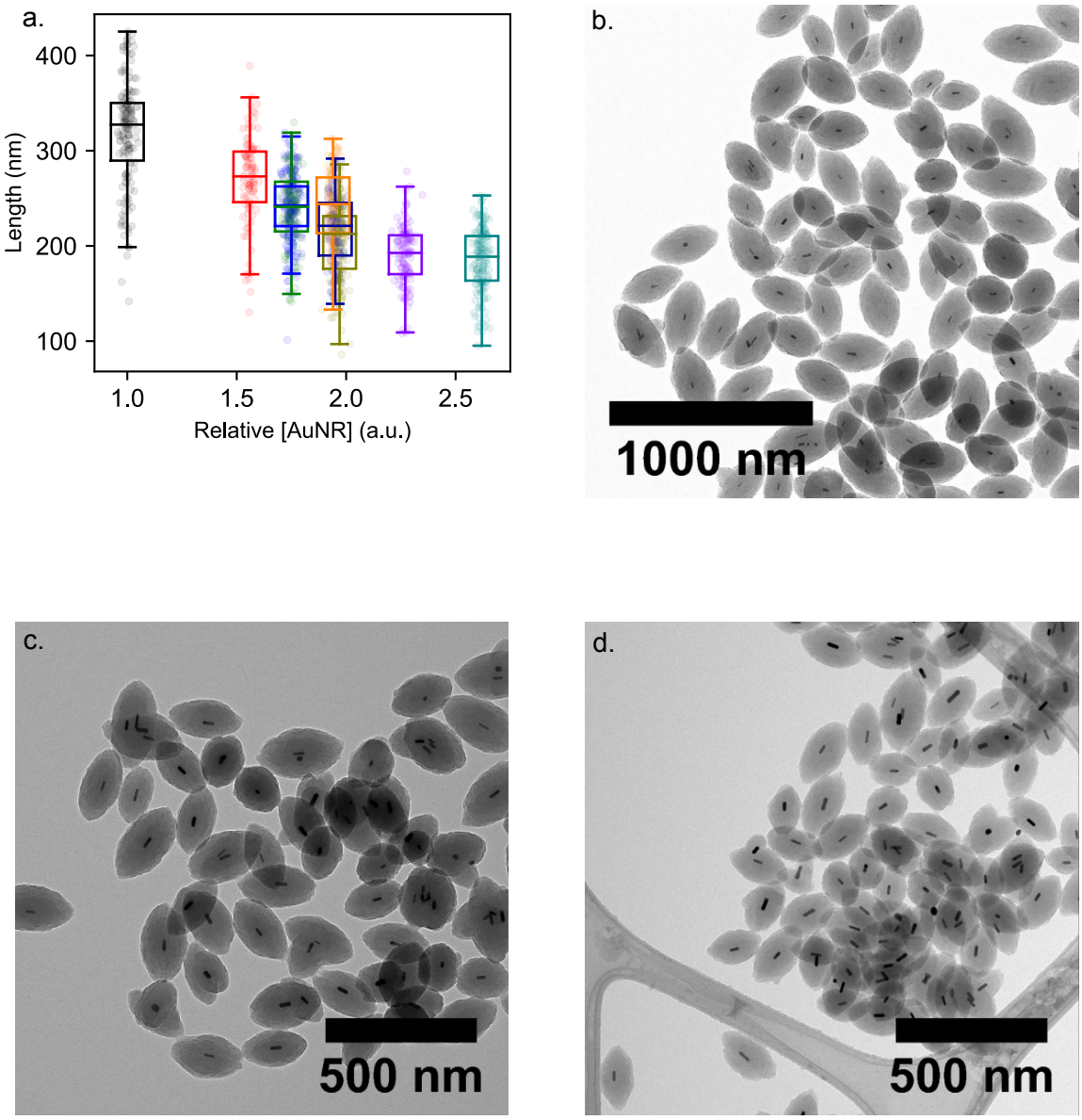

Fig. 2.13 Tuning AuNR@NU-901 Particle Size | a. Statistical analysis of TEM micrographs of AuNR@NU-901 batches synthesised with different AuNR concentrations (>150 particles each). Length measured along the principal prolate axis. Line: median; box: interquartile range; whiskers: data range. b-d. TEM micrographs of AuNR@NU-901 batches synthesised with different AuNR concentrations. Relative concentrations: b. 1 c. 1.9 d 2.6. Note that the crystallite size decreases as the relative AuNR concentration increases.

Figure 2.13 a. clearly shows the inverse relationship between the particle size and the AuNR concentration, which allowed the composite size to be robustly tuned between 200 and 350 nm. ANOVA pairwise testing between the samples shown in Figure 2.13 shows that

	1.00	1.56	1.75	1.75	1.94	1.95	1.97	2.27	2.62
1.00		***	***	***	***	***	***	***	***
1.56			***	***	***	***	***	***	***
1.75				ns	ns	***	***	***	***
1.75					ns	**	***	***	***
1.94						***	***	***	***
1.95							ns	***	***
1.97								ns	**
2.27									ns
2.62									

Table 2.1 Tuning AuNR@NU-901 Particle Size ANOVA Test | ANOVA testing matrix showing statistical significance of difference in populations plotted in Figure 2.13a. (*) $p < 0.05$, (**) $p < 0.01$, (***) $p < 0.001$; ns not significant

the sets are significantly different unless the relative AuNR concentrations are very close (Table 2.1).

2.4.3 Other Encapsulation Attempts

Following the success of the PEGylation and syringe pump methods described above, attempts were made to generalise this procedure to other Zr-MOFs and gold nanoparticles. The following sections describe the results obtained for the encapsulation of spherical AuNPs by NU-901, as well as the attempted encapsulation of AuNRs by UiO-66. These results are representative of a wide set of experiments, none of which were as successful as the AuNR@NU-901 synthesis.

2.4.3.1 Gold Nanoparticle - NU-901 Encapsulation

AuNPs were PEGylated using the same phase transfer method used for the AuNRs (Section 2.4.2.2), and as before an aliquot was added to the $Zr_6O_4(OH)_4$-bearing mother solution. Similar to experiments in Section 2.4.2.4, H_4TBAPy was added either directly using a pipette, or dropwise with a syringe pump. Figure 2.14 shows the results from a synthesis in which H_4TBAPy was added directly. The TEM micrographs show AuNPs attached to the outside of NU-901 crystallites in their familiar prolate shape, however, no encapsulation was observed. This was attributed to the MOF nucleation occurring too rapidly in free solution. Attempts to slow down the nucleation process by adding the linker dropwise resulted in fast and visible aggregation of AuNPs on the stirrer bar and were not further characterised.

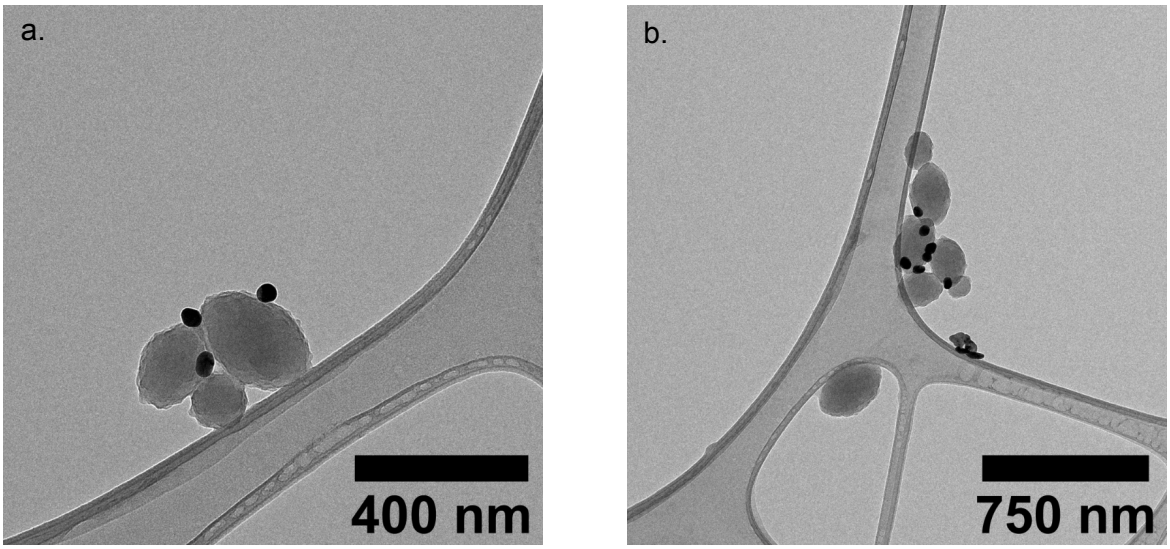

Fig. 2.14 Attempted AuNP@NU-901 Encapsulation | a-b. Representative TEM micrographs of attempted AuNP@NU-901 encapsulations by fast the addition of the H_4TBAPy linker. Note the AuNPs attached to the external surface of prolate NU-901 nMOFs.

2.4.3.2 Gold Nanorod - UiO-66 Encapsulation

Protocols to encapsulate AuNRs by UiO-66 were adapted from DeStefano's room temperature UiO-66 synthesis [89]. The attempted encapsulations were run under more dilute concentrations in order to slow down nucleation. Initial experiments showed that this was only possible by increasing the DMF content, as a corresponding increase in the AcOH content lead complete suppression of MOF formation (data not shown).

Figure 2.15 shows the preliminary encapsulations that were possible so far. Unlike NU-901, UiO-66 with the **fcu** topology forms rhombohedral crystals with sharper crystal facets. The obtained crystallites (Figure 2.15 a.) are consistent with previous observations for UiO-66, as are the crystals obtained under more dilute conditions (Figure 2.15 b.) [138]. The UiO-66 nMOFs have a less uniform size and appear more intergrown and aggregated than NU-901.

Addition of AuNRs to the mixture did not lead to the desired outcome, but resulted in aggregated AuNRs attached to the external facets of the nMOFs (Figure 2.15 c.). To slow down the nucleation of UiO-66 further, the syringe pump method described in Section 2.4.2.4 was employed again, but yielded similar results to the previous experiments (Figure 2.15 d.).

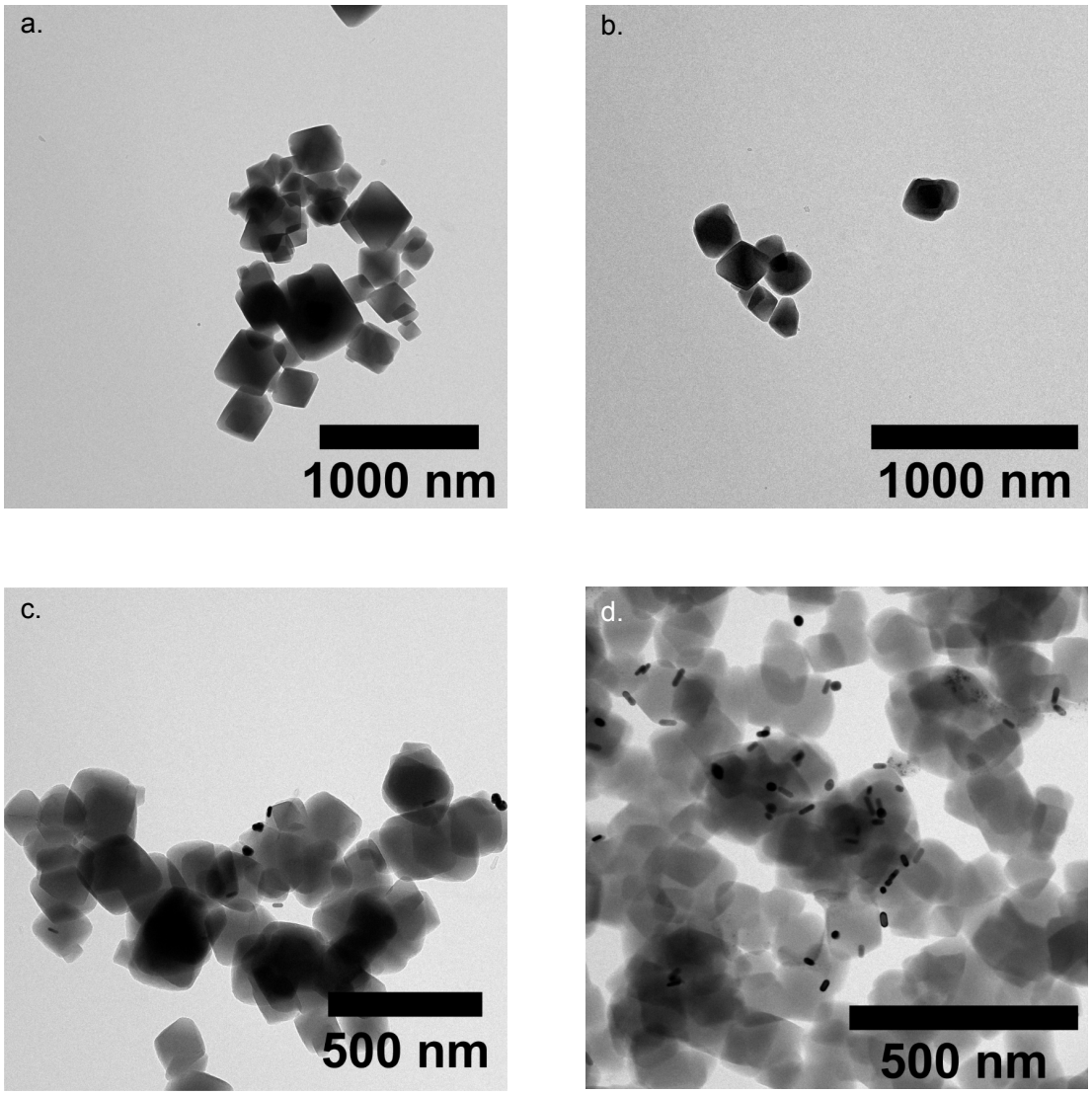

Fig. 2.15 Attempted AuNR@UiO-66 Encapsulation | Representative TEM micrographs of a. 'Standard' synthesis of RT UiO-66 as described by DeStefano *et al.* [89] b. RT UiO-66 synthesised at higher dilution levels. The morphology of the particles is consistent with the 'standard' method shown in a. c. Addition of AuNR@PEG-SH results in aggregated AuNRs attached to the external surface of the crystallites. d. Slow addition of the BDC linker using a syringe pump yields comparable results that do not suggest encapsulation

2.5 Conclusion & Outlook

In this study, the encapsulation of plasmonic gold nanomaterials into Zr-MOFs was investigated. To this end, two Zr-MOFs that can be assembled at room temperature, UiO-66 and NU-901, were chosen as the encapsulating agents, as the colloidal stability of NPs at high temperature is not suitable to conventional solvothermal methods.

AuNRs and AuNPs were added to MOF growth solutions and the encapsulations were characterised using TEM. Following an extensive screening of suitable surface-ligand/MOF pairings, AuNR@PEG-SH and NU-901 emerged as remarkable encapsulation partners, yielding aesthetically pleasing core-shell AuNR@NU-901 composites. A more in-depth analysis of the growth mechanism showed that outstanding morphology yields in excess of 99% are possible if the organic linker is added using a syringe pump. Further, tentative results towards a room temperature synthesis of NU-1000 were obtained. This analysis of the growth mechanism clearly demonstrated that PEGylated AuNRs can seed the NU-901 growth, a mechanism which was later exploited to tune the particle size of AuNR@NU-901 with the AuNR concentration.

So far, the success of AuNR@NU-901 encapsulations could not be translated to other AuNP encapsulations or other MOFs. In initial experiments, spherical AuNPs do not seem to seed NU-901 as effectively as AuNRs, preferentially attaching themselves to the external surface of the nMOF crystallites. Likewise, the room temperature synthesis of AuNR@UiO-66 has so far not yielded results as promising as those for AuNR@NU-901. It is clear that for both of these systems the synthetic protocols must be further optimised, or other ligand pairings must be tested.

In any case, the successful preparation of AuNR@NU-901 is an important step in the preparation of gold nanomaterial/Zr-MOF composites. In the next chapter, the unique photophysical properties of AuNRs are exploited, both towards biomedical applications and optical sensing of analytes.

Chapter 3

Photophysical Applications of AuNR@NU-901

This chapter introduces the reader to some of the photophysical applications of the plasmonic MOF composite AuNR@NU-901. As such, it is organised in two-parts: Section 3.1 features experimental efforts to exploit AuNR@NU-901 as a drug delivery platform. This project aims to use the photothermal energy conversion of AuNRs to heat the composites internally and facilitate the breakdown of the MOFs. Composites loaded with a therapeutic agent could then release the drug under nIR-irradiation with spatiotemporal control. The reader is first introduced to plasmonic photothermal therapy in Section 3.1.1 and the preliminary data is discussed in the following. Next, in Section 3.2 AuNR@NU-901 is developed as a size-selective optical sensor in SERS Raman spectroscopy. In this technique, the locally enhanced electric field at the surface of the AuNRs strengthens the fingerprint Raman signature of a molecule by multiple orders of magnitude. The technique and its principles are introduced in Section 3.2.1, and the following sections demonstrate how AuNR@NU-901 can be used to achieve size-selective optical sensing.

3.1 Plasmonic Photothermal Therapy

3.1.1 Background

3.1.1.1 NP@MOF Composites for Drug Delivery

The rapidly emerging field of nanomedicine represents the next great technological revolution in battling diseases, particularly in the area of personalized medicine. Theranostic nanopharmaceuticals combining disease treatment with diagnostic aids are being developed at a rapid pace, spanning diverse disease areas such as neurological (*e.g.*, Parkinson's and Alzheimer's diseases) and oncological malignancies. Cancer, in particular, is the leading cause of death in the industrial age, after cardiovascular disease [139]. It is estimated that in 2018, 18.1 million new cancer patients were reported, including 9.6 million deaths [140]. Despite advances in diagnosis, early detection, and cancer therapies, current treatments frequently require surgical procedures and other invasive methods such as radiation or chemotherapy, which are associated with significant side-effects [141, 142]. Problems with these current treatment options include insufficient drug delivery to the tumour site, issues with cell membrane penetration, drug degradation and drug solubility problems, and off-target toxicity, to only name a few [143].

Nanomedicine seeks to address these issues by transporting drug molecules using vehicles that can protect drugs from degradation and deliver them safely and efficiently to the tumour site [143–145]. Among the wide set of proposed delivery vehicles, MOFs have recently been proposed for this application [32]. In this field, MOFs have shown promising characteristics such as high drug loading with values of up 2 g of drug per g of empty MOF, *i.e.* a capacity of >66 wt% [146, 147], and slow drug release profiles over the course of weeks, preventing therapeutically inactive burst-releases [36, 37, 148, 35]. Particle sizes below 100-200 nm are regularly achieved in recent syntheses [85, 138] enabling the crossing of cell membranes [148, 149]. In addition, MOFs containing biocompatible metals such as Zn, Fe, or Zr (LD_{50} of 0.45, 4.1, 0.45 g kg^{-1}, respectively) and organic linkers such as BDC, BTC and 2-methyl imidazole (LD_{50} of 1.12, 5.5, and 8.5 g kg^{-1}, respectively) are also frequently unstable at acidic pH or in the presence of phosphates, providing an effective clearance pathway of the delivery vehicle from the patient's body [150].

Encapsulation of NPs into MOFs can further increase their biomedical potential [151], often moving it from the strictly therapeutic to the theranostic treatment space. The inclusion of magnetic NPs for instance has two principle applications: (i) Magnetophoretic therapy uses external magnetic fields for targeting a composite to a particular site [152–160]; and (ii) magnetic NP@MOF composites can be used for magnetic resonance imaging (MRI) contrast.

Here, superparamagnetic NPs encapsulated in a MOF can reduce the spin-spin T_2*-relaxation time, leading to enhanced contrast in T_2*-weighted images [161, 126, 162–165].

3.1.1.2 Plasmonic Photothermal Therapy

The photophysical properties of AuNPs were briefly introduced in Section 1.3.3. Here the absorptive properties and photothermal energy conversion are discussed in more detail.

Irradiation of light on an AuNP produces a non-thermal distribution of electrons at the Fermi-level, which quickly thermalises on a timescale of 2-5 ps *via* electron-phonon and phonon-phonon coupling [49] (Figure 3.1). This results in heat dissipation at the particle-medium interface, raising the temperature of the local environment [166]. The therapeutic use of this principle was first demonstrated by Hirsch *et al.* in 2003 using near-infrared (nIR) irradiation on Au nanoshells [130]. Local tumour hyperthermia was induced by a temperature increase of 40 °C with nIR-light intensities of 4 W cm^{-2}. This approach, termed plasmonic photothermal therapy (PPTT), has since received great interest due to its mild delivery and high temporal and spatial precision [167–169]. Compared to other phototherapeutic treatments such as photodynamic therapy (PDT) which requires short-wavelength UV-light, PPTT uses nIR-irradiation with greater tissue penetration (up to 10 cm through soft tissue) and therefore has a larger therapeutic window. Strong absorbance and photothermal conversion efficiencies in the nIR-region make AuNRs one of the most studied NPs for PPTT [168].

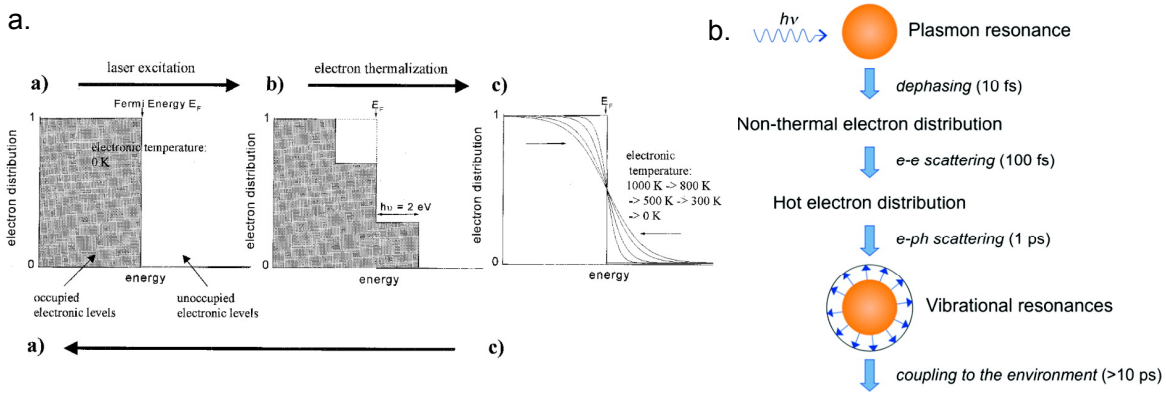

Fig. 3.1 Plasmonic Photothermal Therapy | Reprinted with permission from a. [170] and b. [49]

3.1.1.3 Plasmonic NP@MOF Composites for Drug Delivery

The integration of plasmonic nanoparticles into MOFs for biomedical applications was first considered by Khaletskaya *et al.*, who demonstrated the model drug anthracene release from

a toxic AuNR@[Al(OH)(1,4-napthalenedicarboxylic acid)]$_n$ core-shell composite under nIR-irradiation [171]. Later, Roch-Marchal *et al.* synthesised an AuNP/polyoxometalate/MIL-101(Cr) impregnation composite with potential catalytic and biomedical applications [172]. The first major study however was carried out by Li *et al.* on AuNR@ZIF-8 composites [131]. In this study, PVP-capped AuNRs were used to seed the ZIF-8 growth, yielding core-shell composites. The authors observed mesoporous volumes of 4-9 nm, which were attributed to multidomain growth of ZIF-8 on AuNR, allowing the uptake of larger molecules such as Doxorubicin (Dox) through the otherwise narrow ZIF-8 window size of 3.3-4.3 Å [173]. Next, they demonstrated photothermal energy conversion using a 0.1 mg mL^{-1} AuNR@ZIF-8 solution and an 808 nm nIR-laser (1 W cm^{-2}), resulting in a large temperature increase from 25 to 50 °C within 5 minutes. Dox-loaded AuNR@ZIF-8 exhibited both pH and light-dependent release, with roughly four times more Dox released at pH 5.5 compared to pH 7.4 in the dark, and roughly six times more Dox released under nIR-irradiation at pH 5.5 (Figure 3.2).

Whilst this was the first major study in the field, similar AuNR@ZIF-8 systems were reported by Fang *et al.* with a substantially thinner ZIF-8 shell [174], and later by Zhang *et al.* [175]. More related to the AuNR@NU-901 developed in Chapter 2, Zeng *et al.* encapsulated PEG-functionalised AuNRs with the porphyrin-based MOF-545, also containing the $Zr_6O_4(OH)_4$-cluster [176]. They achieved a 25 % wt. loading capacity for the anticancer drug camptothecin (CPT). Given the much larger aperture size of MOF-545 compared to ZIF-8 [173], this high loading capacity is understandable and makes claims for drug infiltration into the porosity more credible than those for the ZIF-8 system. The composite exhibited strong photothermal energy conversion under nIR-irradiation for 10 minutes, which heated a 0.1 mg ml^{-1} sol of AuNR@MOF-545 in water from room temperature to 73.4 °C. Additionally, the porphyrinic linker is PDT-capable by generating reactive-oxygen species under UV-light.

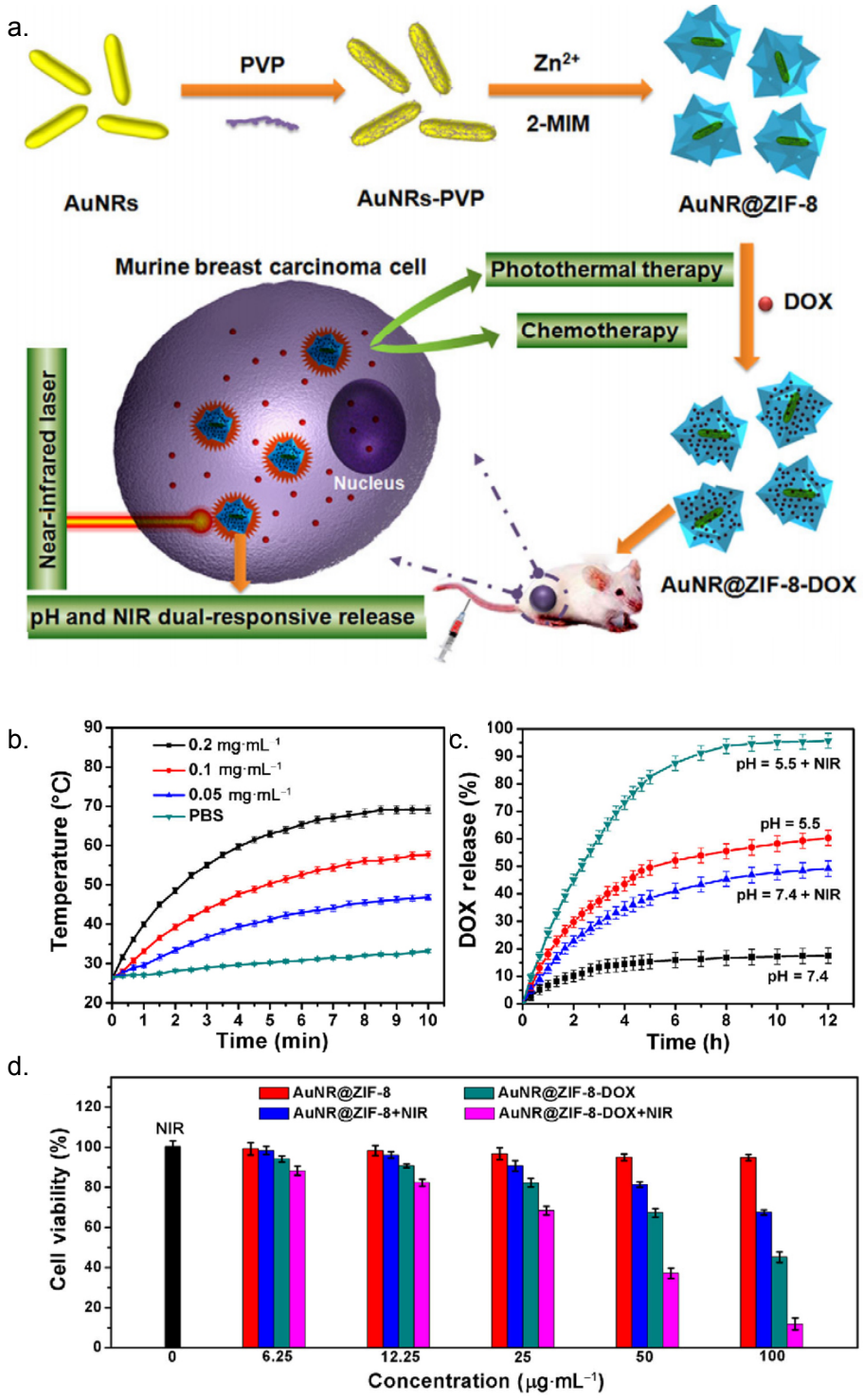

Fig. 3.2 AuNR@ZIF-8 | a. Scheme for synthesis, Dox-loading and release of AuNR@ZIF-8 composites. b. Plasmonic heating of PBS solutions at varying concentrations of AuNR@ZIF-8 using 1 W cm^{-2} nIR laser irradiation c. pH and nIR-dependent Dox release in PBS d. CCK-8 assay on $4T_1$ cells. All figures reproduced with permission [136].

3.1.2 Aims & Objectives

Encouraging results in the preceding works from this authors' research group have shown that the H_4TBAPy Zr-MOFs have strong therapeutic potential [37, 96]. The large porosity of NU-901 enables the uptake of large drug molecules and the MOF has shown to be biologically compatible. In addition, the plasmonic moiety in this study's system could enable nIR-triggered release.

As part of a wider effort to utilise H_4TBAPy MOFs in drug delivery, this proof-of-principle study therefore attempts to demonstrate light-triggered molecular release from AuNR@NU-901 – in fact, the composite was first developed with this particular application in mind (Section 2.2). Due to safety concers and easier handling, calcein, which is structurally similar to Doxorubicin, was selected as a model drug in accordance with previous reports [36, 35, 148, 149, 82]. Resonant energy transfer renders calcein a partially inert fluorophore when adsorbed in a MOF (self-quenching fluorophore) [177], however, its fluorescence quantum yield increases drastically upon desorption. The increase in its fluorescence intensity can therefore be used to monitor the rate of release. AuNR@NU-901 composites were loaded with calcein by liquid-phase infiltration and the release was studied in two experiments. First, a set of steady-state experiments were used to confirm calcein desorption under both chemical degradation and thermal influence. Next, the loaded composite was subjected to nIR-irradiation and the calcein fluorescence intensity was monitored *in situ*. Experiments and results are described below.

3.1.3 Materials & Methods

3.1.3.1 General Methods

Chemicals were purchased from Sigma Aldrich, Alfa Aesar, or used as synthesised in the preceding chapter.

3.1.3.2 Calcein Incubation

Calcein was loaded into the AuNR@NU-901 porosity using a liquid phase infiltration. A sol of AuNR@NU-901 (0.1 mg mL^{-1}, MeOH) was added to a calcein solution (1 mg mL^{-1}, MeOH) and stirred overnight. The resulting sol, cal@AuNR@NU-901, was kept in the dark for several months and used as described in subsequent sections. Before use, the samples were centrifuged and washed in MeOH to remove excess calcein from the solution and the external surface of the MOFs.

3.1.3.3 Plate-reader Release Experiments

UV/vis and fluorescence spectra were recorded on a TECAN Spark. Aqueous or methanolic solutions were prepared and diluted until the absorbance was in the linear Beer-Lambert regime. Aliquots of the samples (0.1 mL) were then placed in a 96 well-plate and loaded in the plate reader. The UV/vis absorption spectrum was recorded between 350 and 600 nm. Two fluorescence spectra were also recorded; the first with an excitation at 470 nm and scanned between 485 and 650 nm with a step-size of 2 nm and a bandwidth of 5 nm. The second spectrum was recorded from an excitation wavelength of 390 nm; this spectrum was recorded between 410 and 600 nm with the same step-size and bandwidth as above. The PBS destruction experiments were carried out in Eppendorf tubes. The cal@AuNR@MOF sol was diluted to a concentration of 1 mg mL^{-1} and 0.1 mL of a PBS solution at pH 7.4 was added. The samples were then shaken and an aliquot was pipetted into the well-plate. In the heating experiment, a sample of identical concentration was placed in a 5 mL glass vial and heated in an oil bath to 70 °C for 2 hrs.

3.1.3.4 nIR-Laser Release Experiments

All experiments were carried out with Dr Ermanno Miele of the Nanophotonics Group at the Cavendish Laboratory in Cambridge. Time-resolved fluorescence spectra under nIR-irradiation were recorded on a custom-built spectroscopy rig. An aliquot of the calcein-loaded AuNR@NU-901 stock solution (50 µL) was dispersed in water, centrifuged, washed once more, and then dispersed in a quartz fluorescence cuvette in DI water. The cuvette was then

placed in a holder with two fibre-coupled ports right-angled at one another. Collimation lenses at the windows of the port focus on the same spot inside the cuvette. Through the first port, the nIR-light source (782 nm laser, final power at the sample *ca.* 100 mW) was coupled, as well as the fluorescence excitation source (470 nm LED). The scattered light was coupled back through the other fibre optic cable to an Ocean Optics qe65000 spectrometer.

3.1.4 Results & Discussion

3.1.4.1 Calcein Release Data - Thermal

First, the basic photophysical properties of AuNR@NU-901 and cal@AuNR@NU-901 were investigated. The UV/vis absorption spectrum of the H_4TBAPy linker in water showed distinct sharp absorption bands in the blue and UV regions of the spectrum. Direct excitation into the absorption bands at 390 nm resulted in strong fluorescence from the S_1 state with a peak occurring at 443 nm (Figure 3.3 a., red line). The free calcein dye on the other hand has stronger absorption in the visible region, with the S_1 band centered at *ca.* 470 nm. Excitation into this absorption band resulted in a longer wavelength emission with a peak at 510 nm (Figure 3.3 b., blue line), as did excitation at 390 nm (Figure 3.3 b., red line), which is consistent with Kasha's rule, albeit with a lower intensity.

Matters were complicated when moving to the bound state of H_4TBAPy that occurs in NU-901. Interchromophoric π-π stacking causes a bathochromic shift in the emission band of roughly 50 nm (Figure 3.3 c., red line) [178]. Crucially, however, this only applies to excitation at 390 nm; excitation of the sample with 480 nm light led only to little fluorescence as the samples' weak absorption at this wavelength excited the ground state inefficiently (Figure 3.3 c., blue line). Spectra recorded from different excitation wavelengths were therefore split into a MOF channel (excitation at 390 nm, red line), in which H_4TBAPy was excited, and a calcein channel (excitation at 470 nm, blue line). Cal@AuNR@NU-901 had mixed absorption from both the calcein and H_4TBAPy, and displayed calcein emission when excited at 470 nm and 390 nm (Figure 3.3 d., blue and red line, respectively). The fluorescence intensity increased when the sample was held for two hours at room temperature (dotted lines). This was attributed to self-quenching calcein diffusing out the of MOF pores, where their fluorescence is activated.

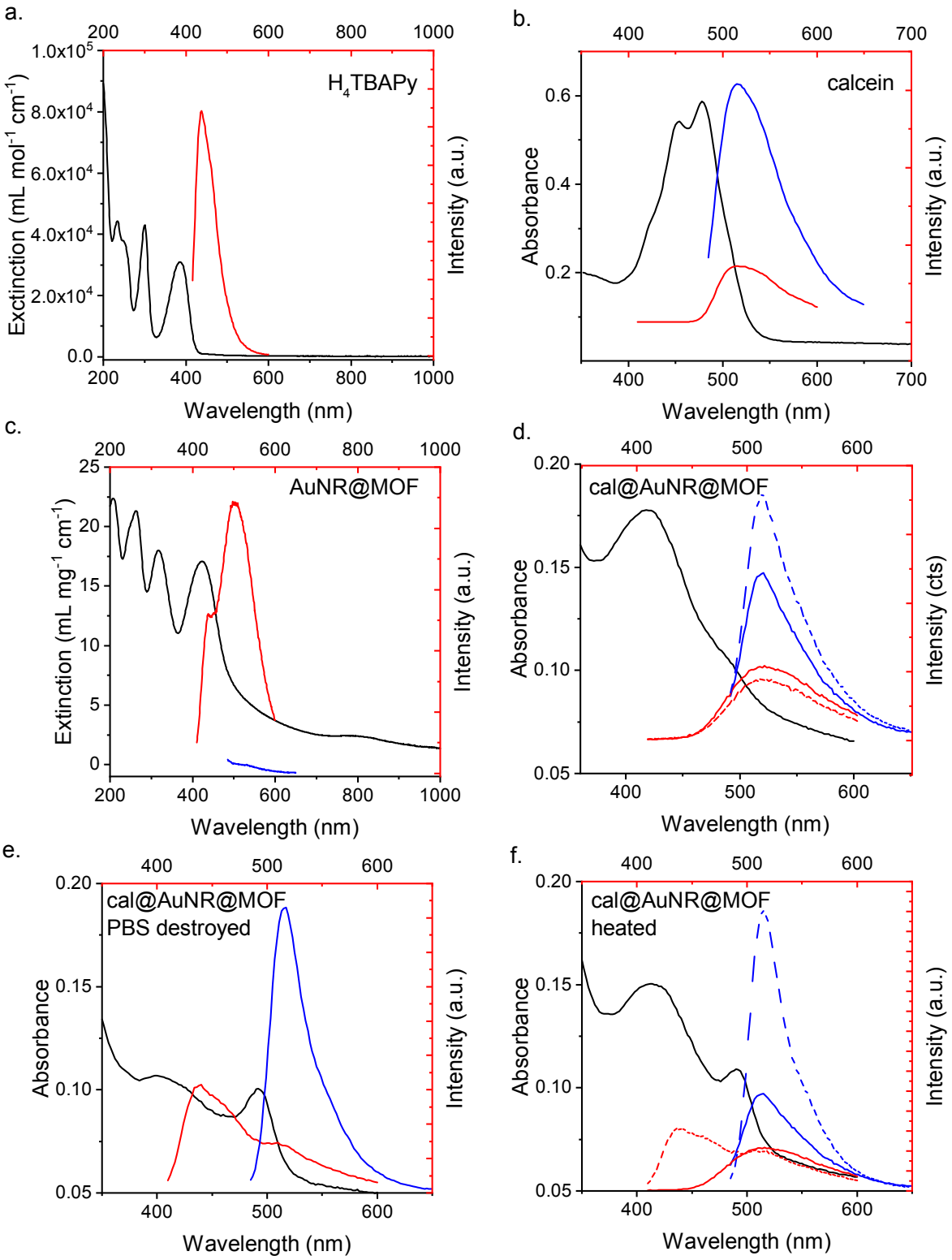

Fig. 3.3 Calcein Release Data - Thermal | Absorption spectra in black were recorded between 350 and 600 nm; fluorescence spectra acquired following excitation at 390 nm are shown in red, following excitation at 470 nm in blue.

This trend was further observed when the sample was reacted with PBS at pH 7.4 (Figure 3.3 e.). PBS is known to degrade Zr-MOFs by breaking the Zr−O bonds and replacing them with more oxophilic phosphates [36, 148, 33, 95]. Consequently, the fluorescence levels in the calcein channel increased drastically. At the same time, H_4TBAPy linkers were released from the MOF and their fluorescence emission reverted back to 440 nm as they no longer stacked. The evolution of the 440 nm peak could therefore be used to track the degradation of the MOF. Similar spectra were observed when the sample was heated in an oil bath for two hours (Figure 3.3 f., dotted lines). The calcein fluorescence intensity increased, as did the free H_4TBAPy concentration. Whilst it is plausible that the increased thermal energy favours desorption and diffusion of calcein from the composite, the blue-shift of the pyrene-containing band appears to suggest partial MOF breakdown as well.

In any case, these preliminary experiments were supportive of the hypothesis that a drug molecule can be released from the composite under heating. Next, attention is therefore paid to the internal heating of AuNR@NU-901 under nIR-light.

3.1.4.2 Calcein Release Data - Photothermal

To study the calcein release in more detail, a cal@AuNR@NU-901 sol was dispersed in a cuvette which was placed in a four-port sample holder. A 470 nm LED was used for the calcein excitation, and a 782 nm nIR-laser for plasmonic heating. Time-resolved fluorescence spectra were integrated over the calcein emission peak and the integrals plotted against the time of recording (Figure 3.4 a.).

The evolution of the calcein emission was very similar under dark (no nIR-irradiation) and plasmonic heating (with nIR-light) conditions (Figure 3.4 a., black and red lines respectively). Both follow a first-order increase, saturating after roughly 5 hrs. Under plasmonic heating, the calcein fluorescence emission did increase further, which could indicate light-triggered release. In any case, this effect was relatively small. There are multiple explanations for this: (i) limited light-sample interaction, either due to weak nIR-absorption of AuNR@NU-901 (Figure 3.3 a., black line) or insufficient irradiation intensities; (ii) sampling averaging causing a relatively small plasmonic-triggered release to be lost in the experimental noise; (iii) poor photothermal energy conversion, perhaps due to plasmon damping by the MOF; (iv) the heating is too localised at the center of the crystallite, leading to no additional diffusion at the outer surfaces. It is also not clear whether the small increase in calcein release under nIR-irradiation can be attributed to plasmonic heating or bulk heating of the solution by the laser. These experimental challenges remain in order to prove plasmonic triggered release.

Time-resolved chemical degradation by the addition of PBS to cuvette at the beginning of the recording causes an immediate increase in the fluorescence intensity indicative of

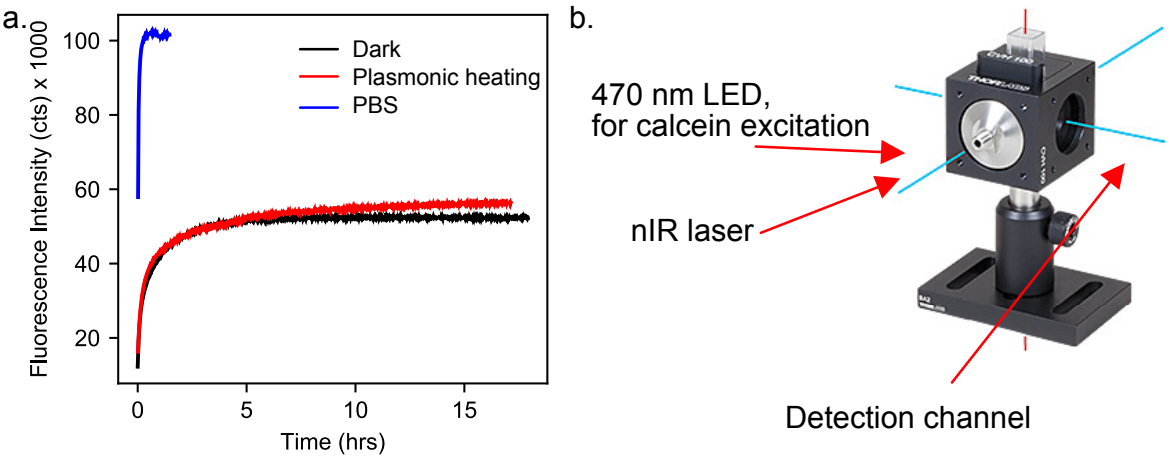

Fig. 3.4 Calcein Release - Photothermal | a. Band evolution of calcein fluorescence spectra (integrated from 494-563 nm) against time. Note that the fluorescence under plasmonic heating is a little higher and faster than in the control experiment. The addition of PBS immediately destroys the MOF and releases calcein into the solution. This process saturates within almost 10 minutes. b. Schematic of the experimental setup used to study the calcein release. Image credit Thorlabs.

fast degradation of the AuNR@NU-901 crystallites (Figure 3.4 a., blue line). Here, the release saturates within the first ten minutes, suggesting near-complete breakdown of the MOF within this time-frame. This implies that if AuNR@NU-901 were used in drug delivery applications, the stability of the Zr-MOF in phosphate-containing media would present a major obstacle.

3.1.5 Conclusion & Outlook

Here the potential biomedical applications of AuNR@NU-901 were investigated. The photothermal energy conversion of AuNRs under nIR-irradiation could present a powerful handle in spatiotemporally controlled drug release. In these experiments, the shift of the H_4TBAPy emission wavelength and the change in the fluorescence intensity of calcein were used as indicators to gauge the extent of MOF degradation and calcein release. Preliminary steady-state experiments suggested that the composite was able to adsorb a model drug and release it under heating and chemical degradation by PBS.

The following *in situ* release experiments were less encouraging. Under nIR-irradiation, the composite did appear to release calcein faster than in the dark, but due to the lack of a suitable control experiment, this effect could not be conclusively attributed to plasmonic heating. In any case, the effect was very small. Whilst the experimental setup does show potential for *in situ* measurements, further efforts need to be undertaken to improve the experimental conditions and to yield more conclusive results.

Addition of PBS, the chemical degradant to NU-901, caused a very fast destruction of the MOF and concomitantly a fast drug release. These results are alarming as they suggest that NU-901 is indeed very unstable in phosphate containing media, which raises critical concerns over its ability to transport drugs in the bloodstream.

In response to these concerns, it was proposed that AuNR@NU-901 could have plasmonic properties that could be utilised elsewhere. In search of such novel applications, the following study on AuNR@NU-901 as a size-selective optical sensor emerged.

3.2 Surface-enhanced Raman Spectroscopy

3.2.1 Background

3.2.1.1 Surface-enhanced Raman Spectroscopy

Surface-enhanced Raman Spectroscopy (SERS) is a vibrational spectroscopy technique in which the characteristic Raman signal of a molecule (Section 1.4.4) is enhanced by more than six orders of magnitude. SERS was first experimentally observed in 1974 [179] but it was not interpreted correctly until 1977 by van Duyne [180].

The principles of this technique can be likened to those of a driven mechanical oscillator [181, 182]. An incident electromagnetic wave can stimulate the coherent oscillations of surface electrons known as localised surface plasmons resonances (LSPR, Section 1.3.3) if the frequency of the wave matches the plasma frequency of the metal nanoparticle. Radiative outcoupling from the plasmons occurs at the same frequency – in other words, the metal acts as an optical nanoantenna enhancing an elastic scatter. The presence of an analyte molecule within the enhanced field, however, can modulate the outcoupling frequency if the polarisability of the molecule changes during a vibrational mode with the same frequency. In this case, the outgoing wavevector will be different from the incident wave – an inelastic Raman scatter has been amplified by LSPR. Since SERS-scattering is a resonance phenomenon, the greatest enhancements are observed when the incident and outgoing wavevector are in resonance with the LSPR. Thus, although the Raman shift remains independent of the incident wavelength, the scattering intensity is wavelength-dependent. The enhanced field rapidly decays exponentially normal to the NP surface, hence only molecules that are in very close proximity to the surface are within the enhanced field.

Originally a peculiar technique only used by few experts in Raman spectroscopy and electrochemistry, SERS has become a powerful, state-of-the-art method for the characterisation of plasmonic materials. Advances in the wet synthesis and preparation of plasmonic support structures have since spawned the field of plasmonics [181]. The applications of SERS in numerous fields, including the detection of environmental pollutants [183, 184], inorganic molecules and ions [185], and sensing of biological markers [186] and bacteria [187], are described in reviews elsewhere.

3.2.1.2 SERS using NP@MOF Composites

The encapsulation of SERS-active NPs into MOFs provides a unique opportunity to harness the optical properties of plasmonic materials with the adsorptive capabilities of MOFs in tandem. The role of the MOFs, which is discussed in more detail in a recent review by Huang

et al. [188], is here principally two-fold: (i) MOFs can selectively filter molecules before detection at the plasmonic core, either by size-exclusion by the porosity (molecular sieving) or by preferential adsorption of certain target analytes; (ii) adsorption can raise the local concentration of an analyte above the detection limit – as such MOFs can act as analyte pre-concentrators.

The first study to recognise the potential for SERS using NP@MOF composites came from Sugikawa *et al.* in 2011 by encapsulating AuNRs in MOF-5 [189], but it was only later that size-selective sensing was demonstrated with a set of model pyridine derivatives [137]. In more recent years the technique has matured considerably [190]. SERS has been realised in multiple platforms, including Zn [191, 192], Zr [193], and Fe-MOFs [194–196]. These platforms have been proposed for a wide range of analytes ranging from volatile organic compounds (VOCs) as biomarkers for lung cancer by Qiao *et al.* [197], to peptides responsible for cardiovascular diseases [198]. Other common applications include food safety analysis [199, 200] and pollutant sensing [193, 201, 202].

Many of the systems cited above lack precise morphological control, and it is unclear whether the NPs are fully encapsulated – required for filtering – or attached to the external surface of the crystallites. While the synthesis of a core-shell AuNR@ZIF-8 composite was demonstrated by Zheng *et al.* [191], the use of much more chemically stable core-shell Zr-MOF composites has been insufficiently explored due to the difficulty in their preparation. In addition, despite its flexibility [173], the use of a ZIF-8 shell limits the number of analytes that can access the porosity due to the very narrow 3.4 Å pore window, a problem that can be overcome using other structures with larger pore sizes.

3.2.2 Aims & Objectives

This project aimed to demonstrate the SERS capabilities of AuNR@NU-901. The aforementioned properties of NU-901 make it a promising candidate for the detection of various analytes: made from the chemically stable $Zr_6O_4(OH)_4$-clusters, it is able to withstand a number of solvents and pH. The excellent core-shell yield achieved in this system can reduce concerns over unencapsulated plasmonic material. In addition, the wide porosity facilitates fast diffusion of analytes, and the pores are oriented towards the AuNR tips and therefore the center of plasmonic activity (plasmonic hotspots [203]).

In this proof-of-principle study, small thiolated aromatic analytes with high Raman cross-sections were infiltrated into the MOFs and the Raman spectra were recorded. Further, a bulky polymer was added together with the smaller analytes to see if size-selective sensing was possible. Details of the experiments and results are found in the following sections.

3.2.3 Materials & Methods

3.2.3.1 Analyte Incubation

The thiolated analytes were incubated into the MOF porosity, by liquid-phase infiltration. Powdered AuNR@NU-901 were dispersed in a sol in acetone or MeOH (1 mg mL^{-1}). An aliquot of this stock solution (50 µL) was added to acetone or MeOH (450 µL) and the analyte (500 µL, 1 mg mL^{-1}) was added. The suspensions were stirred overnight, washed twice in their native solvents to remove excess thiols, and dried in a desiccator to remove most of the residual volatile solvents.

3.2.3.2 Raman Spectroscopy of Incubates

All experiments were carried out either by or with the help of Demelza Wright of the Nanophotonics group in the Cavendish Laboratory at Cambridge University. Dried powders were mounted to a standard microscopy slide and SERS spectra were acquired using a 785 nm laser (typically 0.3 mW) using a Renishaw InVia Raman microscope. Scattered light was coupled into a x100 long working distance objective. A grating of 1200 lines mm^{-1} and an acquisition time of 30 s was used for all spectra. Larger laser powers were found to degrade the samples.

3.2.3.3 Raman Spectroscopy of Diffusion

All experiments were carried out either by or with the help of Demelza Wright of the Nanophotonics group in the Cavendish Laboratory at Cambridge University. For *in situ* diffusion experiments, AuNR@NU-901 was drop cast from an acetone suspension and fully dried under N_2 onto a coverslip. The slip was mounted onto a liquid chamber (325 µL) containing DI water and spectra were recorded through the coverslip before and after injection of a 10 % acetone:water (v:v) solution of BPTCN (0.1 mg mL^{-1}) into the chamber. The injection at a rate of 0.5 mg mL^{-1} took roughly 10-15 s. Spectra were recorded similarly to above, but with an increased power of 6.485 mW and 2 s acquisition time and a cycle time of 4.8 s.

3.2.3.4 Molecular Dynamics Simulation

The movement of BPTCN inside the NU-901 porosity was modelled by Dr Peyman Moghadam of the Adsorption & Advanced Materials group in Cambridge. Dr Moghadam used molecular dynamics (MD) simulations in the multipurpose simulation suite RASPA.The crystallographic information from NU-901 was taken from Kung *et al.* [92]. Lennard-Jones (LJ)

parameters for C, O and H were obtained from the Dreiding force field, and, likewise, the LJ parameters for Zr were taken from the Universal Force Field (UFF). The extended charge equilibrium method (EQeq) was used to assign the partial atomic charges of the framework. The BPTCN structure was first obtained in Avogadro, where the geometry was optimized. GAFF4RASPA and AmberTools were then used to generate the force field description of the molecule, using AMBER for the LJ parameters and partial charges for the molecule. The Lorentz-Berthelot mixing rules were used to calculate the adsorbate/framework cross LJ parameters. A cut-off distance of 12.8 Å was used for all interactions; Ewald summations method was used to compute the electrostatic interactions. A time step of 0.0005 ps was used, with 10^7 steps simulate 5 ns of BPTCN diffusion in NU-901.

3.2.4 Results & Discussion

3.2.4.1 Background Spectra

All numeric data processing of the SERS spectra was carried out by Demelza Wright.

First, standard powder Raman spectra (non-SERS) were obtained for the pristine MOF and its components. To remain consistent with later experiments, all Raman spectra were recorded on a Raman microscope and a 785 nm laser line, in order to achieve efficient excitation into the plasmon bands of AuNR@NU-901. The Raman spectrum of NU-901 is largely dominated by its H_4TBAPy component, which is unsurprising given the large Raman cross-section of polyaromatic species [185]. Evidence for the $Zr_6O_4(OH)_4$-cluster was not found in the spectra. The strongest modes in the NU-901 spectrum at 1265 cm^{-1} and 1609 cm^{-1} were assigned to the ring breathing modes on the single and polyaromatic moieties respectively (Figure 3.5 a.) [204].

The corresponding SERS spectrum of AuNR@NU-901 shows an unwanted large broad-band emission, in which, however, the ring breathing modes assigned in virgin NU-901, can be clearly resolved (Figure 3.5 b.). The SERS spectrum of AuNR@PEG shows a similar background, whilst that for AuNR@CTAB is much weaker, suggesting that the PEGylation of the AuNR surface is responsible for the background. A polynomial fit to the AuNR@PEG spectrum was therefore removed from all following spectra (Figure 3.5 c. and d).

3.2.4.2 Size-selective Raman Spectroscopy

All numeric data processing of the SERS spectra was carried out by Demelza Wright.

AuNR@NU-901 was incubated with two small-molecule aromatic thiolated analytes: biphenyl thiol (BPT) and the related mercaptobiphenylcarbonitrile (BPTCN). Stock solutions of BPT and BPTCN were combined with AuNR@NU-901 suspensions in MeOH and acetone, and left to impregnate the porosity overnight. Next day, they were centrifuged, washed to remove excess BPT or BPTCN from the external surface, and mounted on a Raman microscope.

The incubation of BPT resulted in a number of additional modes in the SERS spectra (Figure 3.6 a.). The strongest ones were observed at 1078 and 1282 cm^{-1}, and they were assigned by density functional theory (DFT) as the δ(C—H) and ν(ring), respectively. Dr Charles Readman from the Nanophotonics group is accredited for all DFT calculations (data not shown) in this chapter. Likewise, the incubation of BPTCN also adds further modes to the SERS spectra, namely at 1091, 1189, 1288, and 2230 cm^{-1}, all assigned by DFT as δ(C—H) (thiol-phenyl ring), δ(C—H) (both phenyl rings), ν(ring), and ν(C≡N), respectively. These modes match well in intensity and position to control spectra obtained when the analytes

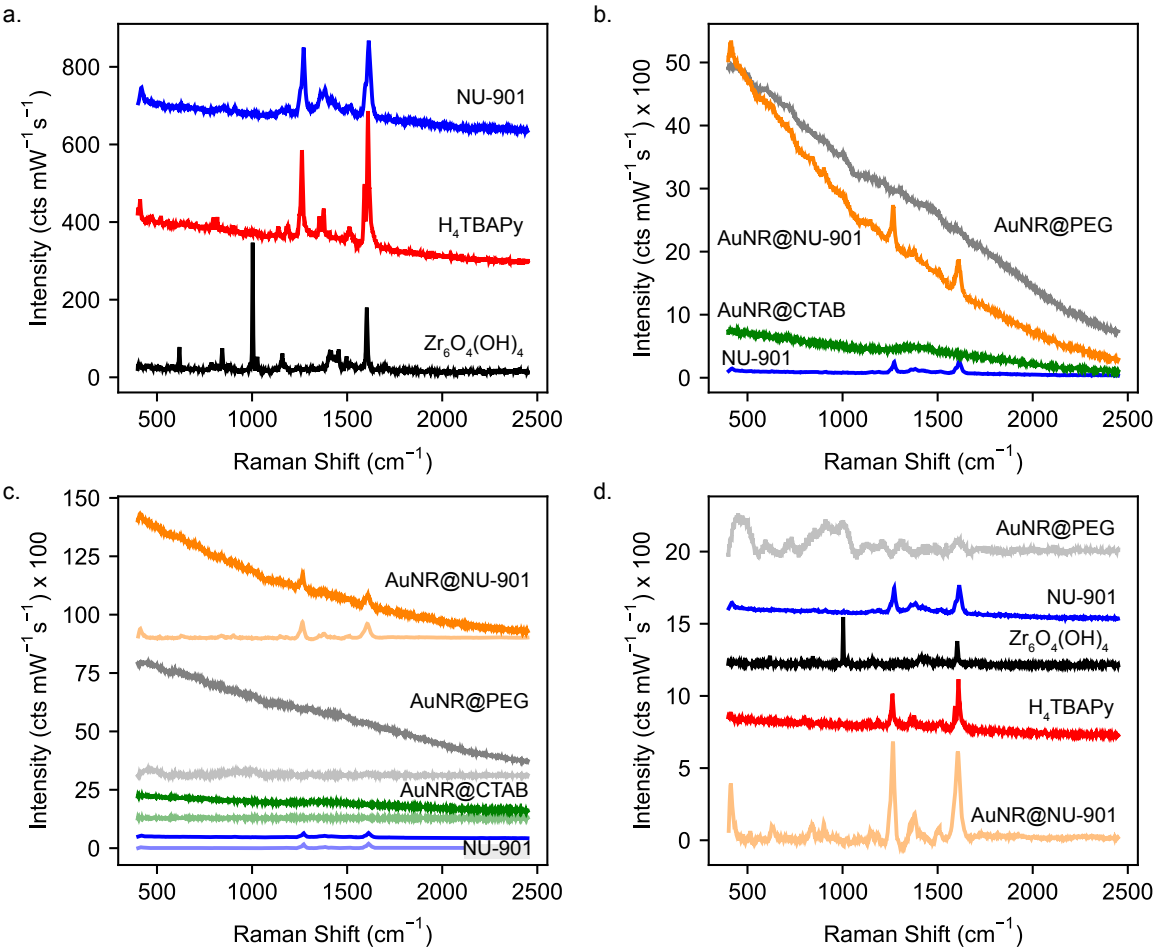

Fig. 3.5 AuNR@NU-901 Component Spectra | a. Control spectra of $Zr_6O_4(OH)_4$, H_4TBAPy, and NU-901. The principle ring breathing modes for the single and polyaromatic rings in H_4TBAPy and NU-901 are positioned at 1265 cm^{-1} and 1609 cm^{-1} respectively b. Control spectra of AuNR@NU-901 and its components. The AuNR@NU-901 spectrum features an unwanted large broadband emission, which can be attributed to the PEGylation of the AuNR surface c. A polynomial fit to AuNR@PEG can serve as a background which can be removed from the spectra. Spectra shown in a lighter shade have their backgrounds removed d. Background-removed control spectra of AuNR@NU-901 components

were exposed to AuNR@PEG directly. This suggests that in the composite, the analytes have infiltrated the porosity and interacted with the AuNR tips, where the plasmon field is concentrated (Figure 3.6 a.).

Next, AuNR@NU-901 were impregnated with thiolated polystyrene (PST-SH, M_w = 5,000 g mol^{-1} to demonstrate the size-selectivity of the porosity. The Raman spectrum of PST-SH shows additional marker bands which are not present in PST-SH/AuNR@NU-901 (Figure 3.6 a.).

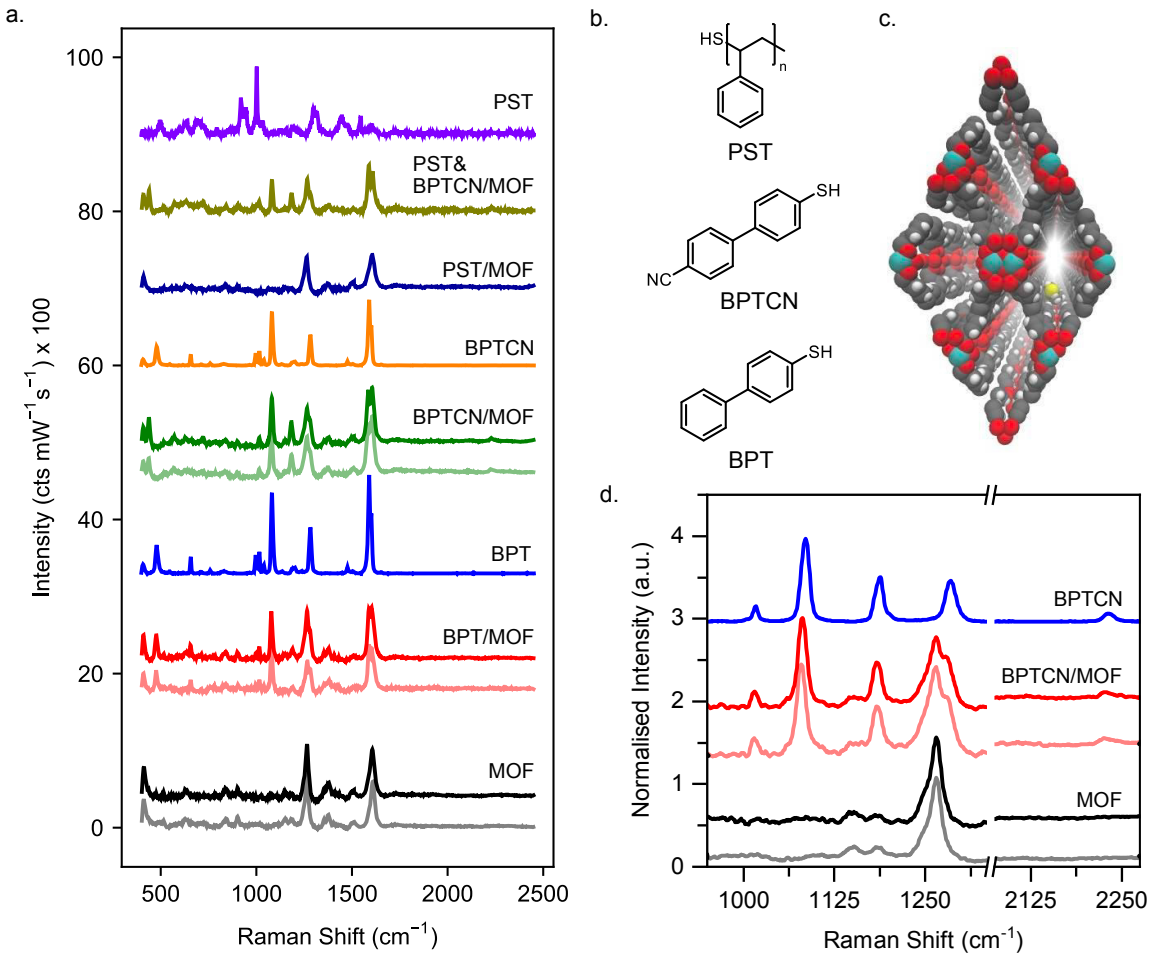

Fig. 3.6 SERS spectra of AuNR@NU-901 impregnated with analytes | a. SERS spectra of AuNR@NU-901 (here labelled simply 'MOF' for greater visual clarity) before and after impregnation with various analytes, labelled in the format analyte/MOF. Spectra in a lighter shade were recorded from impregnations in MeOH, all others in acetone. Spectra labelled with the analyte name only were recorded from incubation with AuNR@PEG-SH to retain the plasmonic enhancement effect. All spectra were background subtracted, scaled and offset for greater visual clarity. b. Analytes used in the molecular filtration experiments. c. Snapshot of a molecular dynamics simulation carried out by Dr Peyman Moghadam. View along the NU-901 z-axis. The BPTCN is in the right-hand diamond-like channel, and can be recognized by the yellow S atom. The close proximity between BPTCN and H_4TBAPy pore-wall suggests effective π-π stacking interactions. d. SERS spectra of AuNR@NU-901 (MOF) and BPTCN. The notation is identical to that in a. All peaks were normalised; the AuNR@NU-901 peaks were normalised to the pyrene Raman mode at 1266 cm^{-1}, and BPTCN containing spectra were normalised to the band at 1080 cm^{-1}. The nitrile mode ν(C≡N) is visibly weaker in BPTCN/MOF than in BPTCN/AuNR, suggesting either a misalignment of BPTCN along the plasmonic field axis or a hydrolysis reaction of the nitrile group.

It can therefore be concluded that the porosity AuNR@NU-901 restricts the entry of larger molecules, prohibiting diffusion into the MOF core. For size-selectivity to be a useful property however, the composite must be able to selectively filter from a mixed solution. In that case, an incubation featuring both PST-SH and BPTCN clearly only shows the Raman peaks of the smaller BPTCN (Figure 3.6 a.).

3.2.4.3 BPTCN Impregnation Spectra in Detail

All numeric data processing of the SERS spectra was carried out by Demelza Wright.

The successful infiltration of BPTCN into AuNR@NU-901 was further supported by molecular dynamics (MD) simulations. A BPTCN molecule of molecular dimensions 15 x 7 Å along the thiol-CN axis can easily transverse the main channels of NU-901. Figure 3.6 c. shows a snapshot of the molecular dynamics simulation for a trajectory of BPTCN at 5 ns at room temperature modelled by Dr Peyman Moghadam. The movement along the channel is *via* a hopping mechanism, with BPTCN and the NU-901 pore walls in close contact. This suggests π-π stacking between the aromatic rings in BPTCN and pyrene linkers in NU-901 as a main force of attraction.

Whilst the majority of the intensity ratios between peaks of the BPTCN modes were retained following incubation, there was a notable decrease at the high frequency CN-stretching mode, ν(C≡N) (Figure 3.6 d.). Two possible scenarios can account for this reduction in intensity: (i) the ν(C≡N) is preferentially enhanced in AuNR@PEG compared to AuNR@NU-901. Porous constraints could force the orientation of the CN axis to no longer align with the plasmonic field enhancement, normal to the AuNR surface. Scenario (ii) sees a reaction of the nitrile group at the Lewis-acidic $Zr_6O_4(OH)_4$-cluster, potentially hydrolysing to an ester. In this case, fewer nitrile groups would be present in the sample, resulting in a slight decrease of this mode.

3.2.4.4 Diffusion Studies

All numeric data processing of the SERS spectra was carried out by Demelza Wright.

A set of *in situ* experiments was performed to observe the binding of BPTCN to the AuNR core in real-time. To this end, a small amount of AuNR@NU-901 was deposited on a glass cover slip and inverted over a small reservoir filled with water on a standard microscopy glass slide. The Raman spectra were then recorded in time-lapse as a syringe pump added a solution of the analyte into the reservoir. Quickly after the injection, the characteristic modes at 1091, 1189, and 1588 cm^{-1} appear. This intensity saturates roughly 200 s after the injection starts. Raman spectra recorded away from the AuNR@NU-901 depositions (not

shown) did not yield any BPTCN peaks, confirming that the signal originates from the SERS enhancement and not the analyte solution.

The mechanical action of the syringe pump caused some focal drift and the resultant loss of signal can be observed in the stacked Raman spectra. The adsorption onto the AuNR surface can nevertheless be tracked by fitting the spectra to a Lorentzian curve and analysing the areas under two modes, one of which, peak 5 centered at 1588 cm^{-1}, originates from BPTCN and the other, peak 6 centered at 1608 cm^{-1}, from AuNR@NU-901. The evolution of the peak ratios is plotted in Figure 3.7 and shows a first-order adsorption like behaviour.

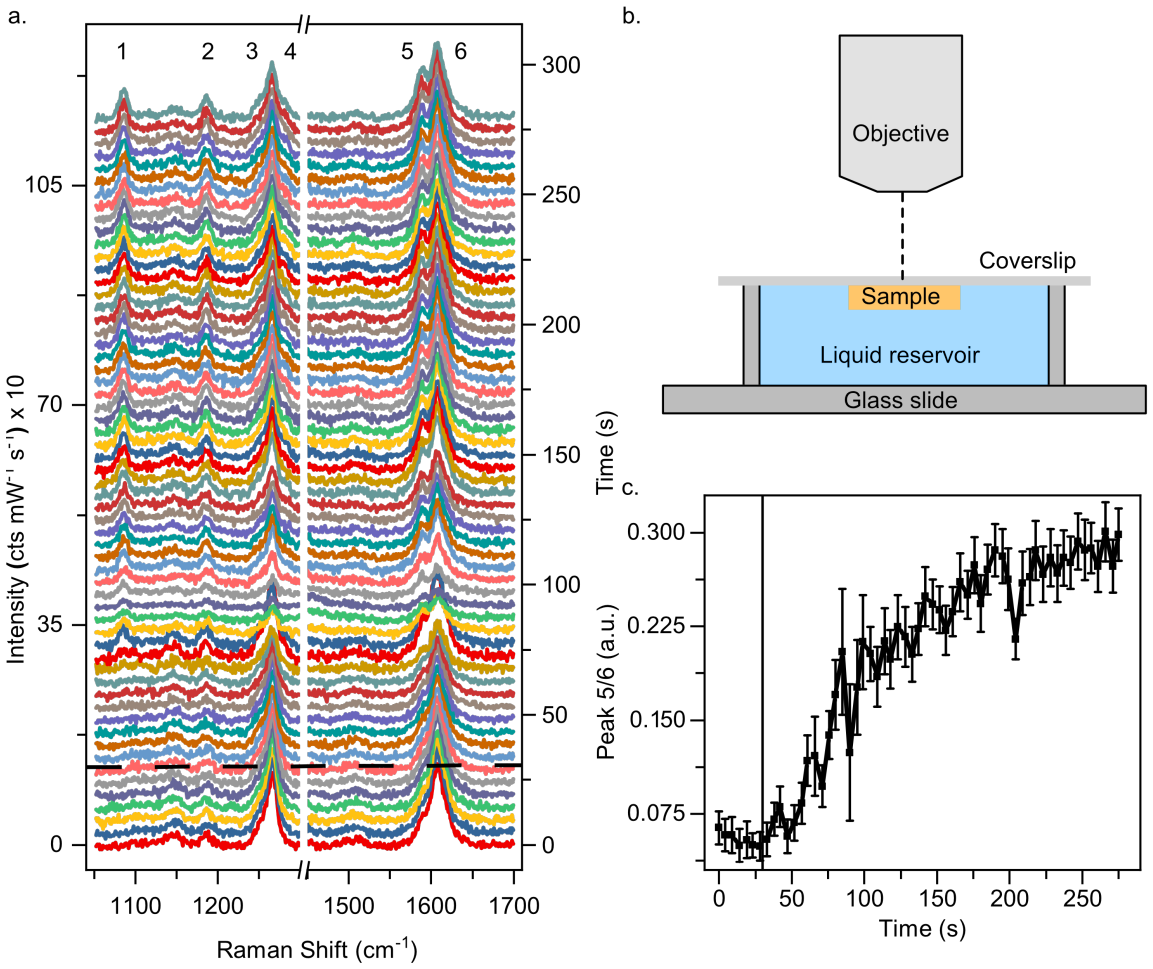

Fig. 3.7 *In situ* SERS measurements of BPTCN infiltration into AuNR@NU-901 in an aqueous environment | a. Stacked spectra, all spectra are background subtracted; dashed line marks the beginning of the BPTCN injection. Peaks in spectra are labelled 1-6, analyte peaks that increase in intensity throughout the measurement are most notably 1, 2, and 5. Note that there is some focussing drift immediately after the addition, which causes a slight decrease in the AuNR@NU-901 peak intensities. b. Scheme of experimental setup. c. Peak integral ratios between analyte peak 5 and AuNR@NU-901 peak 6. The spectra were fitted with a Lorentzian curve and integrated along the peaks. The error bars mark the fitting errors, and the black vertical line marks the beginning of the BPTCN injection.

3.2.4.5 Post-incubation TEM

It must be noted here that, apart from the molecular filtration, the discussed results could also have been caused by a breakdown of AuNR@NU-901 following the impregnation procedure. A composite that would be destroyed with exposed AuNRs would equally bind BPT and BPTCN and result in similar spectra to those shown in Section 3.2.4.2. The high chemical

stability of NU-901 in water [205] makes this unlikely, but, nevertheless, a control TEM experiment following the impregnation procedure was conducted (Figure 3.8).

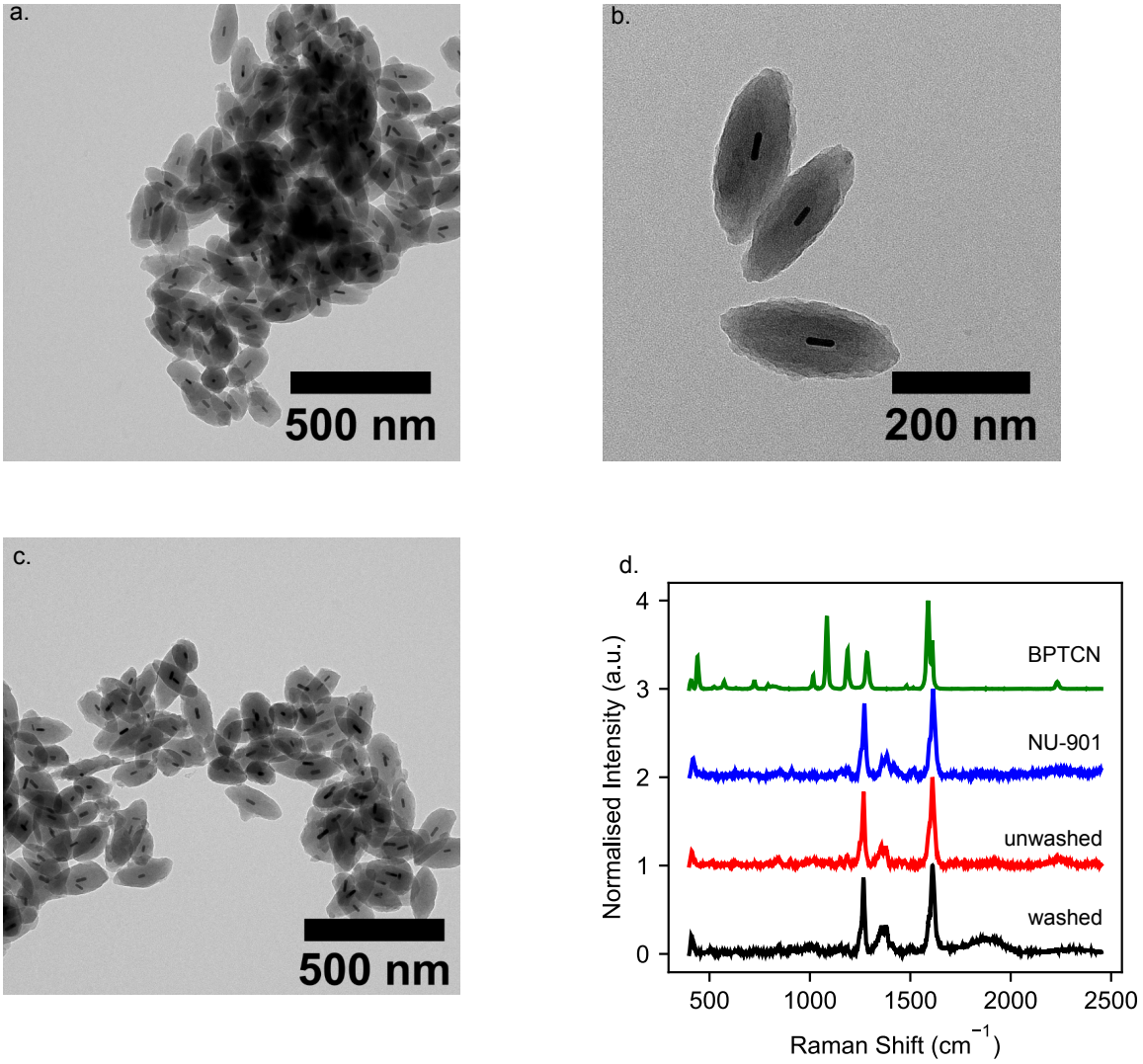

Fig. 3.8 Post-incubation TEM | a-c. Representative TEM micrographs of AuNR@NU-901 taken after impregnation with BPTCN in MeOH. d. Normalised Raman spectra of virgin NU-901 infiltrated with BPTCN. The results are inconclusive as only very weak BPTCN modes are observed, which may or may not come from inside the porosity. After washing, these modes disappear.

Whilst the micrographs suggest some aggregation of the AuNR@NU-901 crystallites, they do not show any unencapsulated plasmonic material. It can therefore be strongly assumed that all plasmonic signal generation must result from inside the AuNR@NU-901, and correspondingly that the analytes diffuse through the porosity.

3.2.4.6 Virgin NU-901 Incubations

Virgin NU-901 was incubated with BPTCN to analyse the standard (non-SERS) Raman spectra of the analytes in the MOFs. NU-901 crystallites were subjected to the same impregnation procedure as AuNR@NU-901, and, subsequently, Raman spectra of both washed and unwashed NU-901 were obtained (Figure 3.8 d.). These results were inconclusive. Very weak BPTCN modes were observed in the unwashed sample and it is unclear whether they originate from BPTCN inside or around the crystallites. No BPTCN modes were observed after washing, which is most likely due to the removal of the analyte from the sample altogether. It can therefore be assumed with high confidence that the BPTCN and molecules with a similar Raman cross-section can only be sensed at these levels of concentrations when plasmonic enhancement increases the Raman signals.

3.2.5 Conclusion & Outlook

In this proof-of-principle study, SERS generation inside AuNR@NU-901 composites was shown. Small thiolated analytes, BPT and BPTCN, were allowed to diffuse through the porosity and sensed at the AuNR ends where the plasmon field is concentrated. The composite showed size-selective uptake of these analytes from a mixture containing a larger molecule, PST-SH. The CN stretch in SERS signal of AuNR@NU-901 incubated BTPCN was weakened, which could be due to a reaction with the Lewis-acidic $Zr_6O_4(OH)_4$-cluster of NU-901. Finally, TEM micrographs of AuNR@NU-901 confirmed that the morphology of the crystallites was unchanged, making the composite viable for use in solution.

The results obtained in this proof-of-principle study are promising. Next, the composite should be tested against more relevant analytes, such as pharmaceutical pollutants, pesticides, or biological markers. The detection of VOCs by Qiao *et al.* is a fascinating study and it would be interesting to probe if the results could be replicated with AuNR@NU-901. The high physicochemical stability of NU-901 could also enable an application in gas sensing of industrial waste streams. However, the large porosity of NU-901 limits its size-selective sensing to the rejection of very large moieties such as enzymes.

Chapter 4

BET Surface Identification

'All models are wrong, but some are useful' – George Box

Porosity and surface area analysis play a prominent role in modern materials science, where their determination spans the fields of natural sciences, engineering, geology, and medical research. At the heart of this sits the Brunauer-Emmett-Teller (BET) theory, a remarkably successful contribution to physical chemistry which will be reviewed in this chapter and contextualised for modern adsorbents. The theory is reviewed in Section 4.1 as is its state-of-the-art implementation in the calculation of surface areas for porous materials. These BET areas are quintessential figures of merit for porous materials and, consequently, they must be obtained reliably and reproducibly. In particular, this chapter raises the often-overlooked question of how reproducible BET area calculations are *from the same isotherm*. To this end, the author conducted an unprecedented round-robin evaluation of BET areas, sending 18 anonymised isotherms to 60 international research groups and gathering their results. This major study, involving over 120 contributors, is introduced in Section 4.4.1 and reveals critical reproducibility concerns. To mitigate these problems, an algorithmic approach called BET Surface Identification, or more simply BETSI, is introduced (Section 4.4.2.1). This software makes – for the first time – an unambiguous BET area assignment from gas adsorption isotherms of microporous adsorbents possible.

4.1 Background

The Brunauer-Emmett-Teller (BET) equation is arguably one of the most used equations in physical chemistry and porosimetry. Since its conception in the 1930s [206] to estimate open surfaces whilst working with adsorbents of the time such as Fe/Cu catalysts, silica gel, and charcoal, it has found widespread use in the characterisation of synthetic zeolites [207]. Furthermore, it has gained considerable momentum following the discovery of more complex porous materials such as mesoporous silicas [208–210], porous coordination polymers (PCPs) [1], MOFs [4], and covalent organic frameworks (COFs) [16] (Figure 4.1).

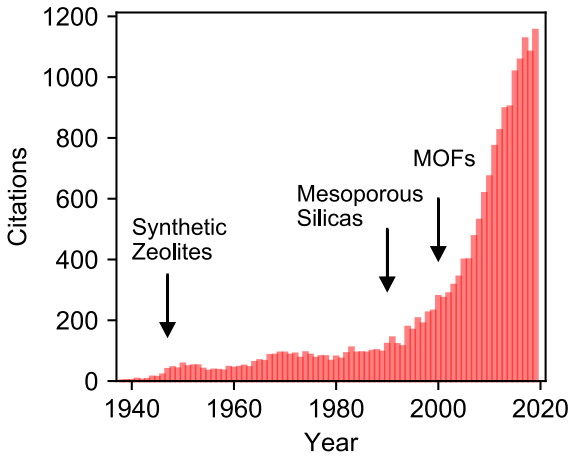

Fig. 4.1 BET Publication Citation Report | Annual number of citations for 'Adsorption of gases in multimolecular layers' [206]. Web of Science, 2020

The BET equation is used to calculate surface areas from gas adsorption isotherms. Langmuir was the first to relate the uptake measured in gas adsorption isotherms with surface areas, assuming only a monolayer formation on the adsorbent [211]. This idea stood in contrast to Dubinin's proposition of pore volumes for microporous materials which is also still used today [212]. Langmuir's adsorption theory was later extended for multilayer adsorption into the titular BET model [206]. At this point, an important distinction has to be made: the *BET model* is a physical model for multilayer adsorption on open surfaces. Its derivation and assumption are reviewed in Section 4.1.2. In the *BET method*, on the other hand, a physical constant from the BET model, the monolayer capacity, is converted into a hypothetical surface area called the BET area (Section 4.1.5).

Naturally, the BET method is derived from the BET model, and it is now the *de facto* standard for the characterisation of porous materials. As such, it has been recognised by the IUPAC as "*the most widely used procedure for evaluation the surface area of porous and finely-divided materials*" [71, 74]. It has also been a standard by the International

Organisation for Standardization (ISO) for surface area measurements since 1995 [213]. This makes it arguably the most important figure of merit in porosimetry. Due to its origin, any theoretical discussion of the BET method must begin with a review of the BET model.

4.1.1 Derivation of the Langmuir Isotherm

Since the BET model is an extension of the Langmuir adsorption model to multilayers, it is sensible to review the origin of this theory first.

Langmuir adsorption rests on the following assumptions:

1. Adsorption takes place between an adsorptive A and a surface S. A dynamic equilibrium is established, where $\mathrm{A(g)} + \mathrm{S(s)} \rightleftharpoons \mathrm{AS(s)}$
2. The surface is uniform and consists of discrete adsorption sites
3. A only adsorbs in a monolayer onto S, multilayer adsorption does not take place
4. Neighbouring adsorbates do not interact; the only energetic interaction is between the adsorptive and an adsorbent site

As adsorption only takes place in a monolayer, adsorbing molecules deplete the surface of its adsorption sites. The fractional surface coverage can therefore be defined as

$$\theta = \frac{\text{Number of adsorbed molecules}}{\text{Total number of adsorption sites}} = \frac{N}{N_{sites}} \tag{4.1}$$

The rate of change of θ is then

$$\frac{d\theta}{dt} = \underbrace{NPk_1(1-\theta)}_{\text{rate of adsorption}} - \underbrace{Nk_{-1}\theta}_{\text{rate of desorption}} \tag{4.2}$$

where k_1 and k_{-1} are the adsorption and desorption rate constants respectively and P is the pressure

The physical equilibrium $\mathrm{A(g)} + \mathrm{S(s)} \rightleftharpoons \mathrm{AS(s)}$ takes place when the rate of adsorption and desorption are the same

$$NPk_1(1-\theta) = Nk_{-1}\theta \tag{4.3}$$

Rearranging for θ yields

$$\theta = \frac{KP}{1+KP} \tag{4.4}$$

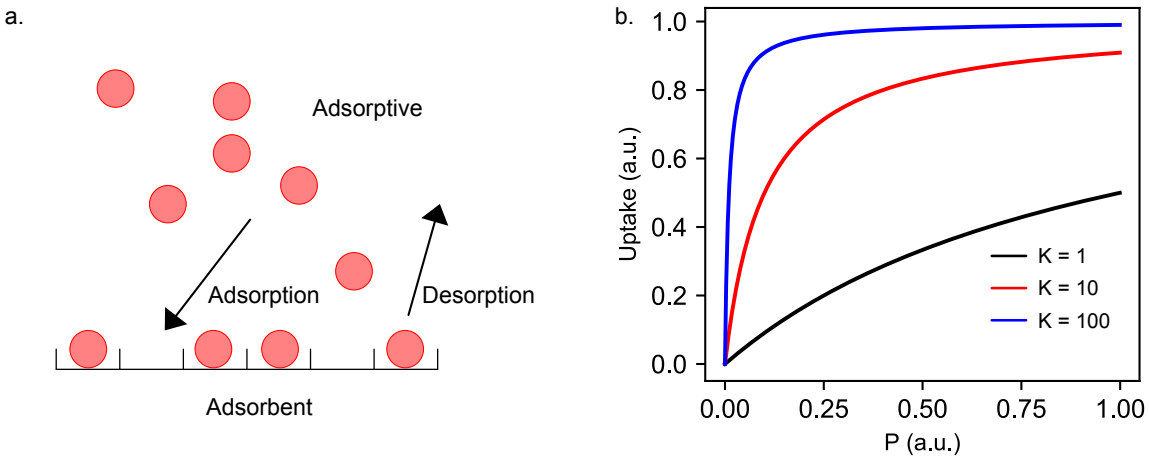

Fig. 4.2 The Langmuir Isotherm | a. Langmuir adsorption model b. Langmuir isotherm plotted for different values of K.

with $K = \frac{k_1}{k_{-1}}$.

Equation 4.4 is shown for different values of K in Figure 4.2. The Langmuir isotherm is a simple algebraic function that increases at low pressures and plateaus at higher pressures; the physical interpretation of this being saturation of the adsorbent surface. Increasing values of K correspond to stronger adsorbent-adsorbate interactions and accordingly to a steeper increase at low pressures and earlier saturation – isotherms develop a more strongly pronounced 'knee'. Langmuir isotherms resemble Type I isotherms of microporous adsorbents under the IUPAC definition [18]; however, it should be noted here that the plateaus in the adsorption isotherms of microporous materials apply to constriction of further adsorption by the pore volume and not due to the exclusive formation of a monolayer. Since multilayer adsorption does take place in porous materials, the BET equation can be considered more suitable at low pressures as it includes multilayer formation [214].

4.1.2 Derivation of the BET Equation

The following kinetic derivation of the BET equation has been modified from Atkins' approach [215]. The same assumptions are made as in Langmuir theory, with the exception of the following.

1. Multilayer formation is possible. Each adsorbate molecule provides a new adsorption site for another adsorptive.

2. Adsorption from an adsorptive molecule on another adsorbate is energetically equivalent to condensation.

3. Adsorbed molecules are immobile and do not migrate between layers

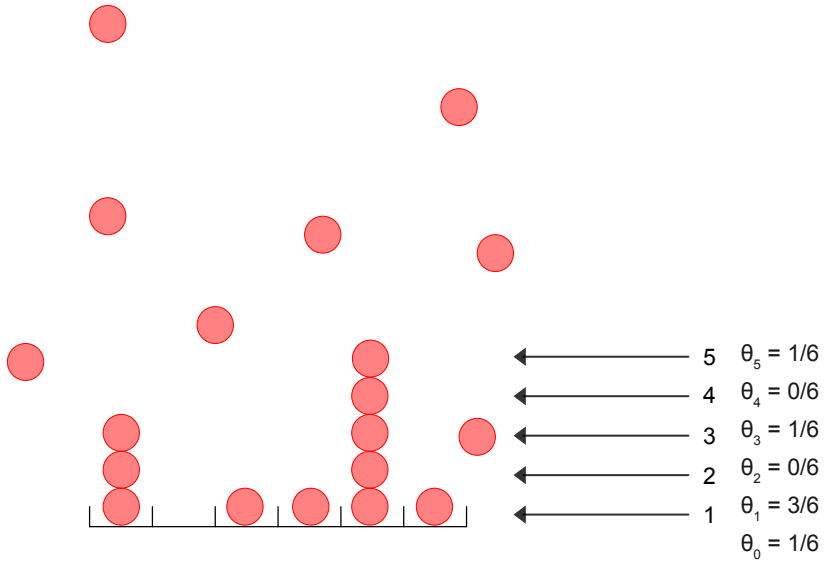

Fig. 4.3 The BET Model | Multilayer adsorption on an adsorbent surface. Each adsorbate molecule provides an site for another adsorptive.

At equilibrium, θ_0 is the fraction of surface sites that are unoccupied, θ_1 is the fraction with a monolayer coverage, θ_2 the bilayer fraction, and so on. Generally, θ_i denotes the fraction of adsorption sites with i molecules in it (vertical stacks) (Figure 4.3).

The total number of molecules, N, is therefore

$$N = N_{sites} \left(\sum_{i=1}^{\infty} i\,\theta_i \right) \tag{4.5}$$

Next, the rate of adsorption *to form* the $i'th$-layer is defined as

$$\frac{d\theta_i}{dt} = N\,P\,k_i\,\theta_{i-1} \tag{4.6}$$

and accordingly the rate of desorption from the $i'th$-layer as

$$\frac{d\theta_i}{dt} = N\,k_{-i}\,\theta_i \tag{4.7}$$

Therefore, the adsorption on the bare surface is Langmuir-like with

$$\frac{d\theta_0}{dt} = \underbrace{-N\,P\,k_1\,\theta_0}_{\text{adsorption onto bare surface}} + \underbrace{N\,k_{-1}\,\theta_1}_{\text{desorption from monolayer}} \tag{4.8}$$

and at equilibrium

$$\frac{d\theta_0}{dt} = 0 \tag{4.9}$$

This gives

$$\theta_1 = P\,\frac{k_1}{k_{-1}}\,\theta_0 \tag{4.10}$$

For θ_1, the same procedure gives

$$\frac{d\theta_1}{dt} = P\,k_1\,N\,\theta_0 + k_{-2}\,N\,\theta_2 - P\,k_2\,N\,\theta_1 - k_{-1}\,N\,\theta_1 \tag{4.11}$$

substituting the expression for θ_1 from Equation 4.10, this becomes

$$\frac{d\theta_1}{dt} = P\,k_1\,N\,\theta_0 + k_{-2}\,N\,\theta_2 - P\,k_2\,N\,\theta_1 - k_{-1}\,N\left[P\,\frac{k_1}{k_{-1}}\,\theta_0\right] \tag{4.12}$$

and with the equilibrium condition $\frac{d\theta_1}{dt} = 0$ in place, this becomes

$$0 = k_{-2}\,N\,\theta_2 - P\,k_2\,N\,\theta_1 \tag{4.13}$$

which, after using Equation 4.10, can be rearranged to

$$\theta_2 = \frac{k_2 k_1}{k_{-2}k_{-1}}P^2\,\theta_0 \tag{4.14}$$

Thus, generalising for the $i'th$-layer

$$\theta_i = P^i\,\theta_0\prod_{j=1}^{i}\frac{k_j}{k_{-j}} \tag{4.15}$$

Next, the BET assumption is made that all multilayer adsorption is identical and condensation-like, thus $K_0 = \frac{k_1}{k_{-1}}$ and $K_1 = \frac{k_j}{k_{-j}}$ for all $j > 1$. Further, $\sum_{i=0}^{\infty}\theta_i = 1$, and therefore

$$
\begin{aligned}
&\underbrace{\theta_0}_{\theta_0} + \underbrace{P\,K_0\,\theta_0}_{\theta_1} + \underbrace{P^2\,K_0\,K_1\,\theta_0}_{\theta_2} + \underbrace{P^3\,K_0\,K_1^2\,\theta_0}_{\theta_3} + \ldots \\
&= 1 \\
&= \theta_0 + K_0\,P\,\theta_0\left[1 + K_1\,P + K_1^2\,P^2 + \ldots\right] \\
&= \theta_0 + K_0\,P\,\theta_0\left[\sum_{j=0}^{i}(K_1\,P)^j\right] \\
&= \theta_0 + K_0\,P\,\theta_0\left[\frac{1}{1 - K_1\,P}\right] \\
&= \left[\frac{1 - K_1\,P + K_0\,P}{1 - K_1\,P}\right]\theta_0
\end{aligned}
\tag{4.16}
$$

This expression can be rearranged to yield

$$
\theta_0 = \frac{1 - K_1\,P}{1 - (K_1 - K_0)\,P} \tag{4.17}
$$

Similarly, N can be written as

$$
\begin{aligned}
N &= N_{sites}\,K_0\,P\,\theta_0 + 2\,N_{sites}\,K_0\,K_1\,P^2\,\theta_0 + \ldots \\
&= N_{sites}\,K_0\,P\,\theta_0\left[\sum_{i=0}^{\infty} i\,K_1^{i-1}\,P^{i-1}\right] \\
&= \frac{N_{sites}\,K_0\,P\,\theta_0}{(1 - K_1\,P)^2}
\end{aligned}
\tag{4.18}
$$

Combining expressions 4.17 and 4.18, this yields for N

$$
N = \frac{N_{sites}\,K_0\,P}{(1 - K_1\,P)[1 - (K_1 - K_0)\,P]} \tag{4.19}
$$

Equation 4.19 can be further simplified by defining $C = \frac{K_0}{K_1}$, and $K_1 = \frac{1}{P_0}$

$$
\frac{N}{N_{sites}} = \frac{C\,\frac{P}{P_0}}{\left(1 - \frac{P}{P_0}\right)\left[1 - (1 - C)\,\frac{P}{P_0}\right]} \tag{4.20}
$$

Equation 4.20 is the titular BET equation. It is often rewritten in the linearised version that is used in the BET method

$$\frac{\frac{P}{P_0}}{N\left(1-\frac{P}{P_0}\right)} = \frac{1}{N_{sites}C} + \frac{C-1}{N_{sites}C}\frac{P}{P_0} \tag{4.21}$$

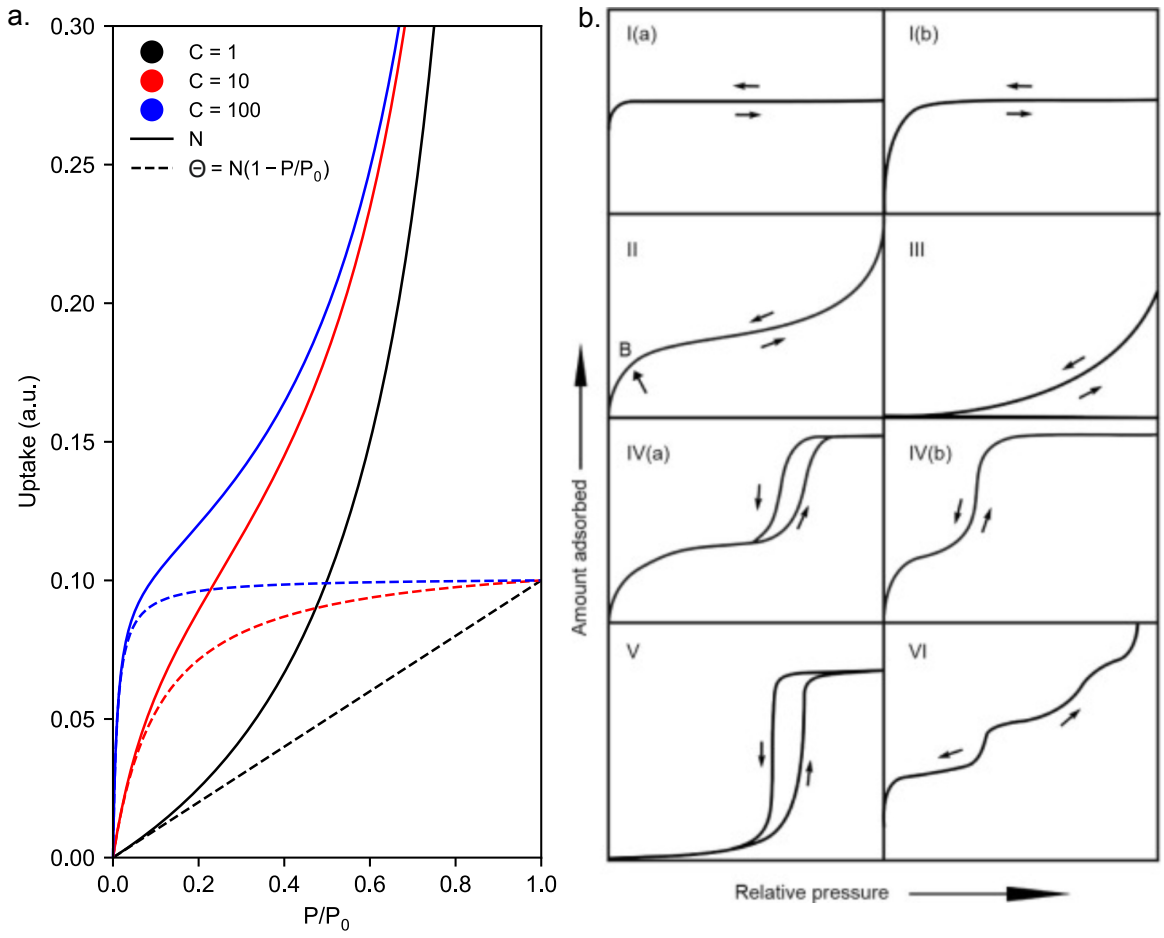

Fig. 4.4 The BET Isotherm | a. Variation of the BET isotherm under different values of C. Also shown is the $N(1-P/P_0)$ term, which is equal to the Langmuir-like monolayer contribution to the BET isotherm (Section 4.1.4). For $C=1$ this transforms into the Henry relationship. b. IUPAC classification of isotherms. Details found in Section 1.3.5. Reprinted with permission [71].

4.1.3 Interpreting the Physical Constants in the BET Model

By definition

$$C = \frac{K_0}{K_1} \tag{4.22}$$

$$= P_0 \frac{k_1}{k_{-1}} \tag{4.23}$$

From Equation 4.10, this gives

$$C = \frac{\theta_1}{\theta_0} = e^{\frac{\Delta_{des}H - \Delta_{vap}H}{RT}} \tag{4.24}$$

C, therefore, expresses the enthalpy of adsorption on the bare surface relative to the enthalpy of condensation. For high values of C, the adsorbate-adsorbent interactions are strong, favouring Langmuir-like adsorption at low relative pressures. Lower values of C in turn correspond to greater adsorbate-adsorptive interactions: extensive multilayer formation is observed even at low pressures due to unfavourable adsorption on the bare surface.

Inspection of the isotherm in Figure 4.4 and of the algebraic form of the BET equation (Equation 4.20) reveals that at no point the BET model stipulates a complete monolayer formation. It is therefore imprecise to talk about the N_m as the BET monolayer *loading*; instead, the preferred term is monolayer *capacity*, which can be thought of as the hypothetical loading that were achieved if $\theta_1 = 1$ for infinite values of C. A physical interpretation of N_m is difficult; according to Rouquerol "*it embraces the major part of the amount of adsorptive in energetic interaction with the surface*" [73]. All in all, N_m is a critical constant in physical chemistry due to its conversion into the BET area, as is done in the BET method (Section 4.1.5).

4.1.4 The BET Isotherm as a Sum of a Type I and Type III Isotherm

The BET equation can be separated into a sum of a Langmuir-like Type I monolayer isotherm and a Type III multilayer isotherm.

Equation 4.18 can be slightly modified by adding and subtracting 1

$$N = N_{sites} P K_0 \theta_0 \left[1 - 1 + \sum_{i=0}^{\infty} i K_1^{i-1} P^{i-1} \right] \tag{4.25}$$

$$= N_{sites} P K_0 \theta_0 - N_{sites} P K_0 \theta_0 + \frac{N_{sites} P K_0 \theta_0}{(1 - K_1 P)^2} \tag{4.26}$$

As before, inserting the expression for θ_0 (Equation 4.17) and dividing by N_{sites} yields

$$\frac{N}{N_{sites}} = \frac{K_0 P}{1-(K_1-K_0)P}\left[(1-K_1 P)-(1-K_1 P)+\frac{1}{(1-K_1 P)}\right] \tag{4.27}$$

$$\frac{N}{N_{sites}} = \frac{K_0 P}{1-(K_1-K_0)P}\left[1+\frac{K_1 P}{(1-K_1 P)}\right] \tag{4.28}$$

With the same simplifications as above, this becomes

$$\frac{N}{N_{sites}} = \frac{C\frac{P}{P_0}}{1-(1-C)\frac{P}{P_0}}\left[1+\frac{\frac{P}{P_0}}{(1-\frac{P}{P_0})}\right] \tag{4.29}$$

$$= \Theta_1 + \Theta_1\left[\frac{\frac{P}{P_0}}{(1-\frac{P}{P_0})}\right] \tag{4.30}$$

where, in the last line, the same definitions for C and K_1 as above were applied, as well as

$$\Theta_1 = \frac{C\frac{P}{P_0}}{1-(1-C)\frac{P}{P_0}} \tag{4.31}$$

In Equation 4.30 the BET isotherm has thus been separated: Θ_1 becomes identical to a Langmuir isotherm for reasonably high values of C, for which $C \approx C-1$. It can therefore be treated as the monolayer content of the BET isotherm. Additionally, there is an added multilayer term with a pressure-dependence of $(P/P_0)^2/(1-P/P_0)$. Note also that the multilayer term scales with Θ_1, which is consistent with the BET model's premise that each molecule from the first layer is a new site for adsorption for the next adsorptive molecule. A similar proof for this relationship was found by Tóth [216, 217].

4.1.5 The BET Method for Surface Area Measurements

In the BET method, N_m is converted into the BET area [206]. An experimental adsorption isotherm is linearised according to Equation 4.21 and fitted with an ordinary least squares (OLS) regression. The resulting regression line of the form $y = mx + b$ is then used to calculate C and N_m by

$$C = 1 + \frac{m}{b} \tag{4.32}$$

$$N_m = \frac{1}{m+b} \tag{4.33}$$

Assuming that the adsorbate forms a hexagonal close-packed layer, the surface area of the adsorbent is then

$$A_{BET} = N_m V_m N_A \sigma_m \tag{4.34}$$

where V_m is the molar volume of the adsorptive, N_A is Avogadro's number, and σ_m the molecular cross-sectional area. For nitrogen this generally taken to be 0.162 nm, taken from the bulk density of liquid N_2 [71].

Early applications of the BET method by Brunauer *et al.* on various adsorbents showed that the obtained BET isotherms tended to overestimate adsorption at higher pressures [206], hence it is usually fitted over a restricted pressure range at lower relative pressures. The original authors suggested a standard range between 0.05 and 0.35 relative pressure for open surfaces, however, subsequent studies have shown that for most materials this pressure range does not yield linear fits [218, 74].

The accuracy of the BET model to the adsorption isotherms of microporous solids has been the topic of much debate, since it was developed for open surfaces and not for porous frameworks [219, 220, 214, 71]. Specifically, the microporous materials that have been rapidly developed in the last 20 years are (i) highly adsorbent at low relative pressures, and (ii) have a porosity that restricts multilayer formation to only a few layers. In consequence, the Point B occurs at much lower pressures than in the standard range proposed by Brunauer *et al.* It should be noted that proponents of Dubinin's micropore filling mechanism have touted the BET model as obsolete, and suggest using pore volumes as a metric of porosimetry instead [212]. Especially at low pressures and for very narrow porosities, a substantial part of the uptake can be attributed to pore-filling rather than adsorption in contrast with the BET model [221]. Indeed, IUPAC warns users specifically to apply "*extreme caution* [when using the BET equation] *in the presence of micropores.* (...) [The BET area] *represents an apparent surface area, which may be regarded as a useful adsorbent 'fingerprint'*".

In any case, despite such cautionary words, the BET area remains a deeply engrained metric in the fields of physical chemistry and materials science. In response to these complications and as a safeguard for reproducibility, Rouquerol developed the now eponymously named linearity and consistency criteria to ensure good practice in BET fittings [214] (Figure 4.5).

1. In the chosen linear range, the function $N(1-P/P_0)$ must increase monotonically with the relative pressure P/P_0
2. The C constant resulting from the fit must be positive
3. The pressure corresponding to the monolayer volume when reported on the isotherm must lie within the linear range

4. The pressure at the calculated $N_m(BET)$ which is equal to $1/(\sqrt{C}-1)$ must be equal to the pressure corresponding to the monolayer volume when reported on the isotherm. A tolerance threshold of 20% is considered acceptable here.

In addition, Rouquerol *et al.* considered it important to choose a linear range of at least 10 points and observe a regression coefficient no smaller than $R^2 = 0.995$.

Given the impact these criteria have had in porosimetry it is surprising that their theoretical origin has not been discussed in much detail. Most mechanistic studies of the Rouquerol criteria apply them practically and compare the BET areas with corroborating data [222]. As such, Walton and Snurr applied the Rouquerol criteria in the BET method for MOFs and compared resultant areas with geometric surface areas obtained from crystallographic information [220, 223]. The same group later carried out a similar study on ultramicroporous adsorbents [224], confirming their previous findings that BET areas generally correlate well with the geometrically calculated surface areas. Later, Gomez-Gualdron *et al.* assessed the criteria with snapshots of molecular simulations of the adsorption mechanism to validate the notion of monolayer formation [219]. It is pointed out here that the premise of this study is questionable, since the BET model does not predict the formation of a complete monolayer at any pressure.

In Rouquerols' own work, the significance of the $N(1-P/P_0)$ function is only discussed fleetingly [73], drawing parallels to Keii's [225] and Parra's [226] BET transforms on adsorption isotherms. In this dissertation, it is argued that the $N(1-P/P_0)$ term is equal to the partial loading of the first adsorption layer at any point as proven below from Section 4.1.4.

Consider the multiplying Equation 4.29 with $(1-P/P_0)$. Then

$$N\left(1-\frac{P}{P_0}\right) = \frac{C\,\frac{P}{P_0}\,N_{sites}}{1-(1-C)\frac{P}{P_0}}\left[1+\frac{\frac{P}{P_0}}{1-\frac{P}{P_0}}\right]\left(1-\frac{P}{P_0}\right) \tag{4.35}$$

$$= \frac{C\,\frac{P}{P_0}\,N_{sites}}{1-(1-C)\frac{P}{P_0}} \tag{4.36}$$

After transforming to volumetric units again, note that this is the same as the monolayer loading Θ_1 derived in Section 4.1.4 (Equation 4.29). Since this is a Langmuir-like term, it must necessarily monotonically increase with P/P_0, and any deviation from linearity marks the end of a BET valid range. To this author's best knowledge, this proof is the first to justify the first Rouquerol criterion theoretically.

Justification of the second criterion is more straightforward. According the Equation 4.24, C must be positive as it is an exponential term. A negative value for C would be physically as meaningless as a negative BET area.

Criteria 3 and 4 are more complex and require a more detailed discussion. It is here argued that "*the pressure corresponding to the monolayer volume when reported on the isotherm...*" [73], to which the third and fourth criteria pertain, is poorly defined in the literature and consequently frequently misunderstood. It refers to the pressure at the point of intersection of N_m, as calculated by applying Equation 4.33, with the real isotherm, $N_m(Read)$ (Figure 4.5 d.). Note that this is a fictitious point as it is near impossible that a pressure-equilibration on the isotherm was sampled exactly here. Rouquerol [73] and others [71] make no recommendation on how to reconstruct this fictitious point, leaving the implementation of this criterion open to ambiguity.

Further, it is here argued that criteria 3 and 4 must be interpreted with more nuance. Whilst the first two Rouquerol criteria can be thought of validity or linearity criteria, the latter two must strictly be identified as criteria of self-consistency. The words *consistency criteria* are frequently but incorrectly used in the literature to address all four Rouquerol criteria [222, 220, 219]. Only the last two are self-consistency criteria because they rely to some extent on circular logic: $N_m(Read)$ and $N_m(BET)$ are both functions of a particular linear range. Therefore, choosing a particular linear range based on the difference between two parameters that are dependent on it can only be a consistency check. Unlike criteria 1 and 2, the internal validity of the model is not probed here, but rather how well the model corresponds to the data at an arbitrary point defined by the fit.

4.1.6 State of the Art Problems with the BET Method

The development of the Rouquerol criteria has revolutionised the BET method for microporous materials and they are now standard practice [71]. However, reliance on manual calculations of surface areas using the BET method remains commonplace. In this context, 'manual' refers to the judicious selection of a pressure range by a scientist, be it through a self-developed spreadsheet or commercial software. In contrast to isotherm reproducibility [227], due to sample quality, synthesis condition, activation procedures, equipment calibration, *etc.*, this raises the neglected question of the reproducibility of BET calculations *from the same isotherm*. An adsorption isotherm with 150 points has more than 10,000 consecutive combinations of points, all of which are potentially correct fitting ranges and will return different BET areas. The answer to the question of which is the optimal fitting region is far from obvious, and the consequence of any irreproducibility or different interpretations are serious. Consider two groups synthesising the same compound and reporting two different

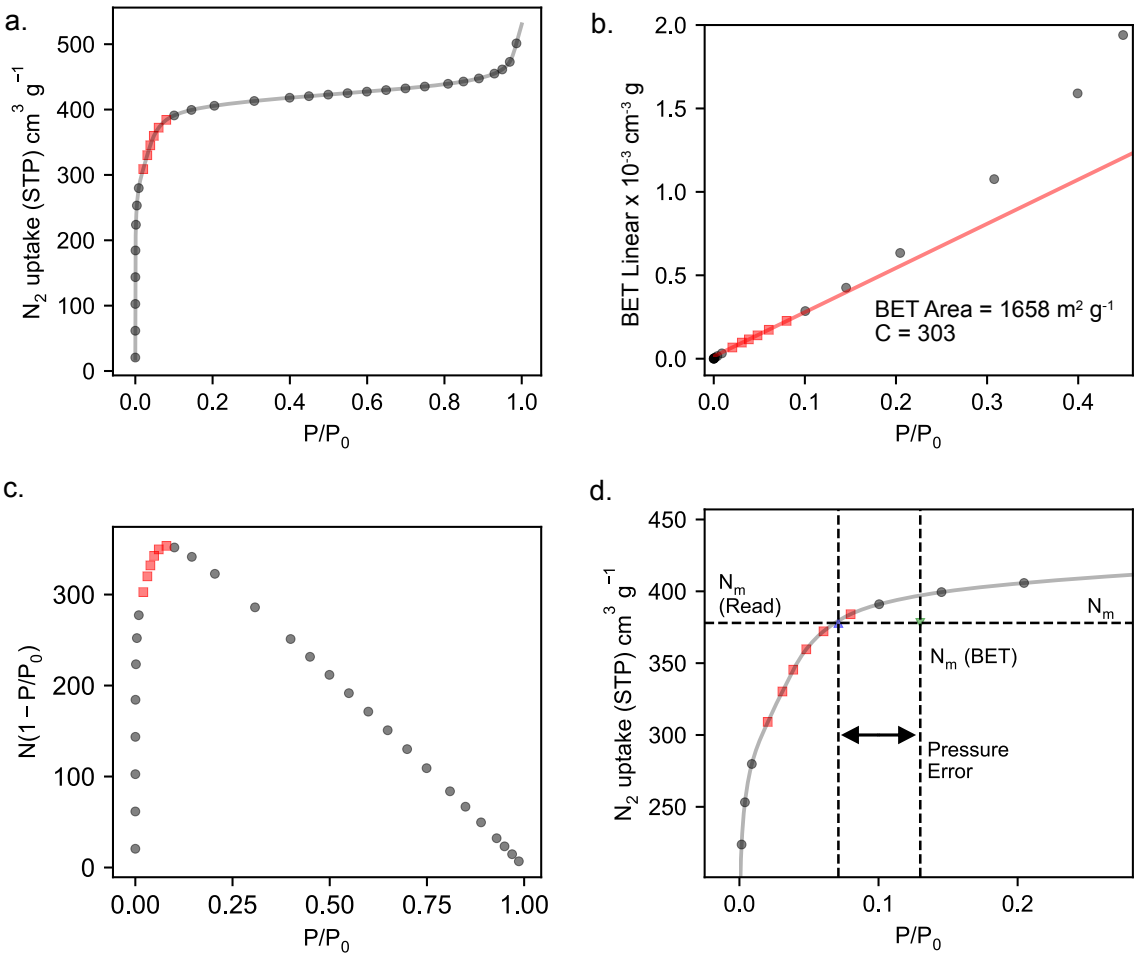

Fig. 4.5 BET Method for Microporous Materials | a. An exemplary, simplified N_2 adsorption isotherm for a microporous material (in this case ZIF-8) at 77 K. The fitting region is highlighted in red on the isotherm. b. The BET transform with a regression line through the fitting region (linear region). c. The Rouquerol-transform. For a BET fit to be acceptable, $N(1-P/P_0)$ must be monotonically increasing with respect to P/P_0 in the entire fitting region. The C constant obtained from the BET fit must be positive. This exemplary fit is acceptable both under the first and second Rouquerol criterion. d. Close-up view of the adsorption isotherm near the fitting region. The pressure corresponding to the monolayer volume when reported on the isotherm, $N_m(Read)$, must lie within the linear range. This point is marked where the calculated N_m intercepts the isotherm. The pressure corresponding to the N_m in the BET model, $N_m(BET)$, must be close to that corresponding to $N_m(Read)$. This exemplary BET fit is consistent under the third but not the fourth criterion, as the pressure error exceeds 20%.

BET areas; Sample A is reported to have a BET area of 1,500 m^2 g^{-1} and Sample B's reported BET area is 2,000 m^2 g^{-1}. Unless there is a common standard and protocol for calculating BET areas, the quality and adsorption performance of Sample A cannot be concluded as being inferior to that of Sample B. Indeed, the lack of reproducibility of MOF syntheses and adsorption performance, by comparing reported BET areas, has been highlighted already, but the natural spread of BET calculations was not included in the analysis [228].

4.2 Aims & Objectives

Herein, the hypothesis is made that the current implementation of the BET method is flawed, yielding irreproducible results for two reasons. First, the Rouquerol criteria are indeterminate in identifying the optimal fitting range, as they can apply to multiple regions simultaneously. Second, it is hypothesised that even if they were determinate, practically they are too cumbersome and lengthy to implement and are therefore often neglected in practice.

To probe these two hypotheses and to assess the current spread of BET calculations, 18 experimental isotherms spanning four classes of porous materials (zeolites, mesoporous silicas, MOFs and COFs) were shared with 60 international laboratories with an expertise in adsorption science and porous materials. In this round-robin exercise, the researchers were asked to calculate the BET areas in the way they saw most fit.

Next, a computer algorithm was developed that automates the BET calculation, implements the existing Rouquerol criteria and refines them further, and identifies all passable BET areas under these. This program is called *BET Surface Identification*, or more simply BETSI. Under the modified Rouquerol criteria, BETSI makes – for the first time – an unambiguous assingment of BET areas possible. Methods and results are discussed in the following.

4.3 Methods

4.3.1 Round-robin Evaluation

N_2 adsorption isotherms of 18 different materials were sent out to international collaborators: HKUST-1, ZIF-8, NU-1000, MIL-101, UiO-66, Al fumarate, Zeolite13X, Mg-MOF-74, UiO-66-NH2, MOF-5, DMOF-1, MCM-41, TPB-DMTP-COF, MIL-100, NU-1102, NU-1104, NU-1105, and PCN-777; they were anonymised and labelled A-R, respectively. The isotherms were sampled from the authors' own group measurements and from the NIST Adsorption Database. Arbitrary scaling factors on the amounts adsorbed were introduced to minimise the recollection bias of the isotherms. The isotherms were sent out in .csv format. All colleagues received the same email with the same set of instructions: to calculate the BET area from the data in the way they saw most fit. For easier data handling, the answers, once re-scaled, were all rounded to the next integer. The data is presented as a jitter plot for each material, with a superimposed kernel-density estimation obtained in python.

4.3.2 BETSI

The BETSI algorithm is fully published on GitHub https://github.com/fairen-group/betsi-gui. The program is written in python, and principally uses the numpy library [229]. Looped linear regressions over all consecutive combinations of at least three points, perform full BET analyses and store the fitting parameters in $n \times n$ results matrices, where the (j,i)-matrix element denotes a linear regression from the j'th to the i'th point on the isotherm. Binary pass/fail matrices with the same dimensionality are used independently to assess compliance with linearity and fitting criteria. The 'filtering' of BET areas is achieved by element-wise matrix multiplication of the results matrices and the pass/fail matrices. This allows independent 'activation' and 'deactivation' of the criteria and observing the effects on the results. The minimum fitting requirement of ten points is coded in a pass/fail matrix to allow for some minimum point flexibility, as is the cut-off value for R^2 of 0.995. To avoid low-leverage non-linearity in the linear region, the first Rouquerol criterion has been extended to also require the linearised BET function to increase monotonically with P/P_0, as well as $N(1-P/P_0)$. The third and fourth Rouquerol criteria are implemented through a 10,000-point PChip interpolation of the isotherm to reconstruct the $N_m(Read)$. As the third and fourth criteria require the $N_m(BET)$ to be real value, *i.e.* they require C to be positive, the second criterion cannot be independently deactivated from the third and the fourth. The associated logic has been written into the program. Following the BETSI filtering by multiplication of results and pass/fail matrices, the isotherm knee is identified as the

subset of BET areas whose fitting region ends on the highest permissible pressure point. In most cases, this will the highest permissible point under the first Rouquerol criterion but this is not necessarily so. The optimal BETSI prediction is chosen as the fitting region with the lowest percentage error under the fourth criterion and belonging to the isotherm knee subset.

BETSI only requires the adsorption isotherm as input data and returns six plots used to validate the results: the isotherm itself, with the optimal linear region highlighted, as well as the BET fit; the Rouquerol-transform of the isotherm, $N(1-P/P_0)$ plotted against P/P_0; the linearised plot with the OLS regression and the regression parameters; the filtered percentage error vs BET areas plot with the isotherm knee and optimal BET area highlighted; the filtered monolayer-capacities plot showing all permissible monolayer capacities on the isotherm; and the statistical distribution of permissible BET areas superimposed on a boxplot. Additionally, BETSI returns four regression diagnostics plots which can be used to assess whether the assumptions of OLS regression have been met: the Residuals vs Fitted values plot can be used to visually inspect whether the residuals are normally distributed around the regression line, and similar information can be obtained from the (quantile-quantile) QQ-plot. Finally, the Scale-Location plot can be used to assess whether the distribution of studentised residuals is homoscedatic or heteroscedatic and the Residuals vs Leverage plot can be used to identify high-leverage points that have an abnormally large influence on the regression line.

4.3.3 Comparison between Round-robin Evaluation and BETSI Results

Statistical analysis of the results was performed in python again using the numpy library [229]. The *BETSI variation coefficient* and the *round-robin variation coefficient* are standard deviations relative to the average of each set. The *pass rate* for each isotherm is the number of permissible BET fits as a fraction of all consecutive combination of points. To account for non-equal spacing of the points on each isotherm, the *pressure-adjusted pass rate* is obtained by integrating along the pressure axis and dividing the total sum of permissive pressure intervals by the sum of all consecutive pressure intervals. The *hit rate* is the fraction BET fits calculated in the round-robin evaluation that lie within the BETSI range. The terms are

defined below.

$$\text{BETSI variation coefficient} = \frac{\text{Standard deviation of BETSI results}}{\text{Average of BETSI results}} \tag{4.37}$$

$$\text{Pass rate} = \frac{\text{Number of passable fits}}{\frac{(n-9)^2}{2}} \tag{4.38}$$

$$\text{Pressure-adjusted pass rate} = \frac{\sum_k \left(P_{i,k} - P_{j,k}\right)}{\sum_l \left(P_{i,l} - P_{j,l}\right)} \tag{4.39}$$

$$\text{Hit rate} = \frac{\text{Number of passable fits in round-robin evaluation}}{\text{Number of participants}} \tag{4.40}$$

Where n denotes the number of points on the isotherm, k is the index of all passable fits, l is the index of all possible pressure ranges, and i and j denote the upper and lower indices of the pressure ranges respectively. To only account for 10-point fits, $i - j > 9$.

4.4 Results & Discussion

4.4.1 Round-robin Review of the BET Method

To assess the current spread of BET calculation results, 18 experimental isotherms representing four classes of different materials (zeolites, mesoporous silicas, MOFs and COFs) were shared with 60 laboratories with an expertise in adsorption science and synthesis of porous materials. Researchers were only asked to calculate results in the way they saw most fit. To avoid recognition bias, all isotherms were scaled off arbitrarily.

Figure 4.6 shows the large spread of results which are shown tabulated in Table A.1 found in Appendix A. Most groups (92%) reported using the Rouquerol criteria in their manual calculation, 27% used a commercial software package, and 6% used a self-developed code (note that these groups are not mutually exclusive). Bar from a few exceptions, virtually no two groups of experts reported identical BET areas for any given isotherm. There was a spread of at least 300 m^2 g^{-1} for each isotherm. However, that number was significantly higher for some individual isotherms. For NU-1104, a modern MOF with substantial porosity [81], the highest estimate of 9,341 m^2 g^{-1} and the lowest estimate of 1,757 m^2 g^{-1} differed by an astonishing 7,584 m^2 g^{-1}, making the highest estimate more than five times higher than the lowest estimate. The spread of BET areas from frequently reproduced MOFs such as HKUST-1, MOF-5, and ZIF-8 was slightly lower than that of literature-cited values [228]. While this affirms the natural assumption that material synthesis and isotherm measurement play a more important role in determining the BET area than the calculations do, a significant portion of this spread can nevertheless be attributed to inconsistencies in manual BET fittings.

The results of this social study clearly prove that there is significant variation in BET area calculations from the same isotherm, as it is extremely unlikely for two researchers to select identical fitting regions.

4.4.2 BET Surface Identification

To address the critical reproducibility concerns raised in Section 4.4.1, an algorithm was developed that automatically analyses BET areas from gas adsorption isotherms and fully implements and refines the Rouquerol criteria. This method, called *BET Surface Identification*, or BETSI, only requires the adsorption isotherm as input data and returns a full BET analysis of the isotherm.

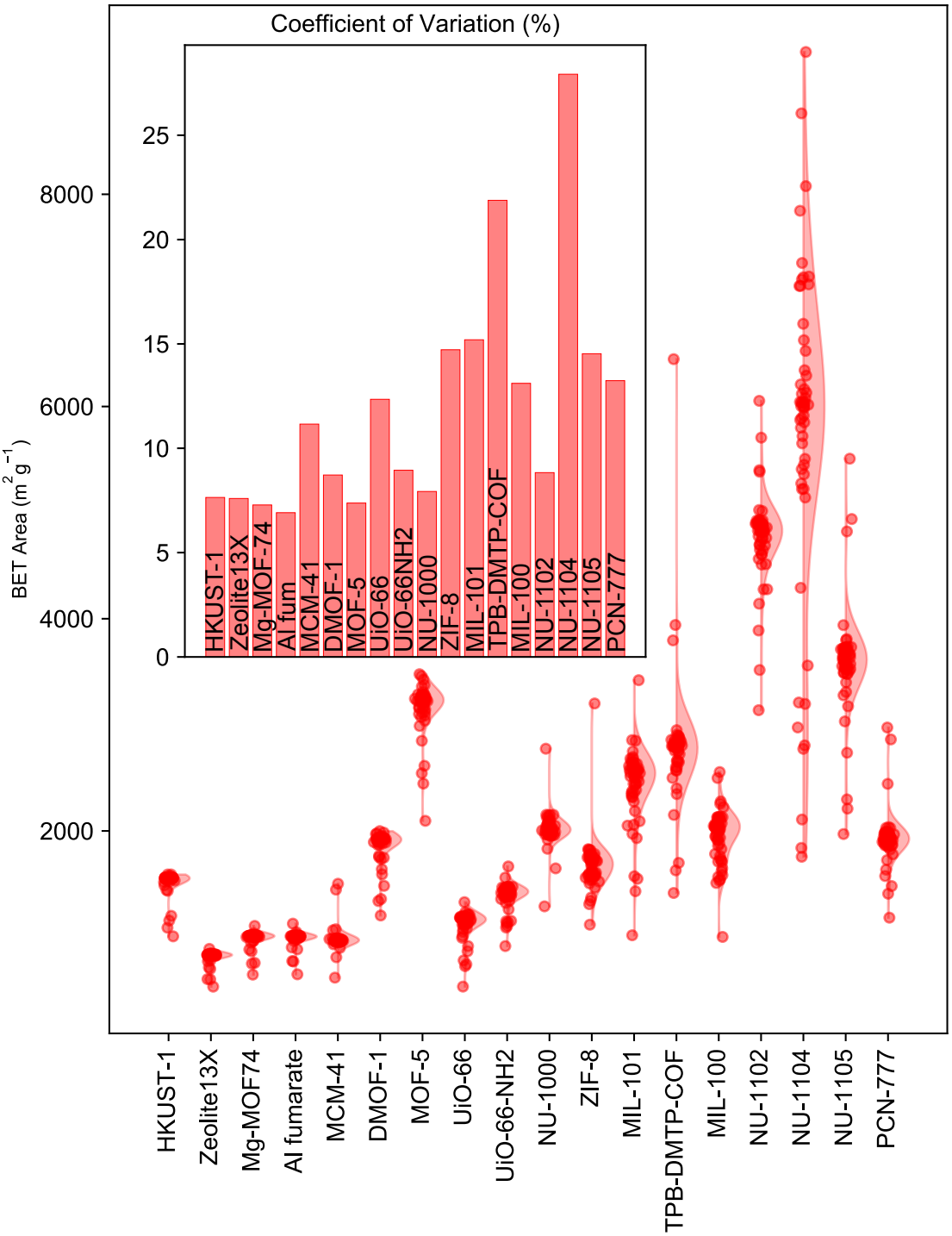

Fig. 4.6 Round-robin Evaluation Results | Distribution of BET area results from identical isotherms as calculated by 60 laboratories with an expertise in adsorption science and synthesis of porous materials. Superimposed are normalised probability density functions obtained by kernel density estimation. Inset shows the coefficient of variation of the results for each material.

4.4.2.1 The BETSI Algorithm

The algorithm steps through all possible consecutive combinations of points on the isotherm that have at least three points, and calculates from a linear regression the N_m and C parameters as laid out in Section 4.3.2. Binary pass/fail matrices with the same dimensionality are used as Rouquerol-'filters' for each of the four Rouquerol criteria. The remaining N_m are then converted into BET areas by applying Equation 4.34. Crucially, BETSI, therefore, calculates *all* BET areas that are possible under the Rouquerol criteria from the isotherm and produces a full distribution, rather than a single estimator.

4.4.2.2 Finding the BET Area

Several views may be taken on how to treat the resulting data. BETSI produces a distribution of possible BET areas that does not always make it easy to choose the most suitable ones. Four possibilities to treat the results are enumerated below:

1. A case-by-base decision based on visual inspection of the isotherm.
2. Treating all surviving BET areas as equally valid and report the median or average value along with other statistical parameters, *e.g.* the standard deviation, interquartile range, *etc*.
3. Ranking the surviving BET areas according to some parameter of choice, such as the highest number of points in the linear region, the highest regression coefficient, lowest error under the fourth Rouquerol criterion, *etc*.
4. Re-evaluation of the Rouquerol criteria and addition of new linearity criteria.

Option 1. is not suitable, as it re-introduces subjectivity into the selection of a linear region, although obviously a much more justified decision can be made. Option 2. is universally applicable and plausible as it, arguably, introduces statistical rigour. However, it fails to distinguish between more and less suitable fits. A combined approach between Option 3. and 4. is therefore taken, whereby the optimal BET area is chosen as the one with the lowest percentage error under the fourth Rouquerol criterion, which ends on the highest permissible pressure point. In most cases, this will be the first maximum in the $N(1-P/P_0)$ vs P/P_0 plot. This point marks the end of the isotherm knee, where the bulk of the adsorptive activity of the material and monolayer adsorption ends. The set of all linear-regions ending at this highest permissible pressure point is therefore of particular importance and is labelled the *isotherm knee* group. Note here that while it may have been common practice among some groups in the past to report BET areas ending at this point, it is not explicitly stated

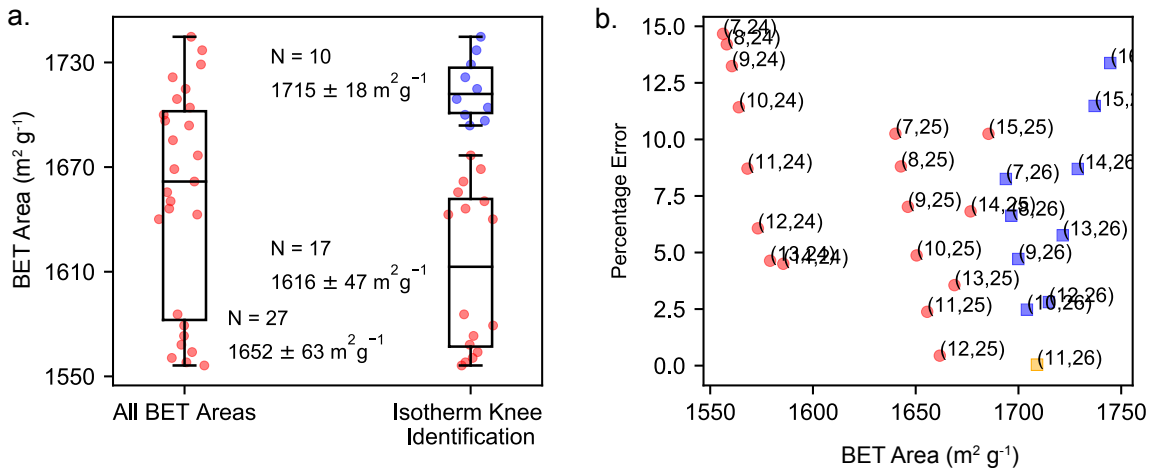

Fig. 4.7 Finding the BET Area | a. Boxplot showing statistical distribution of BET areas for ZIF-8 that pass under the Rouquerol criteria. The corresponding BET areas are presented as a jitter plot alongside. Blue squares represent BET areas belonging to the isotherm knee subset, *i.e.* they end on the highest permissible pressure points. b. BET areas plotted against the percentage error under the fourth Rouquerol criterion. Indices of the corresponding linear ranges are plotted alongside. BET areas belonging to the isotherm knee subset are plotted in blue. The BETSI optimum (yellow) is chosen as the area belonging the isotherm knee subset with the lowest percentage error under the fourth criterion.

in the Rouquerol criteria. In any case, the large spread observed in Figure 4.6 suggests that even this practice was not consistently implemented amongst the participants.

The selection of the optimal BET area is shown in Figure 4.7. For an exemplary ZIF-8 isotherm, the spread of BET areas depreciates considerably under consideration of the isotherm knee group (Figure 4.7 a., in blue). Figure 4.7 b. on the other hand shows the BET areas ranked against their respective percentage errors under the fourth criterion, with the indices of the corresponding linear regions (lower, upper) printed next to it. The optimal BET area (in yellow) is chosen as belonging to the isotherm knee group and having the lowest error under the fourth Rouquerol criterion.

Under these rules, BETSI, for the first time, assigns BET areas to adsorption isotherms unambiguously. The author stresses here, however, that this should not render BETSI a 'black box', and that the isotherm, the selected fitting range, and all other consistent fits should be reported alongside in the future to remain aware of the limitations of the BET method and the Rouquerol criteria. In this case, it is also prudent to report regression diagnostics that assess how valid the fit is under the assumptions of OLS. BETSI result reports for typical materials are introduced in the next section, and all others used in this study can be found in Appendix B.

4.4.2.3 Examples of BETSI Results

Herein, typical BETSI result reports (captions Figure 4.8 and Figure 4.9) are presented for different materials: HKUST-1 (Figure 4.10), ZIF-8 (Figure 4.12), MIL-101 (Figure 4.14), NU-1000 (Figure 4.16), and NU-1104 (Figure 4.18). Shown alongside are the regression diagnostics (Figure 4.9). Results for all other isotherms used in this study are found in Appendix B.

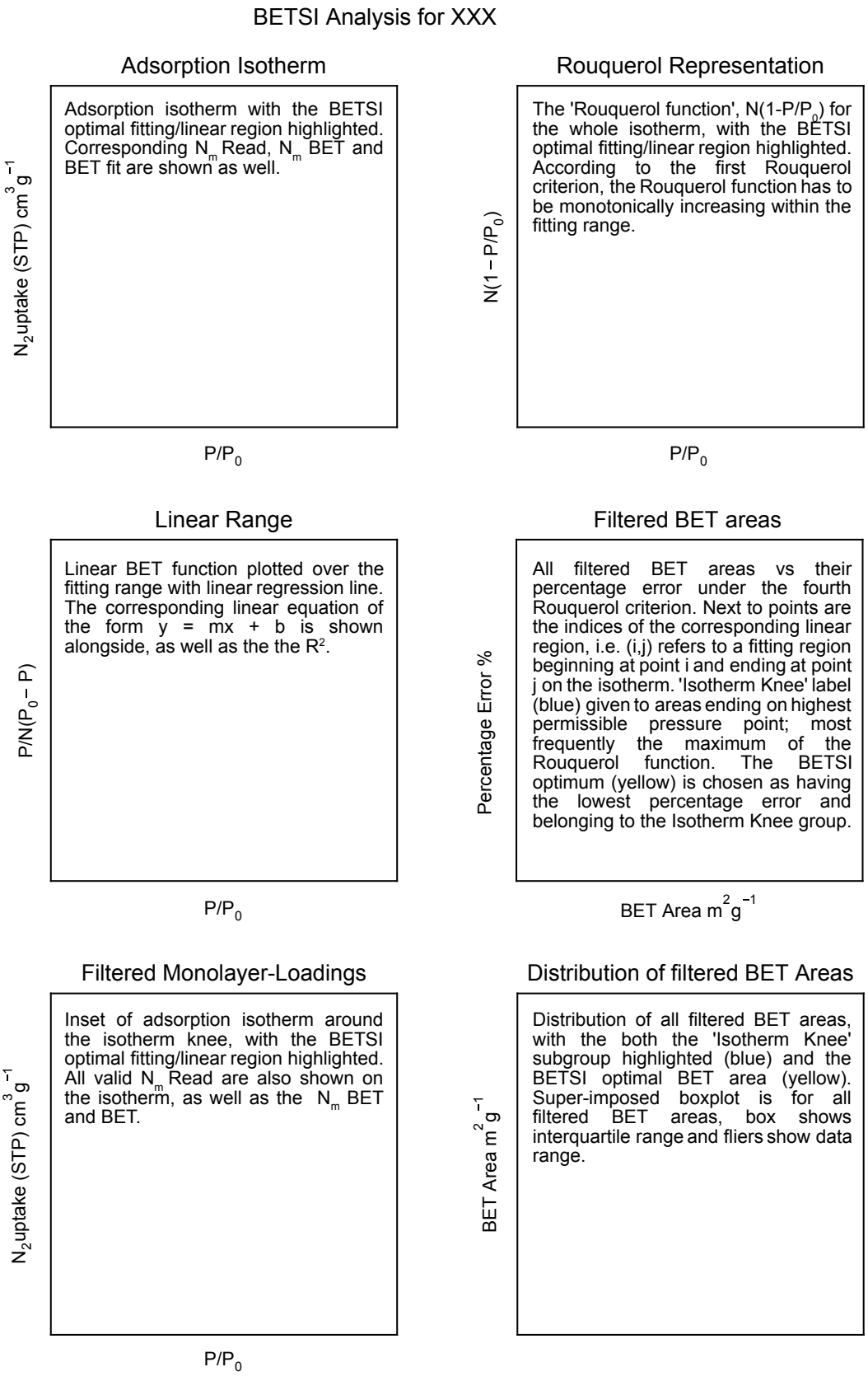

Fig. 4.8 BETSI Results Figures explained

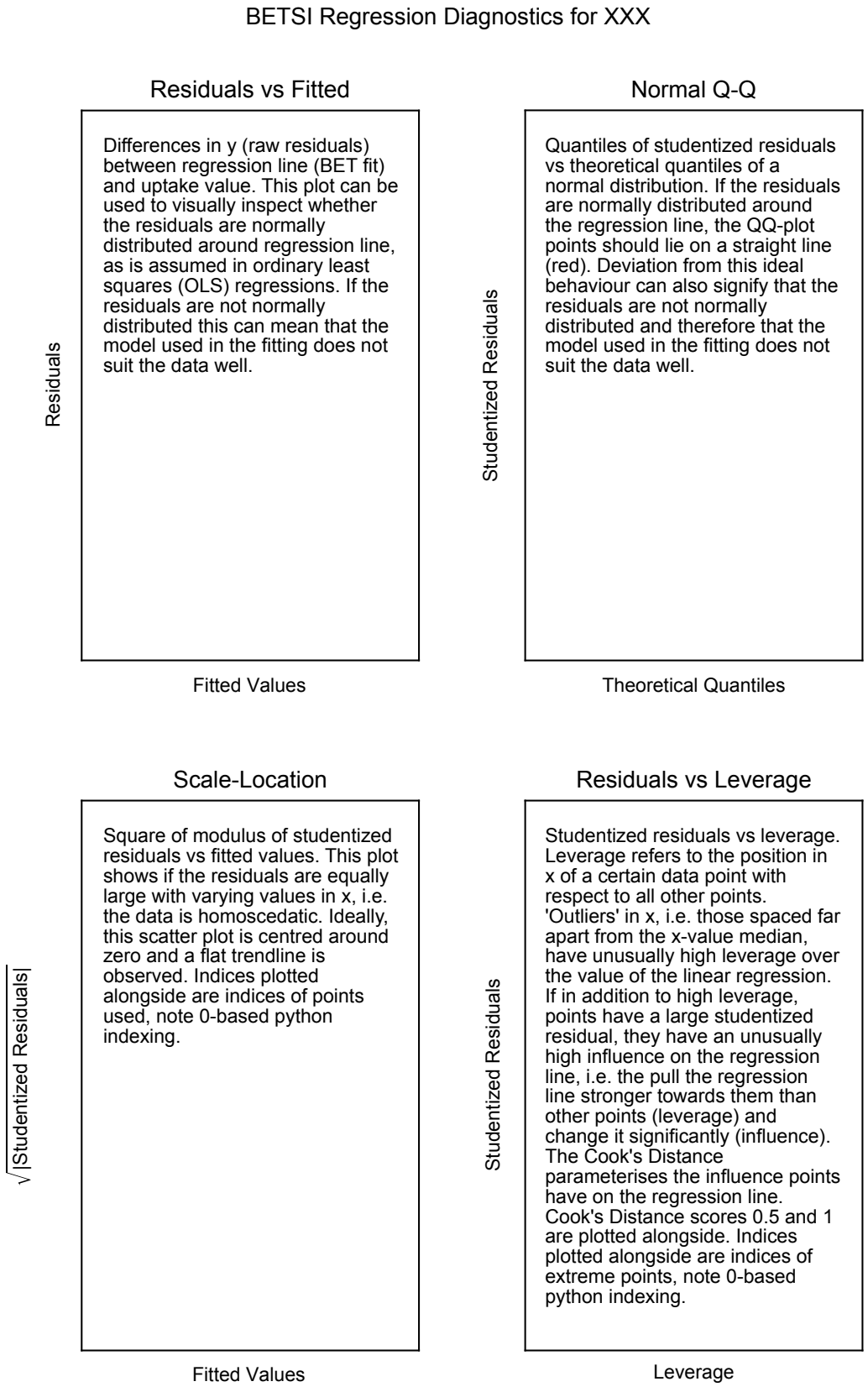

Fig. 4.9 BETSI Regression Diagnostics explained

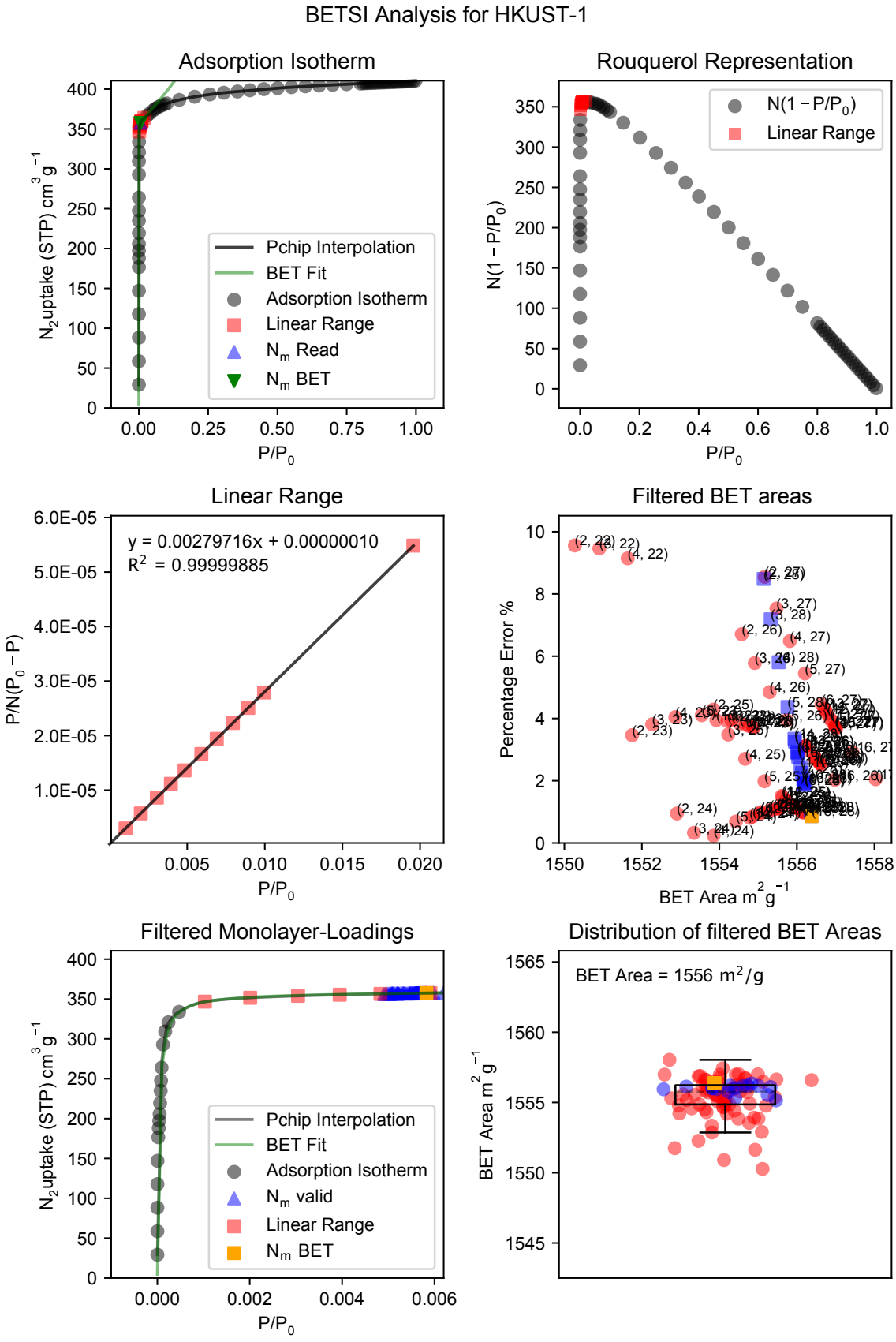

Fig. 4.10 BETSI Results for HKUST-1

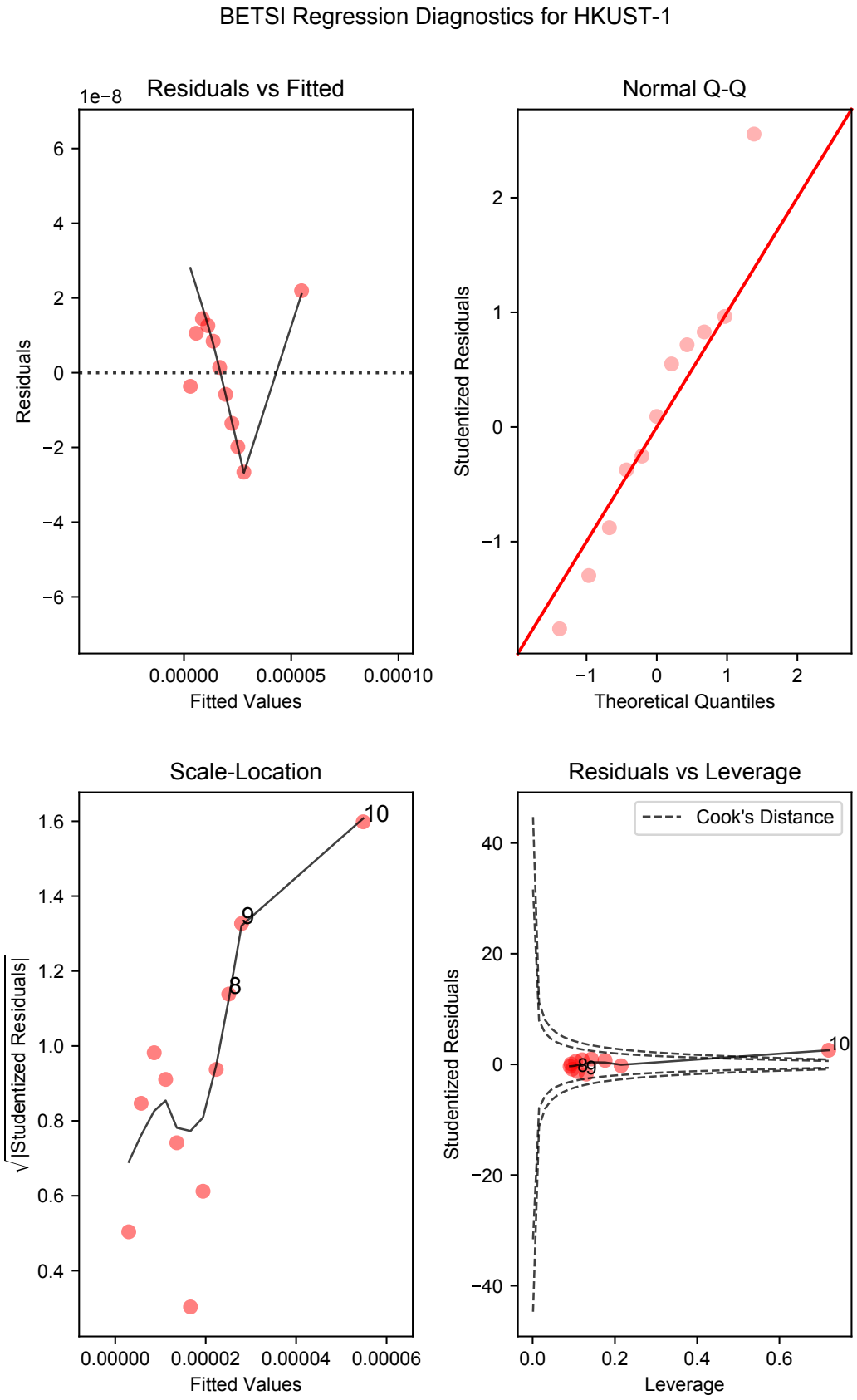

Fig. 4.11 Regression Diagnostics for HKUST-1

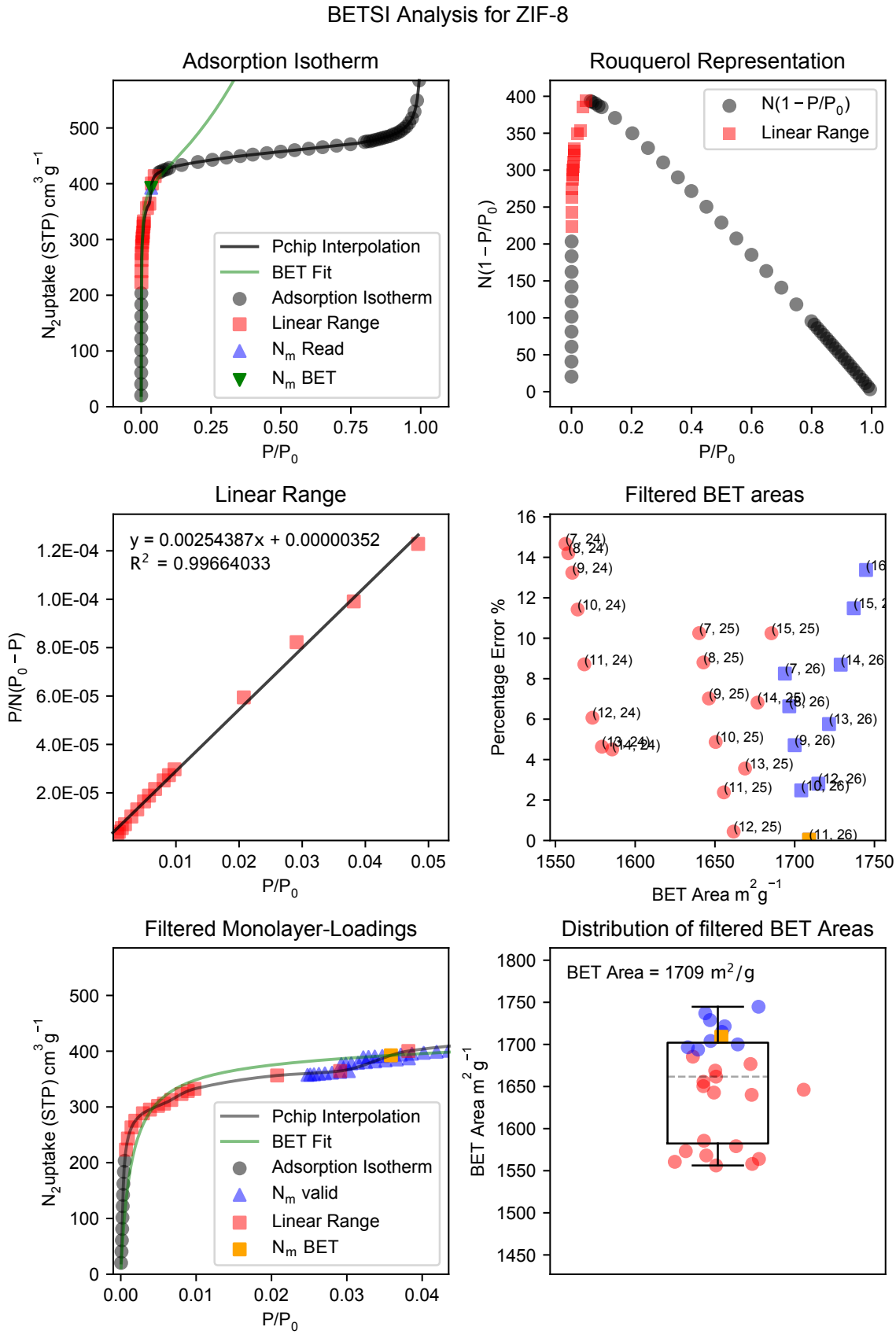

Fig. 4.12 BETSI Results for ZIF-8

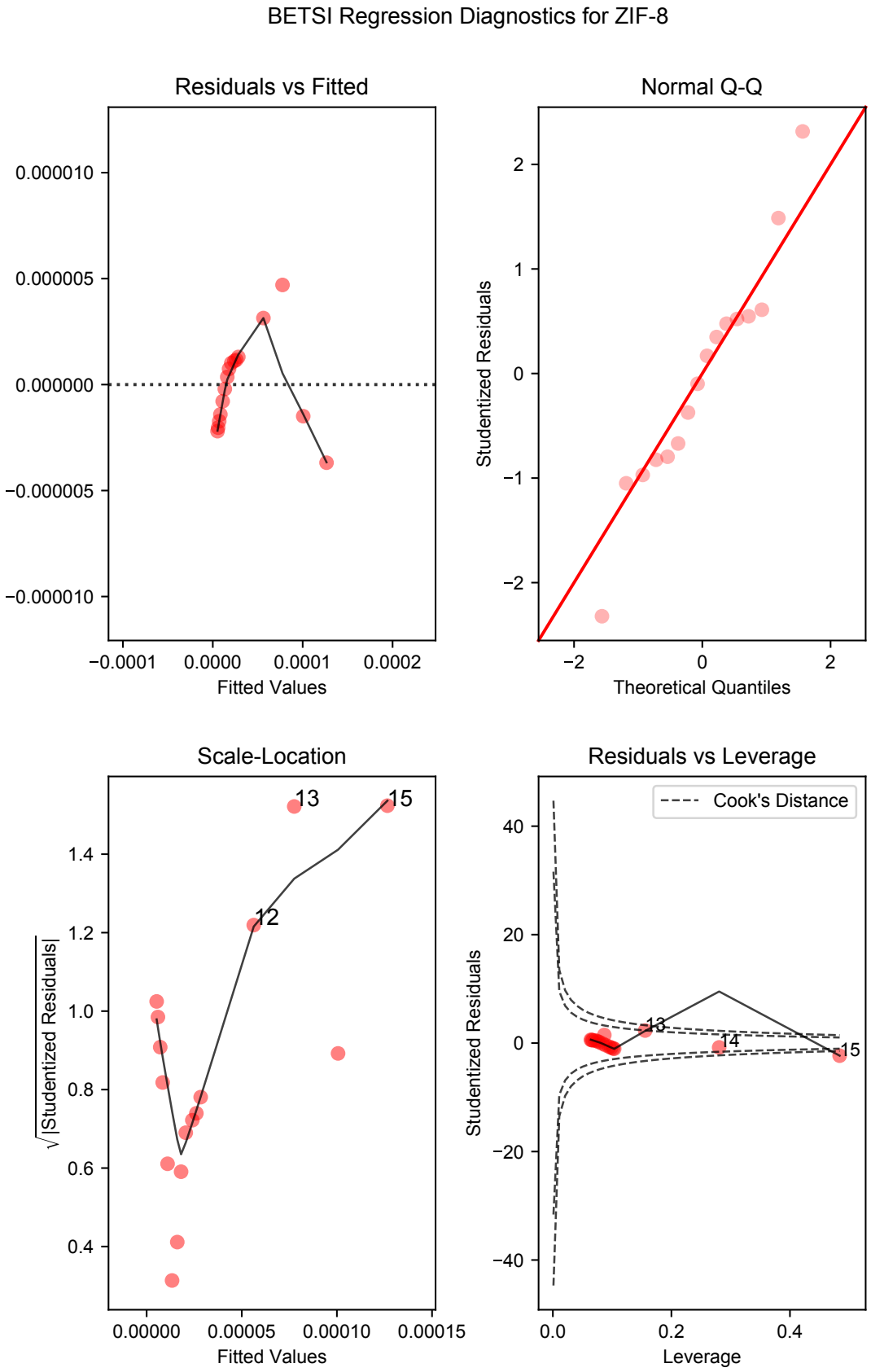

Fig. 4.13 Regression Diagnostics for ZIF-8

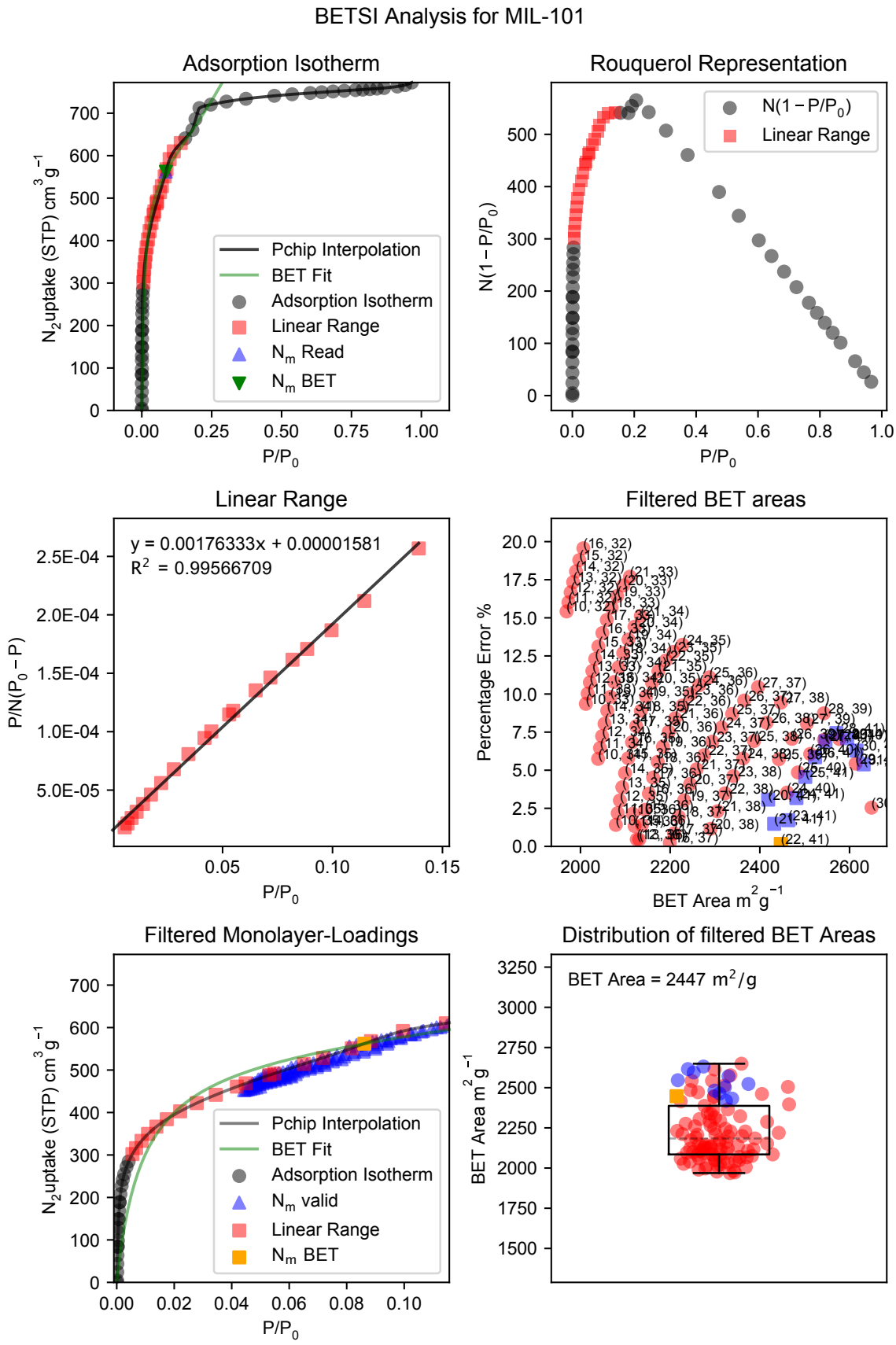

Fig. 4.14 BETSI Results for MIL-101

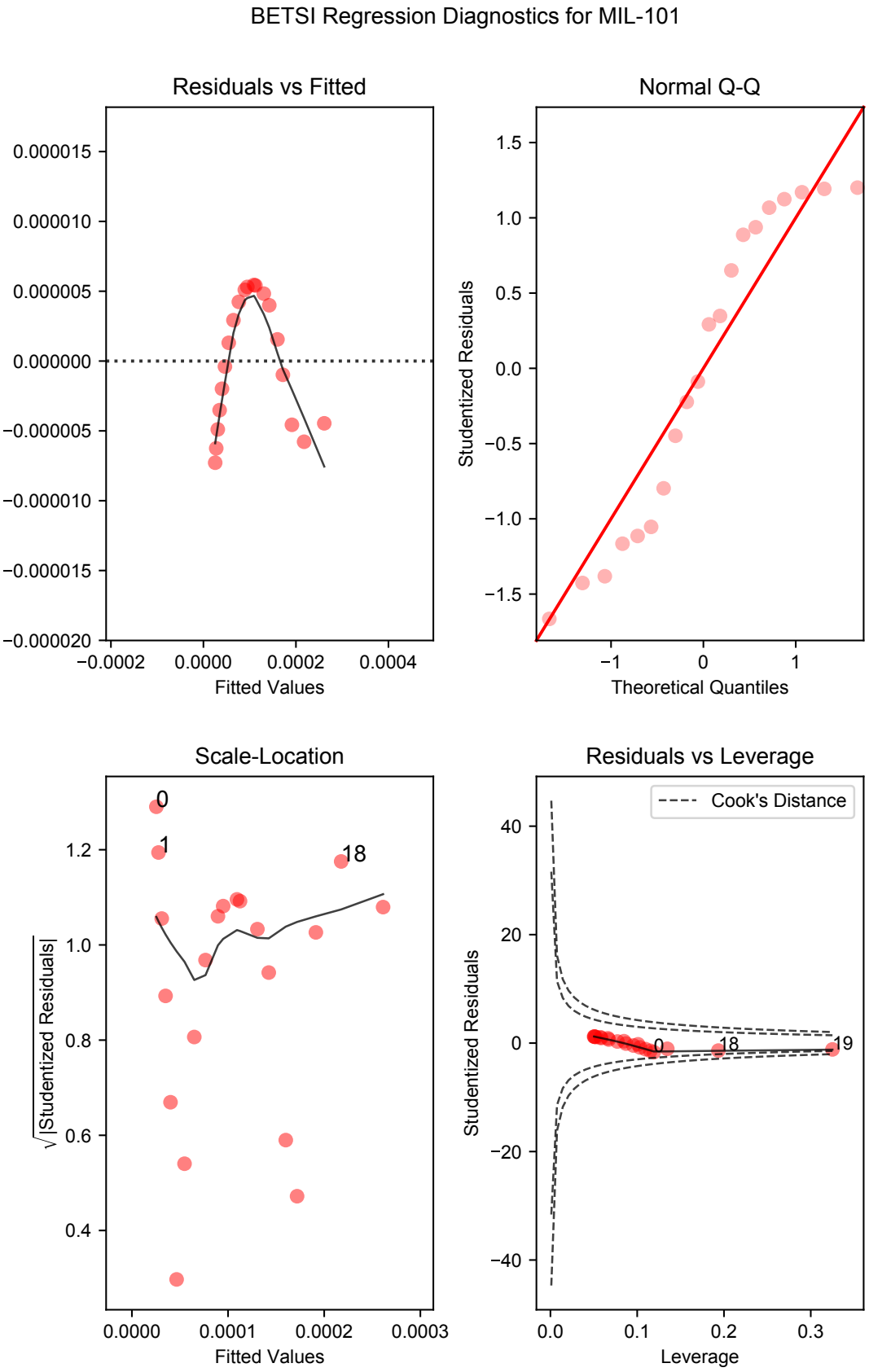

Fig. 4.15 Regression Diagnostics for MIL-101

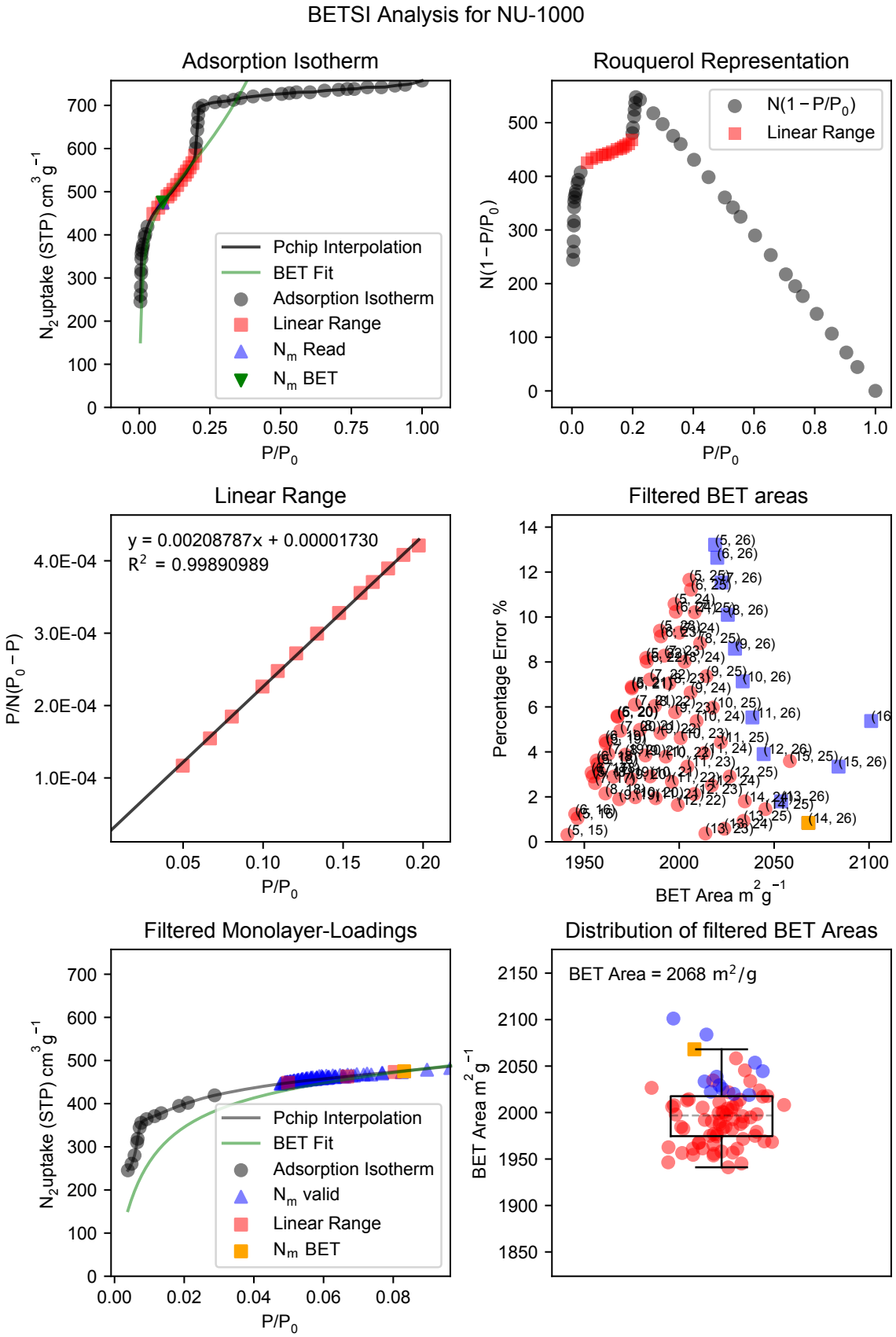

Fig. 4.16 BETSI Results for NU-1000

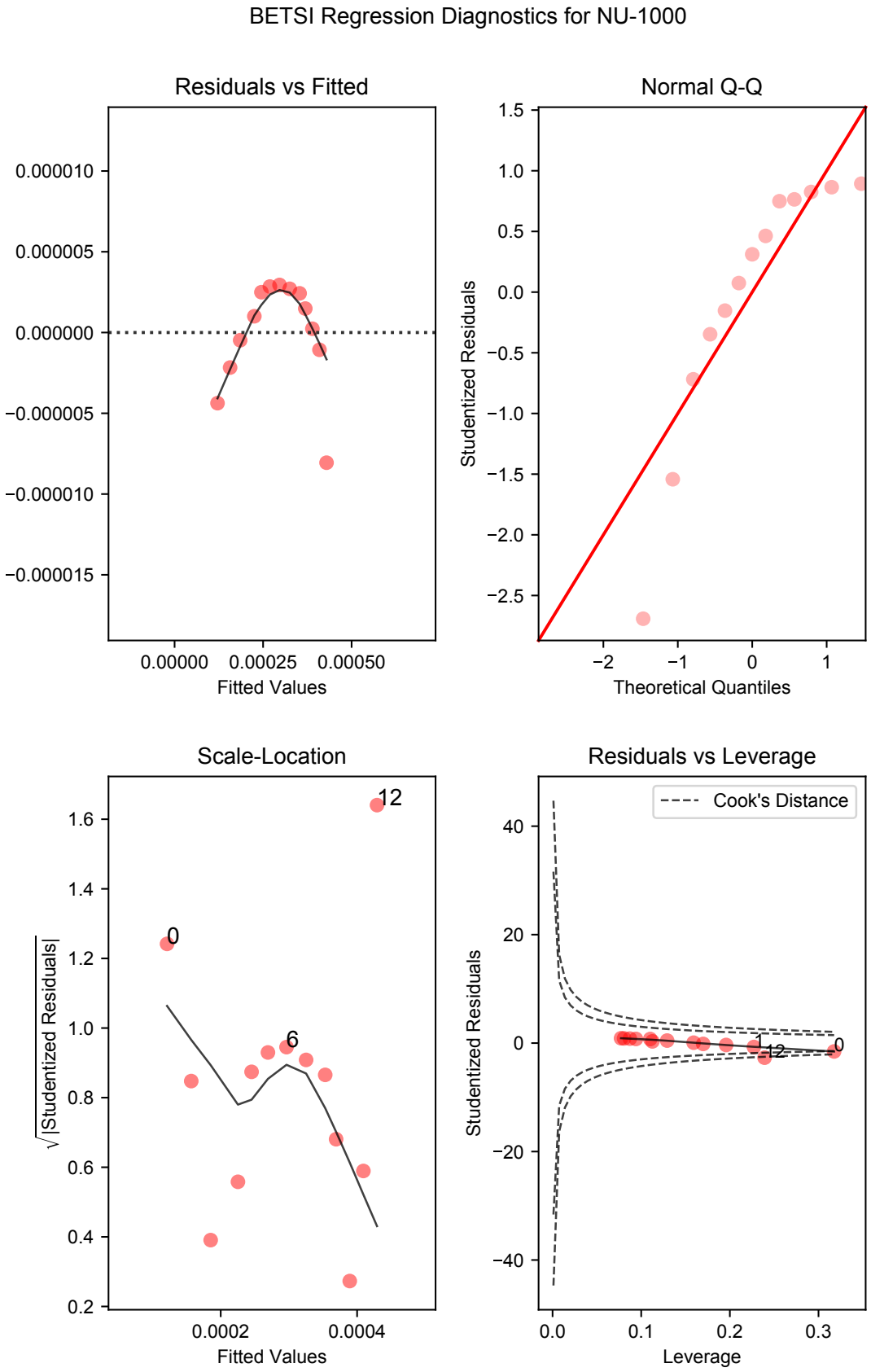

Fig. 4.17 Regression Diagnostics for NU-1000

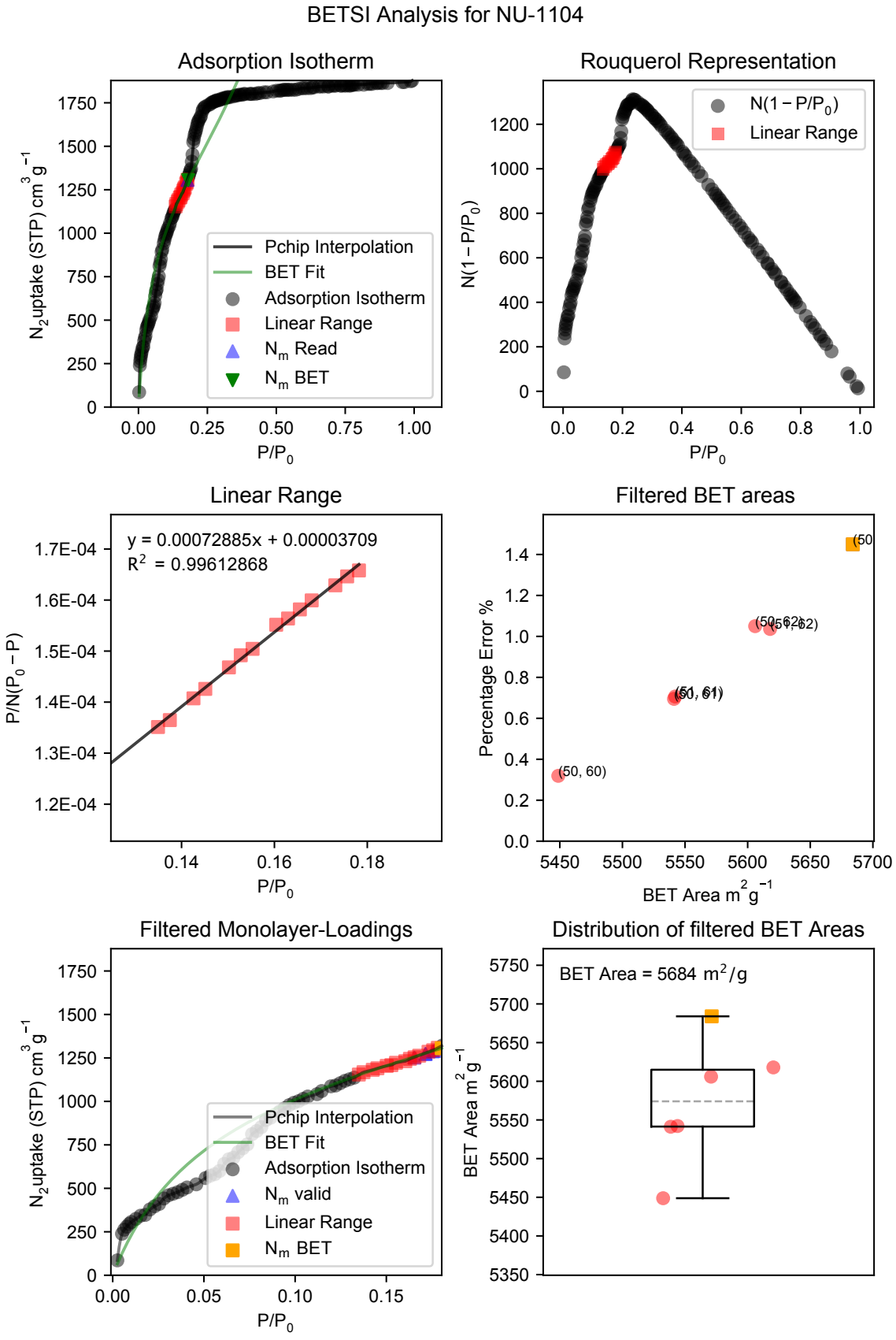

Fig. 4.18 BETSI Results for NU-1000

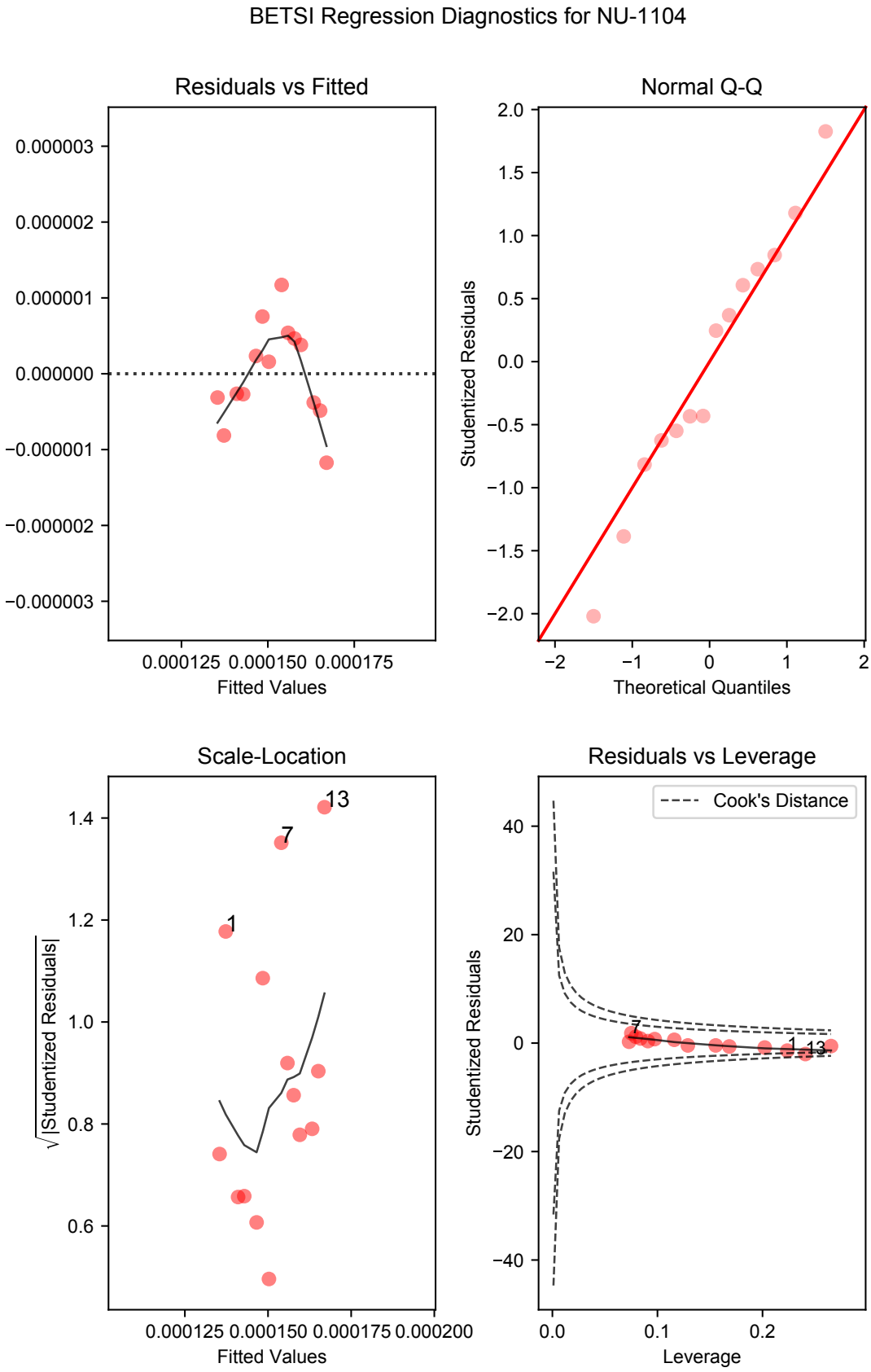

Fig. 4.19 Regression Diagnostics for NU-1104

4.4.3 BETSI compared to Round-robin Evaluation Results

Next, the BETSI results were compared with those from individual researchers in the round-robin exercise. Figure 4.20 shows the comparison between the results; the corresponding variation coefficient are shown in the inset. In all cases, the spread of BETSI results was considerably narrower than those obtained by manual calculation. For instance, in the case of NU-1104, the range of estimates dramatically decreases from 7,584 m^2 g^{-1} in the round-robin evaluation to 234 m^2 g^{-1} under BETSI.

Since most groups reported using the Rouquerol criteria to calculate their BET areas, this substantiates the hypothesis that the manual implementation of Rouquerol criteria is cumbersome and difficult to carry out in practice. This is rationalised best by the counter-factual: if all manual BET fits were consistent under the criteria, they would lie within the BETSI range; BETSI effectively maps out the population distribution of possible BET fits and the round-robin results are samples of that population. An alternative representation of these results in shown in Figure 4.21; here the results from the round-robin evaluation have been normalised to the BETSI range, by subtracting the BETSI median and dividing by the BETSI range. They are visually represented as a red jitterplot, and the corresponding BETSI distribution is shown as a boxplot. This graph illustrates how accurate the manual calculation results were considering the underlying distribution of passable BET areas. Points lying inside the box – the box and whiskers spanning, by definition, a distance of 1 – correspond to fittings that lie inside the Rouquerol-consistent range, whilst those outside the box correspond to incorrect fits. It is therefore not surprising that for materials like DMOF-1, which have a very narrow Rouquerol-consistent range, very few groups have reported passable fits. At this point, it is sensible to define a new metric that quantifies the success of individual BET fittings, the *hit rate*. This number is simply the fraction of BET areas lying inside the BETSI range for each material, and it demonstrates that some isotherms are generally easier to fit manually than others (Figure 4.21 b.)

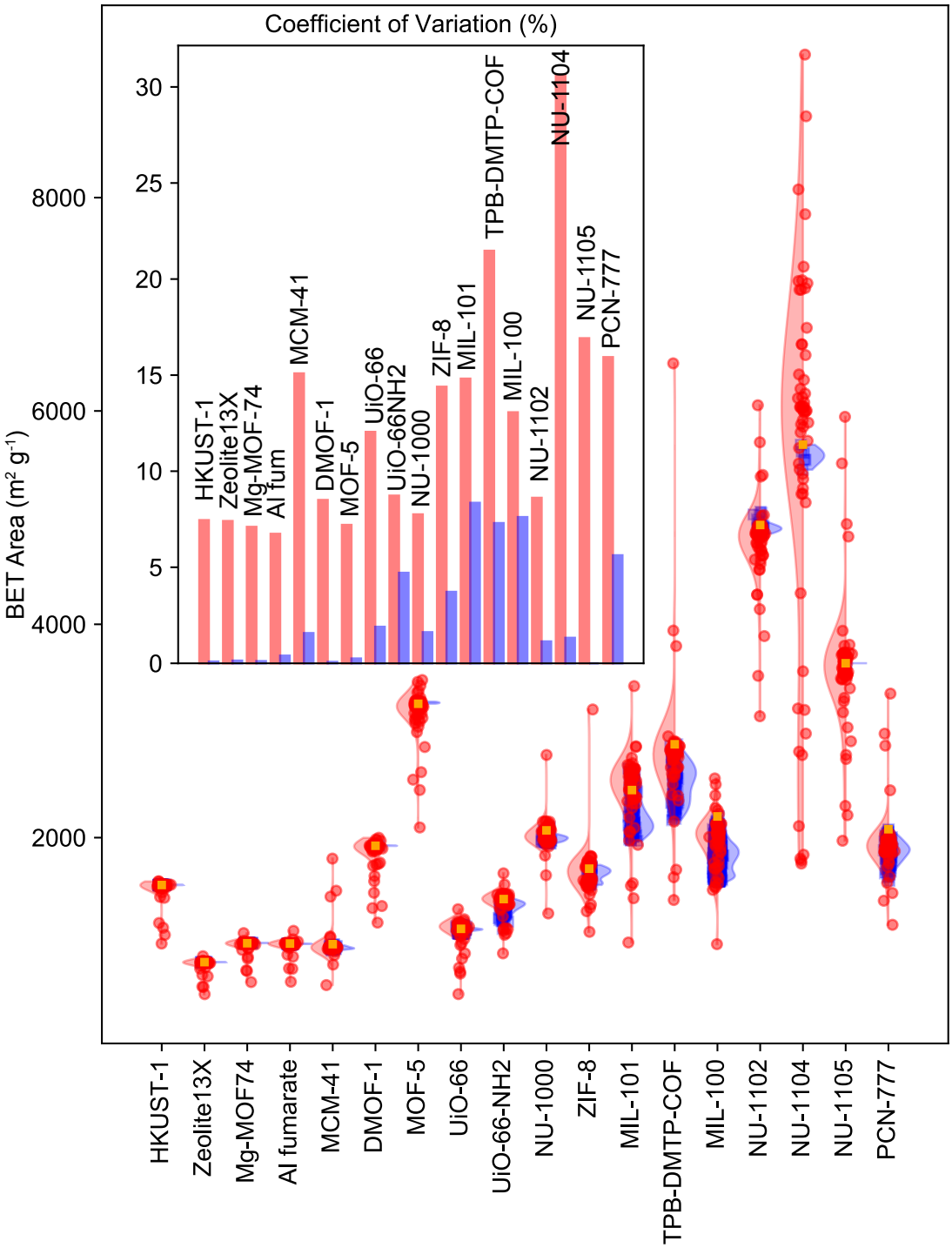

Fig. 4.20 BETSI compared to Round-robin Evaluation | Distribution of BET area results from identical isotherms as calculated by BETSI (blue) and from round-robin evaluation (red). Superimposed are normalised probability density functions obtained by kernel density estimation. Inset shows the coefficient of variation of results for each material, in red for the round-robin exercise and in blue for BETSI.

Material	BETSI $m^2\ g^{-1}$	BETSI Range $m^2\ g^{-1}$	BETSI Variation Coefficient %	Pass Rate %	Round-robin Average $m^2\ g^{-1}$	Round-robin Range $m^2\ g^{-1}$	Round-robin Variation Coefficient %	Hit Rate %
HKUST-1	1556	8	0.090	2.419	1520	583	7.451	52
Zeolite13X	833	4	0.140	0.538	813	356	7.405	35
Mg-MOF74	1010	5	0.114	2.300	990	459	7.101	48
Al fumarate	1007	14	0.398	1.736	989	478	6.740	60
MCM-41	1001	60	1.573	3.329	994	1186	15.090	85
DMOF-1	1924	4	0.074	0.107	1860	795	8.500	15
MOF-5	3255	20	0.250	0.071	3170	1382	7.203	13
UiO-66	1145	91	1.901	0.870	1120	796	12.045	65
UiO-66-NH2	1424	285	4.710	1.722	1388	750	8.727	48
NU-1000	2068	160	1.619	4.218	2014	1486	7.752	80
ZIF-8	1709	188	3.718	0.861	1672	2085	14.396	58
MIL-101	2446	680	8.353	3.738	2429	2404	14.816	78
TPB-DMTP-COF	2875	711	7.298	5.375	2787	5031	21.472	80
MIL-100	2199	616	7.611	12.111	1959	1554	13.065	79
NU-1102	4931	204	1.139	0.862	4769	2915	8.614	39
NU-1104	5684	235	1.327	0.024	5592	7584	30.623	5
NU-1105	3635	0	0.000	0.011	3596	3974	16.921	0
PCN-777	2079	483	5.624	6.960	1947	2168	15.936	86

Table 4.1 Tabulated BETSI and Round-robin Results | *Material*, isotherm of material under investigation; *BETSI*, optimal BET area predicted by BETSI; *BETSI Range*, full spread of BET areas that pass under BETSI; *BETSI Variation Coefficient*, relative standard deviation BET areas that pass under BETSI; *Pass Rate*, number of BET areas that pass under BETSI expressed as a fraction of all hypothetical fittings; *Round-robin Range*, full spread of BET areas determined in round-robin evaluation; *Round-robin Variation Coefficient*, relative standard deviation of BET areas calculated in round-robin evaluation; *Hit Rate*, fraction of BET areas calculated in the round-robin evaluation that lie within the BETSI range.

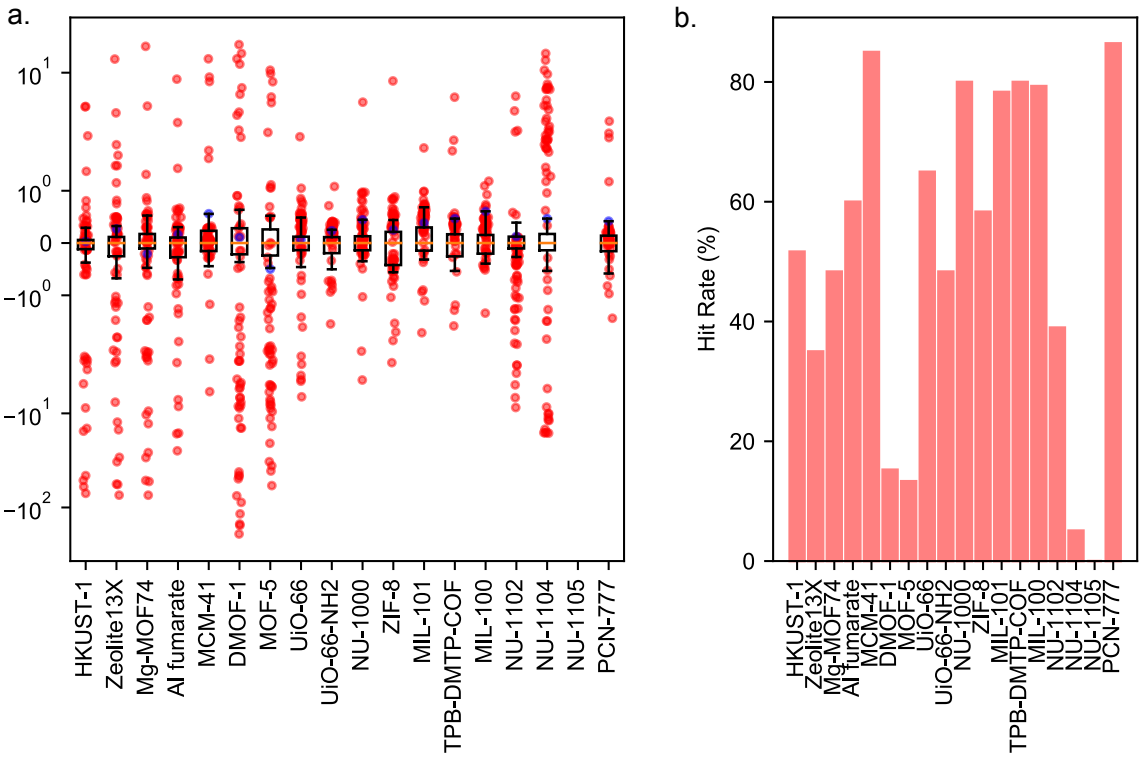

Fig. 4.21 Round-robin Results normalised to the BETSI Range | Round-robin results, subtracted by the BETSI median and divided by the BETSI range (red). The boxes and whiskers represent the distribution of BETSI results subjected to the same treatment, therefore spanning, by definition, a distance of 1. Blue points represent the BETSI Optimal prediction. Note that this treatment is not possible for NU-1105, due to a BETSI range of 0 (only one passable fit under BETSI).

4.4.4 Type A, B & C Isotherm Fittings

It is evident that in BETSI some isotherms give much larger spreads of results than others (Figure 4.20), suggesting that they are not described by the BET model as naturally, and that, consequently, they are less susceptible to filtering by the Rouquerol criteria. The spread of these results was quantified by the *BETSI variation coefficient*, which is defined as the relative standard deviation of BETSI results, and the *pass rate*, as the number of BET fits that pass under the Rouquerol criteria as a fraction of all potential fits. To account for the non-equal spacing of points on the pressure axis of all isotherms, the *pressure-adjusted pass rate* expresses the total sum of pressure intervals that fit the Rouquerol criteria as a fraction of the sum of all pressure intervals of the hypothetical fitting ranges. All functions are defined Section 4.3.3.

Figure 4.22 shows the correlation between the pass rate, the BETSI variation coefficient, and the hit rate introduced in Section 4.4.3. This figure affirms the intuitive expectation, that,

simply put, the more BET fits are valid, the greater the spread of possible results is, and the more likely individual researchers are to make a successful fit.

While it is difficult to generalise about the shape of these isotherms, they can broadly be categorised into three types:

Type A isotherms suit the BET model 'best'. Under BETSI, they have a relatively high pass rate and return a narrow spread of results. Examples include materials such as Al fumarate, NU-1000, Zeolite-13X and MCM-41. Many of these isotherms do not have strongly pronounced isotherm knees and some have mesoporous steps. Hit rates greater than 70% were generally observed for these materials, as the majority of researchers did not struggle with the fits.

Type B isotherms only fit the BET model over a very narrow range. Therefore, these have extremely low pass rates, meaning that only a few BET fits are valid, which in turn will be spread narrowly. Examples include MOF-5, DMOF-1, NU-1104, HKUST-1, NU-1105. For the latter, out of 9,409 hypothetical 10-point fits, only one is permissible under the Rouquerol criteria. Such prohibitively low pass rates make the correct BET assignment by hand virtually impossible and demonstrate the need for a program like BETSI. In contrast to type A isotherms, type B isotherms, often have sharp isotherm knees, following strong adsorptive interactions at low relative pressures. Isotherms with more complex shapes such as NU-1104 also appear in this category.

Type C isotherms are arguably the most problematic as they return large spreads of BET results. Typical materials that fit into this category are MIL-101, MIL-100, TPB-DMTP-COF, and PCN-777. Like type A isotherms, these have rounded isotherm knees, which appear at higher relative pressures. It is for these materials that the necessity to extend the Rouquerol criteria is demonstrated and the BETSI algorithm makes an unambiguous BET assignment possible.

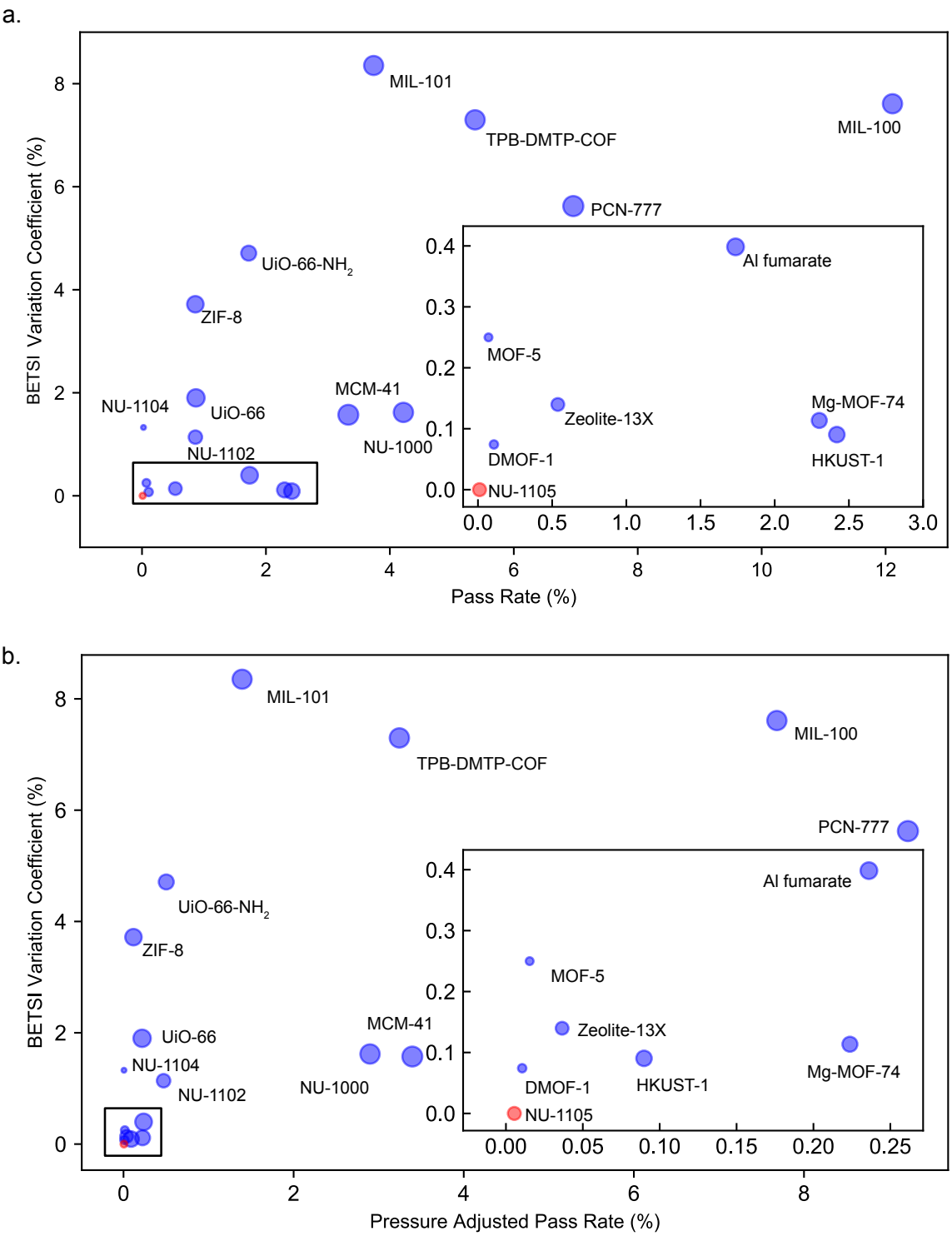

Fig. 4.22 Isotherm Classification Fit | a. Correlation between the pass rate, the relative number of all fittings that pass under BETSI and the BETSI Variation Coefficient. Bubble-size correlates with the hit rate; the red symbol has a hit rate of zero. Inset shows zoom-in into highlighted box on bottom-left b. Correlation between the pressure-adjusted pass rate and the BETSI Variation Coefficient

4.5 Conclusion

In conclusion, BET theory is a great success story. Developed in the 1930s for open surfaces, it continues to this day to be applied to modern adsorbents with much more complex porosity. Despite advances from classical DFT methods, BET theory will likely continue playing a crucial role in porosimetry for decades to come, with impacts in energy research, transport, medical applications, and climate-change mitigations. In light of these enormous future challenges, it will become increasingly important to share critical scientific metrics reliably to find a common language to report both academic and industrial progress.

To this end, the BET method has been contextualised in a modern way in this study. The important Rouquerol criteria have been reviewed and been given the theoretical justification they lacked so far in the literature. It was also hypothesised that they are (i) insufficiently determinate and (ii) too difficult and cumbersome to apply manually. To probe these hypotheses, 18 experimental isotherms were shared with international colleagues along with the instruction to calculate the BET area in a way they see most fit. The wide spread of results from this inter-rater reproducibility study speaks for itself and raises critical concerns over the reliability of one of the most prominent metrics in physical chemistry. Next, an algorithmic approach called BET Surface Identification (BETSI) was developed that automates the BET calculations and makes, for the first time, an unambiguous BET area determination under the extended Rouquerol criteria possible. The need for extending the Rouquerol criteria is in support of the first hypothesis, that the former version of the criteria was in itself indeterminate. Regarding the second hypothesis, the much narrower results in BETSI compared to the round-robin evaluation affirm the suspicion that even though most scientists are aware of the Rouquerol criteria, they struggle to implement them manually. The full BETSI method is published and it is this author's sincere hope that it will make BET calculations in the future easier, faster, and – crucially – more transparent and reproducible.

Despite the advances associated with the BETSI method, it is herein stressed that for BETSI to become a step towards greater transparency and critical assessment, researchers must remain aware of the underlying limitations of BET theory. It is neither the function nor the purpose of BETSI to eliminate doubt and treat a particular BET area as 'true'. It is recommended that ideally for future use, the full BETSI reports are shown which show the underlying distribution of possible BET areas, as well as the regression diagnostics. Most importantly however, the pressure range and number of points used in the fits should always be reported, as well as the isotherm in linear and semi-log representation to show low-pressure regions.

Dr Conchi Ania, who contributed to this study, summarised this sentiment so cogently, that this chapter ends on her note: *The 'experiment' is the adsorption isotherm – not the BET area.*

Chapter 5

Reticular Colouring Design

'*It is better to be lucky. But I would rather be exact. Then when luck comes you are ready*' - Ernest Hemingway, The Old Man and the Sea

In this final results chapter of the thesis, the reader is drawn to the many parallels between MOF chemistry and structural DNA nanotechnology. Much like reticular chemistry has formalised the design of MOFs, an analogous design strategy here called *Reticular Colouring Design* (RCD) can be used to create DNA frameworks, which are porous DNA crystals. The concepts of this design strategy are here developed and it is argued that RCD is a binding narrative that connects the dots between previously unfamiliar branches of science. Unlike previous chapters, this chapter is more conceptual and entails designs that have only begun to be realised experimentally. The preliminary results are however encouraging.

5.1 Background

5.1.1 Reticular Design – Revisited

Following the introductory words in Section 1.3.1.2, which serve the purpose of explaining reticular design strategies to the new reader in the field, the discussion in this chapter requires a more detailed understanding of the use of graph theory in chemistry.

The word *reticular* (from '*rete*', Latin for 'net') denotes the governing principle of framework design, which lies in the abstraction of a crystal structure as a periodic graph or net [230, 231]. In this context, the underlying net is called the *topology* of the framework; however, it should be noted here that it strictly refers to the *embedding* topology of the net [232]. Periodic nets are characterised by rings, a feature that is mirrored in the porous frameworks. Describing crystals as periodic graphs and enumerating the underlying nets dates back to Well's work in the 1970's [233], but only in the last twenty years this concept has evolved from a mere structural descriptor to a design strategy [5].

In Section 1.3.1.2, reticular design was defined as a retrosynthetic strategy to assemble frameworks from chemically discreet, often isolable species. A central feature of this paradigm is the *deconstruction* of a net into nodes, or vertices, and edges (Figure 5.1). The net and its real-life counterpart, the crystal, are related to each other *via abstraction* (framework-to-net) and *realisation* (net-to-framework). Just as the net can be realised in the framework, nodes can be realised as chemical subunits, which are held together by strong bonds, and edges can be realised as the weak bonds connecting these subunits with one another. A common convention here is to abstract the chemical subunits as geometric clusters defined by their maximum points of extension and connectivity with their topological neighbours, the aforementioned *secondary building units* (SBUs) [234]. SBUs and the nodes in the underlying topology are related to each other by the *augmentation* operation [235], a special kind of node decoration in which each node is replaced with a polyhedron in the shape of its coordination environment (Figure 5.1).

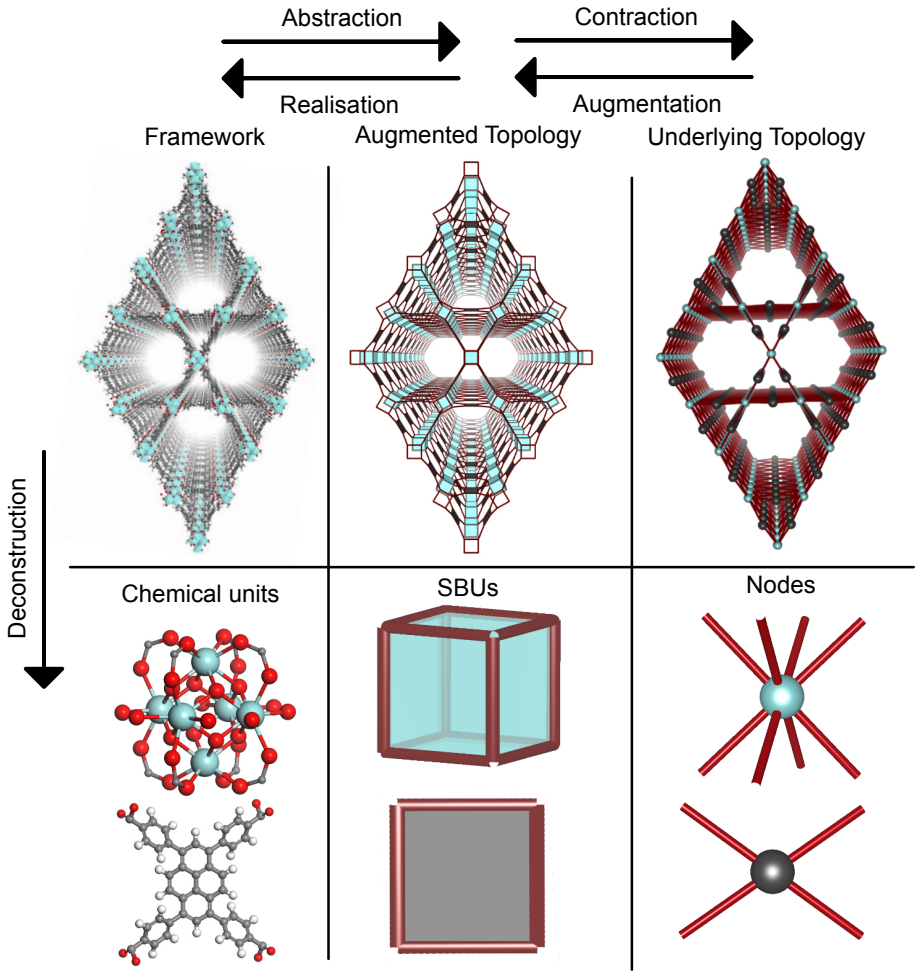

Fig. 5.1 Relationship between Framework and Topology | A framework such as a MOF can be deconstructed into discrete chemical units. The framework and the chemical units can be abstracted as an augmented topology, or net, and secondary building units (SBUs) respectively. The augmented topology is often shown for greater visual clarity than the underlying topology and likewise the nodes, here shown with red edges attached, are better represented as SBUs.

From the deconstruction of a net into constituent SBUs emerges a useful property: if the structure of a chemical subunit is known, an SBU can be derived from it. This logic can also be applied backwards by starting with a target net and realising it in a framework. A reticular design sequence can thus be summed up in four steps (Figure 5.2): (i) choosing an embedded net (target topology); (ii) deconstructing the net into SBUs; (iii) realising SBUs to yield chemical subunits that can be manipulated independently; (iv) assembling the framework with the target topology from the chemical subunits. In addition, the chemical units can be exchanged relatively freely, as long as their abstracted SBUs and their connectivity do not

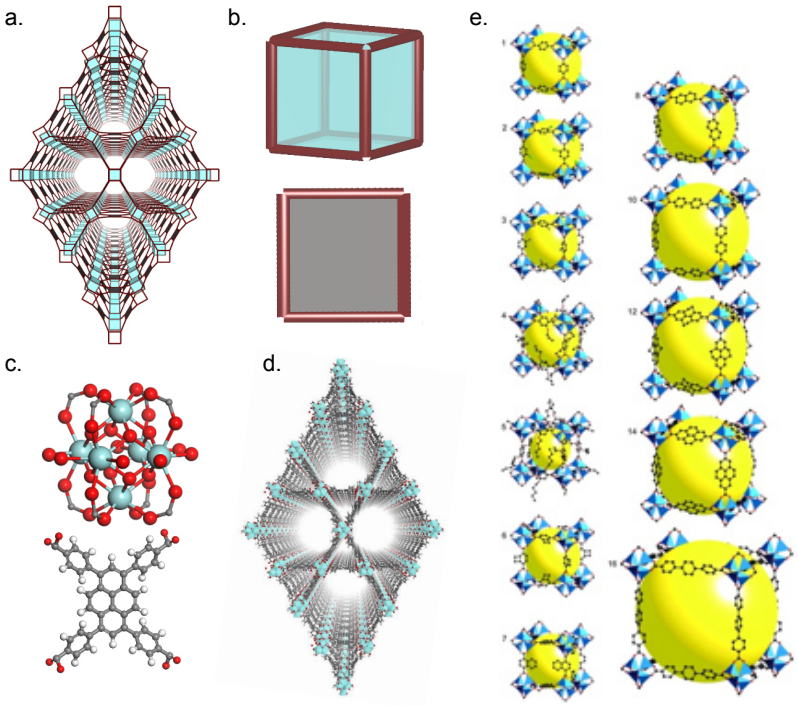

Fig. 5.2 Reticular Design Sequence | a. A target topology is chosen, in this case the **csq-a** (augmented **csq**) net. b. The augmented net is deconstructed into SBUs. c. SBUs are realised as independent chemical subunits. d. A MOF can be assembled by combining the chemical subunits. e. So long as the SBUs do not change, they can be realised in different molecules. This has been famously demonstrated in the isoreticular MOF (IRMOF)-series, an example of an isoreticular expansion. The organic struts connecting the blue metal clusters are exchanged in structures 1-16 so that the size of the unit cell and the pore volume (yellow sphere) increase. All linkers are abstracted in the same way and thus the underlying topology is preserved. Reprinted with permission [18].

change. Consequently, the framework assembled from new chemicals has the same topology as the original one; it is *isoreticular* [18].

The origin of crystallinity in MOFs is two-fold: (i) few distinguishable chemical species (most commonly two, the organic and inorganic moiety), and (ii) strong directionality in bonding, *i.e.* well-defined local structure. This local geometry is repeated everywhere in the material giving rise to crystalline order. In graph theoretical terms, this is mirrored in the embedding of nodes and edges relative to one another. Nodes of Type A and nodes of Type B are connected to one another in one particular way only because there are local geometric rules on bonding, that are observed everywhere in the material. Combinatorial topology, which first and foremost describes connectivity between nodes, emerges from these local geometric constraints: a certain size of ring forms in the net because the angles

between the nodes are fixed – *structure imposes topology*. This point is further illustrated in a thought-experiment below (Section 5.1.3).

5.1.2 DNA Nanotechnology

This is different in DNA nanotechnology. DNA single-strands are naturally flexible, but have programmable connectivity based on Watson-Crick base-pairing. DNA nanotechnology employs these programmable interactions to judiciously assemble nanostructures – *topology imposes structure* [236]. For this reason, DNA nanostructures are primed to be considered as graphs, and indeed they have been [237, 238]. *Sequence symmetry minimisation* inhibits unwanted interactions by breaking the sequence symmetry in the nanostructure, giving 'uniqueness' to each interaction [239]. The power of this approach has been most impressively realised in DNA origami, which allows for arbitrary shapes to be designed using a long scaffold strand and multiple short staple strands [240]. However, in order to make larger periodic structures translational symmetry forbids 'uniqueness' in bonding, limiting this design principle to finite structures.

Efforts to make DNA crystals have been made for decades [241, 242], and it is here argued that strong parallels exist between their designs and reticular chemistry. Seeman's early work was aimed at utilizing DNA crystals as scaffolds for biological macromolecules, which could be used in protein crystallography. In order to build periodic structures, DNA nanotechnologists have made DNA building motifs as stiff as possible, emulating the reticular design tenet that rigid, highly directional subunits can carry a particular net. Prominent designs are the immobile Holliday junction [239], star motifs [243], the double crossover (DX) tile [244], and tensegrity triangles [245], the latter being highly successful in forming a 3D DNA crystal [246]. For 2D arrays, to avoid out of plane twisting and bending, two main strategies were pursued: corrugated designs have alternating tiles 'flipped' by 180º to cancel out arm bending [247–250]. Alternatively, deliberately using sequence symmetry to construct rotational symmetry in star motifs forces twists and bends to be isotropic and therefore cancel each other out [251, 249]. As with reticular chemistry, periodic nets will only form if the local geometry around each node is fixed.

5.1.3 Thought-experiment

This informal thought-experiment serves to illustrate the differences between reticular design in MOF chemistry and sequence-symmetry minimisation in structural DNA nanotechnology in graph-theoretical terms.

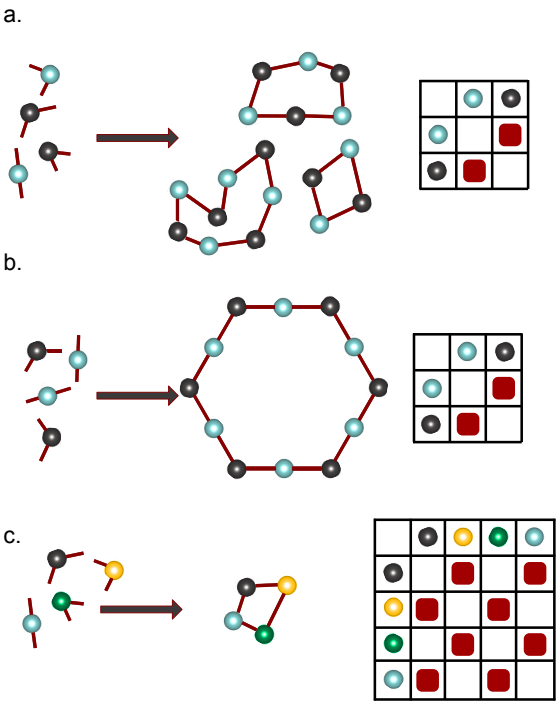

Fig. 5.3 Thought-experiment | The notional assembly of a net with two different kinds of vertices (blue and black). The graph is bipartite so that only black-blue interactions are allowed. a. The deconstructed nodes have spatially non-directional half-edges; in responses multiple ring sizes can form. b. The edges are highly directional, *i.e.* there is a specified local geometry around each node, which imposes a specific topology, here a 12-ring. Both a. and b. have the same adjacency matrix. c. The half-edges are spatially non-directional (flexible) but combinatorically selective. The four-cycle is programmed into the adjacency matrix.

Consider the notional assembly of a net in the same way that framework (or a DNA nanostructure) is assembled – from its constituent nodes and edges. In the case of a MOF, there usually exist two kinds of nodes, here called Type A (black) and Type B (blue), representing the organic and the inorganic moiety, respectively. For simplicity, each node is assigned the coordination number 2, and it is further defined that only nodes of Type A are allowed to connect to Type B (bipartite graph). This can be thought of as attaching two half-edges to each node and only allow them to combine to form full edges if the colours of the associated nodes are opposite. It can also be represented in an adjacency matrix. In the first case (Figure 5.3 a.), the half-edges are undirected and there is no specified geometric relationship between them. The resultant graph does not have a pre-determined size of ring, multiple rings of various sizes conform to the connectivity constraints.

In the second case (Figure 5.3 b.), there is a specified fixed local geometry around each node, *i.e.* there is an embedding between the nodes and edges. Half-edges around Type A nodes have a 120° angle, and half-edges around Type B nodes are 180° apart. Even

though the adjacency matrix of this graph is the same as in the Figure 5.3 a., the ring size in the second case is pre-determined by the angular constraints around each node – *structure imposes topology*.

Sequence-symmetry minimisation resembles more the third case (Figure 5.3 c.). Four different kinds of nodes are used, A, B, C and D, and flexible half-edges are placed around each one. Despite the flexibility, a particular ring size can be combinatorically programmed by allowing A to bond to B, B to C, C to D and D to A again. As before, this connectivity can be represented in the adjacency matrix.

5.2 Aims & Objectives

It is here argued that both DNA nanotechnology and MOF chemistry can be described by a unifying design strategy and language, herein termed *reticular colouring design* (RCD). Where reticular chemistry uses the deconstruction of nets into nodes and edges to design new MOFs, RCD complements this approach with *network colourings* in the design of DNA crystals. It is hypothesised that both fields can learn from one another in a concerted effort to make *DNA frameworks* (DNAFs). From this synergy, scientists could add DNA to their toolbox of materials, and DNA nanotechnologists can exploit the rich mathematical links between graph theory and crystallography discovered by O'Keeffe and others [234, 230, 232].

5.3 Reticular Colouring Design

5.3.1 Network Colouring

A network colouring is the assignment of colours to nodes on the graph, with the rule that no two identical colours are allowed to be connected. Figure 5.4 demonstrates this principle for an exemplary **sql** net (Figure 5.4 a.). Nodes in the net are coloured in such a way that no nodes of identical colours are connected (Figure 5.4 b.). For periodic graphs such as **sql**, this stipulates local symmetry breaking, but long-range translational symmetry may be preserved. For greater visual clarity and for reasons that will become apparent soon, the net colouring here is visually represented as a half-edge colouring rather than a node colouring as shown below (Figure 5.4 c.). An additional rule of this half-edge colouring is that two like-coloured half-edges combine to form a full coloured edge (Figure 5.4 d. and e.).

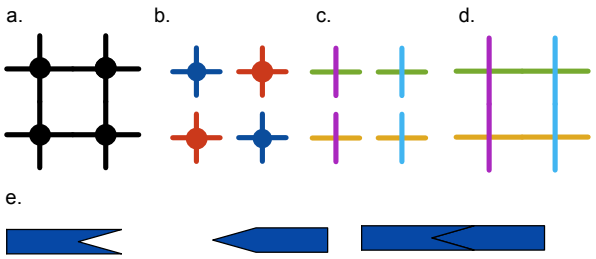

Fig. 5.4 Network Colouring | a. 4-ring of the square lattice **sql** net. b. Vertex colouring of the **sql** net. No like-coloured nodes are connected to each other as is the requirement of a proper vertex colouring. c. Coloured half-edges, the 'nodes' are here visually removed and are represented by the coloured half edges which cross over at them. d. Edge-coloured net e. Like-coloured half-edges combine to form one coloured edge. They are realised as complementary sticky-ends.

5.3.2 Abstractions & Realisations of Colour

In RCD, a DNAF can be abstracted as an edge-coloured net and deconstructed into nodes and edges. Branching points in DNA nanostructures, such as a 3-point or 4-point star motif are abstracted as nodes. Sticky-ends, single-stranded, unhybridized 'overhangs', are abstracted as coloured half-edges. Two complementary sticky-ends come together to form a coloured full edge (Figure 5.5 a.). Other than strand sequences, colour can also be realised as helical pitch and corrugation of tiles/nodes (Figure 5.5 b.). A geometrically satisfied DNAF has cycles with an even number of helical half-turns in order to close up. For visual clarity, edge

colourings based on flipped strands in corrugated structures are shown in a lighter shade of the same colour.

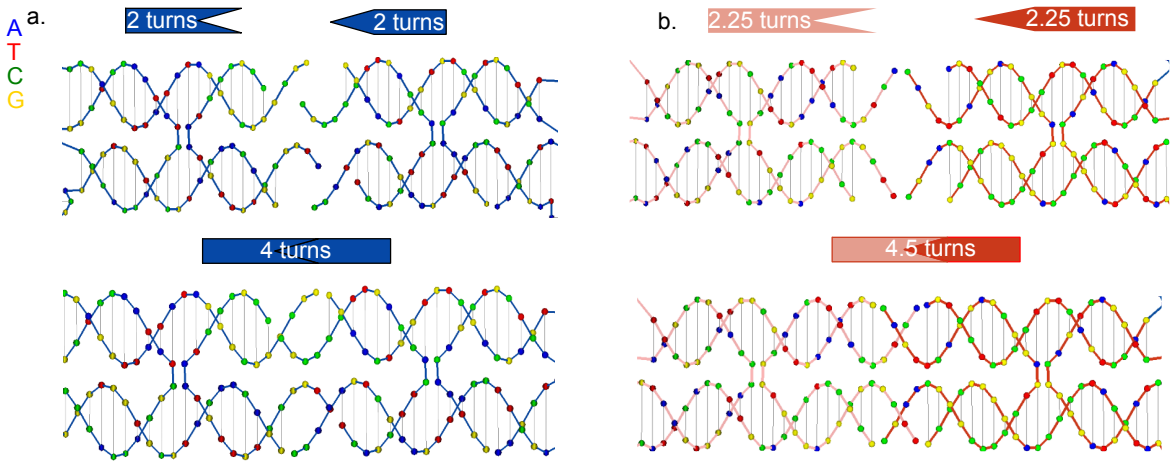

Fig. 5.5 Colour Realisations | a. Two like-coloured half-edges (two complementary sticky-ends) hybridise to form a coloured full edge. b. Colour can also be realised as helical pitch; visually this is represented as a shade; two like-coloured edges in a different shade come together, the two-helical domains in the lighter shade are rotated by 180° along the helical propagation axis.

5.3.3 Reticular Colouring Design

RCD bridges the gap between reticular design and sequence-symmetry minimization (Table 5.1). The net of a MOF has essentially two kinds of nodes (two colours, bipartite graph), an organic and an inorganic one. A finite DNA nanostructure with unique interactions everywhere on the other hand, has a net with as many individual colours as nodes. RCD attempts to find a colouring of the net, that allows a certain 'topological unit cell' to be specified combinatorically, that is, through its sequence-complementarity alone. This topological unit cell then connects onto a topological neighbour in order to build a periodic structure. The objective of RCD is to find the smallest number of colours (smallest number of non-identical strands) needed to specify the target net of a DNAF.

Due to the importance that rings play in network topologies, RCD considers, as a starting point, rings to be the 'topological unit cells' that have to be uniquely coloured. *For edge-coloured nets, this means as many colours (unique pairs of complementary strands) are required as there are edges in the rings of a net.*

Table 5.1 Reticular Colouring Design | Similarities and differences between reticular design and sequence-symmetry minimisation. RCD can be seen as bridging the gap between those design strategies.

Reticular Design	Reticular Colouring Design	Sequence-symmetry Minimization
Translational symmetry	Long-range translational symmetry	No translational symmetry
Rigid components	Semi-flexible components	Flexible components
Topology through local structure	Topology through structure and connectivity	Topology through connectivity

5.3.4 RCD of the sql and fes Nets

This concept is here illustrated with the established 2D square lattice (**sql** net) synthesised by Yan [247], and its augmented partner, the **fes** net [250]. The RCD sequence can be summed up in five steps: (i) choose an embedded net (Figure 5.6 a.); (ii) create a supercell that includes all strong rings of the net (Figure 5.6 b.); (iii) find a proper vertex colouring for all vertices in the supercell making them uniquely coloured (Figure 5.6 c.); (iv) deconstruct the net into vertices and coloured half-edges so that like-coloured half-edges are complementary (Figure 5.6 d.). Join up loose half-edges that point outside the unit cell with their topological neighbour in all crystallographic directions. This can be done either using the same edges used inside the unit cell (same colours, Figure 5.6 d.), or with a different set of edges (Figure 5.6 h.). Corrugation strategies can reduce the number of required sticky-ends for the designs (Figure 5.6 d-e. and h-i.) and the associated orientations of the tiles are shown in Figure 5.6 k.). Finally, the realisation of the design, step (v) is shown in the succeeding section. Steps (i-iv) are shown in Figure 5.6, and step (v), the realisation, is addressed in Section 5.3.5.

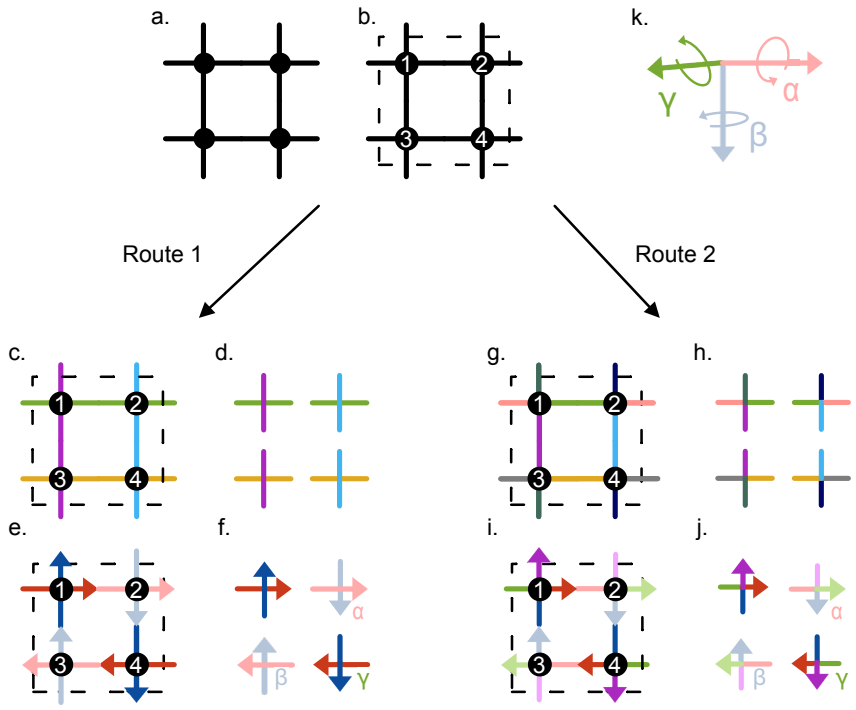

Fig. 5.6 RCD of the **sql** Net | a. An embedded network topology is chosen (**sql**). b. A supercell is chosen in which all strong rings of the net are included. c. Route 1: The vertices in the cell are uniquely coloured through an edge-colouring; the topological neighbour cell is connected with the same colours. d. The tiles are broken up. Four sets of complementary sticky-ends are required to combinatorically define the 4-cycle of the **sql** net. e. Corrugation can reduce the number of required pairs of sticky-ends to two. Each half-edge is an odd number of helical half-turns and only flipped pairs hybridise. Visually this is represented as a shade in the same colour. In order to close the 4-cycle, four tiles have to join up. g-j. Identical to c-d., but in this Route 2, the topological neighbour cells are connected onto with different colours. k. The rotations associated with the nodes (pitch, roll, yaw)

5.3.5 RCD Realisation of the sql Net

The last step in RCD is to realise the vertices as junctions and half-edges as sticky ends. To minimise geometric frustration during the assembly, in the realisation of the vertices, angular dependencies between the terminal strands (arms) must be accounted for, *e.g.* through bulged T-loops [250]. The choice of net embedding dictates this process. The RCD realisation of the **sql** net is shown below in Figure 5.7; the full structure can be found in Appendix C, designed using the TIAMAT software [252]. The corrugated **sql** net can be realised in a single 4-point star motif, with DX crossovers and 2.25 helical turns along each arm [247] (Figure 5.7 a.). These tiles come together in a four-cycle labelled 1-4, in which alternating tiles are flipped in accordance with the rotations in Figure 5.6 f.

The close topological relationship between the **sql** net and its augmented partner, the **fes** net, are further demonstrated in Figure 5.7 e-h. Here, the 4-point star motif used in **sql** design is replaced by a four 3-point star motifs which are connected onto another to form an augmented 4-point star. This augmented star behaves topologically identically to its contracted partner in the **sql** design, and indeed the same terminal strands can be used.

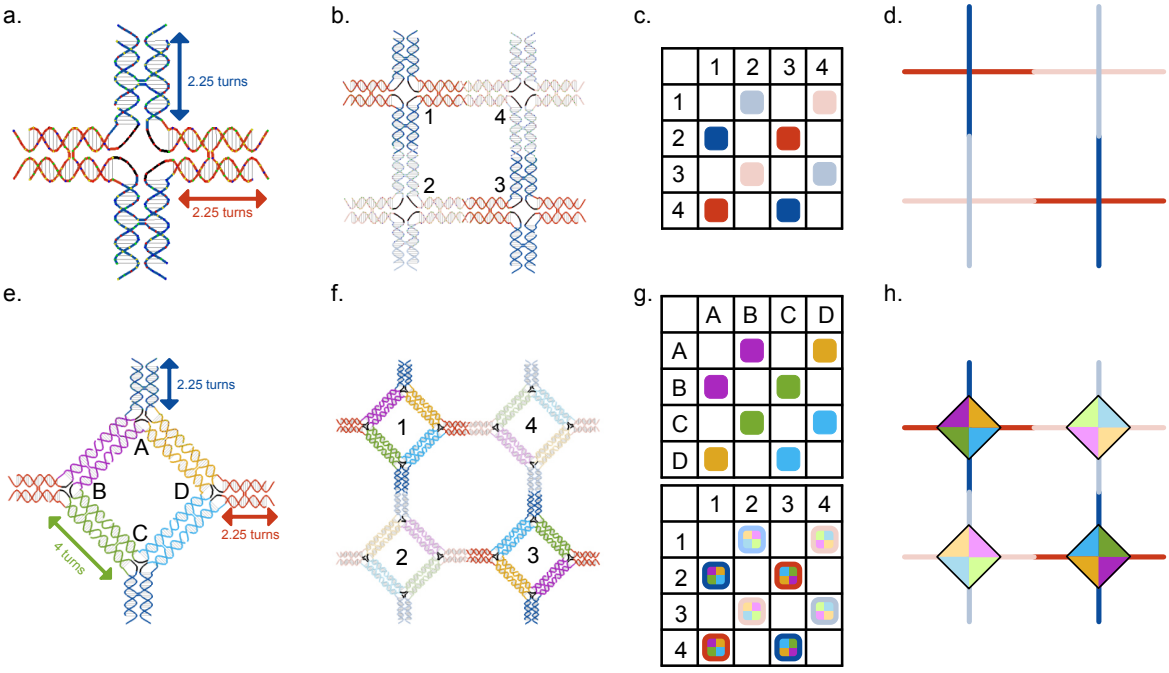

Fig. 5.7 RCD Realisation of the **sql** and the **fes** Net | a. One 4-point star motif is used to construct a corrugated **sql** net. b. The 4-cycle of the **sql** net with labelled nodes. The 'flipped' 4-point stars are shown in a lighter shade. Nodes 2 and 4 are flipped with respect to node 1 by 180° around the z and x-axis respectively. Node 3 is rotated by 180° around the y-axis. These are the same rotations as in Figure 5.6 f. c. The adjacency matrix of the coloured **sql** net. The colour shown in the (i,j)-matrix element is the colour of the half-edge linking node i to node j. d. the coloured **sql** net. e. 4-point star of the **fes** net. This tile is made up of four 3-point stars, labelled A, B, C and D. Since A, B, C and D are not rotated with respect to each other, four colours are used to combinatorically set the 4-ring. The terminal strands (arms) of the 4-point star motif have the same sticky-ends as the **sql** 4-point star motif. f. The 4-cycle and 8-cycle of the augmented **sql** net, the **fes** net. The rotational relationship between the nodes 1,2,3, and 4 and the augmented nodes 1,2,3 and 4 in the **fes** net are the same g. The adjacency matrix of the coloured **fes** net. The 3-connected nodes A,B,C, and D are shown above, the augmented 4-connected nodes 1,2,3, and 4 below, with corrugation indicated by shading as above. h. The coloured **fes** net

The tiles the **sql** and **fes** nets were designed using the TIAMAT software and their strand sequences are found in Appendix C. Preliminary experimental results for the **sql**-realisation are shown below.

5.4 Materials & Methods

5.4.1 General Methods

DNA strands were purchased from Integrated DNA Technologies (IDT). The sequence of the strands is given in Appendix C. All strands were ordered on a 100 nM scale and were purified using standard desalting, except for strand 1, which due to its length was purified by polyacrylamide gel electrophoresis (PAGE) by IDT. All strands were diluted using sterilised, milliQ water to a concentration of 100 μM.

5.4.2 Strand Hybridisation

To hybridise the strands, they were mixed with TE buffer (10 mM Tris, 1 mM EDTA, pH 8) with 10 mM $MgCl_2$ and diluted to a final concentration of 1 μM unit cell at a final volume of 100 μL. The samples were split into two 50 μL batches and pipetted into Eppendorf vials, which were placed in a polymerase chain reaction (PCR) machine, where they were heated to 94 °C and slowly cooled over the course of 12 hrs.

5.4.3 Gel Electrophoresis

Gel electrophoresis was run with the help of William David Stockham of the Fruk Group, Department of Chemical Engineering & Biotechnology, Cambridge. A 12% polyacrylamide gel with Tris-boric acid EDTA (TBE) buffer was cast and the samples were run under a DC current for 3 hrs. Following the run, the gel was imaged using a Syngene G:BOX Chemi XX6 System.

5.4.4 Atomic Force Microscopy

All experiments were conducted by Dr Ioanna Mela of the Laser Analytics Group, Department of Chemical Engineering & Biotechnology, Cambridge. 15 μL of the sample were deposited undiluted on freshly cleaved mica and incubated at room temperature for 10 minutes. The samples were then washed three times with 1 mL of Tris-HCl buffer, containing 10mM $MgCl_2$ and imaged using a Bruker Bioscope Resolve AFM. The AFM was operated in Scanasyst mode and the Peakforce setpoint was kept between 150 and 250 pN to avoid damaging the sample. The cantilevers were Scanasyst fluid +, with a nominal spring constant of 0.7 N m^{-1}.

5.5 Results & Discussion

5.5.1 sql Net Realisation

To demonstrate a proof-of-principle, the design for the **sql** net (Appendix C) was realised experimentally with the help of William David Stockham and Dr Ioanna Mela. The strands were combined and diluted to a concentration of 1 µM unit cell and left to anneal under slow cooling over 12 hrs. The assembled nets were then characterised using gel electrophoresis and AFM (Figure 5.8). Gel electrophoresis of the samples shows that a new product has formed, which is substantially larger than any other species. Additionally, there was no substantial evidence for unhybridised, constituent strands in the product, suggesting that hybridisation has taken effect.

AFM results of the samples show that in at least one batch, a roughly 150 x 150 nm patch with the correct topology has formed (Figure 5.8 b.). Unfortunately, so far no larger areas were found, but the existence of at least a small patch proves that the programmed topology can be realised experimentally. It remains to be seen whether larger areas can be produced from the same strands by optimising the hybridisation protocol.

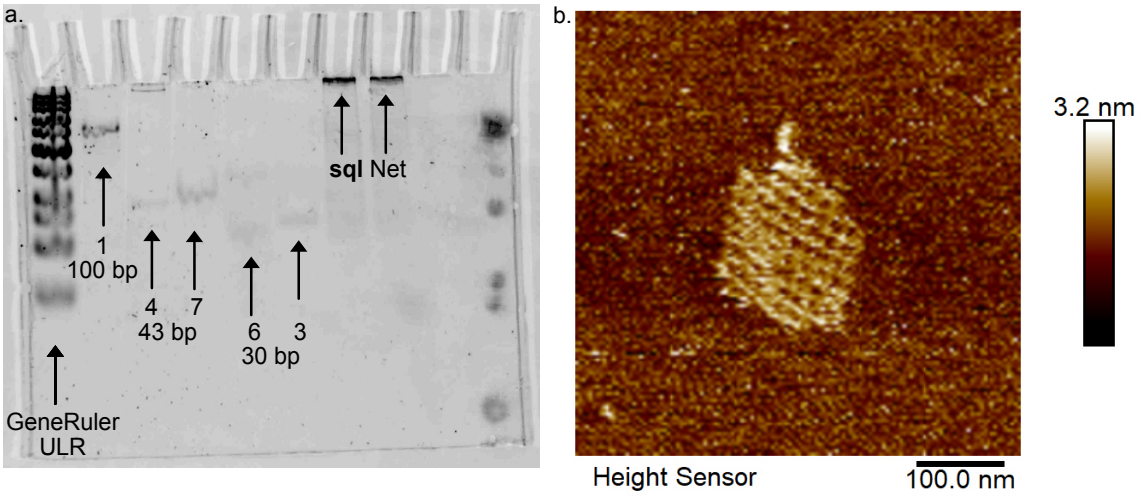

Fig. 5.8 Towards experimental **sql** Nets | a. Imaged gel. The strand identifier and corresponding lengths are shown under each band. Note that in the **sql** net samples, the band hardly moved, suggesting that a large assembly has moved. No significant amounts of the constituent strands were found in the **sql** sample either. b. AFM micrograph of the **sql** net (Dr Ioanna Mela, Laser Analytics Group, Department of Chemical Engineering & Biotechnology, Cambridge). Albeit being a small patch, the square lattice topology is clearly visible, affirming that the design yields the desired net topology.

5.6 Conclusion & Outlook

The principles laid out in this chapter connect MOF chemistry and DNA crystal designs but many experimental and potentially mathematical findings are further required to strengthen this association. RCD has been introduced as an extension of the familiar reticular chemistry strategy and a possible realisation of this protocol has been implemented for the **sql** and **fes** nets, with experimental results for **sql**. Whilst no large scale areas 2D DNA frameworks were found, a proof-of-principle was obtained in the form of a small patch featuring an **sql** topology.

In the following outlook, some questions that need to be addressed scientifically, and potential applications of RCD are raised.

5.6.1 Scope & Experiments

The principle of RCD should extend to all nets, both in 2D and in 3D. As shown in Section 5.5, for experimental efforts on this project it was easy to commence with 2D nets, as they are readily characterised by AFM. For the already obtained **sql** net, it would be important to study whether the hybridisation process can be optimised to yield larger areas. Multiple experiments may be performed to improve the yield of larger arrays, which bear a striking resemblance to MOF synthesis techniques: (i) an extended folding protocol achieved by slower negative temperature ramping over more incremental steps and a for a longer period of time may lead to greater reversibility in the hybridisation step and to improved shape yield for larger arrays; (ii) reducing the concentration of the oligonucleotide strands could reduce the number of nucleation events. This would consequently lead to the formation of fewer patches which in turn would be larger. (iii) It could even be considered to study whether a competing monohaptic oligonucleotide could act like a modulator like the acetic acid of Chapter 2. Additionally, (iv) it has been shown for 2D structures directed growth on silica greatly improves the shape yield [250]. It should be noted here to suggested experiments (i)-(iii) above all aim to reduce the growth kinetics and achieve greater reversibility during the hybridisation. This is based on the assumption that a fully hybridised, geometrically satisfied larger array is thermodynamically more favourable than multiple smaller, misfolded patches. Computational studies using for instance the coarse-grain oxDNA simulation platform may be of help here to challenge this assumption, and check, if any particular sequences or lengths of sticky-ends are particularly favourable [132]. Additionally, oxDNA could be used analyse whether the corrugation strategy improves or worsens the geometric frustration of a 2D net.

Once larger areas are obtained, the next logical step would be to create an **fes** net, specifically using identical terminal (North, West, South, East) strands from the **sql** design.

Another set of easy experiments would be to introduce a linear DX tile that acts as a spacer between the star motifs to realise an isoreticular expansion. It is also possible to combine the realisations of isoreticular expansion and augmentation. The linear DX tile could sit as a spacer either inside the smaller ring, creating larger 4-point star-motifs as seen in Figure 5.7, or between the star-motifs leading to larger 8-node circles. These expansions also do not necessarily have to be isotropic and can occur along one dimension alone, breaking the 4-fold rotational symmetry of the DNAF whilst preserving the original topology.

Next, TIAMAT designs for the kagome net (**kgm**) and the honeycomb net (**hcb**), their respective isoreticular expansions and augmentations could be easily derived. It should be noted here that a corrugation strategy is not possible for **kgm** nets because corrugation requires even ring sizes [253].

Characterisation in 3D could be more challenging. Should 3D assemblies be crystalline and diffract, scattering techniques can probe the structure with atomic precision.

While all the designs mentioned above pertain to relatively small DNA nanostructures, it would be interesting to expand the principles of RCD to DNA metamaterials, such as assemblies of larger DNA origamis. The bottom-up construction of nanomaterials on the micrometer scale presents a challenge, that could be addressed by RCD. In this sense, RCD could be used to organise nanoparticles into pre-determined structures, similar to the nanoparticle crystals by Mirkin [254] and Sleiman [255] with applications as photonic sensors.

5.6.2 Combinatorics, Flexibility, Stoichiometry, and Symmetry

A fundamental part this project is the interplay between combinatorics and symmetry. Combinatorically set interactions between DNA sticky-ends are crucial for the success of DNA nanotechnology, but they imply uniqueness between interactions which will be eliminated under symmetry.

The forced assembly of certain ring sizes as laid out in Section 5.3 for instance can fail and yield helical structures that have the same adjacency matrix instead. Stoichiometry could also prove to be a crucial factor: if the number of constituent strands is small, sequences might have a greater tendency to close onto themselves to form rings rather than continue to grow and form helical domains. Another example is that planar RCD designs could fold up onto themselves by bending in the third dimension, as is sometimes observed [250]. It would be interesting to see if such bends could be avoided in 3D crystals due to the geometric constrains.

The only answer to these kinds of malformation issues might be to have more rigid motifs. In that case it would be interesting to study how much flexibility the system could tolerate

and under which conditions periodic arrays form. Rigidity and geometric constrains might also be able to mitigate other topological effects which are not subject to connectivity, such as weaving, knots, and interpenetration of nets.

Chapter 6

Final Conclusions

At the end of this dissertation, attention is again directed to the triangular relationship of *frameworks – surfaces – self-assembly*. The three projects that make up this thesis are herein briefly recounted as well as their main achievements and how they fit together. In the first project, MOF-composites were synthesised and their photophysical properties were investigated. The physical calculation of this composite sparked a wider study on surface area calculations in porosimetry, which lead to the development of the BETSI algorithm. Finally, the observation of some polymorphic phases in the first project started a discussion about framework design from graph theory and some parallels were drawn to DNA nanotechnology and the possible use of the reticular design principle in this field.

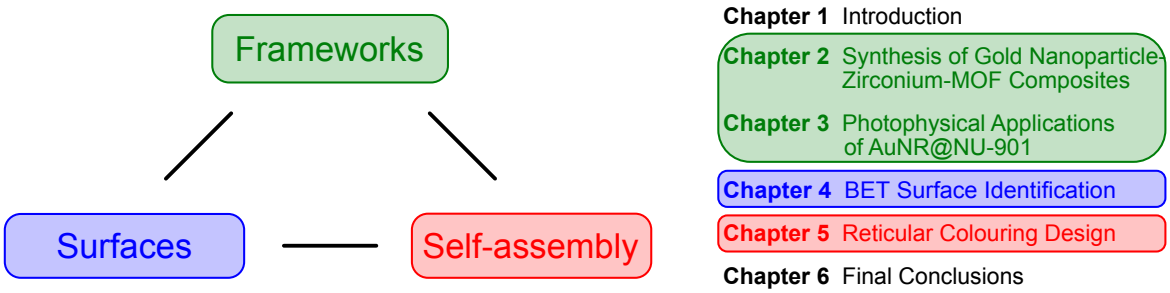

Fig. 6.1 Conclusion of Dissertation | The triangular relationship between frameworks, surfaces and self-assembly and the dissertation's projects.

6.1 Frameworks | Metal-organic Framework Composites

In this project, MOFs were introduced as prototypical frameworks – porous materials that are self-assembled from metal atom clusters and organic linkers. The Zr-MOF NU-901 was grown around plasmonic AuNRs to yield the AuNR@NU-901 core-shell composites. The challenging assembly of this material was made possible by choosing a suitable pair of MOF and AuNR surface ligands whose favourable interactions would cause the MOF to nucleate on the AuNRs. The synthesis was further optimised extensively, resulting in an outstanding core-shell morphology yield and robust size-control over the resulting composite crystallites; however, attempts to generalise the procedure to other MOFs were so far unsuccessful.

The following photophysical applications of the plasmonic moiety were explored next. For the first application, plasmonic photothermal therapy, it was hypothesised that the large pore size and surface area of the NU-901 can be exploited in tandem with the photothermal energy conversion of AuNRs. The aim was to adsorb drug molecules onto the MOF and release them from an external photothermal stimulus. The poor stability of the AuNR@NU-901 in phosphate-containing media, however, raised concerns over their practical use as a drug delivery vehicles. To move this project forward, it would be advisable to go back to synthesis stage of Chapter 2 and explore the stabilisation of MOFs through PEG-layers on the external surface of the crystallites.

In the next potential optical application, surface-enhanced Raman spectroscopy, the AuNR@NU-901 is used as a size-selective molecular filter which gates the access of small molecules to the AuNR optical 'antenna' inside the core-shell composite. In this proof-of-principle study, size-selective SERS sensing was achieved, making AuNR@NU-901 a potentially viable candidate for pollutant sensing or else. The large size of NU-901's pores however do limit size-exclusion to extremely large molecules. The development of an AuNR@UiO-66 composite, with a much smaller pore size, would be therefore be of great

interest. This synthetic target was actively pursued both by the author and undergraduate students under his supervision, but the synthesis has proved difficult.

6.2 Surfaces | BET Theory and Adsorption

This chapter investigated how surface-areas are quantified from gas adsorption isotherms. The fundamentals of the BET adsorption model were reviewed and contextualised in a modern way with modern adsorbents. It was assumed that the Rouquerol criteria that guide scientists in choosing a suitable BET fitting range were (i) indeterminate and (ii) too cumbersome to practically implement, resulting in reproducibility concerns of BET areas *from the same isotherm*.

Thus, a major round-robin evaluation was launched in which over 115 international collaborators were sent 18 anonymised isotherms with the instructions to calculate the BET area in the way they saw most fit. The astonishing spread of results that was returned cemented the reproducibility concerns, and in response an algorithmic approach called BET Surface Identification (BETSI) based on the Rouquerol criteria was developed by the author. On the same dataset, BETSI produced a much narrower range than that obtained by manual calculations. While the presence of a range affirmed that the Rouquerol criteria are indeterminate, it also proved that most researchers struggled with their implementation. BETSI was further developed to make an unambiguous assignment of the BET area from the isotherm possible.

The introduction of BETSI to the community of framework chemists presents a great step towards more transparency in BET area determinations. However, in this study only the tip of the iceberg has been explored.

6.3 Self-assembly | Reticular Chemistry and DNA Crystals

In this project, the author connects the dots between MOF chemistry and DNA nanotechnology, two areas of science that have been previously unconnected and that can benefit from one another greatly.

Extending on the well-known reticular design principle for rigid framework assemblies, the author figuratively adds colour to the process, by abstracting base complementarity of sticky-ends as a network colouring. The design principle that emerges from this abstraction, reticular colouring design (RCD), is a unifying and binding narrative for both MOF design and a novel class of porous DNA crystal called a DNA framework.

RCD streamlines and greatly simplifies the designs of novel DNA crystals which could be used for in multiple biomedical and nanotechnological applications. The principles that were outlined here on a relatively straightforward square-lattice net are universally applicable and can be used to build arbitrary nets of arbitrary complexity and beauty.

The triangular relationship *frameworks – surfaces – self-assembly* has appeared throughout this dissertation and my academic career at Cambridge. It has blessed me with an unconventionally multipolar PhD with interdisciplinary research and outside-the-box inspirations at the forefront. I hope that my work has made a small contribution academic research and society and remain optimistic about its future progress.

References

[1] Susumu Kitagawa, Ryo Kitaura, and Shin Ichiro Noro. Functional porous coordination polymers. *Angewandte Chemie - International Edition*, 43(18):2334–2375, 2004.

[2] Omar M Yaghi, Michael O'Keeffe, Nathan W Ockwig, Hee K Chae, Mohamed Eddaoudi, and Jaheon Kim. Reticular synthesis and the design of new materials. *Nature*, 423(6941):705–714, 2003.

[3] Hiroyasu Furukawa, Kyle E Cordova, M. O'Keeffe, and Omar M Yaghi. The Chemistry and Applications of Metal-Organic Frameworks. *Science*, 341(6149):1230444–1230444, 2013.

[4] Hong Cai Zhou, Jeffrey R. Long, and Omar M. Yaghi. Introduction to metal-organic frameworks. *Chemical Reviews*, 112(2):673–674, 2012.

[5] Omar M. Yaghi. Reticular Chemistry - Construction, Properties, and Precision Reactions of Frameworks. *Journal of the American Chemical Society*, 138(48):15507–15509, 2016.

[6] Pia Vervoorts, Andreas Schneemann, Inke Hante, Jenny Pirillo, Yuh Hijikata, Takashi Toyao, Kenichi Kon, Ken Ichi Shimizu, Takayoshi Nakamura, Shin Ichiro Noro, and Roland A. Fischer. Coordinated Water as New Binding Sites for the Separation of Light Hydrocarbons in Metal-Organic Frameworks with Open Metal Sites. *ACS Applied Materials and Interfaces*, 12(8):9448–9456, 2020.

[7] Hallian Li, Mohamed Eddaoudi, M. O'Keeffe, and O. M. Yaghi. Design and synthesis of an exceptionally stable and highly porous metal-organic framework. *Nature*, 402(6759):276–279, 1999.

[8] G Ferey. A Chromium Terephthalate-Based Solid with Unusually Large Pore Volumes and Surface Area. *Science*, 309(5743):2040–2042, 2005.

[9] Stephen S.-Y. Chui. A Chemically Functionalizable Nanoporous Material [Cu3(TMA)2(H2O)3]n. *Science*, 283(5405):1148–1150, 1999.

[10] Sung Ha Park, Constantin Pistol, Sang Jung Ahn, John H. Reif, Alvin R. Lebeck, Chris Dwyer, and Thomas H. LaBean. Finite-size, fully addressable DNA tile lattices formed by hierarchical assembly procedures. *Angewandte Chemie - International Edition*, 45(5):735–739, 2006.

[11] Peyman Z. Moghadam, Aurelia Li, Seth B. Wiggin, Andi Tao, Andrew G.P. Maloney, Peter A. Wood, Suzanna C. Ward, and David Fairen-Jimenez. Development of a Cambridge Structural Database Subset: A Collection of Metal-Organic Frameworks for Past, Present, and Future. *Chemistry of Materials*, 29(7):2618–2625, 2017.

[12] Jie Peng Zhang, Yue Biao Zhang, Jian Bin Lin, and Xiao Ming Chen. Metal azolate frameworks: From crystal engineering to functional materials. *Chemical Reviews*, 112(2):1001–1033, 2012.

[13] Kevin J. Gagnon, Houston P. Perry, and Abraham Clearfield. Conventional and unconventional metal-organic frameworks based on phosphonate ligands: MOFs and UMOFs. *Chemical Reviews*, 112(2):1034–1054, 2012.

[14] Norbert Stock and Shyam Biswas. Synthesis of Metal-Organic Frameworks (MOFs): Routes to Various Topologies, Morphologies, and Composites. *Chemical Reviews*, 112:933–969, 2012.

[15] Ivo Stassen, Mark Styles, Gianluca Grenci, Hans Van Gorp, Willem Vanderlinden, Steven De Feyter, Paolo Falcaro, Dirk De Vos, Philippe Vereecken, and Rob Ameloot. Chemical vapour deposition of zeolitic imidazolate framework thin films. *Nature Materials*, 15(3):304–310, 2016.

[16] Christian S. Diercks and Omar M. Yaghi. The atom, the molecule, and the covalent organic framework. *Science*, 355(6328), 2017.

[17] Michael O'Keeffe, Maxim A Peskov, Stuart J Ramsden, and Omar M Yaghi. The Reticular Chemistry Structure Resource (RCSR) Database of , and Symbols for , Crystal Nets. *Accounts of Chemical Research*, 41(12):1782–1789, 2008.

[18] Mohamed Eddaoudi, Jaheon Kim, Nathaniel Rosi, David Vodak, Joseph Wachter, Michael O'Keeffe, and Omar M. Yaghi. Systematic design of pore size and functionality in isoreticular MOFs and their application in methane storage. *Science*, 295(5554):469–472, 2002.

[19] Jonathan Y.S. Leung, Bayden D. Russell, and Sean D. Connell. Special report: global warming of 1.5°C. *IPCC*, 1(3):374–381, 2019.

[20] Kenji Sumida, David L. Rogow, Jarad A. Mason, Thomas M. McDonald, Eric D. Bloch, Zoey R. Herm, Tae Hyun Bae, and Jeffrey R. Long. Carbon dioxide capture in metal-organic frameworks. *Chemical Reviews*, 112(2):724–781, 2012.

[21] Myunghyun Paik Suh, Hye Jeong Park, Thazhe Kootteri Prasad, and Dae Woon Lim. Hydrogen storage in metal-organic frameworks. *Chemical Reviews*, 112(2):782–835, 2012.

[22] Rachel B. Getman, Youn Sang Bae, Christopher E. Wilmer, and Randall Q. Snurr. Review and analysis of molecular simulations of methane, hydrogen, and acetylene storage in metal-organic frameworks. *Chemical Reviews*, 112(2):703–723, 2012.

[23] Haohan Wu, Qihan Gong, David H. Olson, and Jing Li. Commensurate adsorption of hydrocarbons and alcohols in microporous metal organic frameworks. *Chemical Reviews*, 112(2):836–868, 2012.

[24] Tian Tian, Zhixin Zeng, Diana Vulpe, Mirian E. Casco, Giorgio Divitini, Paul A. Midgley, Joaquin Silvestre-Albero, Jin Chong Tan, Peyman Z. Moghadam, and David Fairen-Jimenez. A sol-gel monolithic metal-organic framework with enhanced methane uptake. *Nature Materials*, 17(2):174–179, 2018.

[25] Mohammed Kadhom and Baolin Deng. Metal-organic frameworks (MOFs) in water filtration membranes for desalination and other applications. *Applied Materials Today*, 11:219–230, 2018.

[26] Marta Mon, Rosaria Bruno, Jesus Ferrando-Soria, Donatella Armentano, and Emilio Pardo. Metal-organic framework technologies for water remediation: Towards a sustainable ecosystem. *Journal of Materials Chemistry A*, 6(12):4912–4947, 2018.

[27] Jeongyong Lee, Omar K. Farha, John Roberts, Karl A. Scheidt, Sonbinh T. Nguyen, and Joseph T. Hupp. Metal-organic framework materials as catalysts. *Chemical Society Reviews*, 38(5):1450–1459, 2009.

[28] Pengfei Ji, Xuanyu Feng, Pau Oliveres, Zhe Li, Akiko Murakami, Cheng Wang, and Wenbin Lin. Strongly Lewis Acidic Metal-Organic Frameworks for Continuous Flow Catalysis. *Journal of the American Chemical Society*, 141(37):14878–14888, 2019.

[29] Vlad Pascanu, Greco González Miera, A. Ken Inge, and Belén Martín-Matute. Metal-Organic Frameworks as Catalysts for Organic Synthesis: A Critical Perspective. *Journal of the American Chemical Society*, 141(18):7223–7234, 2019.

[30] Lauren E Kreno, Kirsty Leong, Omar K Farha, Mark Allendorf, Richard P Van Duyne, and Joseph T Hupp. Metal-Organic Framework Materials as Chemical Sensors. *Chemical Reviews*, 112:1105 – 1125, 2012.

[31] Sophie E Miller, Michelle H Teplensky, Peyman Z Moghadam, and David Fairen-Jimenez. Metal-organic frameworks as biosensors for luminescence-based detection and imaging. *Interface Focus*, 6(4):20160027, 2016.

[32] Patricia Horcajada, Ruxandra Gref, Tarek Baati, Phoebe K. Allan, Guillaume Maurin, Patrick Couvreur, Gérard Férey, Russell E. Morris, and Christian Serre. Metal-organic frameworks in biomedicine. *Chemical Reviews*, 112(2):1232–1268, feb 2012.

[33] Elena Bellido, Tania Hidalgo, Maria Victoria Lozano, Mazheva Guillevic, Rosana Simón-Vázquez, Manuel J. Santander-Ortega, África González-Fernández, Christian Serre, Maria J. Alonso, and Patricia Horcajada. Heparin-Engineered Mesoporous Iron Metal-Organic Framework Nanoparticles: Toward Stealth Drug Nanocarriers. *Advanced Healthcare Materials*, 4(8):1246–1257, 2015.

[34] Patricia Horcajada, Christian Serre, María Vallet-Regí, Muriel Sebban, Francis Taulelle, and Gérard Férey. Metal-organic frameworks as efficient materials for drug delivery. *Angewandte Chemie - International Edition*, 45(36):5974–5978, 2006.

[35] Claudia Orellana-Tavra, Ross J. Marshall, Emma F. Baxter, Isabel Abánades Lázaro, Andi Tao, Anthony K. Cheetham, Ross S. Forgan, and David Fairen-Jimenez. Drug delivery and controlled release from biocompatible metal–organic frameworks using mechanical amorphization. *J. Mater. Chem. B*, 4(47):7697–7707, 2016.

[36] Claudia Orellana-Tavra, Emma F. Baxter, Tian Tian, Thomas D. Bennett, Nigel K. H. Slater, Anthony K. Cheetham, and David Fairen-Jimenez. Amorphous metal–organic frameworks for drug delivery. *Chem. Commun.*, 51(73):13878–13881, 2015.

[37] Michelle H. Teplensky, Marcus Fantham, Peng Li, Timothy C. Wang, Joshua P. Mehta, Laurence J. Young, Peyman Z. Moghadam, Joseph T. Hupp, Omar K. Farha, Clemens F. Kaminski, and David Fairen-Jimenez. Temperature Treatment of Highly Porous Zirconium-Containing Metal-Organic Frameworks Extends Drug Delivery Release. *Journal of the American Chemical Society*, 139(22):7522–7532, 2017.

[38] Raffaele Ricco, Constance Pfeiffer, Kenji Sumida, Christopher J. Sumby, Paolo Falcaro, Shuhei Furukawa, Neil R. Champness, and Christian J. Doonan. Emerging applications of metal-organic frameworks. *CrystEngComm*, 18(35):6532–6542, 2016.

[39] Dmitri V. Talapin and Elena V. Shevchenko. Introduction: Nanoparticle chemistry. *Chemical Reviews*, 116(18):10343–10345, 2016.

[40] Thomas L. Moore, Laura Rodriguez-Lorenzo, Vera Hirsch, Sandor Balog, Dominic Urban, Corinne Jud, Barbara Rothen-Rutishauser, Marco Lattuada, and Alke Petri-Fink. Nanoparticle colloidal stability in cell culture media and impact on cellular interactions. *Chemical Society Reviews*, 44(17):6287–6305, 2015.

[41] Nguyen T.K. Thanh, N. Maclean, and S. Mahiddine. Mechanisms of nucleation and growth of nanoparticles in solution. *Chemical Reviews*, 114(15):7610–7630, 2014.

[42] Teri Odom and George Schatz. Introduction to plasmonics. *Chemical Reviews*, 111:3667–3668, 2011.

[43] Floris Dekker, Lars Kool, Anton Bunschoten, Aldrik H. Velders, and Vittorio Saggiomo. Syntheses of gold and silver dichroic nanoparticles; looking at the Lycurgus cup colors. *Chemistry Teacher International*, 0(0):1–6, 2020.

[44] Gustav Mie. Beitraege zur Optik trueber Medien, speziell kolloidaler Metalloesungen. *Annalen der Physik*, 330(3):377–445, 1908.

[45] Tigran V. Shahbazyan and Mark I. Stockman. *Plasmonics: Theory and applications*. Springer, 2013.

[46] Sujit Kumar Ghosh and Tarasankar Pal. Interparticle coupling effect on the surface plasmon resonance of gold nanoparticles: From theory to applications. *Chemical Reviews*, 107(11):4797–4862, 2007.

[47] Craig F. Bohren and Donald R. Huffman. *Absorption and scattering of light by small particles*. Wiley, 1983.

[48] Ian Freestone, Nigel Meeks, Margaret Sax, and Catherine Higgit. The Lycrugus Cup - A Roman Nanotechnology. *Gold Bulletin*, 40(4):270–277, 2007.

[49] Gregory V. Hartland. Optical studies of dynamics in noble metal nanostructures. *Chemical Reviews*, 111(6):3858–3887, 2011.

[50] Qi-Long Zhu and Qiang Xu. Metal–organic framework composites. *Chem. Soc. Rev.*, 43(16):5468–5512, 2014.

[51] Paolo Falcaro, Raffaele Ricco, Amirali Yazdi, Inhar Imaz, Shuhei Furukawa, Daniel Maspoch, Rob Ameloot, Jack D. Evans, and Christian J. Doonan. Application of metal and metal oxide nanoparticles@MOFs. *Coordination Chemistry Reviews*, 307:237–254, 2016.

[52] Qihao Yang, Qiang Xu, and Hai Long Jiang. Metal-organic frameworks meet metal nanoparticles: Synergistic effect for enhanced catalysis. *Chemical Society Reviews*, 46(15):4774–4808, 2017.

[53] Mark Kalaj, Kyle C. Bentz, Sergio Ayala, Joseph M. Palomba, Kyle S. Barcus, Yuji Katayama, and Seth M. Cohen. MOF-Polymer Hybrid Materials: From Simple Composites to Tailored Architectures. *Chemical Reviews*, 2020.

[54] Jordi Aguilera-Sigalat and Darren Bradshaw. Synthesis and applications of metal-organic framework-quantum dot (QD at MOF) composites. *Coordination Chemistry Reviews*, 307:267–291, 2016.

[55] Lars Heinke and Christof Wöll. Surface-Mounted Metal–Organic Frameworks: Crystalline and Porous Molecular Assemblies for Fundamental Insights and Advanced Applications. *Advanced Materials*, 31(26), 2019.

[56] Jingwei Hou, Christopher W. Ashling, Sean M. Collins, Andraž Krajnc, Chao Zhou, Louis Longley, Duncan N. Johnstone, Philip A. Chater, Shichun Li, Marie Vanessa Coulet, Philip L. Llewellyn, François Xavier Coudert, David A. Keen, Paul A. Midgley, Gregor Mali, Vicki Chen, and Thomas D. Bennett. Metal-organic framework crystal-glass composites. *Nature Communications*, 10(1):1–10, 2019.

[57] Xizhen Lian, Yu Fang, Elizabeth Joseph, Qi Wang, Jialuo Li, Sayan Banerjee, Christina Lollar, Xuan Wang, and Hong Cai Zhou. Enzyme-MOF (metal-organic framework) composites. *Chemical Society Reviews*, 46(11):3386–3401, 2017.

[58] Ning Yuan, Xinling Zhang, and Longsheng Wang. The marriage of metal–organic frameworks and silica materials for advanced applications. *Coordination Chemistry Reviews*, 421:213442, 2020.

[59] Christoph Rösler and Roland A. Fischer. Metal-organic frameworks as hosts for nanoparticles. *CrystEngComm*, 17(2):199–217, 2015.

[60] Jack D. Evans, Christopher J. Sumby, and Christian J. Doonan. Post-synthetic metalation of metal-organic frameworks. *Chemical Society Reviews*, 43(16):5933–5951, 2014.

[61] M. Samy El-Shall, Victor Abdelsayed, Abd El Rahman S. Khder, Hassan M.A. Hassan, Hani M. El-Kaderi, and Thomas E. Reich. Metallic and bimetallic nanocatalysts incorporated into highly porous coordination polymer MIL-101. *Journal of Materials Chemistry*, 19(41):7625–7631, 2009.

[62] Renbing Wu, Xukun Qian, Kun Zhou, Hai Liu, Boluo Yadian, Jun Wei, Hongwei Zhu, and Yizhong Huang. Highly dispersed Au nanoparticles immobilized on Zr-based metal–organic frameworks as heterostructured catalyst for CO oxidation. *Journal of Materials Chemistry A*, 1(45):14294, 2013.

[63] Hoi Ri Moon, Dae-Woon Lim, and Myunghyun Paik Suh. Fabrication of metal nanoparticles in metal–organic frameworks. *Chem. Soc. Rev.*, 42(4):1807–1824, 2013.

[64] Guang Lu, Shaozhou Li, Zhen Guo, Omar K. Farha, Brad G. Hauser, Xiaoying Qi, Yi Wang, Xin Wang, Sanyang Han, Xiaogang Liu, Joseph S. DuChene, Hua Zhang, Qichun Zhang, Xiaodong Chen, Jan Ma, Say Chye Joachim Loo, Wei D. Wei, Yanhui Yang, Joseph T. Hupp, and Fengwei Huo. Imparting functionality to a metal–organic framework material by controlled nanoparticle encapsulation. *Nature Chemistry*, 4(4):310–316, 2012.

[65] Liyu Chen and Qiang Xu. Metal-Organic Framework Composites for Catalysis. *Matter*, 1(1):57–89, 2019.

[66] Pei Zhou Li, Kengo Aranishi, and Qiang Xu. ZIF-8 immobilized nickel nanoparticles: Highly effective catalysts for hydrogen generation from hydrolysis of ammonia borane. *Chemical Communications*, 48(26):3173–3175, 2012.

[67] Michal Sabo, Antje Henschel, Heidrun Fröde, Elias Klemm, and Stefan Kaskel. Solution infiltration of palladium into MOF-5: Synthesis, physisorption and catalytic properties. *Journal of Materials Chemistry*, 17(36):3827–3832, 2007.

[68] Abdelmalek Malouche, Claudia Zlotea, and Petra Ágota Szilágyi. Interactions of Hydrogen with Pd@MOF Composites. *ChemPhysChem*, 20(10):1282–1295, 2019.

[69] Serhiy M. Luzan and A. V. Talyzin. Hydrogen adsorption in Pt catalyst/MOF-5 materials. *Microporous and Mesoporous Materials*, 135(1-3):201–205, 2010.

[70] R. Prins. Hydrogen spillover. Facts and fiction. *Chemical Reviews*, 112(5):2714–2738, 2012.

[71] Matthias Thommes, Katsumi Kaneko, Alexander V. Neimark, James P. Olivier, Francisco Rodriguez-Reinoso, Jean Rouquerol, and Kenneth S.W. Sing. Physisorption of gases, with special reference to the evaluation of surface area and pore size distribution (IUPAC Technical Report). *Pure and Applied Chemistry*, 87(9-10):1051–1069, 2015.

[72] K. S.W. Sing, D. H. Everett, R. A.W. Haul, L. Moscou, R. A. Pierotti, J. Rouquerol, and T. Siemieniewska. Reporting Physisorption Data for Gas/Solid Systems with Special Reference to the Determination of Surface Area and Porosity. *Pure and Applied Chemistry*, 57(4):603–619, 1985.

[73] Jean Rouquerol, Françoise Rouquerol, Philip Llewellyn, Guillaume Maurin, and Kenneth S.W. Sing. *Adsorption by Powders and Porous Solids: Principles, Methodology and Applications: Second Edition*. Academic Press, 2013.

[74] K. S.W. Sing, D. H. Everett, R. A.W. Haul, L. Moscou, R. A. Pierotti, J. Rouquerol, and T. Siemieniewska. Reporting Physisorption Data for Gas/Solid Systems with Special Reference to the Determination of Surface Area and Porosity. *Pure and Applied Chemistry*, 57(4):603–619, 1985.

[75] Christian Eggeling, Katrin I. Willig, Steffen J. Sahl, and Stefan W. Hell. Lens-based fluorescence nanoscopy. *Quarterly Reviews of Biophysics*, 48(02):178–243, 2015.

[76] Jasmina Hafizovic Cavka, Søren Jakobsen, Unni Olsbye, Nathalie Guillou, Carlo Lamberti, Silvia Bordiga, and Karl Petter Lillerud. A new zirconium inorganic building brick forming metal organic frameworks with exceptional stability. *Journal of the American Chemical Society*, 130(42):13850–13851, 2008.

[77] Yan Bai, Yibo Dou, Lin-Hua Xie, William Rutledge, Jian-Rong Li, and Hong-Cai Zhou. Zr-based metal–organic frameworks: design, synthesis, structure, and applications. *Chem. Soc. Rev.*, 45(8):2327–2367, 2016.

[78] Tyler G. Grissom, Darren M. Driscoll, Diego Troya, Nicholas S. Sapienza, Pavel M. Usov, Amanda J. Morris, and John R. Morris. Molecular-Level Insight into CO2 Adsorption on the Zirconium-Based Metal-Organic Framework, UiO-66: A Combined Spectroscopic and Computational Approach. *Journal of Physical Chemistry C*, 123(22):13731–13738, 2019.

[79] Amarajothi Dhakshinamoorthy, Andrea Santiago-Portillo, Abdullah M. Asiri, and Hermenegildo Garcia. Engineering UiO-66 Metal Organic Framework for Heterogeneous Catalysis. *ChemCatChem*, 11(3):899–923, 2019.

[80] Ahmed Shahat, Hassan M.A. Hassan, and Hassan M.E. Azzazy. Optical metal-organic framework sensor for selective discrimination of some toxic metal ions in water. *Analytica Chimica Acta*, 793:90–98, 2013.

[81] Shenghao Wang, Luis K. Ono, Matthew R. Leyden, Yuichi Kato, Sonia R. Raga, Michael Vernon Lee, and Yabing Qi. Smooth perovskite thin films and efficient perovskite solar cells prepared by the hybrid deposition method. *J. Mater. Chem. A*, 3(5):14631–14641, 2015.

[82] Claudia Orellana-Tavra, Salame Haddad, Ross J. Marshall, Isabel Abánades Lázaro, Gerard Boix, Inhar Imaz, Daniel Maspoch, Ross S. Forgan, and David Fairen-Jimenez. Tuning the Endocytosis Mechanism of Zr-Based Metal-Organic Frameworks through Linker Functionalization. *ACS Applied Materials and Interfaces*, 9(41):35516–35525, 2017.

[83] Michael J Katz, Zachary J Brown, Yamil J Colón, Paul W Siu, Karl A Scheidt, Randall Q Snurr, Joseph T Hupp, and Omar K Farha. A facile synthesis of UiO-66, UiO-67 and their derivatives. *Chemical Communications*, 49(82):9449, 2013.

[84] Karen Tulig and Krista S Walton. An alternative UiO-66 synthesis for HCl-sensitive nanoparticle encapsulation. *RSC Advances*, 4(93):51080–51083, 2014.

[85] Andreas Schaate, Pascal Roy, Adelheid Godt, Jann Lippke, Florian Waltz, Michael Wiebcke, and Peter Behrens. Modulated synthesis of Zr-based metal-organic frameworks: From nano to single crystals. *Chemistry - A European Journal*, 17(24):6643–6651, 2011.

[86] William Morris, Shunzhi Wang, David Cho, Evelyn Auyeung, Peng Li, Omar K. Farha, and Chad A. Mirkin. Role of modulators in controlling the colloidal stability and polydispersity of the UiO-66 metal-organic framework. *ACS Applied Materials and Interfaces*, 9(39):33413–33418, 2017.

[87] Matthew J. Cliffe, Joshua A. Hill, Claire A. Murray, François Xavier Coudert, and Andrew L. Goodwin. Defect-dependent colossal negative thermal expansion in UiO-66(Hf) metal-organic framework. *Physical Chemistry Chemical Physics*, 17(17):11586–11592, 2015.

[88] Ross S. Forgan. Modulated self-assembly of metal-organic frameworks. *Chemical Science*, 11(18):4546–4562, 2020.

[89] Matthew R. DeStefano, Timur Islamoglu, Sergio J Garibay, Joseph T Hupp, and Omar K Farha. Room-Temperature Synthesis of UiO-66 and Thermal Modulation of Densities of Defect Sites. *Chemistry of Materials*, 29(3):1357–1361, 2017.

[90] Krunoslav Užarević, Timothy C. Wang, Su Young Moon, Athena M. Fidelli, Joseph T. Hupp, Omar K. Farha, and Tomislav Friščić. Mechanochemical and solvent-free assembly of zirconium-based metal-organic frameworks. *Chemical Communications*, 52(10):2133–2136, 2016.

[91] Joseph E Mondloch, Wojciech Bury, David Fairen-Jimenez, Stephanie Kwon, Erica J Demarco, Mitchell H Weston, Amy A Sarjeant, Sonbinh T Nguyen, Peter C Stair, Randall Q Snurr, Omar K Farha, and Joseph T Hupp. Vapor-phase metalation by atomic layer deposition in a metal-organic framework. *Journal of the American Chemical Society*, 135(28):10294–10297, 2013.

[92] Chung Wei Kung, Timothy Chiaan Wang, Joseph E Mondloch, David Fairen-Jimenez, Daniel M Gardner, Wojciech Bury, Jordan Matthew Klingsporn, Jonathan C Barnes, Richard Van Duyne, J Fraser Stoddart, Michael R Wasielewski, Omar K Farha, and Joseph T Hupp. Metal-organic framework thin films composed of free-standing acicular nanorods exhibiting reversible electrochromism. *Chemistry of Materials*, 25(24):5012–5017, 2013.

[93] Joseph E. Mondloch, Michael J. Katz, William C. Isley, Pritha Ghosh, Peilin Liao, Wojciech Bury, George W. Wagner, Morgan G. Hall, Jared B. Decoste, Gregory W. Peterson, Randall Q. Snurr, Christopher J. Cramer, Joseph T. Hupp, and Omar K. Farha. Destruction of chemical warfare agents using metal-organic frameworks. *Nature Materials*, 14(5):512–516, 2015.

[94] Jianyu Li and David J. Mooney. Designing hydrogels for controlled drug delivery. *Nature Reviews Materials*, 1(12):1–17, 2016.

[95] Yijing Chen, Peng Li, Justin A. Modica, Riki J. Drout, and Omar K. Farha. Acid-Resistant Mesoporous Metal-Organic Framework toward Oral Insulin Delivery: Protein Encapsulation, Protection, and Release. *Journal of the American Chemical Society*, 140(17):5678–5681, 2018.

[96] Michelle H. Teplensky, Marcus Fantham, Chetan Poudel, Colin Hockings, Meng Lu, Alina Guna, Marta Aragones-Anglada, Peyman Z. Moghadam, Peng Li, Omar K. Farha, Sandra Bernaldo de Quirós Fernández, Frances M. Richards, Duncan I. Jodrell, Gabriele Kaminski Schierle, Clemens F. Kaminski, and David Fairen-Jimenez. A Highly Porous Metal-Organic Framework System to Deliver Payloads for Gene Knockdown. *Chem*, 5(11):2926–2941, 2019.

[97] Timur Islamoglu, Ken-ichi Otake, Peng Li, Cassandra T. Buru, Aaron W. Peters, Isil Akpinar, Sergio J. Garibay, and Omar K. Farha. Revisiting the structural homogeneity of NU-1000, a Zr-based metal–organic framework. *CrystEngComm*, 2018.

[98] Wei Guang Liu and Donald G. Truhlar. Computational Linker Design for Highly Crystalline Metal-Organic Framework NU-1000. *Chemistry of Materials*, 29(19):8073–8081, 2017.

[99] Thomas E. Webber, Wei Guang Liu, Sai Puneet Desai, Connie C. Lu, Donald G. Truhlar, and R. Lee Penn. Role of a Modulator in the Synthesis of Phase-Pure NU-1000. *ACS Applied Materials and Interfaces*, 9(45):39342–39346, 2017.

[100] Sergio J. Garibay, Ivan Iordanov, Timur Islamoglu, Jared B. DeCoste, and Omar K. Farha. Synthesis and functionalization of phase-pure NU-901 for enhanced CO2 adsorption: the influence of a zirconium salt and modulator on the topology and phase purity. *CrystEngComm*, 20(44):7066–7070, 2018.

[101] Hyunho Noh, Chung Wei Kung, Timur Islamoglu, Aaron W. Peters, Yijun Liao, Peng Li, Sergio J. Garibay, Xuan Zhang, Matthew R. Destefano, Joseph T. Hupp, and Omar K. Farha. Room Temperature Synthesis of an 8-Connected Zr-Based Metal-Organic Framework for Top-Down Nanoparticle Encapsulation. *Chemistry of Materials*, 30(7):2193–2197, 2018.

[102] Hirak K. Patra, Shuvojit Banerjee, Utpal Chaudhuri, Prabir Lahiri, and Anjan Kr Dasgupta. Cell selective response to gold nanoparticles. *Nanomedicine: Nanotechnology, Biology, and Medicine*, 3(2):111–119, 2007.

[103] Yi Cheun Yeh, Brian Creran, and Vincent M. Rotello. Gold nanoparticles: Preparation, properties, and applications in bionanotechnology. *Nanoscale*, 4(6):1871–1880, 2012.

[104] Manimegalai Sengani, Alexandru Mihai Grumezescu, and V. Devi Rajeswari. Recent trends and methodologies in gold nanoparticle synthesis – A prospective review on drug delivery aspect. *OpenNano*, 2(July):37–46, 2017.

[105] Carla Daruich De Souza, Beatriz Ribeiro Nogueira, and Maria Elisa C.M. Rostelato. Review of the methodologies used in the synthesis gold nanoparticles by chemical reduction. *Journal of Alloys and Compounds*, 798:714–740, 2019.

[106] Petr Suchomel, Libor Kvitek, Robert Prucek, Ales Panacek, Avik Halder, Stefan Vajda, and Radek Zboril. Simple size-controlled synthesis of Au nanoparticles and their size-dependent catalytic activity. *Scientific Reports*, 8(1):1–11, 2018.

[107] Hirak K. Patra, Mohammad Azharuddin, Mohammad M. Islam, Georgia Papapavlou, Suryyani Deb, Johannes Osterrieth, Geyunjian Harry Zhu, Thobias Romu, Ashis K. Dhara, Mohammad J. Jafari, Amineh Ghaderi, Jorma Hinkula, Madhavan S. Rajan, and Nigel K.H. Slater. Rational Nanotoolbox with Theranostic Potential for Medicated Pro-Regenerative Corneal Implants. *Advanced Functional Materials*, 29(38):1903760, 2019.

[108] John Turkevich, Peter Cooper Stevenson, and James Hillier. A study of the nucleation and growth processes in the synthesis of colloidal gold. *Discussions of the Faraday Society*, 11:55–75, 1951.

[109] Jörg Polte, T. Torsten Ahner, Friedmar Delissen, Sergey Sokolov, Franziska Emmerling, Andreas F. Thünemann, and Ralph Kraehnert. Mechanism of gold nanoparticle formation in the classical citrate synthesis method derived from coupled in situ XANES and SAXS evaluation. *Journal of the American Chemical Society*, 132(4):1296–1301, 2010.

[110] Yong Yang, Jianlin Shi, Hangrong Chen, Shugang Dai, and Ye Liu. Enhanced off-resonance optical nonlinearities of Au@CdS core-shell nanoparticles embedded in BaTiO 3 thin films. *Chemical Physics Letters*, 370(1-2):1–6, 2003.

[111] Oliver Seitz, Mohamed M. Chehimi, Eva Cabet-Deliry, Stéphanie Truong, Nordin Felidj, Christian Perruchot, Steve J. Greaves, and John F. Watts. Preparation and characterisation of gold nanoparticle assemblies on silanised glass plates. *Colloids and Surfaces A: Physicochemical and Engineering Aspects*, 218(1-3):225–239, 2003.

[112] Leonardo Scarabelli, Ana Sánchez-Iglesias, Jorge Pérez-Juste, and Luis M. Liz-Marzán. A "Tips and Tricks" Practical Guide to the Synthesis of Gold Nanorods. *Journal of Physical Chemistry Letters*, 6(21):4270–4279, 2015.

[113] Babak Nikoobakht and Mostafa A. El-Sayed. Preparation and growth mechanism of gold nanorods (NRs) using seed-mediated growth method. *Chemistry of Materials*, 15(10):1957–1962, 2003.

[114] Jorge Pérez-Juste, Isabel Pastoriza-Santos, Luis M. Liz-Marzán, and Paul Mulvaney. Gold nanorods: Synthesis, characterization and applications. *Coordination Chemistry Reviews*, 249(17-18):1870–1901, 2005.

[115] Danielle K. Smith and Brian A. Korgel. The importance of the CTAB surfactant on the colloidal seed-mediated synthesis of gold nanorods. *Langmuir*, 24(3):644–649, 2008.

[116] Raja Gopal Rayavarapu, Constantin Ungureanu, Petra Krystek, Ton G. Van Leeuwen, and Srirang Manohar. Iodide impurities in hexadecyltrimethylammonium bromide (CTAB) products: Lot-lot variations and influence on gold nanorod synthesis. *Langmuir*, 26(7):5050–5055, 2010.

[117] Xiaowei Liu, Jingwen Yao, Jiangjiang Luo, Xiaoshuang Duan, Yanbo Yao, and Tao Liu. Effect of Growth Temperature on Tailoring the Size and Aspect Ratio of Gold Nanorods. *Langmuir*, 33(30):7479–7485, 2017.

[118] Biao Jin, Maria L. Sushko, Zhaoming Liu, Xiaoxiao Cao, Chuanhong Jin, and Ruikang Tang. Understanding Anisotropic Growth of Au Penta-Twinned Nanorods by Liquid Cell Transmission Electron Microscopy. *Journal of Physical Chemistry Letters*, 10(7):1443–1449, 2019.

[119] Neyvis Almora-Barrios, Gerard Novell-Leruth, Peter Whiting, Luis M. Liz-Marzán, and Núria López. Theoretical description of the role of halides, silver, and surfactants on the structure of gold nanorods. *Nano Letters*, 14(2):871–875, 2014.

[120] Nathan D. Burrows, Samantha Harvey, Fred A. Idesis, and Catherine J. Murphy. Understanding the Seed-Mediated Growth of Gold Nanorods through a Fractional Factorial Design of Experiments. *Langmuir*, 33(8):1891–1907, 2017.

[121] Enrique Carbó-Argibay, Benito Rodríguez-González, Jessica Pacifico, Isabel Pastoriza-Santos, Jorge Pérez-Juste, and Luis M. Liz-Marzán. Chemical sharpening of gold nanorods: The rod-to-octahedron transition. *Angewandte Chemie - International Edition*, 46(47):8983–8987, 2007.

[122] You Qiu He, Shao Pu Liu, Ling Kong, and Zhong Fang Liu. A study on the sizes and concentrations of gold nanoparticles by spectra of absorption, resonance Rayleigh scattering and resonance non-linear scattering. *Spectrochimica Acta - Part A: Molecular and Biomolecular Spectroscopy*, 61(13-14):2861–2866, 2005.

[123] K. Leus, P. Concepcion, M. Vandichel, M. Meledina, A. Grirrane, D. Esquivel, S. Turner, D. Poelman, M. Waroquier, V. Van Speybroeck, G. Van Tendeloo, H. García, and P. Van Der Voort. Au@UiO-66: A base free oxidation catalyst. *RSC Advances*, 5(29):22334–22342, 2015.

[124] Liyu Chen, Huirong Chen, Rafael Luque, and Yingwei Li. Metal-organic framework encapsulated Pd nanoparticles: Towards advanced heterogeneous catalysts. *Chemical Science*, 5(10):3708–3714, 2014.

[125] Hongli Liu, Lina Chang, Liyu Chen, and Yingwei Li. In situ one-step synthesis of metal-organic framework encapsulated naked Pt nanoparticles without additional reductants. *Journal of Materials Chemistry A*, 3(15):8028–8033, 2015.

[126] Huai-Xin Zhao, Quan Zou, Shao-Kai Sun, Chunshui Yu, Xuejun Zhang, Rui-Jun Li, and Yan-Yan Fu. Theranostic metal–organic framework core–shell composites for magnetic resonance imaging and drug delivery. *Chem. Sci.*, 7(8):5294–5301, 2016.

[127] Jiajing Zhou, Peng Wang, Chenxu Wang, Yi Ting Goh, Zheng Fang, Phillip B. Messersmith, and Hongwei Duan. Versatile Core-Shell Nanoparticle@Metal-Organic Framework Nanohybrids: Exploiting Mussel-Inspired Polydopamine for Tailored Structural Integration. *ACS Nano*, 9(7):6951–6960, 2015.

[128] Bunyarat Rungtaweevoranit, Jayeon Baek, Joyce R Araujo, Braulio S Archanjo, Kyung Min Choi, Omar M Yaghi, and Gabor A Somorjai. Copper Nanocrystals Encapsulated in Zr-based Metal-Organic Frameworks for Highly Selective CO2 Hydrogenation to Methanol. *Nano Letters*, 16(12):7645–7649, 2016.

[129] Boris Volosskiy, Kenta Niwa, Yu Chen, Zipeng Zhao, Nathan O. Weiss, Xing Zhong, Mengning Ding, Chain Lee, Yu Huang, and Xiangfeng Duan. Metal-organic framework templated synthesis of ultrathin, well-Aligned metallic nanowires. *ACS Nano*, 9(3):3044–3049, 2015.

[130] L R Hirsch, R J Stafford, J A Bankson, S R Sershen, B Rivera, R E Price, J D Hazle, N J Halas, and J L West. Nanoshell-mediated near-infrared thermal therapy of tumors under magnetic resonance guidance. *Proceedings of the National Academy of Sciences*, 100(23):13549–13554, 2003.

[131] Yantao Li, Jun Jin, Dawei Wang, Jiawei Lv, Ke Hou, Yaling Liu, Chunying Chen, and Zhiyong Tang. Coordination-responsive drug release inside gold nanorod@metal-organic framework core–shell nanostructures for near-infrared-induced synergistic chemo-photothermal therapy. *Nano Research*, 11(6):3294–3305, 2018.

[132] Idah C. Pekcevik, Lester C.H. Poon, Michael C.P. Wang, and Byron D. Gates. Tunable loading of single-stranded DNA on gold nanorods through the displacement of polyvinylpyrrolidone. *Analytical Chemistry*, 85(20):9960–9967, 2013.

[133] Benjamin Thierry, Jane Ng, Tina Krieg, and Hans J. Griesser. A robust procedure for the functionalization of gold nanorods and noble metal nanoparticles. *Chemical Communications*, 1(13):1724, 2009.

[134] A. M. Alkilany, A. I. Bani Yaseen, J. Park, J. R. Eller, and C. J. Murphy. Facile phase transfer of gold nanoparticles from aqueous solution to organic solvents with thiolated poly(ethylene glycol). *RSC Adv.*, 4(95):52676–52679, 2014.

[135] P. Piszczek, A. Radtke, A. Grodzicki, A. Wojtczak, and J. Chojnacki. The new type of [Zr6(μ3-O)4(μ3-OH)4] cluster core: Crystal structure and spectral characterization of [Zr6O4(OH)4(OOCR)12] (R = But, C(CH3)2Et). *Inorganica Chimica Acta*, 26(3):679–685, 2007.

[136] Yang Liu, Fang Yang, Chuxiao Yuan, Mingxi Li, Tuantuan Wang, Bo Chen, Juan Jin, Peng Zhao, Jiayi Tong, Shouhua Luo, and Ning Gu. Magnetic Nanoliposomes as in Situ Microbubble Bombers for Multimodality Image-Guided Cancer Theranostics. *ACS Nano*, 11(2):1509–1519, 2017.

[137] Kouta Sugikawa, Shunjiro Nagata, Yuki Furukawa, Kenta Kokado, and Kazuki Sada. Stable and functional gold nanorod composites with a metal-organic framework crystalline shell. *Chemistry of Materials*, 25(13):2565–2570, 2013.

[138] M. B. Majewski, H. Noh, T. Islamoglu, and O. K. Farha. NanoMOFs: Little crystallites for substantial applications. *Journal of Materials Chemistry A*, 6(17):7338–7350, 2018.

[139] Bernard W Stewart and Christopher P. Wild. World cancer Report 2014. Technical Report 1, 2014.

[140] Freddie Bray, Jacques Ferlay, Isabelle Soerjomataram, Rebecca L. Siegel, Lindsey A. Torre, and Ahmedin Jemal. Global cancer statistics 2018: GLOBOCAN estimates of incidence and mortality worldwide for 36 cancers in 185 countries. *CA: A Cancer Journal for Clinicians*, 68(6):394–424, 2018.

[141] Dan Peer, Jeffrey M Karp, Seungpyo Hong, Omid C Farokhzad, Rimona Margalit, and Robert Langer. Nanocarriers as an emerging platform for cancer therapy. *Nature nanotechnology*, 2(12):751–760, 2007.

[142] Cristina Carvalho, Renato Santos, Susana Cardoso, Sonia Correia, Paulo Oliveira, Maria Santos, and Paula Moreira. Doxorubicin: The Good, the Bad and the Ugly Effect. *Current Medicinal Chemistry*, 16(25):3267–3285, 2009.

[143] Beatriz Pelaz, Christoph Alexiou, Ramon A. Alvarez-Puebla, Frauke Alves, Anne M. Andrews, Sumaira Ashraf, Lajos P. Balogh, Laura Ballerini, Alessandra Bestetti, Cornelia Brendel, Susanna Bosi, Monica Carril, Warren C.W. Chan, Chunying Chen, Xiaodong Chen, Xiaoyuan Chen, Zhen Cheng, Daxiang Cui, Jianzhong Du, Christian Dullin, Alberto Escudero, Neus Feliu, Mingyuan Gao, Michael George, Yury Gogotsi, Arnold Grünweller, Zhongwei Gu, Naomi J. Halas, Norbert Hampp, Roland K. Hartmann, Mark C. Hersam, Patrick Hunziker, Ji Jian, Xingyu Jiang, Philipp Jungebluth, Pranav Kadhiresan, Kazunori Kataoka, Ali Khademhosseini, Jindřich Kopeček, Nicholas A. Kotov, Harald F. Krug, Dong Soo Lee, Claus Michael Lehr, Kam W. Leong, Xing Jie Liang, Mei Ling Lim, Luis M. Liz-Marzán, Xiaowei Ma, Paolo Macchiarini, Huan Meng, Helmuth Möhwald, Paul Mulvaney, Andre E. Nel, Shuming Nie, Peter Nordlander, Teruo Okano, Jose Oliveira, Tai Hyun Park, Reginald M. Penner, Maurizio Prato, Victor Puntes, Vincent M. Rotello, Amila Samarakoon, Raymond E. Schaak, Youqing Shen, Sebastian Sjöqvist, Andre G. Skirtach, Mahmoud G. Soliman, Molly M. Stevens, Hsing Wen Sung, Ben Zhong Tang, Rainer Tietze, Buddhisha N. Udugama, J. Scott VanEpps, Tanja Weil, Paul S. Weiss, Itamar Willner, Yuzhou Wu, Lily Yang, Zhao Yue, Qian Zhang, Qiang Zhang, Xian En Zhang, Yuliang Zhao, Xin Zhou, and Wolfgang J. Parak. Diverse Applications of Nanomedicine. *ACS Nano*, 11(3):2313–2381, 2017.

[144] Ester Polo, Manuel Collado, Beatriz Pelaz, and Pablo Del Pino. Advances toward More Efficient Targeted Delivery of Nanoparticles in Vivo: Understanding Interactions between Nanoparticles and Cells. *ACS Nano*, 11(3):2397–2402, 2017.

[145] Qihang Sun, Xuanrong Sun, Xinpeng Ma, Zhuxian Zhou, Erlei Jin, Bo Zhang, Youqing Shen, Edward A. Van Kirk, William J. Murdoch, Joseph R. Lott, Timothy P. Lodge, Maciej Radosz, and Yuliang Zhao. Integration of nanoassembly functions for an effective delivery cascade for cancer drugs. *Advanced Materials*, 26(45):7615–7621, 2014.

[146] Patricia Horcajada, Tamim Chalati, Christian Serre, Brigitte Gillet, Catherine Sebrie, Tarek Baati, Jarrod F Eubank, Daniela Heurtaux, Pascal Clayette, Christine Kreuz, Jong-San Chang, Young Kyu Hwang, Veronique Marsaud, Phuong-Nhi Bories, Luc Cynober, Sophie Gil, Gerard Ferey, Patrick Couvreur, and Ruxandra Gref. Porous metal-organic-framework nanoscale carriers as a potential platform for drug delivery and imaging. *Nature Materials*, 9(2):172–178, 2010.

[147] María C. Bernini, David Fairen-Jimenez, Marcelo Pasinetti, Antonio J Ramirez-Pastor, and Randall Q Snurr. Screening of bio-compatible metal–organic frameworks as potential drug carriers using Monte Carlo simulations. *J. Mater. Chem. B*, 2(7):766–774, 2014.

[148] Isabel Abanades Lazaro, Salame Haddad, Sabrina Sacca, Claudia Orellana-Tavra, David Fairen-Jimenez, and Ross S. Forgan. Selective Surface PEGylation of UiO-66 Nanoparticles for Enhanced Stability, Cell Uptake, and pH-Responsive Drug Delivery. *Chem*, 2(4):561–578, 2017.

[149] Salame Haddad, Isabel Abánades Lázaro, Marcus Fantham, Ajay Mishra, Joaquin Silvestre-Albero, Johannes W.M. Osterrieth, Gabriele S. Kaminski Schierle, Clemens F Kaminski, Ross S. Forgan, and David Fairen-Jimenez. Design of a Functionalized Metal-Organic Framework System for Enhanced Targeted Delivery to Mitochondria. *Journal of the American Chemical Society*, 142(14):6661–6674, 2020.

[150] Wei Chen and Chunsheng Wu. Synthesis, functionalization, and applications of metal-organic frameworks in biomedicine. *Dalton Transactions*, 47(7):2114–2133, 2018.

[151] Johannes W.M. Osterrieth and David Fairen-Jimenez. Metal–Organic Framework Composites for Theragnostics and Drug Delivery Applications. *Biotechnology Journal*, 16(2), 2021.

[152] Fei Ke, Yu Peng Yuan, Ling Guang Qiu, Yu Hua Shen, An Jian Xie, Jun Fa Zhu, Xing You Tian, and Li De Zhang. Facile fabrication of magnetic metal-organic framework nanocomposites for potential targeted drug delivery. *Journal of Materials Chemistry*, 21(11):3843–3848, 2011.

[153] Martin E. Silvestre, Matthias Franzreb, Peter G. Weidler, Osama Shekhah, and Christof Wöll. Magnetic cores with porous coatings: Growth of metal-organic frameworks on particles using liquid phase epitaxy. *Advanced Functional Materials*, 23(9):1210–1213, 2013.

[154] Yongmei Yang, Feng Xia, Ying Yang, Baoyou Gong, Anjian Xie, Yuhua Shen, and Manzhou Zhu. Litchi-like Fe3O4@Fe-MOF capped with HAp gatekeepers for pH-triggered drug release and anticancer effect. *Journal of Materials Chemistry B*, 5(43):8600–8606, 2017.

[155] Xiang Ke, Xiaoqiong Song, Nianqiao Qin, Yingrun Cai, and Fei Ke. Rational synthesis of magnetic Fe3O4@MOF nanoparticles for sustained drug delivery. *Journal of Porous Materials*, 26(3):813–818, 2019.

[156] Abhik Bhattacharjee, Sasidhar Gumma, and Mihir Kumar Purkait. Fe3O4 promoted metal organic framework MIL-100(Fe) for the controlled release of doxorubicin hydrochloride. *Microporous and Mesoporous Materials*, 259:203–210, 2018.

[157] M. Bellusci, P. Guglielmi, A. Masi, F. Padella, G. Singh, N. Yaacoub, D. Peddis, and D. Secci. Magnetic Metal-Organic Framework Composite by Fast and Facile Mechanochemical Process. *Inorganic Chemistry*, 57(4):1806–1814, 2018.

[158] Sanaz Hashemipour and Homayon Ahmad Panahi. Fabrication of magnetite nanoparticles modified with copper based metal organic framework for drug delivery system of letrozole. *Journal of Molecular Liquids*, 243:102–107, 2017.

[159] Yi Nan Wu, Meimei Zhou, Shu Li, Zehua Li, Jie Li, Baozhen Wu, Guangtao Li, Fengting Li, and Xiaohong Guan. Magnetic metal-organic frameworks: γ-Fe2O3@MOFs via confined in situ pyrolysis method for drug delivery. *Small*, 10(14):2927–2936, 2014.

[160] Alessandra Pinna, Raffaele Ricco, Rossana Migheli, Gaia Rocchitta, Pier Andrea Serra, Paolo Falcaro, Luca Malfatti, and Plinio Innocenzi. A MOF-based carrier for in situ dopamine delivery. *RSC Advances*, 8(45):25664–25672, 2018.

[161] Michael Peller, Konstantin Böll, Andreas Zimpel, and Stefan Wuttke. Metal-organic framework nanoparticles for magnetic resonance imaging. *Inorganic Chemistry Frontiers*, 5(8):1760–1779, 2018.

[162] Ming Xue Wu, Jia Gao, Fang Wang, Jie Yang, Nan Song, Xiaoyu Jin, Peng Mi, Jian Tian, Jiayan Luo, Feng Liang, and Ying Wei Yang. Multistimuli Responsive Core–Shell Nanoplatform Constructed from Fe3O4@MOF Equipped with Pillar[6]arene Nanovalves. *Small*, 14(17):1704440, 2018.

[163] Angshuman Ray Chowdhuri, Dipranjan Laha, Srimanta Pal, Parimal Karmakar, and Sumanta Kumar Sahu. One-pot synthesis of folic acid encapsulated upconversion nanoscale metal organic frameworks for targeting, imaging and pH responsive drug release. *Dalton Transactions*, 45(45):18120–18132, 2016.

[164] Vajihe Nejadshafiee, Hossein Naeimi, Bahram Goliaei, Bahareh Bigdeli, Armin Sadighi, Sadegh Dehghani, Alireza Lotfabadi, Maryam Hosseini, Maryam Sadat Nezamtaheri, Massoud Amanlou, Mohammad Sharifzadeh, and Mehdi Khoobi. Magnetic bio-metal–organic framework nanocomposites decorated with folic acid conjugated chitosan as a promising biocompatible targeted theranostic system for cancer treatment. *Materials Science and Engineering C*, 99:805–815, 2019.

[165] Saad Sene, M. Teresa Marcos-Almaraz, Nicolas Menguy, Joseph Scola, Jeanne Volatron, Richard Rouland, Jean Marc Grenèche, Sylvain Miraux, Clotilde Menet, Nathalie Guillou, Florence Gazeau, Christian Serre, Patricia Horcajada, and Nathalie Steunou. Maghemite-nanoMIL-100(Fe) Bimodal Nanovector as a Platform for Image-Guided Therapy. *Chem*, 3(2):303–322, 2017.

[166] Ke Jiang, David A Smith, and Anatoliy Pinchuk. Size-dependent photothermal conversion efficiencies of plasmonically heated gold nanoparticles. *Journal of Physical Chemistry C*, 117(51):27073–27080, 2013.

[167] Claire M Cobley, Jingyi Chen, Eun Chul Cho, Lihong V Wang, and Younan Xia. Gold nanostructures: a class of multifunctional materials for biomedical applications. *Chem. Soc. Rev. Chem. Soc. Rev*, 40(40):44–56, 2011.

[168] Nardine S. Abadeer and Catherine J. Murphy. Recent Progress in Cancer Thermal Therapy Using Gold Nanoparticles. *Journal of Physical Chemistry C*, 120(9):4691–4716, 2016.

[169] Jiayang Li, Jing Liu, and Chunying Chen. Remote Control and Modulation of Cellular Events by Plasmonic Gold Nanoparticles: Implications and Opportunities for Biomedical Applications. *ACS Nano*, 11(3):2403–2409, 2017.

[170] Stephan Link and Mostafa A. El-Sayed. Shape and size dependence of radiative, non-radiative and photothermal properties of gold nanocrystals. *International Reviews in Physical Chemistry*, 19(3):409–453, 2000.

[171] Kira Khaletskaya, Julien Reboul, Mikhail Meilikhov, Masashi Nakahama, St??phane Diring, Masahiko Tsujimoto, Seiji Isoda, Franklin Kim, Ken Ichiro Kamei, Roland A. Fischer, Susumu Kitagawa, and Shuhei Furukawa. Integration of porous coordination polymers and gold nanorods into core-shell mesoscopic composites toward light-induced molecular release. *Journal of the American Chemical Society*, 135(30):10998–11005, 2013.

[172] Catherine Roch-Marchal, Tania Hidalgo, Hung Banh, Roland A. Fischer, and Patricia Horcajada. A Promising Catalytic and Theranostic Agent Obtained through the In-Situ Synthesis of Au Nanoparticles with a Reduced Polyoxometalate Incorporated within Mesoporous MIL-101. *European Journal of Inorganic Chemistry*, 2016(27):4387–4394, 2016.

[173] D. Fairen-Jimenez, S. A. Moggach, M. T. Wharmby, P. A. Wright, S. Parsons, and T. Düren. Opening the gate: Framework flexibility in ZIF-8 explored by experiments and simulations. *Journal of the American Chemical Society*, 133(23):8900–8902, 2011.

[174] Lin Fang, Weiqi Wang, Yang Liu, Zhigang Xie, and Li Chen. Zeolitic imidazole framework coated Au nanorods for enhanced photothermal therapy and stability. *Dalton Transactions*, 46(28):8933–8937, 2017.

[175] Haipeng Zhang, Qin Zhang, Chunshui Liu, and Bing Han. Preparation of a one-dimensional nanorod/metal organic framework Janus nanoplatform: Via side-specific growth for synergistic cancer therapy. *Biomaterials Science*, 7(4):1696–1704, 2019.

[176] Jin Yue Zeng, Ming Kang Zhang, Meng Yun Peng, Dan Gong, and Xian Zheng Zhang. Porphyrinic Metal–Organic Frameworks Coated Gold Nanorods as a Versatile Nanoplatform for Combined Photodynamic/Photothermal/Chemotherapy of Tumor. *Advanced Functional Materials*, 28(8):1705451, 2018.

[177] Steffen Hamann, Jens Folke Kiilgaard, Thomas Litman, Francisco J. Alvarez-Leefmans, Benny R. Winther, and Thomas Zeuthen. Measurement of Cell Volume Changes by Fluorescence Self-Quenching. *Journal of Fluorescence*, 12(2):139–145, 2002.

[178] Pravas Deria, Jierui Yu, Tanner Smith, and Rajesh P. Balaraman. Ground-State versus Excited-State Interchromophoric Interaction: Topology Dependent Excimer Contribution in Metal-Organic Framework Photophysics. *Journal of the American Chemical Society*, 139(16):5973–5983, 2017.

[179] M. Fleischmann, P. J. Hendra, and A. J. McQuillan. Raman spectra of pyridine adsorbed at a silver electrode. *Chemical Physics Letters*, 26(2):163–166, 1974.

[180] David L Jeanmaire and Richard P VAN Duyne. Surface Raman Spectroelectrochemistry Part I. Heterocyclic, aromatic and aliphatic amines adsorbed on the anodized silver electrode. *Journal Electroanalytical Chemistry*, 84:1–20, 1977.

[181] Sebastian Schlücker. Surface-enhanced raman spectroscopy: Concepts and chemical applications. *Angewandte Chemie - International Edition*, 53(19):4756–4795, 2014.

[182] Song Yuan Ding, En Ming You, Zhong Qun Tian, and Martin Moskovits. Electromagnetic theories of surface-enhanced Raman spectroscopy. *Chemical Society Reviews*, 46(13):4042–4076, 2017.

[183] Shintaro Pang, Tianxi Yang, and Lili He. Review of surface enhanced Raman spectroscopic (SERS) detection of synthetic chemical pesticides. *TrAC - Trends in Analytical Chemistry*, 85:73–82, 2016.

[184] Timothy T.X. Ong, Ewan W. Blanch, and Oliver A.H. Jones. Surface Enhanced Raman Spectroscopy in environmental analysis, monitoring and assessment. *Science of the Total Environment*, 720:137601, 2020.

[185] Ramón A. Alvarez-Puebla and Luis M. Liz-Marzán. SERS detection of small inorganic molecules and ions. *Angewandte Chemie - International Edition*, 51(45):11214–11223, 2012.

[186] T. Joshua Moore, Amber S. Moody, Taylor D. Payne, Grace M. Sarabia, Alyssa R. Daniel, and Bhavya Sharma. In vitro and in vivo sers biosensing for disease diagnosis. *Biosensors*, 8(2), 2018.

[187] Pamela A. Mosier-Boss. Review on SERS of bacteria. *Biosensors*, 7(4), 2017.

[188] Chuanhui Huang, Ailin Li, Xiangyu Chen, and Tie Wang. Understanding the Role of Metal–Organic Frameworks in Surface-Enhanced Raman Scattering Application. *Small*, 2004802:1–17, 2020.

[189] Kouta Sugikawa, Yuki Furukawa, and Kazuki Sada. SERS-active metal-organic frameworks embedding gold nanorods. *Chemistry of Materials*, 23(13):3132–3134, 2011.

[190] Huasheng Lai, Gongke Li, Fugang Xu, and Zhuomin Zhang. Metal-organic frameworks: opportunities and challenges for surface-enhanced Raman scattering-a review. *Journal of Materials Chemistry C*, 8(9):2952–2963, 2020.

[191] Guangchao Zheng, Sarah de Marchi, Vanesa López-Puente, Kadir Sentosun, Lakshminarayana Polavarapu, Ignacio Pérez-Juste, Eric H. Hill, Sara Bals, Luis M. Liz-Marzán, Isabel Pastoriza-Santos, and Jorge Pérez-Juste. Encapsulation of Single Plasmonic Nanoparticles within ZIF-8 and SERS Analysis of the MOF Flexibility. *Small*, 12(29):3935–3943, 2016.

[192] Yaling Liu, Liangcan He, Yong Liu, Jingzhu Liu, Yansong Xiong, Jianzhong Zheng, and Zhiyong Tang. Core-shell noble-metal@metal-organic-framework nanoparticles with highly selective sensing property. *Angewandte Chemie - International Edition*, 52(13):3741–3745, 2013.

[193] Xiaolin Cao, Sihui Hong, Zejun Jiang, Yongxin She, Shanshan Wang, Chan Zhang, Hui Li, Fen Jin, Maojun Jin, and Jing Wang. SERS-active metal–organic frameworks with embedded gold nanoparticles. *The Analyst*, 142(14):2640–2647, 2017.

[194] Anupam Das, Namhyun Choi, Joung Il Moon, and Jaebum Choo. Determination of total iron-binding capacity of transferrin using metal organic framework-based surface-enhanced Raman scattering spectroscopy. *Journal of Raman Spectroscopy*, 52(2):1–10, 2020.

[195] Xiaowei Ma, Hao Liu, Sisi Wen, Qinhui Xie, Linjia Li, Jing Jin, Xiaojun Wang, Bing Zhao, and Wei Song. Ultra-sensitive SERS detection, rapid selective adsorption and degradation of cationic dyes on multifunctional magnetic metal-organic framework-based composite. *Nanotechnology*, 31(31), 2020.

[196] Yuling Hu, Jia Liao, Dongmei Wang, and Gongke Li. Fabrication of Gold Nanoparticle-Embedded Metal-Organic Framework for Highly Sensitive Surface-Enhanced Raman Scattering Detection. *ACS Analytical Chemistry*, 86:3955–3963, 2014.

[197] Xuezhi Qiao, Bensheng Su, Cong Liu, Qian Song, Dan Luo, Guang Mo, and Tie Wang. Selective Surface Enhanced Raman Scattering for Quantitative Detection of Lung Cancer Biomarkers in Superparticle@MOF Structure. *Advanced Materials*, 30(5):1–8, 2018.

[198] Yi He, Yue Wang, Xia Yang, Shunbi Xie, Ruo Yuan, and Yaqin Chai. Metal Organic Frameworks Combining CoFe2O4 Magnetic Nanoparticles as Highly Efficient SERS Sensing Platform for Ultrasensitive Detection of N-Terminal Pro-Brain Natriuretic Peptide. *ACS Applied Materials and Interfaces*, 8(12):7683–7690, 2016.

[199] Qianqian Li, Shanshan Gong, Hui Zhang, Fangzhi Huang, Lina Zhang, and Shikuo Li. Tailored necklace-like Ag@ZIF-8 core/shell heterostructure nanowires for high-performance plasmonic SERS detection. *Chemical Engineering Journal*, 371:26–33, 2019.

[200] Xia Zhou, Guangqiang Liu, Hongwen Zhang, Yue Li, and Weiping Cai. Porous zeolite imidazole framework-wrapped urchin-like Au-Ag nanocrystals for SERS detection of trace hexachlorocyclohexane pesticides via efficient enrichment. *Journal of Hazardous Materials*, 368:429–435, 2019.

[201] Huasheng Lai, Wenjuan Shang, Yuyin Yun, Danjiao Chen, Liqian Wu, and Fugang Xu. Uniform arrangement of gold nanoparticles on magnetic core particles with a metal-organic framework shell as a substrate for sensitive and reproducible SERS based assays: Application to the quantitation of Malachite Green and thiram. *Microchimica Acta*, 186(3), 2019.

[202] O. Guselnikova, P. Postnikov, R. Elashnikov, E. Miliutina, V. Svorcik, and O. Lyutakov. Metal-organic framework (MOF-5) coated SERS active gold gratings: A platform for the selective detection of organic contaminants in soil. *Analytica Chimica Acta*, 1068:70–79, 2019.

[203] Amane Shiohara, Yusong Wang, and Luis M. Liz-Marzán. Recent approaches toward creation of hot spots for SERS detection. *Journal of Photochemistry and Photobiology C: Photochemistry Reviews*, 21:2–25, 2014.

[204] Yek Tann Chua and Peter C. Stair. An ultraviolet Raman spectroscopic study of coke formation in methanol to hydrocarbons conversion over zeolite H-MFI. *Journal of Catalysis*, 213(1):39–46, 2003.

[205] Xiu Liang Lv, Shuai Yuan, Lin Hua Xie, Hannah F. Darke, Ya Chen, Tao He, Chen Dong, Bin Wang, Yong Zheng Zhang, Jian Rong Li, and Hong Cai Zhou. Ligand Rigidification for Enhancing the Stability of Metal-Organic Frameworks. *Journal of the American Chemical Society*, 141(26):10283–10293, 2019.

[206] Stephen Brunauer, P. H. Emmett, and Edward Teller. Adsorption of Gases in Multimolecular Layers. *Journal of the American Chemical Society*, 60(2):309–319, 1938.

[207] Ruby Cid, Renan Arriagada, and Fresia Orellana. Zeolites surface area calculation from nitrogen adsorption data. *Journal of Catalysis*, 80(1):228–230, 1983.

[208] Dongyuan Zhao, Jianglin Feng, Qisheng Huo, Nicholas Melosh, Glenn H. Fredrickson, Bradley F. Chmelka, and Galen D. Stucky. Triblock copolymer syntheses of mesoporous silica with periodic 50 to 300 angstrom pores. *Science*, 279(5350):548–552, 1998.

[209] J. S. Beck, J. C. Vartuli, W. J. Roth, M. E. Leonowicz, C. T. Kresge, K. D. Schmitt, C. T.W. Chu, D. H. Olson, E. W. Sheppard, S. B. McCullen, J. B. Higgins, and J. L. Schlenker. A New Family of Mesoporous Molecular Sieves Prepared with Liquid Crystal Templates. *Journal of the American Chemical Society*, 114(27):10834–10843, 1992.

[210] Avelino Corma. From microporous to mesoporous molecular sieve materials and their use in catalysis. *Chemical Reviews*, 97(6):2373–2419, 1997.

[211] Irving Langmuir. The adsorption of gases on plane surfaces of glass, mica and platinum. *Journal of the American Chemical Society*, 40(9):1361–1403, 1918.

[212] Yu K Tovbin. The volume of micropores and the Dubinin-Radushkevich equation. *Russian Chemical Bulletin*, 47(4):637–643, 1998.

[213] ISO [International Organization for Standardization]. Determination of the specific surface area of solids by gas adsorption - BET method (ISO 9277:2010(E)). 2010.

[214] J. Rouquerol, P. Llewellyn, and F. Rouquerol. Is the BET equation applicable to microporous adsorbents? *Studies in Surface Science and Catalysis*, 160:49–56, sep 2007.

[215] Peter Atkins and Julio de Paula. *Atkins' Physical chemistry - Eight Edition*. Oxford University Press, 2006.

[216] József Tóth. Uniform interpretation of gas/solid adsorption. *Advances in Colloid and Interface Science*, 55:1–239, 1995.

[217] József Tóth, Ferenc Berger, and Imre Dékány. Separation of the first adsorbed layer from others and calculation of the BET compatible surface area from type II isotherms. *Journal of Colloid and Interface Science*, 212(2):411–418, 1999.

[218] S. J. Gregg and K. S. W. Sing. *Adsorption, Surface Area and Porosity Second Edition*. Academic Press, 1982.

[219] Diego A Gómez-Gualdrón, Peyman Z Moghadam, Joseph T Hupp, Omar K Farha, and Randall Q Snurr. Application of Consistency Criteria To Calculate BET Areas of Micro- And Mesoporous Metal-Organic Frameworks. *Journal of the American Chemical Society*, 138(1):215–24, 2016.

[220] Krista S. Walton and Randall Q. Snurr. Applicability of the BET method for determining surface areas of microporous metal-organic frameworks. *Journal of the American Chemical Society*, 129(27):8552–8556, 2007.

[221] Timothy C. Wang, Wojciech Bury, Diego A. Gómez-Gualdrón, Nicolaas A. Vermeulen, Joseph E. Mondloch, Pravas Deria, Kainan Zhang, Peyman Z. Moghadam, Amy A. Sarjeant, Randall Q. Snurr, J. Fraser Stoddart, Joseph T. Hupp, and Omar K. Farha. Ultrahigh Surface Area Zirconium MOFs and Insights into the Applicability of the BET Theory. *Journal of the American Chemical Society*, 137(10):3585–3591, 2015.

[222] Filip Ambroz, Thomas J. Macdonald, Vladimir Martis, and Ivan P. Parkin. Evaluation of the BET Theory for the Characterization of Meso and Microporous MOFs. *Small Methods*, 2(11):1800173, 2018.

[223] Tina Düren, Franck Millange, Gérard Férey, Krista S. Walton, and Randall Q. Snurr. Calculating geometric surface areas as a characterization tool for metal - Organic frameworks. *Journal of Physical Chemistry C*, 111(42):15350–15356, 2007.

[224] Youn Sang Bae, A. Özgür Yazayd'n, and Randall Q. Snurr. Evaluation of the BET method for determining surface areas of MOFs and zeolites that contain Ultra-Micropores. *Langmuir*, 26(8):5475–5483, 2010.

[225] Tominaga Keii, Tokuji Takagi, and Setsuko Kanetaka. A New Plotting of the BET Method. *Analytical Chemistry*, 33(13):1965, 1961.

[226] J.B. Parra, J.C. De Sousa, Roop C. Bansal, J.J. Pis, and J.A. Pajares. Characterization of Activated Carbons by the BET Equation — An Alternative Approach. *Adsorption Science & Technology*, 12(1):51–66, 1995.

[227] Jongwoo Park, Joshua D. Howe, and David S. Sholl. How Reproducible Are Isotherm Measurements in Metal-Organic Frameworks? *Chemistry of Materials*, 29(24):10487–10495, 2017.

[228] Mayank Agrawal, Rebecca Han, Dinushka Herath, and David S. Sholl. Does repeat synthesis in materials chemistry obey a power law? *Proceedings of the National Academy of Sciences of the United States of America*, 117(2):877–882, 2020.

[229] Charles R. Harris, K. Jarrod Millman, Stéfan J. van der Walt, Ralf Gommers, Pauli Virtanen, David Cournapeau, Eric Wieser, Julian Taylor, Sebastian Berg, Nathaniel J. Smith, Robert Kern, Matti Picus, Stephan Hoyer, Marten H. van Kerkwijk, Matthew Brett, Allan Haldane, Jaime Fernández del Río, Mark Wiebe, Pearu Peterson, Pierre Gérard-Marchant, Kevin Sheppard, Tyler Reddy, Warren Weckesser, Hameer Abbasi, Christoph Gohlke, and Travis E. Oliphant. Array programming with NumPy. *Nature*, 585(7825):357–362, 2020.

[230] Olaf Delgado-Friedrichs and Michael O'Keeffe. Identification of and symmetry computation for crystal nets. *Acta Crystallographica Section A: Foundations of Crystallography*, 59(4):351–360, 2003.

[231] Michael O'Keeffe and Omar M. Yaghi. Deconstructing the crystal structures of metal-organic frameworks and related materials into their underlying nets. *Chemical Reviews*, 112(2):675–702, 2012.

[232] Olaf Delgado-Friedrichs and Michael O'Keeffe. Crystal nets as graphs: Terminology and definitions. *Journal of Solid State Chemistry*, 178(8):2480–2485, 2005.

[233] W. Gebert. Three-dimensional nets and polyhedra by A. F. Wells. *Acta Crystallographica Section B Structural Crystallography and Crystal Chemistry*, 34(9):2958–2958, sep 1978.

[234] M. O'Keeffe, M. Eddaoudi, Hailian Li, T. Reineke, and O. M. Yaghi. Frameworks for extended solids: Geometrical design principles. *Journal of Solid State Chemistry*, 152(1):3–20, 2000.

[235] Jean Guillaume Eon. Topological features in crystal structures: A quotient graph assisted analysis of underlying nets and their embeddings. *Acta Crystallographica Section A: Foundations and Advances*, 72(3):268–293, 2016.

[236] Nadrian C. Seeman and Hanadi F. Sleiman. DNA nanotechnology. *Nature Reviews Materials*, 3, 2017.

[237] Fei Zhang, Shuoxing Jiang, Siyu Wu, Yulin Li, Chengde Mao, Yan Liu, and Hao Yan. Complex wireframe DNA origami nanostructures with multi-arm junction vertices. *Nature Nanotechnology*, 10(9):779–784, 2015.

[238] Phiset Sa-Ardyen, Natasha Jonoska, and Nadrian C. Seeman. Self-assembly of irregular graphs whose edges are DNA helix axes. *Journal of the American Chemical Society*, 126(21):6648–6657, 2004.

[239] Nadrian C Seeman and N. R. Kallenbach. Design of immobile nucleic acid junctions. *Biophysical Journal*, 44(2):201–209, 1983.

[240] Paul W.K. Rothemund. Folding DNA to create nanoscale shapes and patterns. *Nature*, 440(7082):297–302, 2006.

[241] Nadrian C. Seeman. Nucleic acid junctions and lattices. *Journal of Theoretical Biology*, 99(2):237–247, 1982.

[242] N. C. Seeman. In the nick of space: Generalized nucleic acid complementarity and DNA nanotechnology. *Synlett*, (11):1536–1548, 2000.

[243] Arun Richard Chandrasekaran and Rebecca Zhuo. A 'tile' tale: Hierarchical self-assembly of DNA lattices. *Applied Materials Today*, 2:7–16, 2016.

[244] Xiaojun Li, Xiaoping Yang, Jing Qi, and Nadrian C. Seeman. Antiparallel DNA double crossover molecules as components for nanoconstruction. *Journal of the American Chemical Society*, 118(26):6131–6140, 1996.

[245] Dage Liu, Mingsheng Wang, Zhaoxiang Deng, Richard Walulu, and Chengde Mao. Tensegrity: Construction of Rigid DNA Triangles with Flexible Four-Arm DNA Junctions. *Journal of the American Chemical Society*, 126(8):2324–2325, 2004.

[246] Jianping Zheng, Jens J Birktoft, Yi Chen, Tong Wang, Ruojie Sha, Pamela E Constantinou, Stephan L Ginell, Chengde Mao, and Nadrian C Seeman. From molecular to macroscopic via the rational design of a self-assembled 3D DNA crystal. *Nature*, 461(7260):74–77, 2009.

[247] Hao Yan, Sung Ha Park, Gleb Finkelstein, John H. Reif, and Thomas H. LaBean. DNA-templated self-assembly of protein arrays and highly conductive nanowires. *Science*, 301(5641):1882–1884, 2003.

[248] Chenxu Wang, Jiajing Zhou, Peng Wang, Wenshan He, and Hongwei Duan. Robust Nanoparticle-DNA Conjugates Based on Mussel-Inspired Polydopamine Coating for Cell Imaging and Tailored Self-Assembly. *Bioconjugate Chemistry*, 27(3):815–823, 2016.

[249] Yu He, Yi Chen, Haipeng Liu, Alexander E. Ribbe, and Chengde Mao. Self-assembly of hexagonal DNA two-dimensional (2D) arrays. *Journal of the American Chemical Society*, 127(35):12202–12203, 2005.

[250] Fei Zhang, Shuoxing Jiang, Wei Li, Ashley Hunt, Yan Liu, and Hao Yan. Self-Assembly of Complex DNA Tessellations by Using Low-Symmetry Multi-arm DNA Tiles. *Angewandte Chemie - International Edition*, 55(31):8860–8863, 2016.

[251] Hua Zuo and Chengde Mao. A minimalist's approach for DNA nanoconstructions. *Advanced Drug Delivery Reviews*, 147:22–28, 2019.

[252] Sean Williams, Kyle Lund, Chenxiang Lin, Peter Wonka, Stuart Lindsay, and Hao Yan. Tiamat: A three-dimensional editing tool for complex DNA structures. In *Lecture Notes in Computer Science (including subseries Lecture Notes in Artificial Intelligence and Lecture Notes in Bioinformatics)*, volume 5347, pages 90–101, 2009.

[253] Yu He, Ye Tian, Alexander E. Ribbe, and Chengde Mao. Highly connected two-dimensional crystals of DNA six-point-stars. *Journal of the American Chemical Society*, 128(50):15978–15979, 2006.

[254] Chad A. Mirkin, Robert L. Letsinger, Robert C. Mucic, and James J. Storhoff. A DNA-Based Method for Rationally Assembling Nanoparticles into Macroscopic Materials. *Nature*, 382:607–609, 1996.

[255] Pongphak Chidchob and Hanadi F. Sleiman. Recent advances in DNA nanotechnology. *Current Opinion in Chemical Biology*, 46:63–70, 2018.

Appendix A

Tabulated Round-robin Results

HKUST 1	Zeo 13X	Mg MOF -74	Al fum	MCM 41	DMOF 1	MOF 5	UiO 66	UiO 66 NH2	NU 1000	ZIF 8	MIL 101	COF	MIL 100	NU 1102	NU 1104	NU 1105	PCN 777
1560	833	1013	1007	970	1913	3218	1171	1464	2153	1601	2387	2836	2043	4607	7218	3527	1973
1536	823	1000	996	970	1906	3210	1167	1452	2099	1734	2550	2839	2256	4913	7845	3574	1990
1551	833	1014	1012	984	1926	3375	1212	1433	2061	1788	2509	2859	1936	4564	6163	3695	2036
1556	832	1010	1005	984	1922	3286	1158	1416	1979	1558	2499	2800	1584	4889	3210	3722	2028
1200	603	756	774	985	1359	2544	915	1141	2152	1341	2363	2792	1784	3889	5999	3667	1952
1556	833	1012	1007	969	1924	3275	1179	1473	1987	1573	2546	2815	1620	4883	7353	3722	1848
1558	831	1009	1009	984	1922	3246	1180	1438	2054	1768	2548	2815	2224	4691	7151	3612	2444
1556	833	1011	1007	972	1913	3206	1165	1446	1961	1601	2445	2754	2129	4278	3559	3635	1898
1555	831	1010	993	971	1753	3226	780	1152	1961	1373	1432	2800	1995	4701	5223	3554	1893
1558	832	1012	1005	970	1950	3251	1168	1452	2009	1466	2612	2805	2130	4928	6017	3651	1928
1553	834	1013	1008	932	1946	3257	1190	1415	1968	1574	2578	2658	1711	4893	5914	3808	1916
1558	833	1010	1009	973	1915	3223	1172	1468	1973	1720	2577	2816	1949	4753	5223	3489	1866
1155	601	750	770	1064	1339	2446	743	1104	2066	1310	2187	6446	1510	3517	4291	4940	1870
1557	834	1013	1009	976	1933	3242	1180	1469	1971	1760	2646	2754					
1555	828	1004	1014	981	1895	3123	1146	1385	2129	1740	2376	2894	1948	4859	6119	3585	1968
1555	834	1011	1009	984	1918	3246	1179	1469	2058	1766	2567	2800	2129	4926	6036	3712	1898
1533	825	1000	1000	971	1898	3040	1120	1426	1963	1623	2749	2825	1999	5400	6080	3724	1950
1558	833	1012	1006	970	1926	3311	1135	1378	1988	1687	2319	2601	1915	4854	6039	3175	1936
1444	713	882	903	968	1591	2850	1074	1412	1986	1623	2680	2659	2133	5385	6130	2737	1780
1559	834	1014	1008	987	1919	3240	1190	1441	2076	1774	2467	2791	2111	4762	5361	3528	1948

Table A.1 Round-robin Results tabulated, Labs 1-20

HKUST 1	Zeo 13X	Mg MOF -74	Al fum	MCM 41	DMOF 1	MOF 5	UiO 66	UiO 66 NH2	NU 1000	ZIF 8	MIL 101	COF	MIL 100	NU 1102	NU 1104	NU 1105	PCN 777
1007	533	646	649	618	1203	2095	533	915	1289	1117	1017	1415	1001	3138	1757	2297	1183
1552	827	1005	1002	970	1907	3115	1183	1417	2044	1729	2058	2725	1721	4928	5799	3591	1908
1555	838	1013	1007	971	1927	3264	1176	1455	2100	1756	2573	2800	2279	4896	7197	3564	1900
1559	831	1014	1012	975	1924	3287	1192	1150	2149	1567	2606	2880	2082	5015	6780	3939	1974
1488	782	960	1001	951	1748	3102	1159	1468	1996	1731	2342	2401	1711	4514	5874	3731	1864
1558	833	1013	1002	972	1937	3250	1179	1406	2041	1720	2652	2804	2129	4926	5983	3688	1930
1552	827	997	1006	973	1881	3160	1131	1441	2006	1720	2572	2858	2113	4842	6039	3688	1898
1589	827	1008	993	957	1870	3477	1124	1390	2009	1702	2444	2568	1934	4907	7225	3310	1973
1556	833	1015	1009	970	1999	3222	1188	1430	2090	1764	2567	2855	2114	4874	6291	3535	1929
1557	827	1004	995	984	1925	3166	1161	1386	1968	1732	2642	2895	2032	4693	5409	3614	1911
1551	830	1004	1004	968	1918	3218	1179	1445	2045	1818	2589	2856	2129	4839	6035	3659	1884
1590	840	1008	1025	985	1870	3162	1200	1407	2070	1607	2624	2792	2099	4646	5999	3738	1635
1566	837	1018	1013	971	1970	3361	1208	1419	2005	1782	2850	2818	2054	4876	5653	3798	1995
1556	699	865	884	960	1483	2614	993	1261	2005	1523	2445	2500	1879	4142	6208	3659	1897
1088	888	1105	1126	1447	1984	3460	1329	1666	2775	3201	3421	3941	2499	5706	9341	4823	2863
1562	838	1013	1000	958	1905	3240	1120	1455	2000	1822	2646	2800	1735	4896	3197	3032	1725
1556	839	1011	1006	966	1917	3225	1157	1433	2014	1579	2588	2800	2046	4831	7136	3528	1914
1572	847	1033	1047	1073	1977	3425	1234	1561	2125	1506	2433	3796	2555	6053	8763	5508	2975
1556	833	1013	1007	952	1923	3238	1109	1322	1961	1579	2277	2800	1648	4884	6342	3640	1575
1552	832	1011	1005	981	1925	3286	866	1412	1992	1579	2526	2779	2068	4889	5507	3645	2028

Table A.2 Round-robin Results tabulated, Labs 21-40

HK UST 1	Zeo 13X	Mg MOF -74	Al fum	MCM 41	DM OF 1	MOF 5	UiO 66	UiO 66 NH2	NU 1000	ZIF 8	MIL 101	COF	MIL 100	NU 11 02	NU 11 04	NU 11 05	PCN 777
1555	833	1014	1002	975	1927	3247	1186	1474	2149	1762	2856	2844	2039	4730	5720	3538	1946
1555	825	1013	985	971	1891	3088	726	1389	2013	1716	1573	2750	1544	4816	2774	3551	1988
1561	835	1015	1014	971	1918	3224	1175	1463	1966	1600	2697	2950	2042	4762	5275	3578	1983
1551	834	1011	1009	976	1938	3222	1176	1474	2049	1540	2565	2855	2030	4604	8077	3527	1970
1557	835	1011	1005	970	1925	3279	1167	1406	2007	1580	2501	2573	1979	4851	7136	3592	1824
1555	832	1011	1005	982	1923	3265	1136	1377	2018	1712	2321	2600	1917	4856	2806	3400	1935
1559	830	1013	1014	968	1916	3236	1217	1427	1647	1599	2681	2906	1763	4510	2975	3493	1926
1518	801	964	987	810	1766	3074	1128	1341	1918	1828	2092	1699	1861	4277	2108	2210	1409
1535	821	998	978	952	1898	3232	1050	1129	1951	1536	1932	2151	1566	4820	6524	3479	1972
1436	771	948	964	964	1640	2990	1010	1444	2039	1732	2515	2348	2073	4823	5851	3725	1865
1557	834	1014	1009	966	1923	3248	1190	1435	1971	1586	2633	2817	2006	4856	5451	3724	1897
1558	833	1014	1002	1502	1926	3165	1149	1375	1994	1731	2050	2842	2006	4649	5142	3508	1970
1529	831	999	995	969	1903	3243	1083	1359	2056	1665	1973	2648	1830	4883	6003	3482	1978
1556	829	1009	1003	968		3259	1153	1394	1979	1560	2361	2662		4889	6625	3278	1873
1556	826	1009	1004	963	1892	3146	1159	1419	2024	1757	2561	2810	2033	4823	5891	3719	1900
1557	831	1010	1002	898	1737	3265	1188	1089	1832	1819	1549	1629	1531	4778	1840	1971	1480
1556	833	1012	1008	968	1931	3275	1180	1434	2021	1752	2554	2830	2031	5024	6043	3733	1909
1555	834	1011	1009	960	1913	3275	1180	1424	2008	1604	2503	2728	1982	4819	1804	2903	1865
1536	823	998	996	1803	1893	3204	1164	1406	1933	1580	2533	2764	2397	4648	6623	5945	3350
1534	820	1000	991	950	1904	3104	1130	1370	2008	1720	2386	2394	2064	4777	1783	2776	1756

Table A.3 Round-robin Results tabulated, Labs 41-60

Appendix B

BETSI Reports

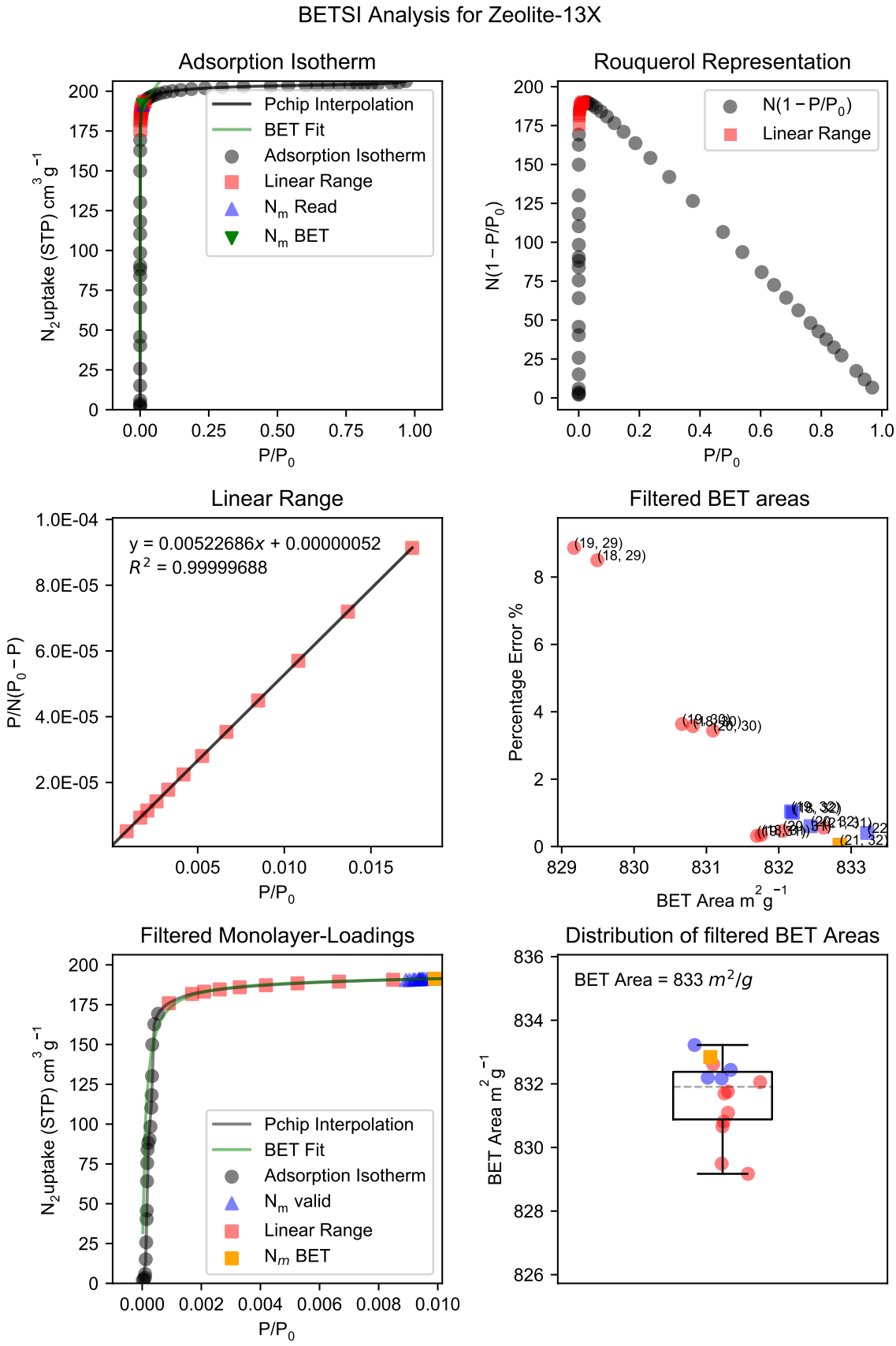

Fig. B.1 BETSI Results for Zeolite-13X

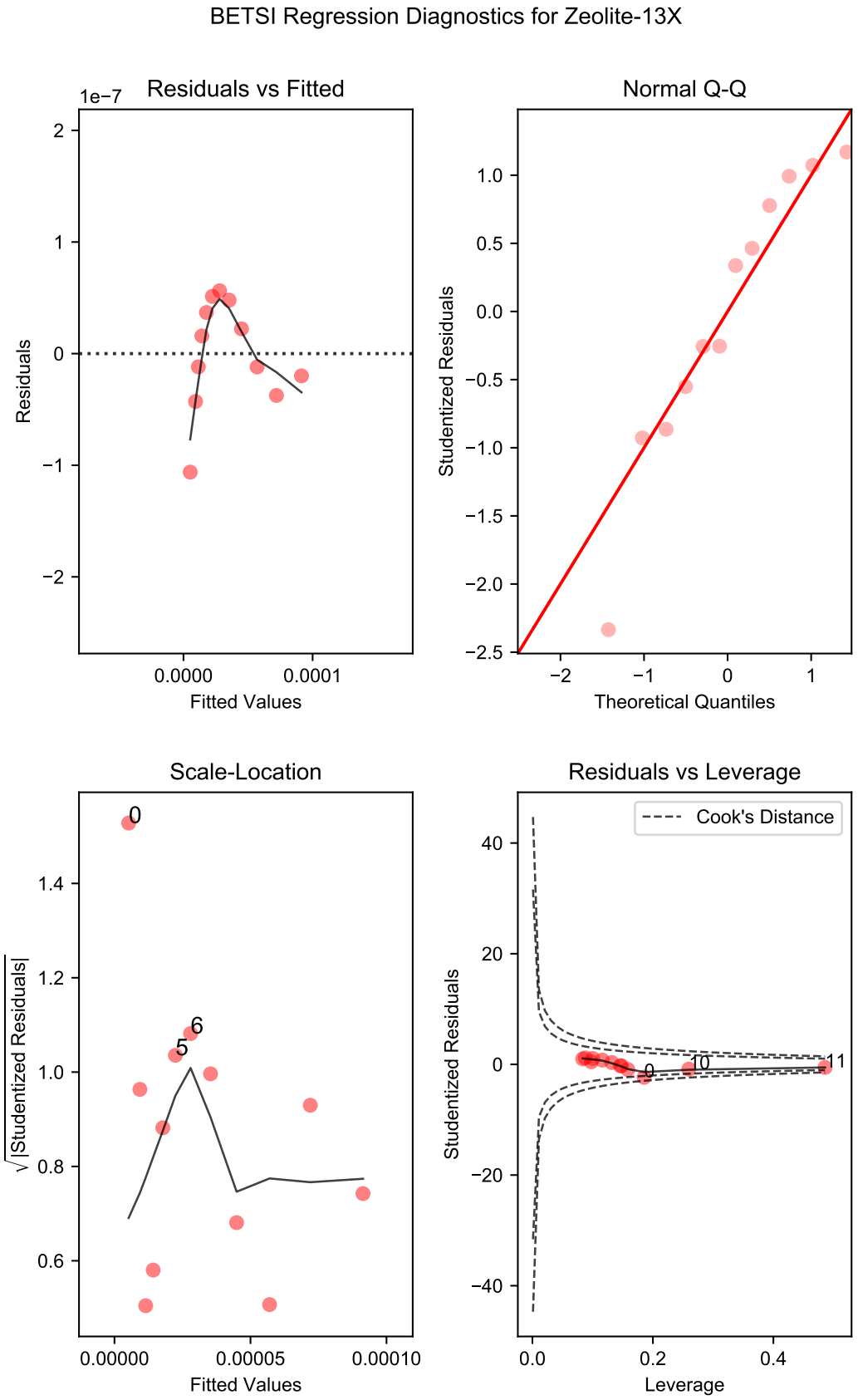

Fig. B.2 Regression Diagnostics for Zeolite-13X

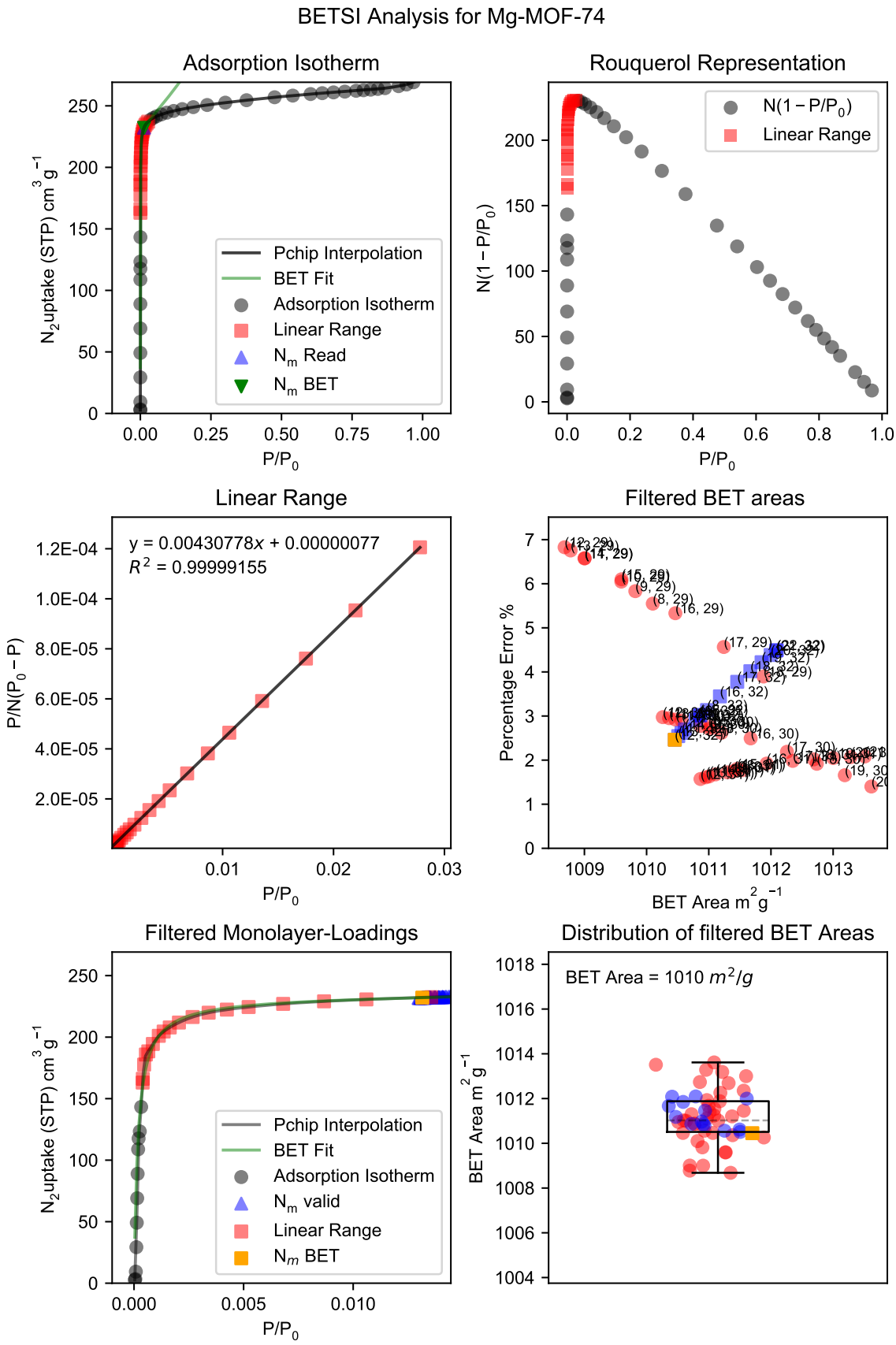

Fig. B.3 BETSI Results for Mg-MOF-74

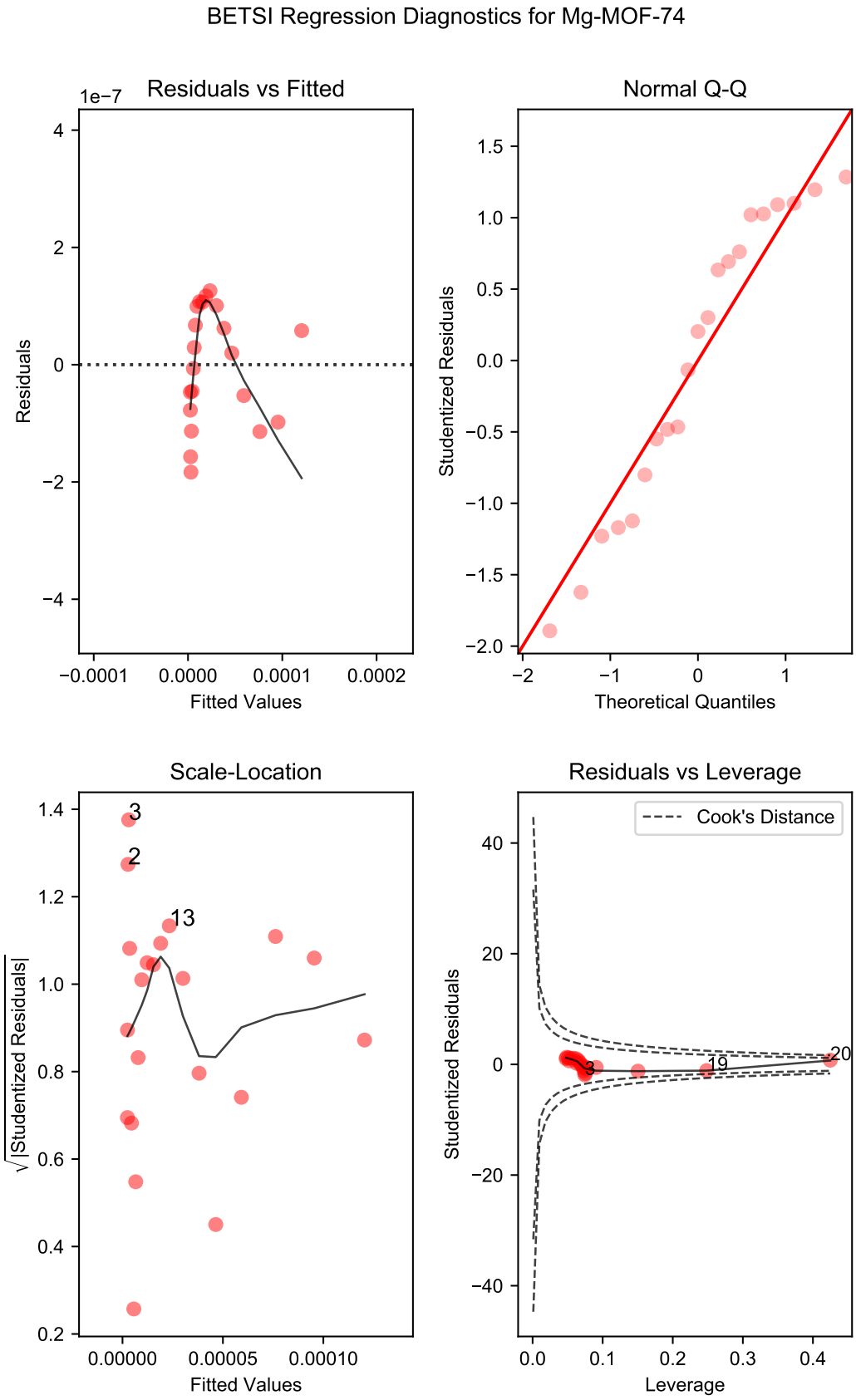

Fig. B.4 Regression Diagnostics for Mg-MOF-74

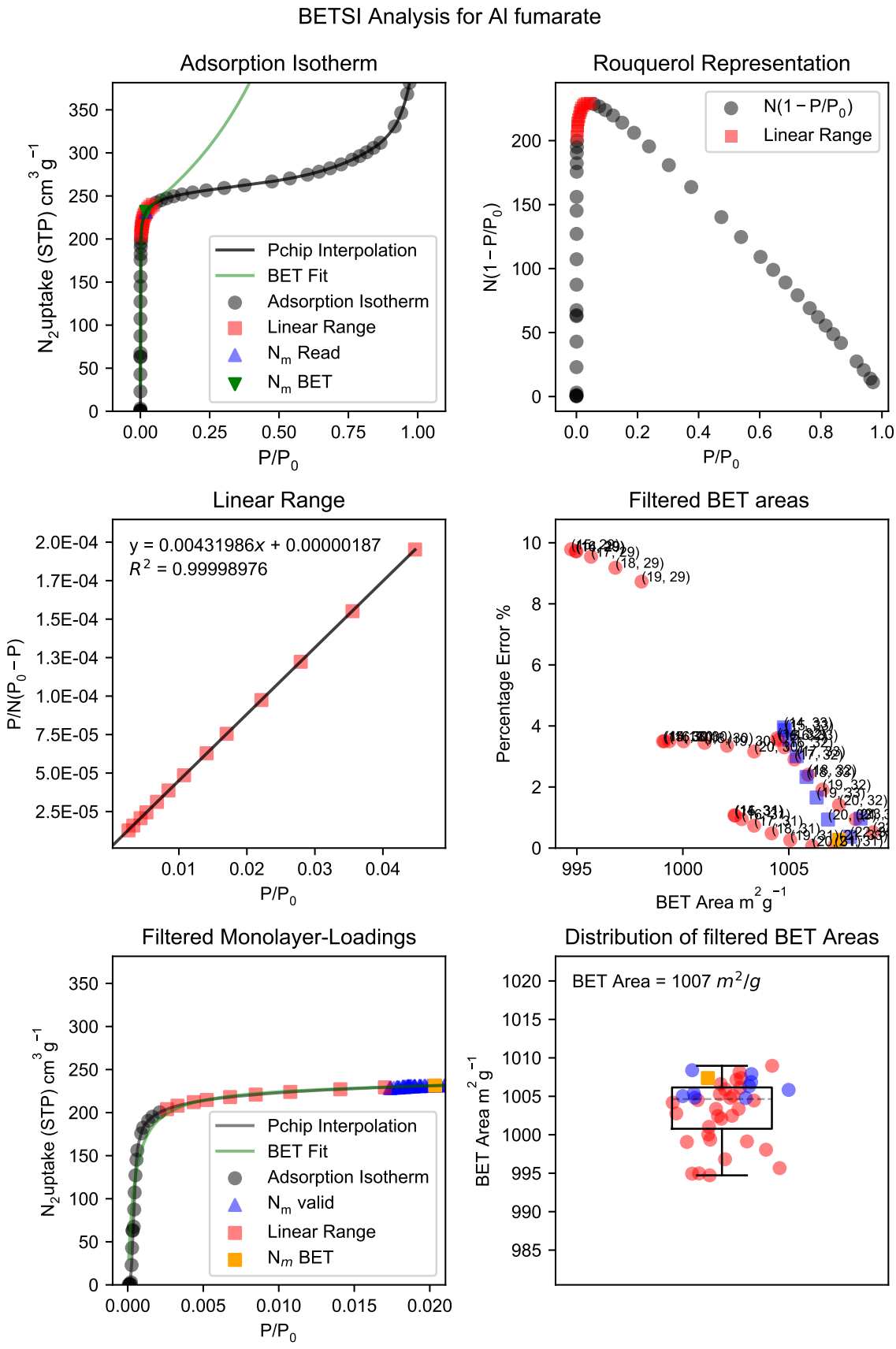

Fig. B.5 BETSI Results for Al fumarate

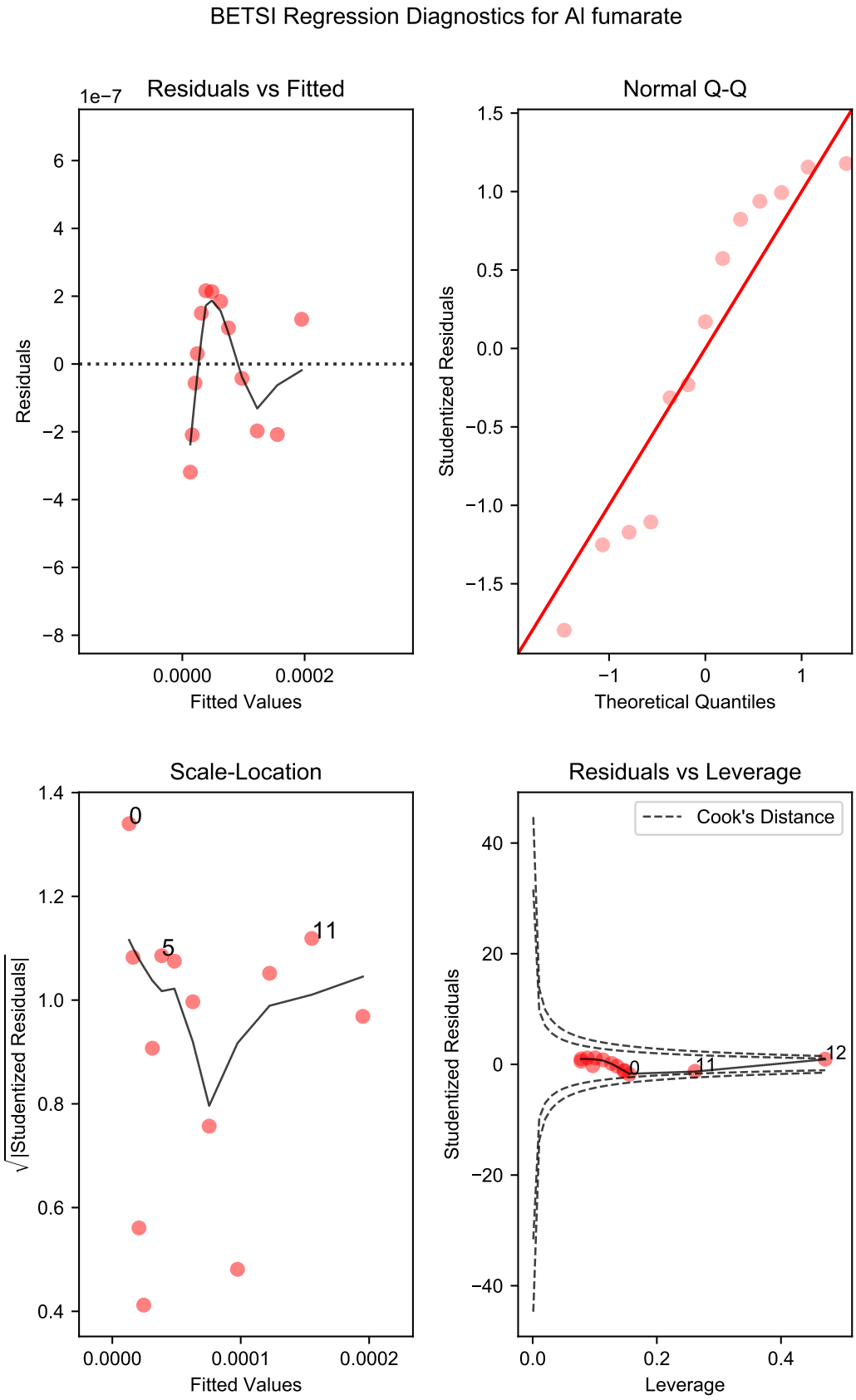

Fig. B.6 Regression Diagnostics for Al fumarate

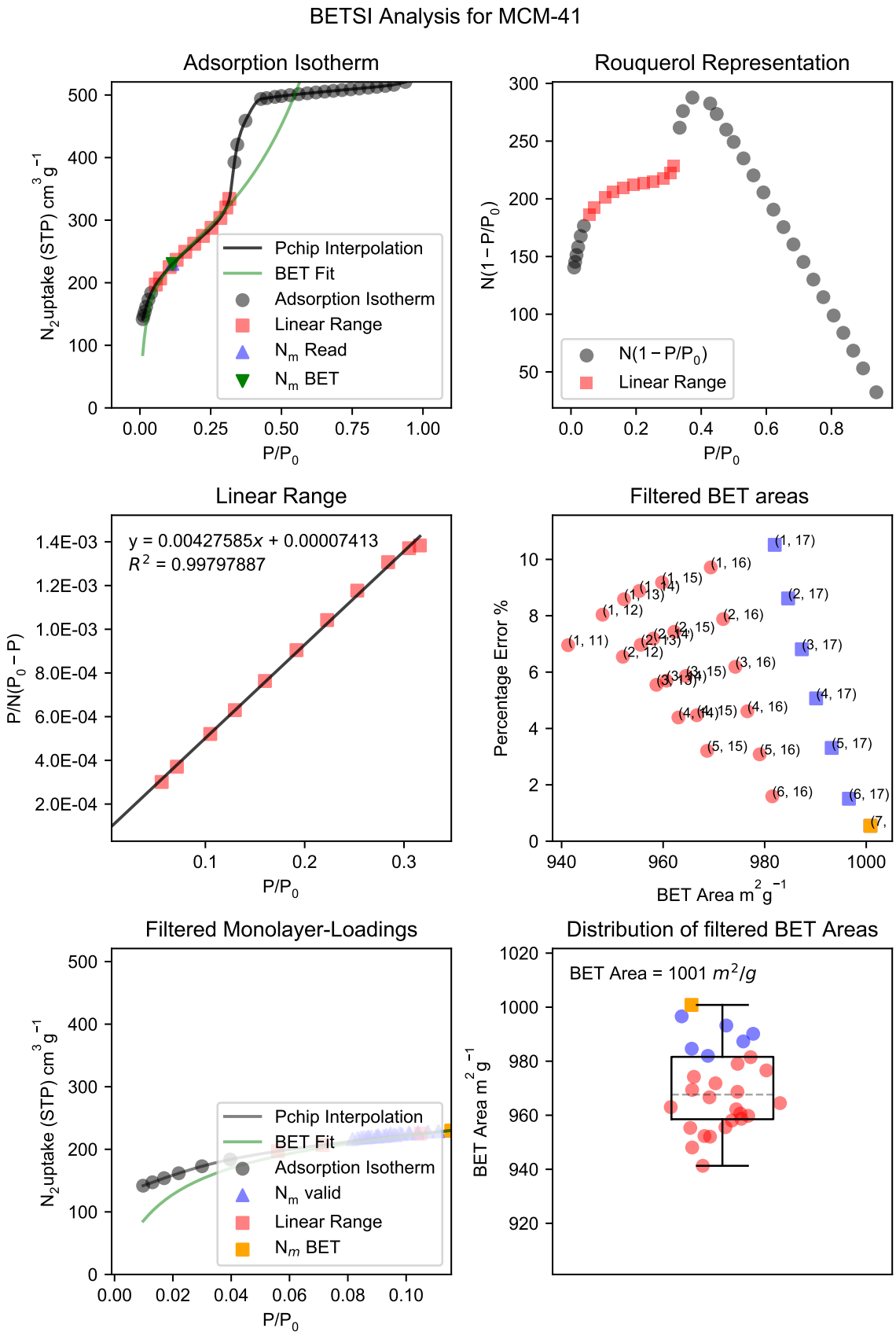

Fig. B.7 BETSI Results for MCM-41

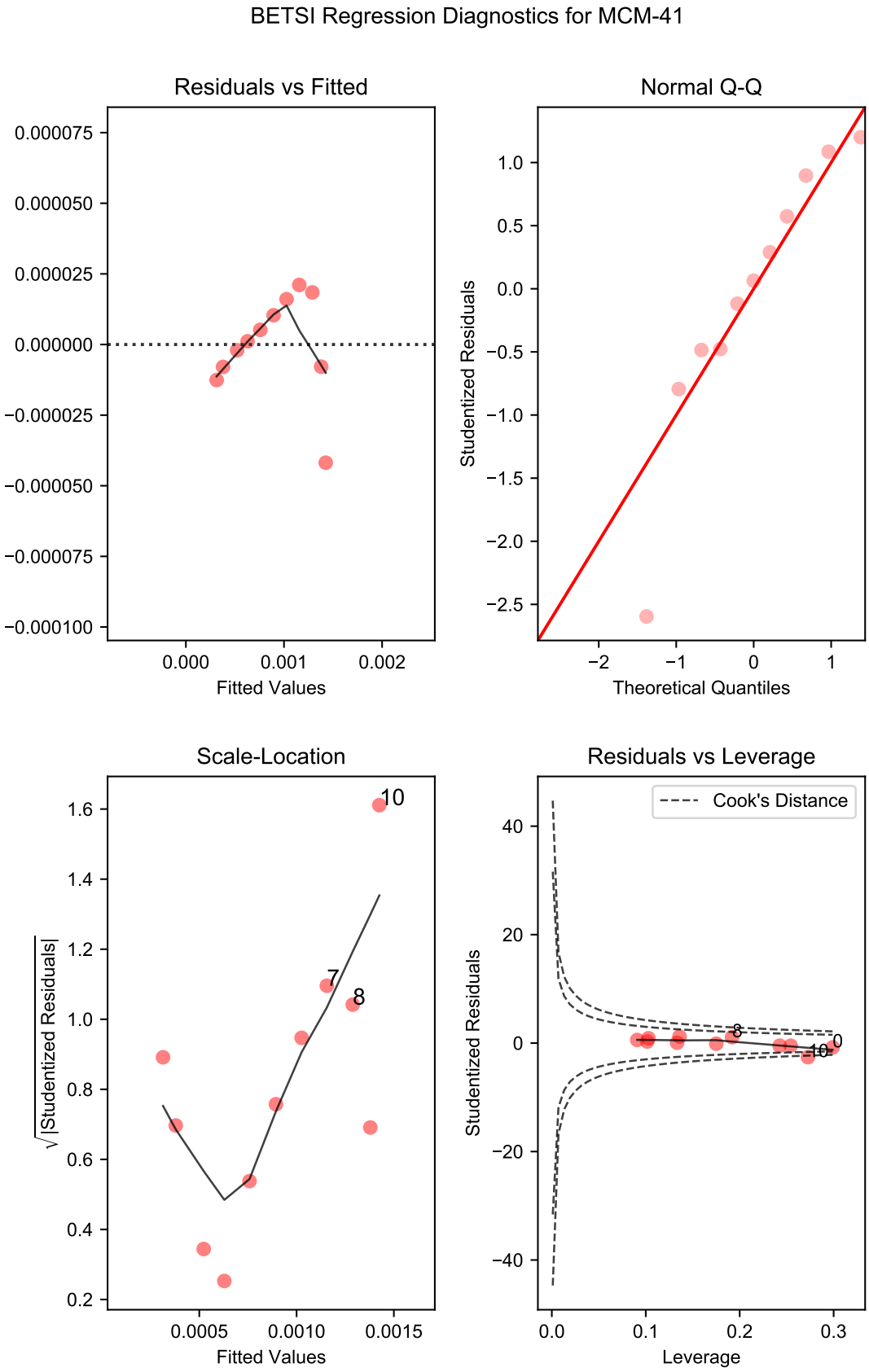

Fig. B.8 Regression Diagnostics for MCM-41

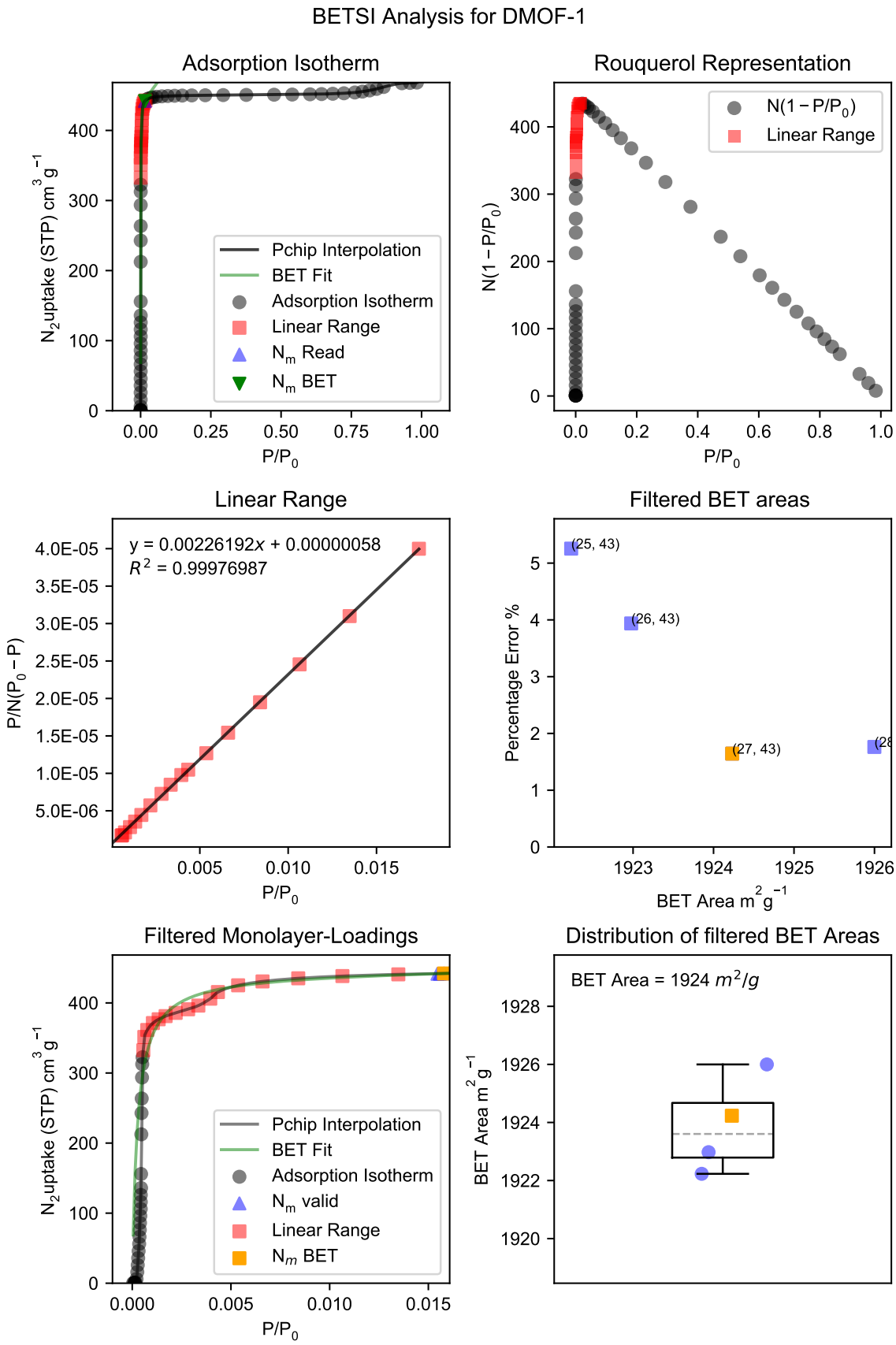

Fig. B.9 BETSI Results for DMOF-1

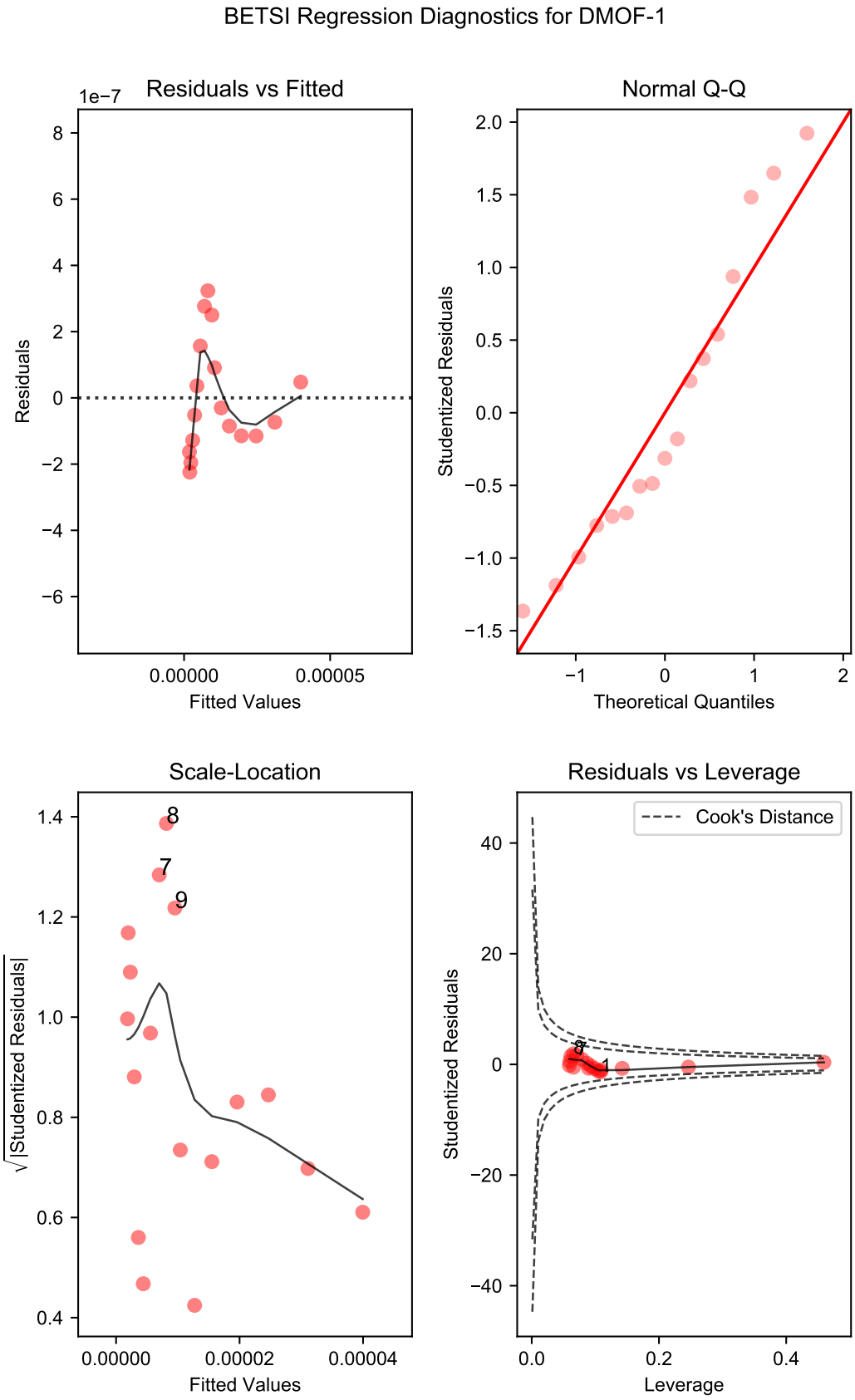

Fig. B.10 Regression Diagnostics for DMOF-1

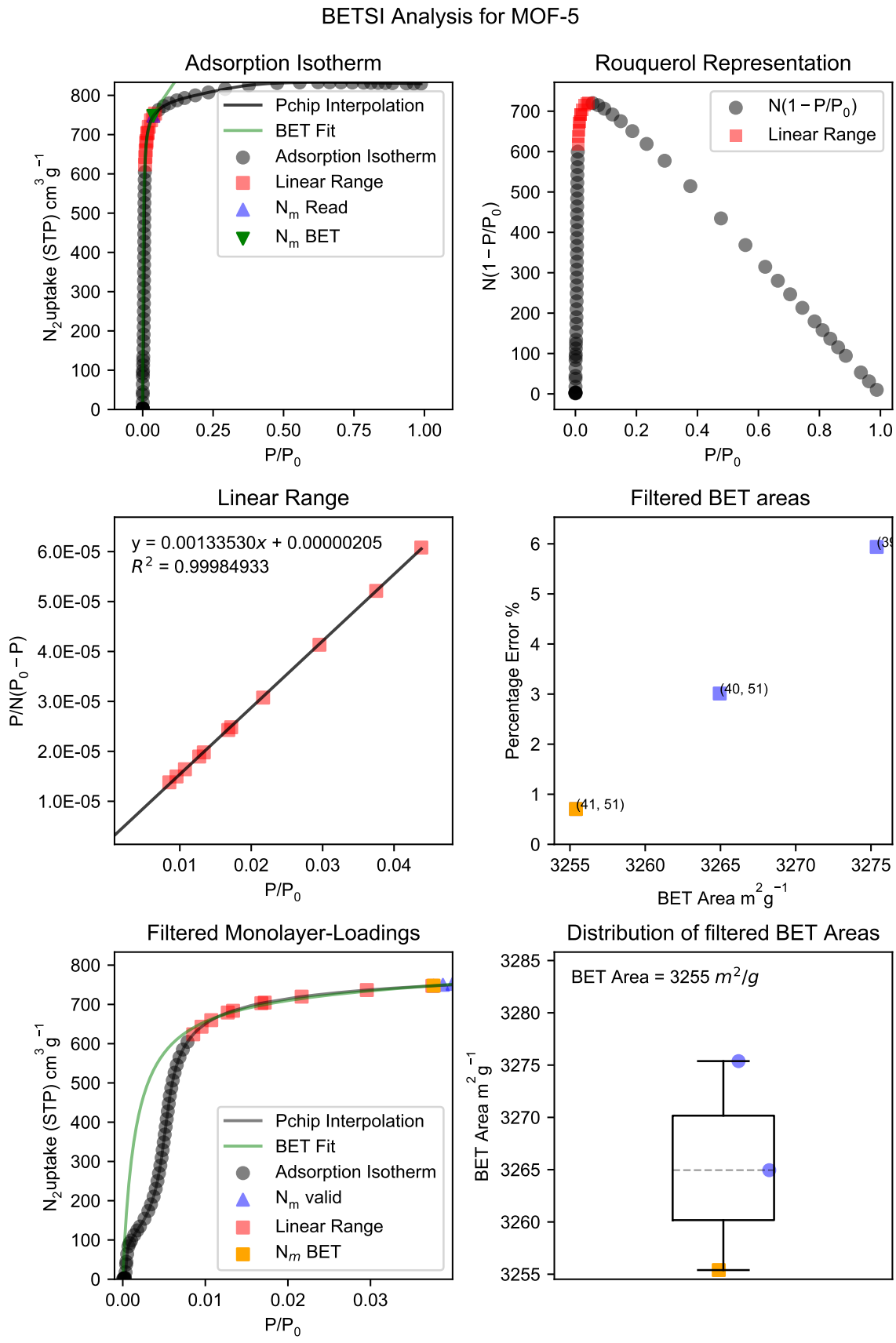

Fig. B.11 BETSI Results for MOF-5

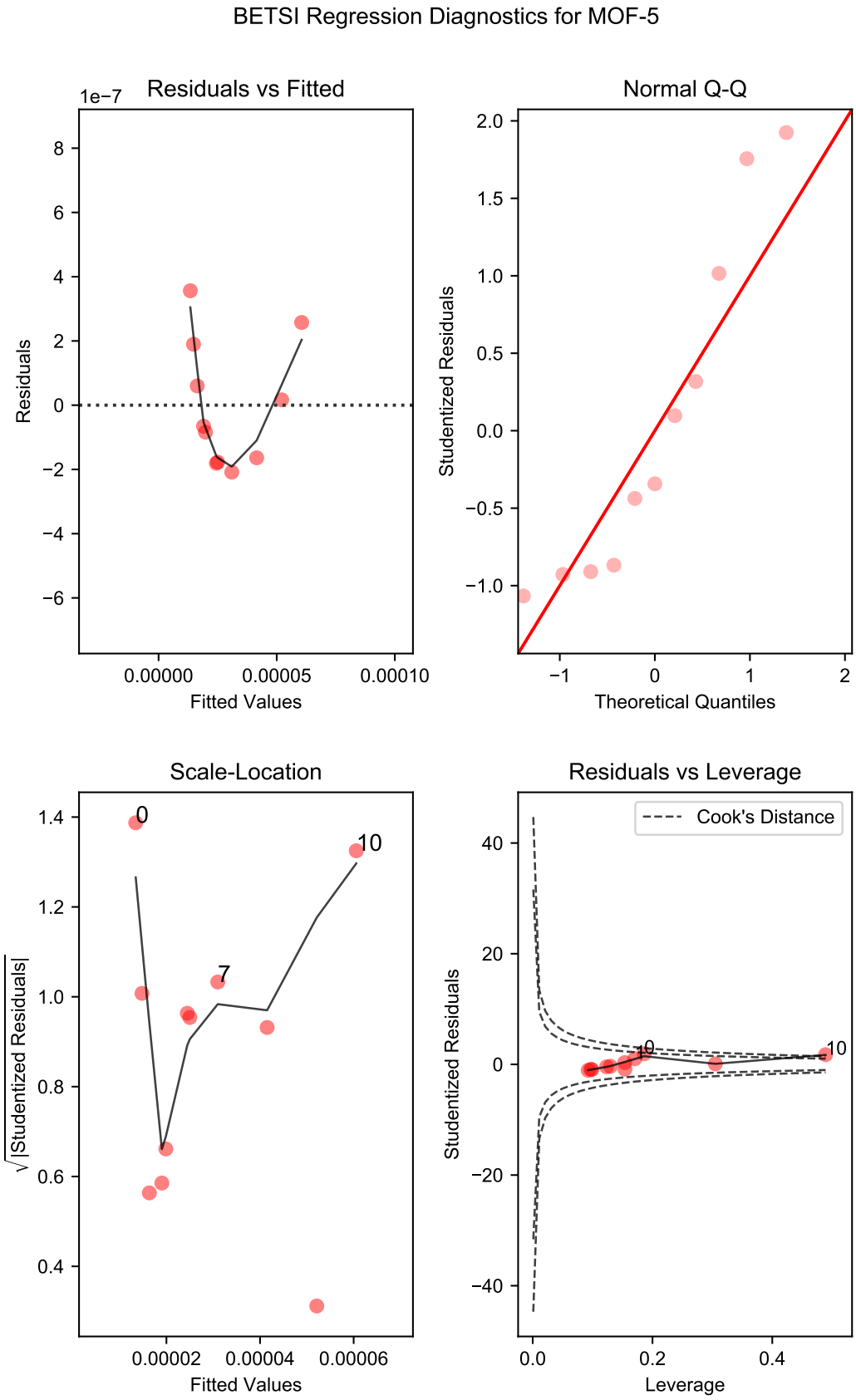

Fig. B.12 Regression Diagnostics for MOF-5

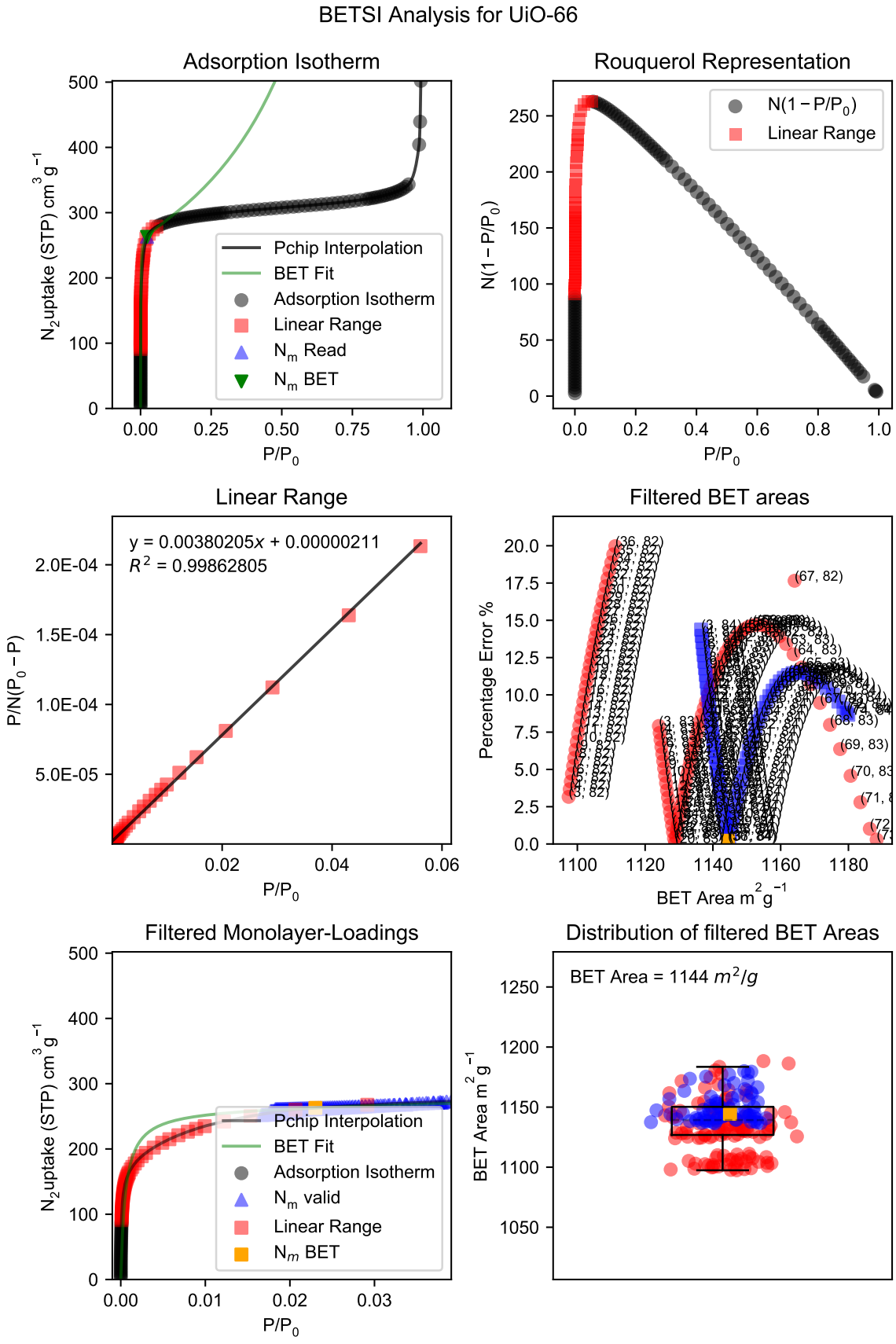

Fig. B.13 BETSI Results for UiO-66

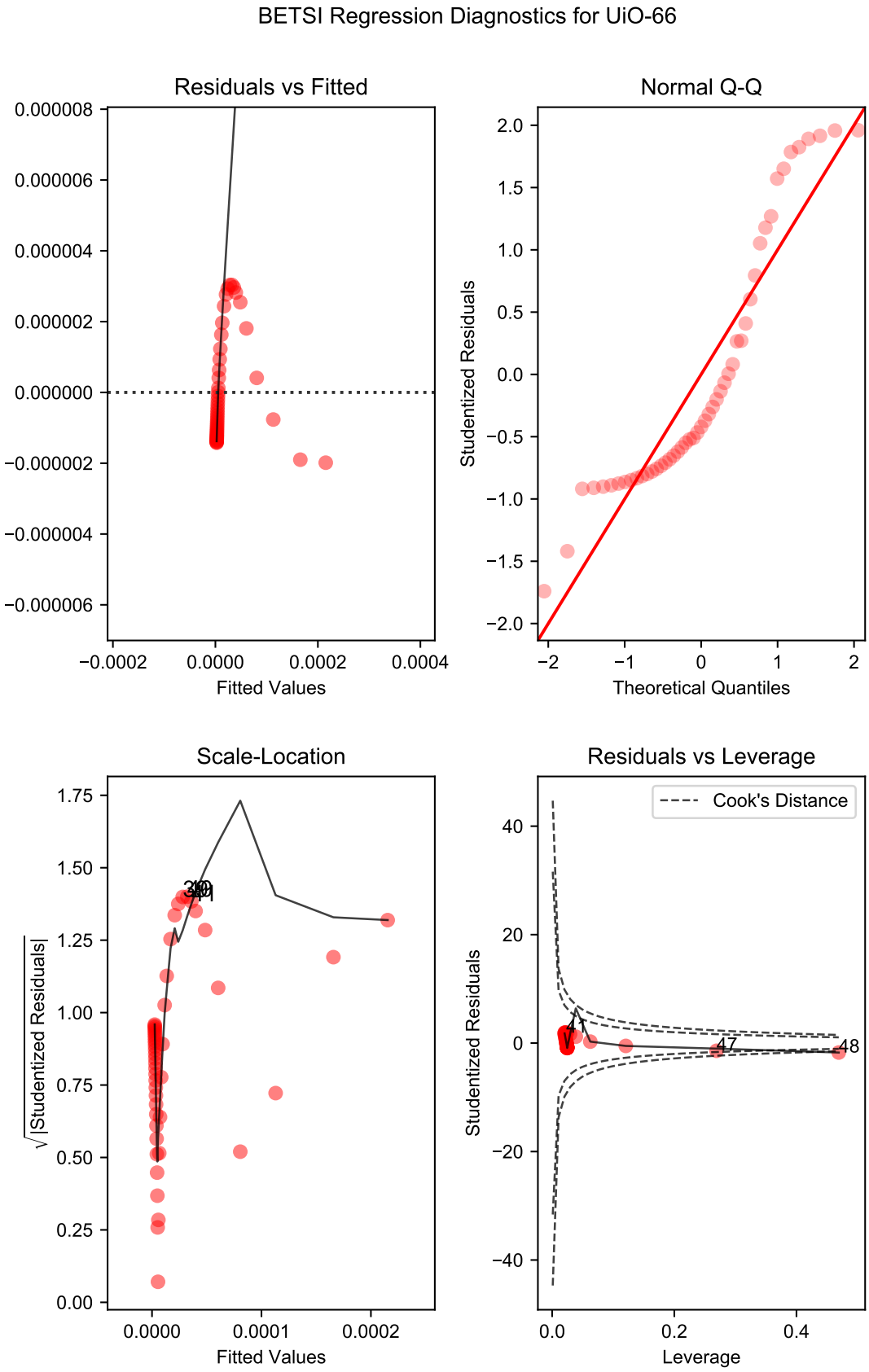

Fig. B.14 Regression Diagnostics for UiO-66

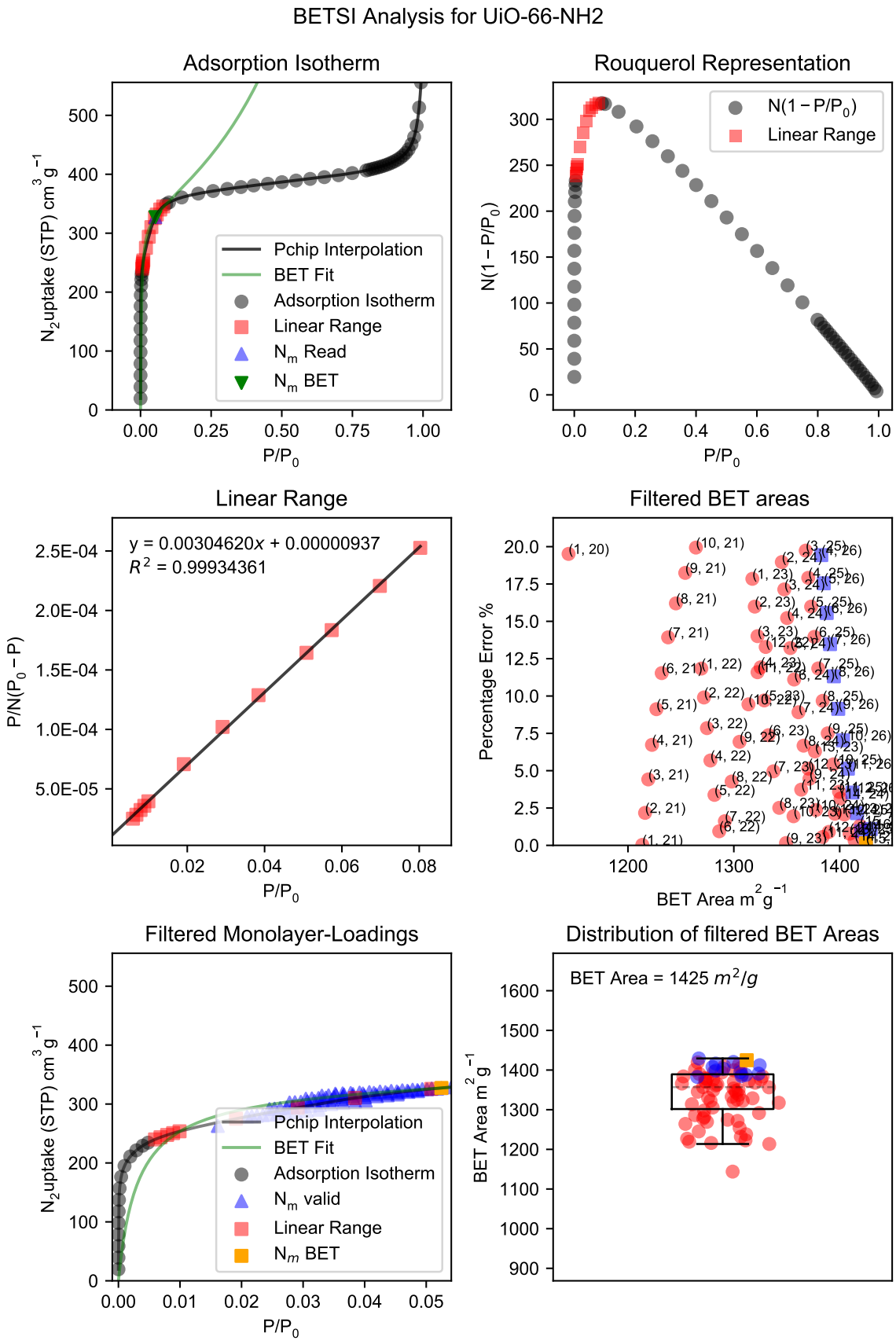

Fig. B.15 BETSI Results for UiO-66-NH2

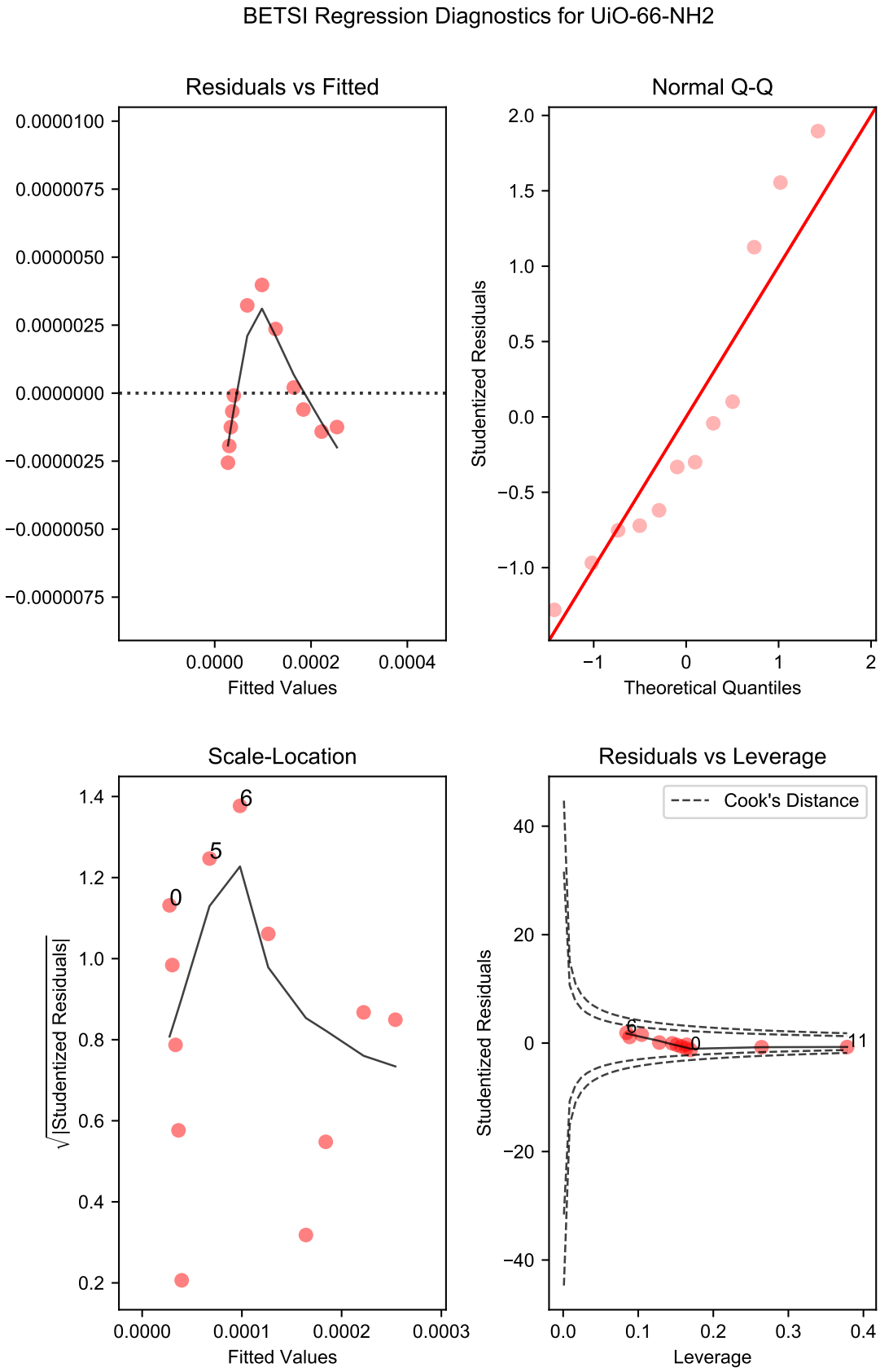

Fig. B.16 Regression Diagnostics for UiO-66-NH2

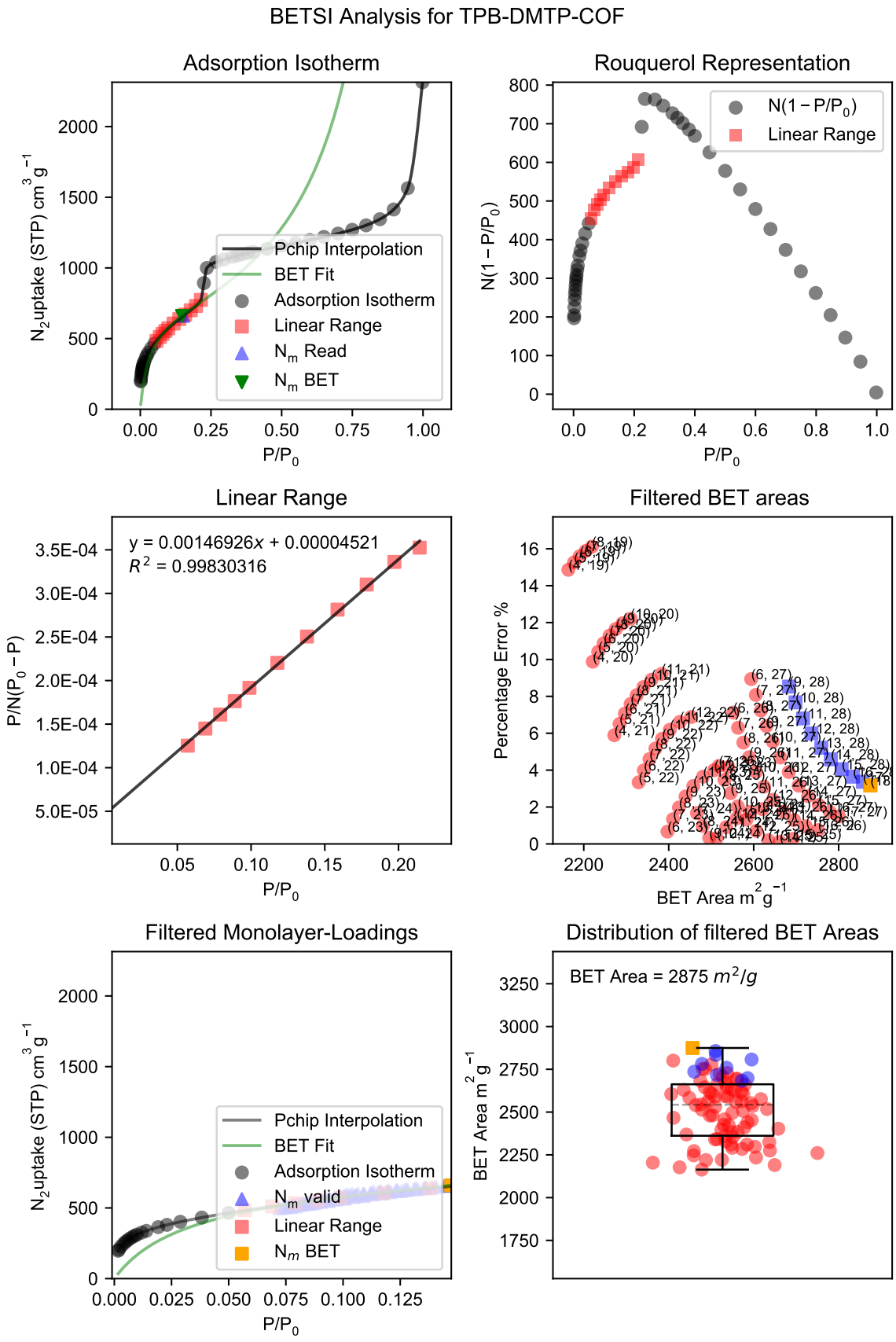

Fig. B.17 BETSI Results for TPB-DMTP-COF

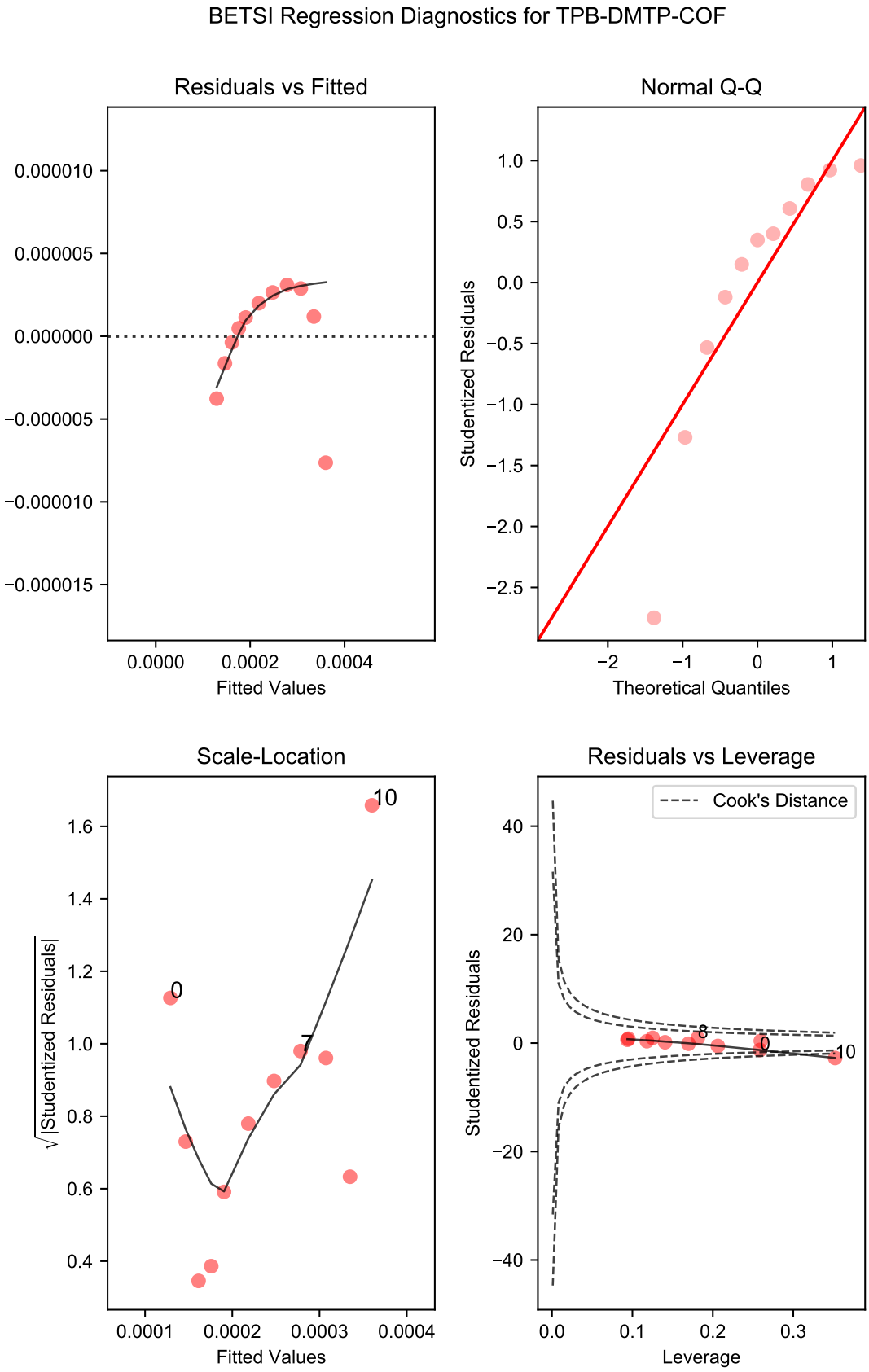

Fig. B.18 Regression Diagnostics for TPB-DMTP-COF

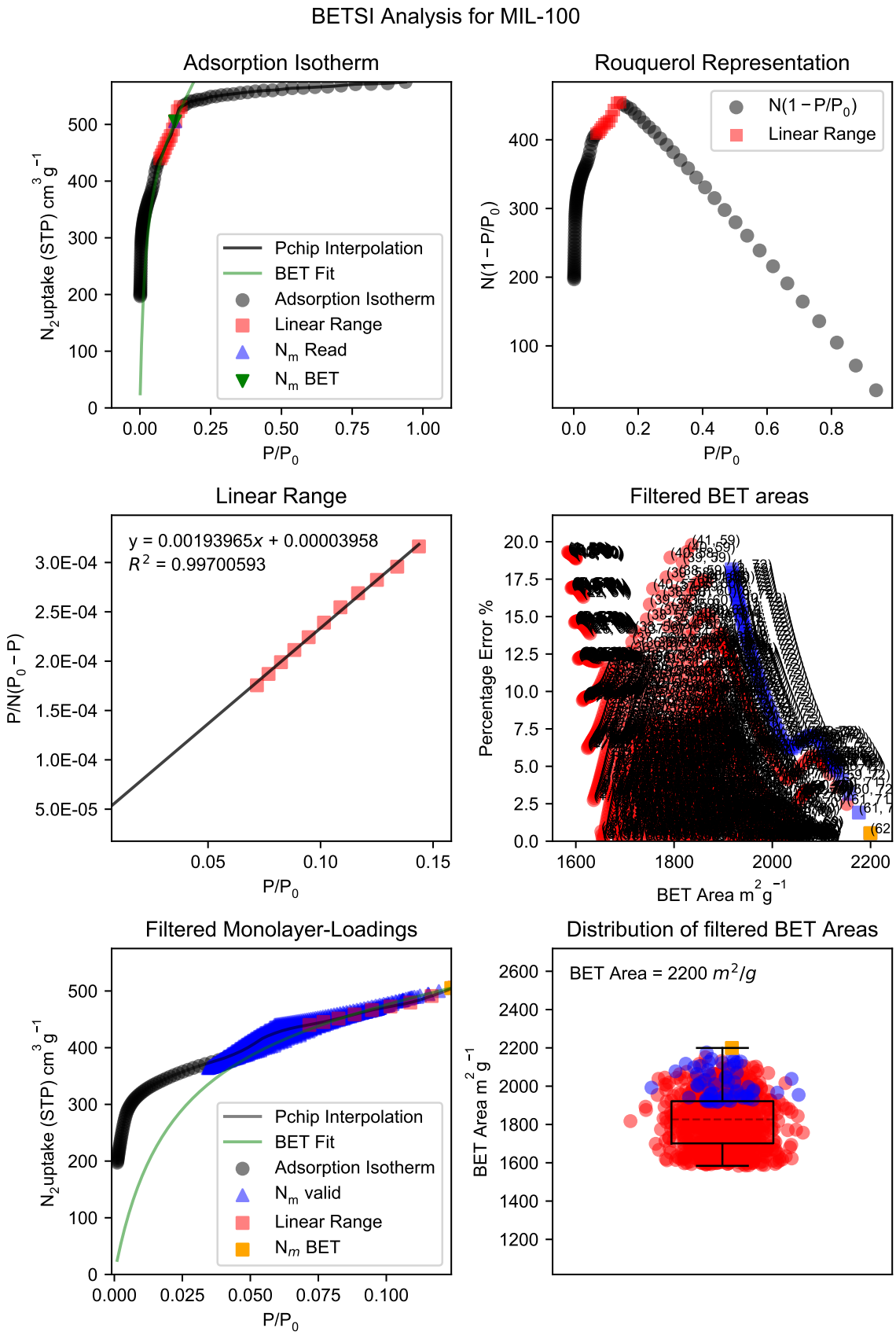

Fig. B.19 BETSI Results for MIL-100

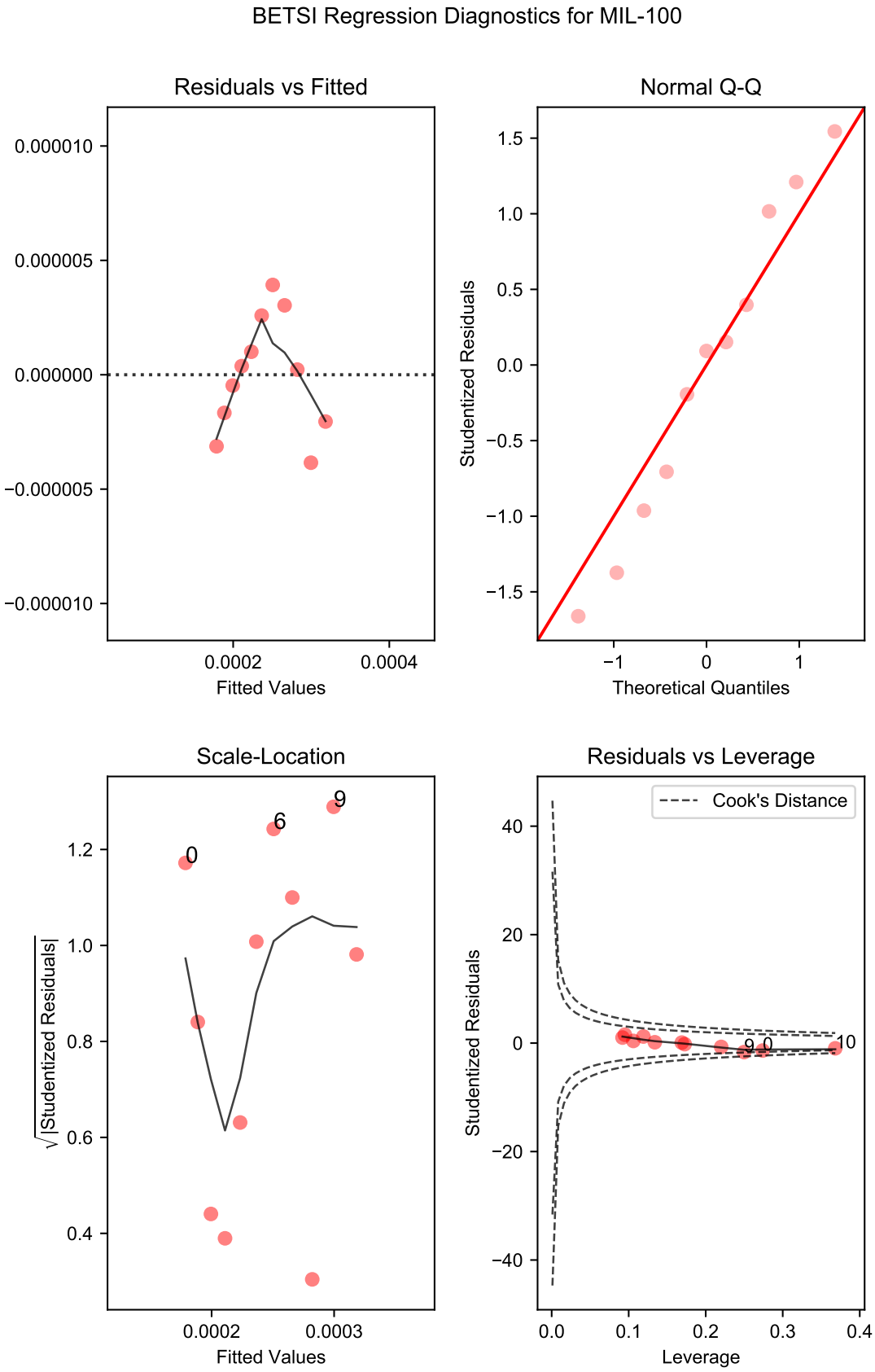

Fig. B.20 Regression Diagnostics for MIL-100

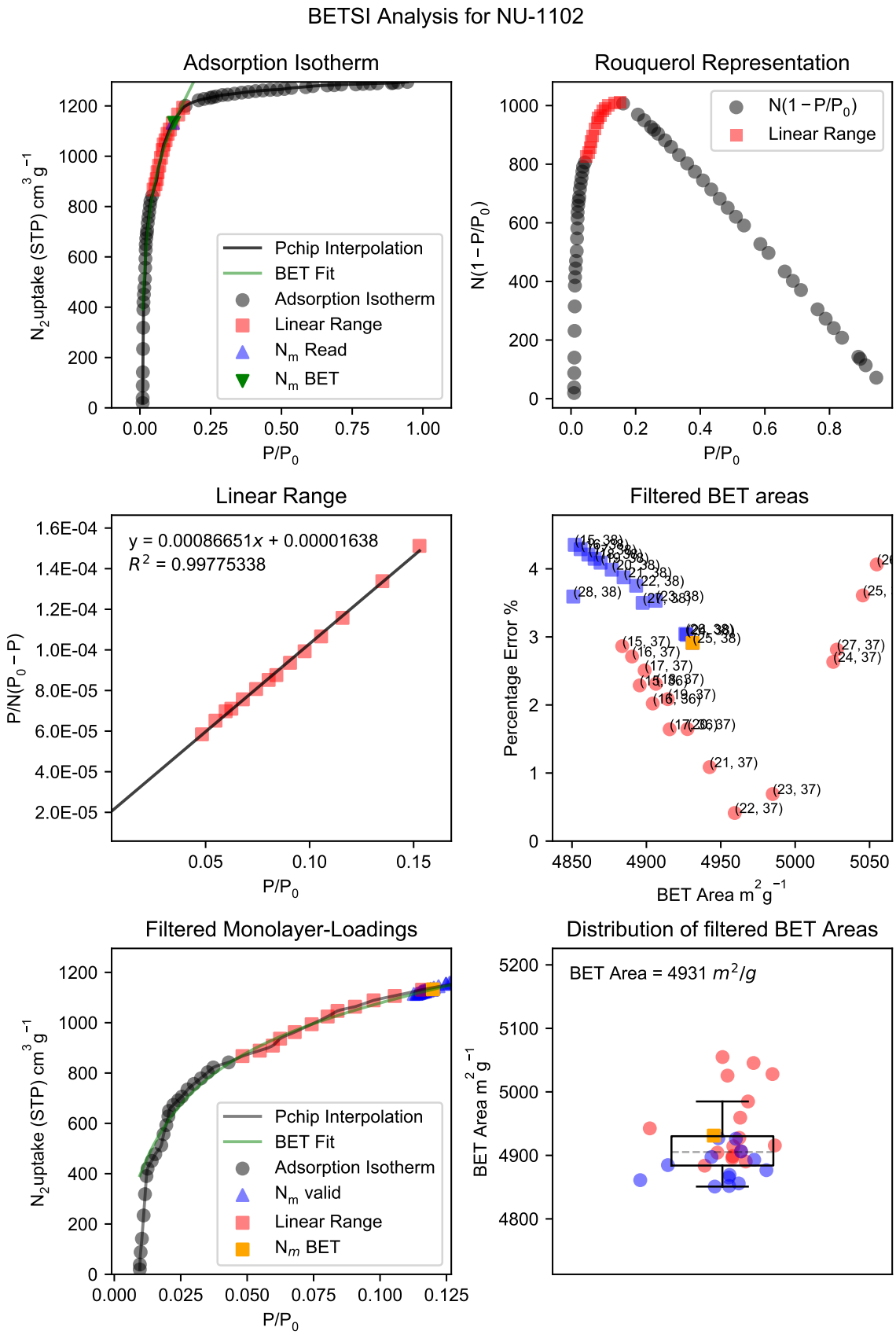

Fig. B.21 BETSI Results for NU-1102

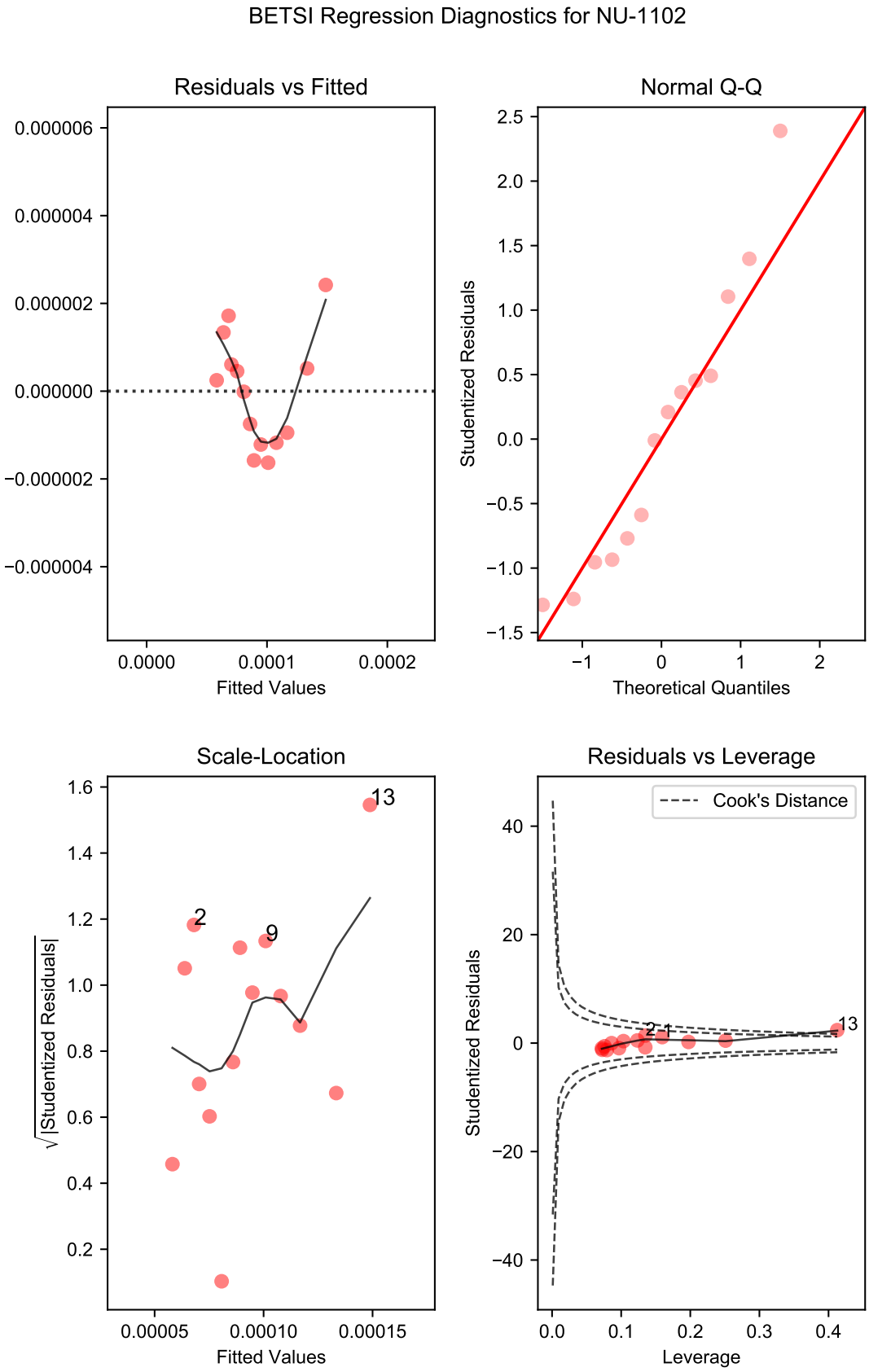

Fig. B.22 Regression Diagnostics for NU-1102

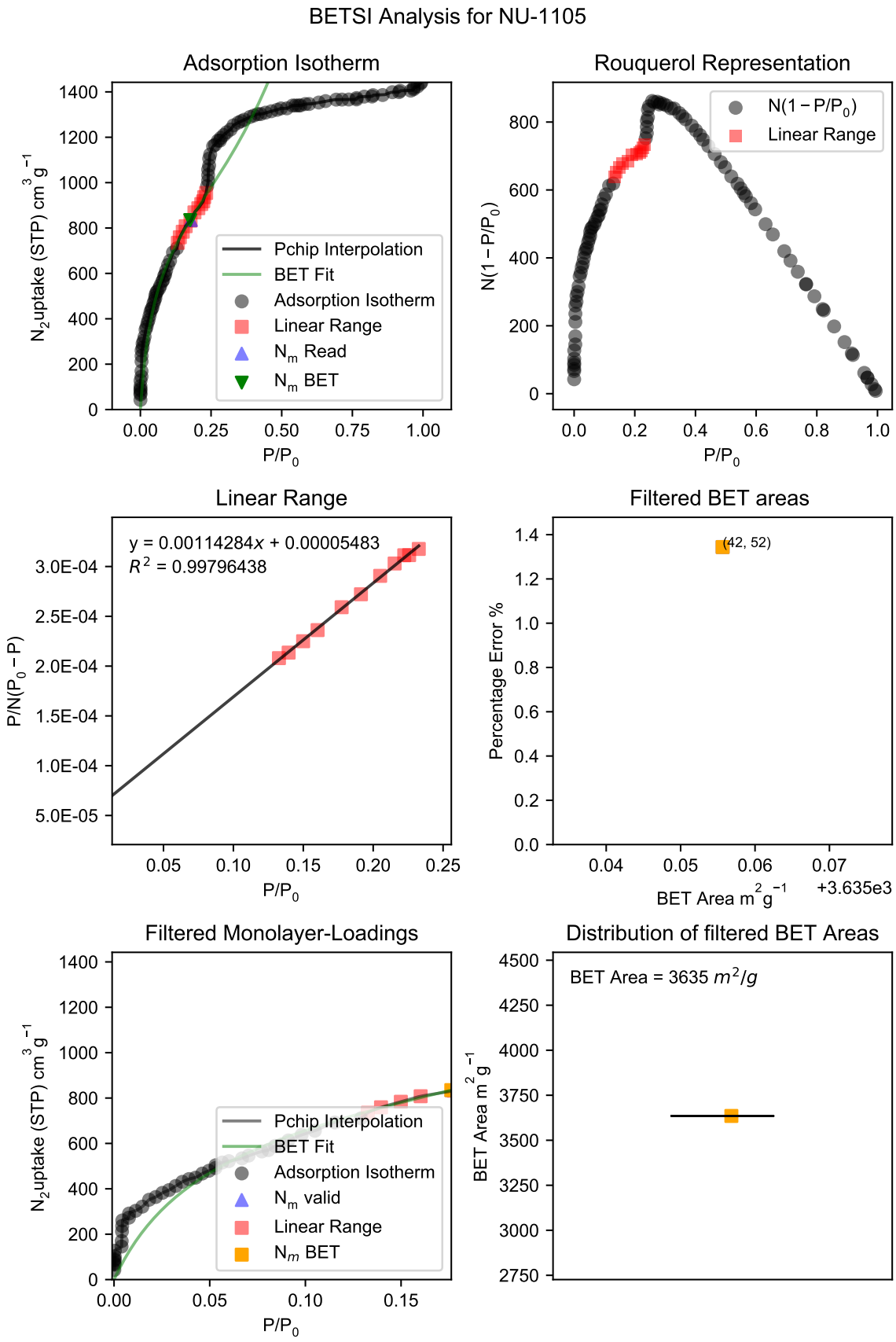

Fig. B.23 BETSI Results for NU-1105

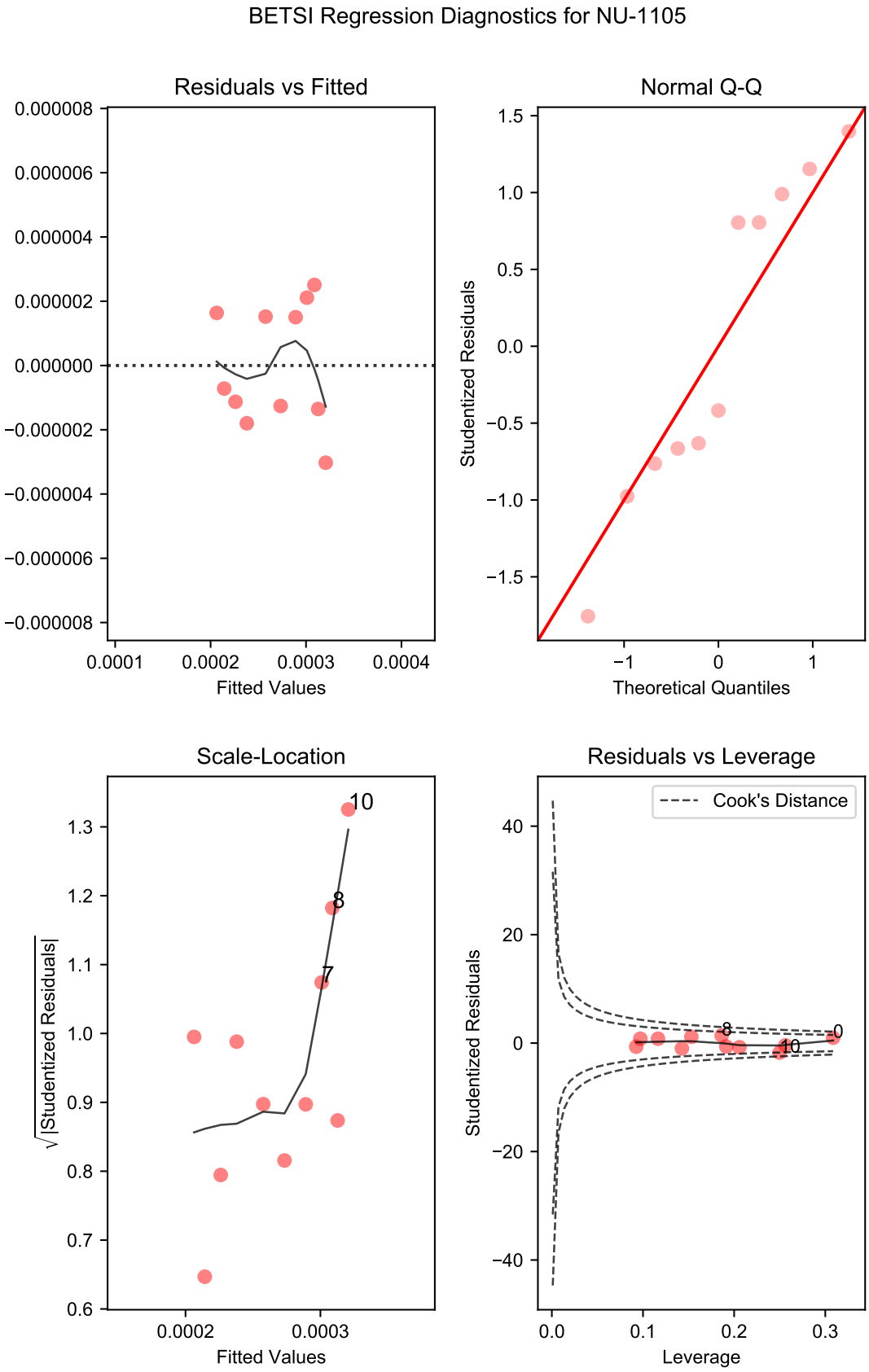

Fig. B.24 Regression Diagnostics for NU-1105

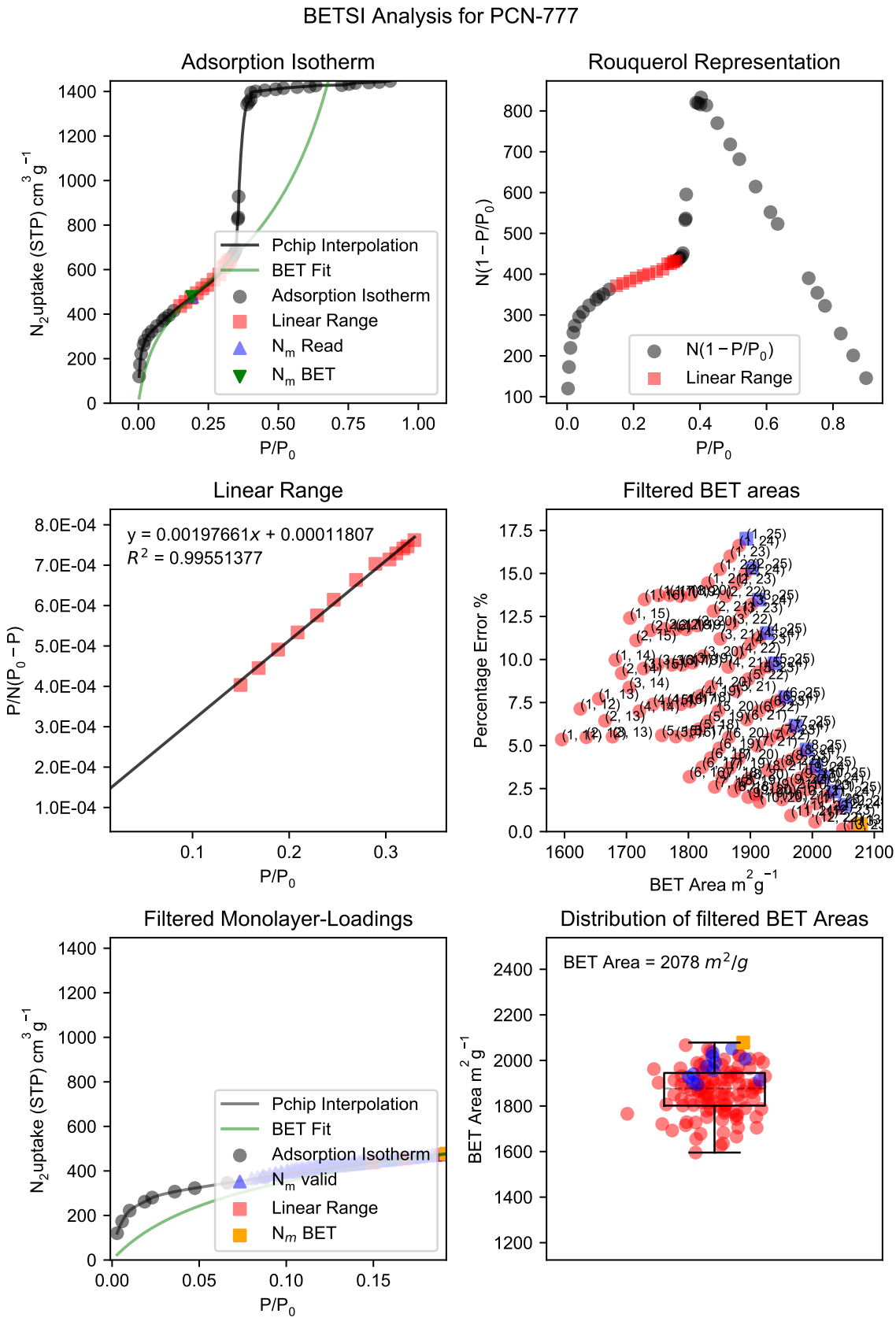

Fig. B.25 BETSI Results for PCN-777

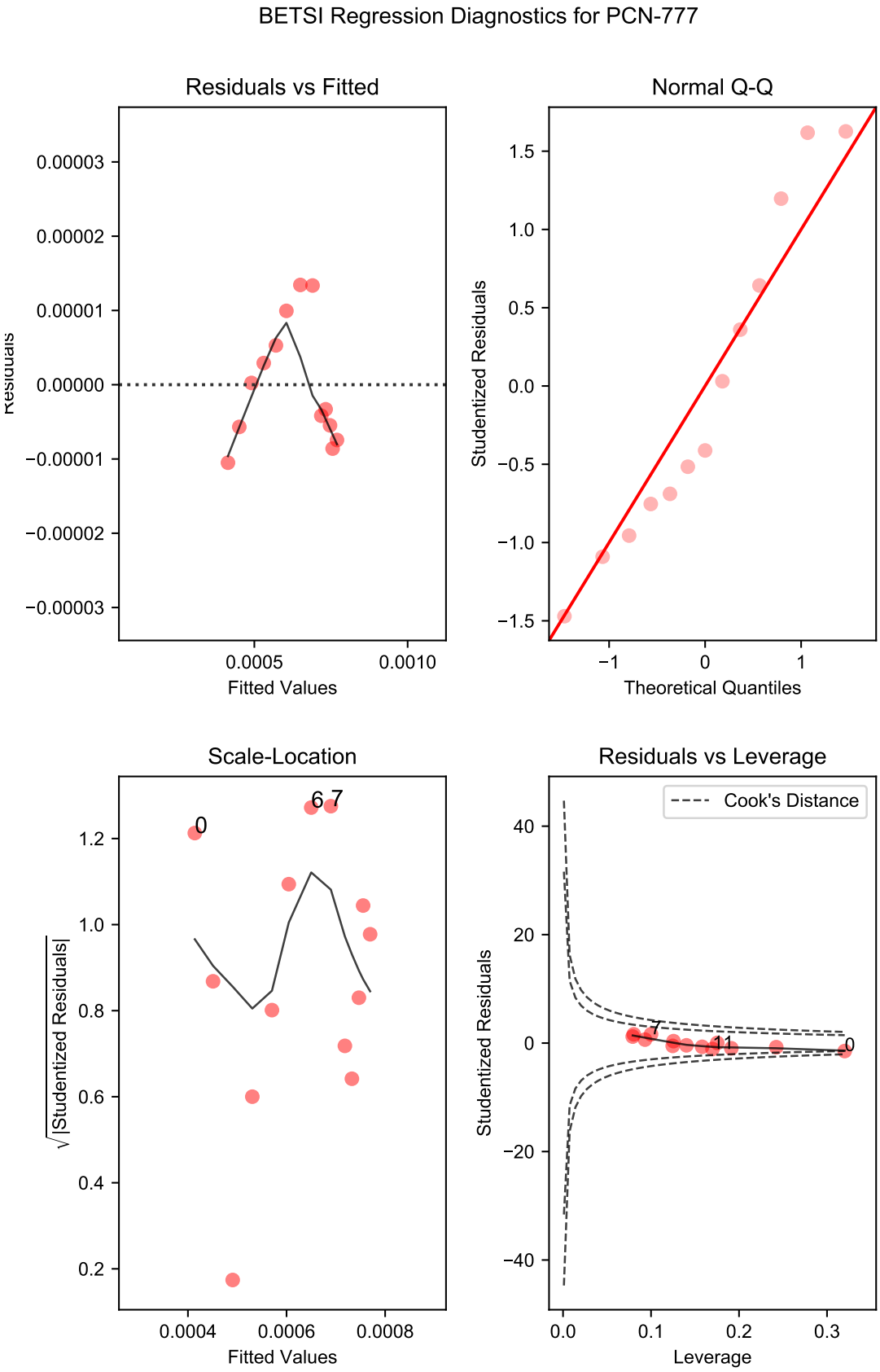

Fig. B.26 Regression Diagnostics for PCN-777

Appendix C

TIAMAT Designs for the sql and fes Nets

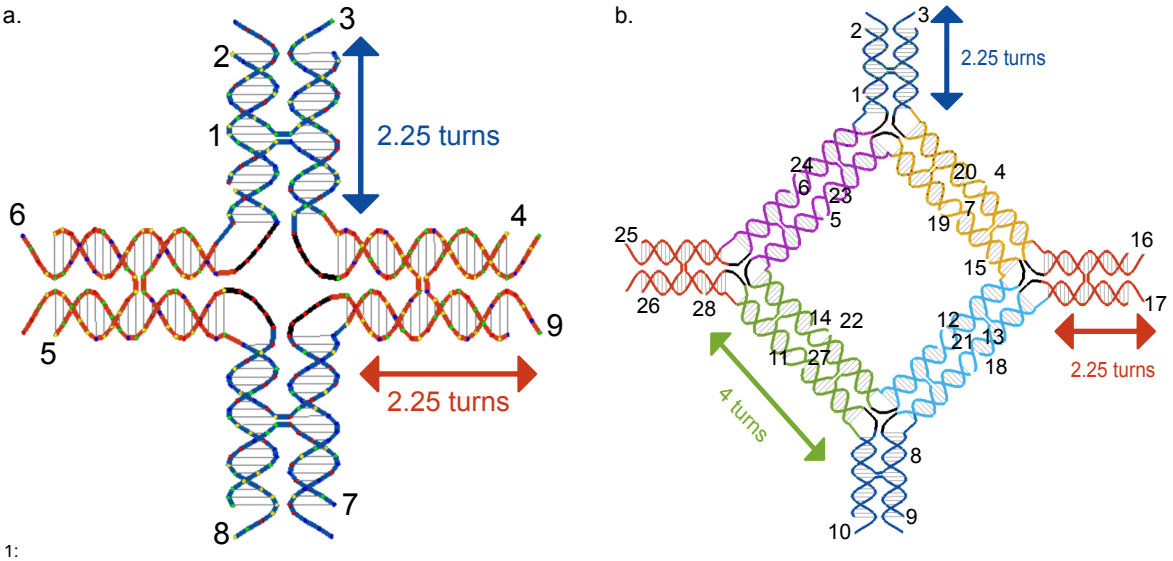

1: TGTTGGAAAGGGATCGTTTTCTACGTAGGGGCAGTCAGGTCTTTTTTCTTATGTCTGTAGAAGTGTTTTTGTAAGTGGAACCCATGCCGAATTTTACGAG; 2: GACCAGTACGGCCAACACTCGTTTCGGCATGGCGTTGAAATGG, 3: CAGCTCACCTCTGGCCCGTACTGGTCTTTA, 4: GCCCGGGGGACCCCCTACGTAGCGATCCCTTTGCCAGAGGTGA, 5: GCGCCTCCCACGTTCCACTTACACACTTCTACGGTAACGGCCC, 6: ACTGCCATTTCAACGGTGGGAGGCGCGCTT, 7: ACTTATGCAAAAGACATAAGAAGACCTGACTGTCCGCTCCTGA, 8: GCTGGGGCCGTTACCTTTGCATAAGTTAAA, 9: CAGTTCAGGAGCGGAGTCCCCCGGGCAAGC;

1: ATTACGTGGCATTGTTTTTGGCTCCAATATCGCACCACCCTTTTGCCGACGGCCCATCTCCAAGTTTCAGCG; 2: GACCAGTACGGCGTAATCGCTGCTTGGAGATGTACCTATAG, **3: CAGCTCACCTCTGGCCCGTACTGGTCTTTA,** 4: GGCGGGCGGGATATATTGGAGCCAACAATGCCAGCCAGAGGTGA, 5: TTCGGGAGGTGCGGCCGTCGGCAGGGTGGTGCGTACAACAGG, 6: AAATCTATAGGTAGCACCTCC, 7: ATGGCCTGTTGTAATCCCGCC, 8: CCTGACAGCAACATAAGTGTTTTTACGGTTCTAGAGCGGCTACCTTTTTGCTTCTCATAGCAACTAGTCTTT, 9: ACTTATGCAAATTGCTGTCAGGGACTAGTTGCTACAGATGG, **10: GCTGGGGCCGTTACCTTTGCATAAGTTAAA** 11: ATATCGGCGTACTCTAGAACCGTAACACTTATGGGTAACGGCCC, 12: AGGCACCGGGGGTATGAGAAGCAAGGTAGCCGCCGAGTTCGA,13: ACCGCCATCTGTACCCCCGGT, 14: GAGCTCGAACTCGGTACGCCG 15: GGTAACAGCTGCTCATTTGAGGTGCAATCCTGTTTGCAGTTTCGCGTAGATCGCGATTCGCTTTTTATCGAA, 16: GCCCGGGGGACGATTGCACCTCTGAGCAGCTGTGGTCAAGG, **17: CAGTTCAGGAGCGGAGTCCCCCGGGCAAGC,** 18: CGGTGATTGGCACGATCTACGCGCTGCAAACAGTCCGCTCCTGA, 19: CCATAGTCGAAGTTACCTTCGATAAGCGAATCGAATAAGACA, 20: CGCCCCTTGACCACTTCGACT, 21: GCCTTGTCTTATTTGCCAATC, 22: GCTCAAGATAGATAAAGGACGGGCGAGGACTCCTCCCCATGT, 23: CGAAACATGGGGAGTCCTAAG, 24: ATTTCTTAGGACGACCGTGCTTGAATCCTGTCACGTTGAAATGG, **25: ACTGCCATTTCAACGGTGGGAGGCGCGCTT,** 26: GCGCCTCCCACGCGCCGGGATCACCGTTCACGTTTCCCCCA, 27: ATATTGGGGGAAATCTATCTT, 28: GGCGCTGACAGGATTTTTCAAGCACGGTCGGAGTCCTCGTTTCCCGTCCTTTACGTGAACGGTTTTGATCCC

Fig. C.1 TIAMAT Designs for the **sql** and **fes** Nets | a. **sql** net b. **fes** net